



Forschungszentrum Karlsruhe
Technik und Umwelt

Wissenschaftliche Berichte
FZKA 6035

Thermo-mechanical Tests with the First Wall Mock-up TS1

G. Hofmann, E. Eggert, M. Kamlah

Institut für Angewandte Thermo- und Fluidodynamik
Institut für Materialforschung
Projekt Kernfusion

Februar 1998

FORSCHUNGSZENTRUM KARLSRUHE
Technik und Umwelt
Wissenschaftliche Berichte
FZKA 6035

Thermo-mechanical Tests
with the First Wall Mock-up TS1

G. Hofmann, E. Eggert, M. Kamlah

Institut für Angewandte Thermo- und Fluidodynamik
Institut für Materialforschung
Projekt Kernfusion

Forschungszentrum Karlsruhe GmbH, Karlsruhe
1998

Als Manuskript gedruckt
Für diesen Bericht behalten wir uns alle Rechte vor
Forschungszentrum Karlsruhe GmbH
Postfach 3640, 76021 Karlsruhe
Mitglied der Hermann von Helmholtz-Gemeinschaft
Deutscher Forschungszentren (HGF)
ISSN 0947-8620

Abstract

A First Wall mock-up of the design for the Next European Torus (NET) was available for experiments as a water-cooled steel structure. The mock-up has not been thought to become a thermal fatigue specimen because of its pre-damage by a large number of thermocouple holes. It was rather used as a prototypical background structure for thermo-mechanical tests of carbon-based protection tiles and their attachment schemes.

In a first series of tests the bare mock-up was thermally loaded by a heat flux to its surface. In this case, the strains measured on its back side verified a corresponding FE model prediction reasonably.

In a second series the mock-up was protected by a radiatively cooled tile that was not in close thermal contact with the mock-up; these tests revealed the great importance of appropriately sized gaps that allow the full differential expansion and bowing also during thermal transients.

Finally, the mock-up was protected by conductively cooled tiles which, with an intermediate layer of flexible graphite, were pressed to the surface of the mock-up. The heat transfer characteristics of the compliant layer turned out to be uniform and reliable even after thermal cycles at high temperatures.

Thermomechanische Versuche mit dem First Wall Mock-up TS1

Zusammenfassung

Ein Ausschnitt (Mock-up) der Ersten Wand vom Design für den Next European Torus (NET) stand als wasser-gekühlte Stahl-Struktur für Experimente zur Verfügung. Weil der Mock-up Vorschädigungen durch eine große Zahl von Thermoelement-Bohrungen aufwies, war er nicht für thermische Ermüdungsexperimente vorgesehen; vielmehr wurde er als prototypische Hintergrundstruktur verwendet für thermomechanische Tests mit Schutzziegeln auf Graphit-Basis und deren Haltevorrichtungen.

In einer ersten Testreihe wurde die Oberfläche des ungeschützten Mock-ups einer thermischen Last ausgesetzt. Die Vorhersage einer FE Modellrechnung konnte mit Dehnungen, die auf seiner Rückseite gemessen wurden, in vernünftigem Umfang bestätigt werden.

In einer zweiten Testreihe wurde der Mock-up mit einem strahlungs-gekühlten Ziegel, der nicht in engem thermischen Kontakt mit dem Mock-up stand, geschützt. Die Tests zeigten, daß es sehr wichtig ist, auf angemessen dimensionierte Spalte zu achten, die Unterschiede in der thermischen Ausdehnung und Verbiegung auch während der thermischen Transienten zulassen.

Schließlich wurde der Mock-up mit leitungs-gekühlten Ziegeln, die mit einer Zwischenschicht aus flexiblem Graphit auf den Mock-up gedrückt wurden, geschützt. Die Testergebnisse zeigten, daß der Wärmeübergang an der Kontaktschicht gleichmäßig war und auch nach thermischen Zyklen auf hohem Temperatur-Niveau zuverlässig erhalten blieb.

Contents

1.	Introduction	1
2.	First Wall Mock-up TS1	2
2.1	Geometry, Material and Manufacturing	2
2.2	Testing at JRC Ispra	3
2.3	Constructive Changes to TS1	4
2.4	Topography of the Heated Surface	6
3.	FIWATKA as a Test Environment for TS1	8
3.1	Experimental Setup	8
3.2	Experimental Procedure in General	9
4.	Thermo-mechanical Testing of the Bare TS1 without Protection Tiles	11
4.1	Goals of the Investigation	11
4.2	Instrumentation of the Specimen TS1	11
4.3	Testing	15
4.3.1	Experimental Set-up	15
4.3.2	Experimental Procedure and Test Sequence	16
4.3.3	Data Processing	19
4.4	Experimental Results and Discussion	20
4.4.1	Temperatures in TS1	20
4.4.2	Strains on the Back Side of TS1	23
4.5	FE Modelling Results and Comparison	28
4.5.1	General Remarks	28
4.5.2	Thermal Analysis	30
4.5.3	Mechanical Analysis	32
4.6	Conclusions	38
5.	Thermo-mechanical Testing of TS1 with Radiatively Cooled Tiles	39
5.1	Design Concept and Specimens	39
5.2	Goals of the Investigation	41
5.3	Instrumentation of Specimens	42
5.3.1	Pyrometer Directed to the Tile Back Side	42
5.3.2	Thermocouples in the Area of the Attachment Studs	42
5.3.3	Displacement Sensors (LVDTs)	44
5.4	Testing	46
5.4.1	Experimental Set-up	46
5.4.2	Experimental Procedure and Test Sequence	47
5.4.3	Data processing	49
5.5	Experimental Results	50
5.5.1	Tile Attachment Scheme	53
5.5.1.1	Clearance at the Spacer Pads	53
5.5.1.2	Survival of the Attachment Scheme	54
5.5.2	Thermal Bowing of TS1 and Tiles	56
5.5.2.1	Shape of the TS1 under Thermal Load	56
5.5.2.2	Change of the Gap between TS1 and Tile under Thermal Load	61

5.5.3	Thermal Conduction through the Attachment Studs	64
5.5.3.1	Mechanical Behaviour at the Tile Attachment	64
5.5.3.2	Temperature Transients at the Attachment Areas of SZ2 and SZ3	66
5.5.3.3	Temperature Transients at the Attachment Areas of SZ1	71
5.6	FE Modelling Results and Comparison	72
5.6.1	General Remarks	72
5.6.2	Clearance at the Spacer Pads	73
5.6.3	Differential Displacement of TS1 and Tile	73
5.7	Conclusions	74
6.	Thermo-mechanical Testing of TS1 with Conductively Cooled Tiles	77
6.1	Design Concept and Goals of the Investigation	77
6.2	Test Specimens	77
6.2.1	Compliant Layer	78
6.2.2	Mounting of the Tiles	78
6.2.3	Instrumentation of Specimens	80
6.3	Testing	83
6.3.1	Experimental Set-up	83
6.3.2	Experimental Procedure and Test Sequence	84
6.3.3	Test Evaluation and Data Processing	87
6.4	Experimental Results	92
6.4.1	Heat Transmittance	92
6.4.2	Break-up of Transmittance into Conduction and Contact Heat Transfer	97
6.4.3	Temperatures in the Structure	100
6.4.4	Behavior of the Compliant Layer	103
6.5	Conclusions	106
	Acknowledgement	107
	References	108
	Appendix A	A1
	Determination of the Heat Flux into the Conductively Cooled Tiles	A1
	Appendix B	B1
	Data on CL Heat Transmittance	B1
	Appendix C	C1
	Influence of the Test History on Heat Transmittance	C1
	Appendix D	D1
	Characterization of the Deformation Behavior of Papyex	D1

1. Introduction

During the development work for the tokamak fusion device called Next European Torus (NET) the NET Team at Garching came up with a first wall (FW) design for this machine. It is a water-cooled FW made from austenitic stainless steel and characterized by a special manufacturing process of the steel wall and by graphite protection tiles mechanically attached to that wall. A manufacturing process called "transparent electron beam welding" was selected for building subunits of the FW each one containing four coolant channels in poloidal direction: Two mechanically machined half-walls each containing open halves of the circular coolant channels are welded together to complete and close the channels and this is done by welding two and a half junctions at the same time (transparently); a total of five welds for the four channels are done by only two welding jobs, one from each side. Several of such subunits are welded together to form a blanket segment. To protect this steel structure from erosion and thermal shocks by the plasma in the tokamak graphite tiles made of carbon fiber carbon composite (CFC) material were to be attached mechanically to the surface. Heat transfer from the tile to the steel structure was to be by one of two different mechanisms:

- (a) with the radiatively cooled tile essentially all heat is transferred by radiation from the tile to the steel; it is mounted with small attachment studs holding the tile's back in a 5-mm distance from the steel surface;
- (b) with the conductively cooled tile all heat is transferred by thermal conduction from the tile to the steel; it is pressed with a central molybdenum bolt to the first wall and the thermal contact between the two is improved by a 5-mm thick compliant layer of flexible graphite; this design should be used in high heat flux areas of the first wall in order to limit the tile temperature by the more effective conductive heat transport mechanism.

This first wall concept was to be heat-flux-tested in order to answer several questions:

- (1) what is the temperature distribution and the resulting stress/strain distribution within the first wall and how do they compare to the results of finite element (FEM) calculations ?
- (2) would the tile attachment survive thermal cycling and would it provide heat transfer to the steel structure as expected for both the radiatively and conductively cooled concepts ?
- (3) would the steel structure survive some 10^4 thermal cycles without failing by thermal-fatigue?

Two mock-ups of the first wall steel structure were manufactured by Framatome.

The first mock-up (TS1) was heavily instrumented with thermocouples and strain gauges (see Chapters 2 and 4.2.2); it was to be used for experimentally answering questions (1) and (2); it actually served as a specimen for the investigations reported below consisting of three parts, namely thermomechanical testing of TS1

- (α) without protection tiles (see Chapter 4),
- (β) with a radiatively cooled tile (see Chapter 5), and
- (γ) with conductively cooled tiles (see Chapter 6).

The second mock-up (TS2) was of the same outer dimensions as TS1 but it was more prototypical for the NET FW since it included all the manufacturing details like "transparent electron beam welding" of the FW, a corrugated FW, and additional tubes brazed into the coolant channel to form a double containment. The strength of TS2 was not influenced by instrumentation in critical positions and it was to be used to answer question (3); the testing of TS2 has been performed at JRC Ispra and is not reported here.

2. First Wall Mock-up TS1

A mock-up of the steel structure of the NET FW concept was designed by the NET Team and manufactured by Framatome and is called TS1 (test section 1); designing and manufacturing included the instrumentation with thermocouples and strain gauges.

2.1 Geometry, Material and Manufacturing

The TS1 consists of a front plate, 223x500 mm in size and 33 mm thick; two side walls are welded to the back of the front plate. In cross section they together are of U-shape as shown in Fig. 2.1. The front plate contains circular cooling channels of 17.4 mm diameter.

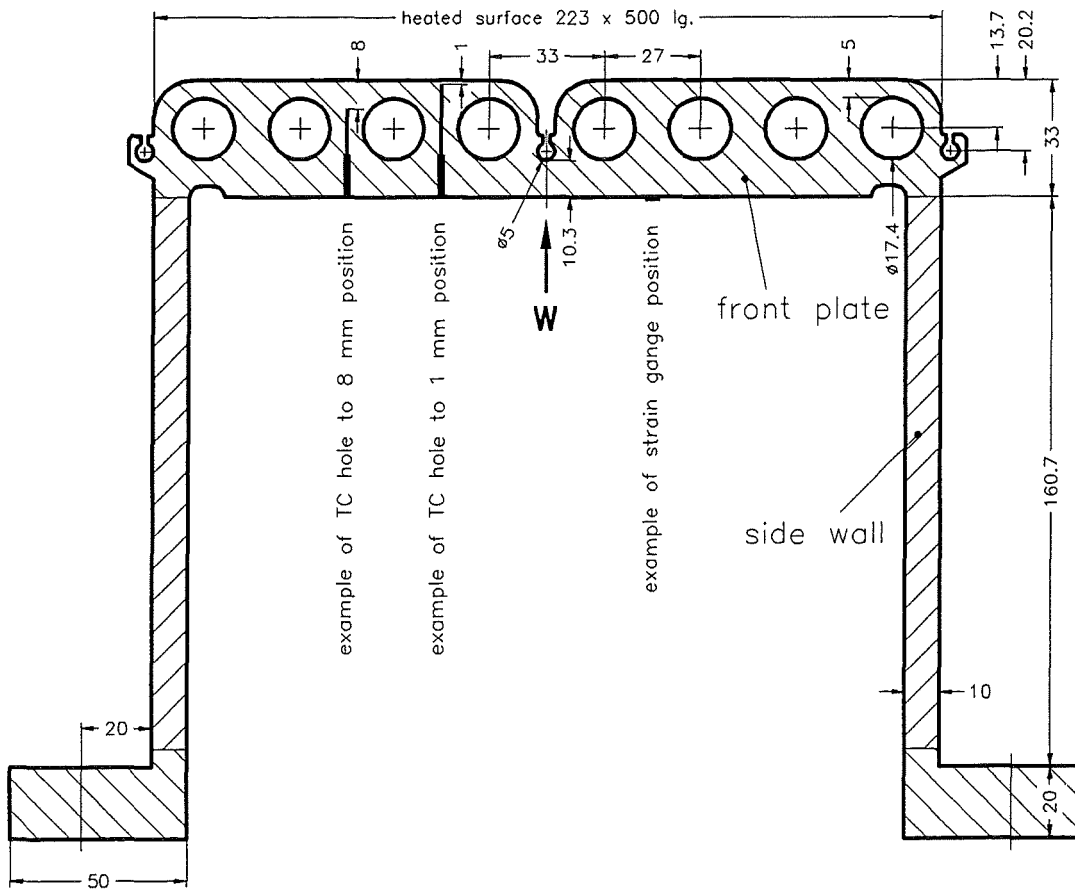


Fig. 2.1 Cross section of first wall mockup TS1

Like in the NET FW design the front plate of TS1 is subdivided into subunits containing four cooling channels each, spaced on a pitch of 27 mm. The minimum thickness of the FW between the heated surface and the cooling channel is 5 mm. Yet, the TS1 front plate was machined and drilled from one piece of steel rather than electron beam welded. Nevertheless, its final shape is that of the original design including the grooved area W between the subunits which is designed such that it may serve as an attachment point to fix any protection tiles. In this area the front plate is grooved parallel to the coolant channels and the remaining thickness is 10.3 mm. In TS1 the front plate consists of two subunits and the heated surface is plane. Similar to the segment side walls of the real device the TS1 side walls also restrain the front plate from bowing in the poloidal

direction. The flanges at the back end of the side walls may be connected to each other with strong steel bars in order to restrain the front plate to some extent also from bowing in the toroidal direction; this effect is limited though since the 10 mm thick side walls are relatively weak against bowing themselves; whenever the side walls were connected that way during a test this test will be named "constrained" through the remainder of this report.

TS1 is made from austenitic stainless steel grade AISI 316 L SPH. The plasma-facing side of the specimen was covered with a blackening layer; this layer was plasma-sprayed (atmospheric pressure spraying) by CENG at Grenoble and consists of 150 μm of $\text{Al}_2\text{O}_3 + 13\%$ TiO_2 on an undercoating of 150 μm of $\text{Ni} + 5\%$ Al . This coating was to heavily improve the emissivity of the heated surface; it was needed especially for the tests with the radiatively cooled tiles but it also in general improved the bare surface's absorption of power from radiative heat sources. The emissivity of the coating layer was determined to be $\epsilon = 0.85$ to 0.9 at layer temperatures of up to 850°C and at wave lengths above $1.3\ \mu\text{m}$ [1]. After the coating the total roughness of the heated surface was measured to be on the order of $10\ \mu\text{m}$.

More details about the manufacturing of TS1 may be found in NET First Wall Test Section, Progress Reports no. 1 (MC/TS 585), no. 2 (MC/TS 588), and no. 3 (MC/TS 892177) of June 1988 through Apr. 1989 by Framatome.

Progress report no. 3 also contains details on the instrumentation of TS1 with thermocouples and strain gauges.

In Fig. 2.1 is indicated where temperatures and strains were measured. For the thermocouples to be positioned in the front plate $2.5\ \text{mm}$ holes were drilled from the back side and were extended as $1.5\ \text{mm}$ holes to the measuring locations $1\ \text{mm}$ or $8\ \text{mm}$ away from the heated surface; this was done between the coolant channels. Strain gauges were attached to back of the front plate also in positions between the coolant channels. More details on the instrumentation that might be useful for the evaluation of the results of the present investigation are given in Chapter 4.2.2.

The photograph of Fig. 2.2 displays the first wall mock-up TS1 as it was delivered by Framatome; the top side represents the heated (plasma-facing) surface. The cooling water enters and leaves the specimen via the headers and the big flanges on the right and is diverted from one subunit to the other through the tubes on the left. The line connections had been designed as heavy pieces since it was planned to check the integrity of the coolant channels from time to time by pressure tests at up to $150\ \text{bar}$.

2.2 Testing at JRC Ispra

The TS1 was shipped in March 1989 to JRC Ispra, Institute for Advanced Materials. The specimen was installed in the thermal cycling facility that uses a bank of infra-red lamps as a heat source. TS1 was thermally cycled by applying heat fluxes of up to an estimated $66\ \text{W}/\text{cm}^2$ to its surface; cycles consisted of a 70 seconds power-on phase followed by a 55 seconds power-off phase, which did not result in steady-state conditions at the end of the phases.

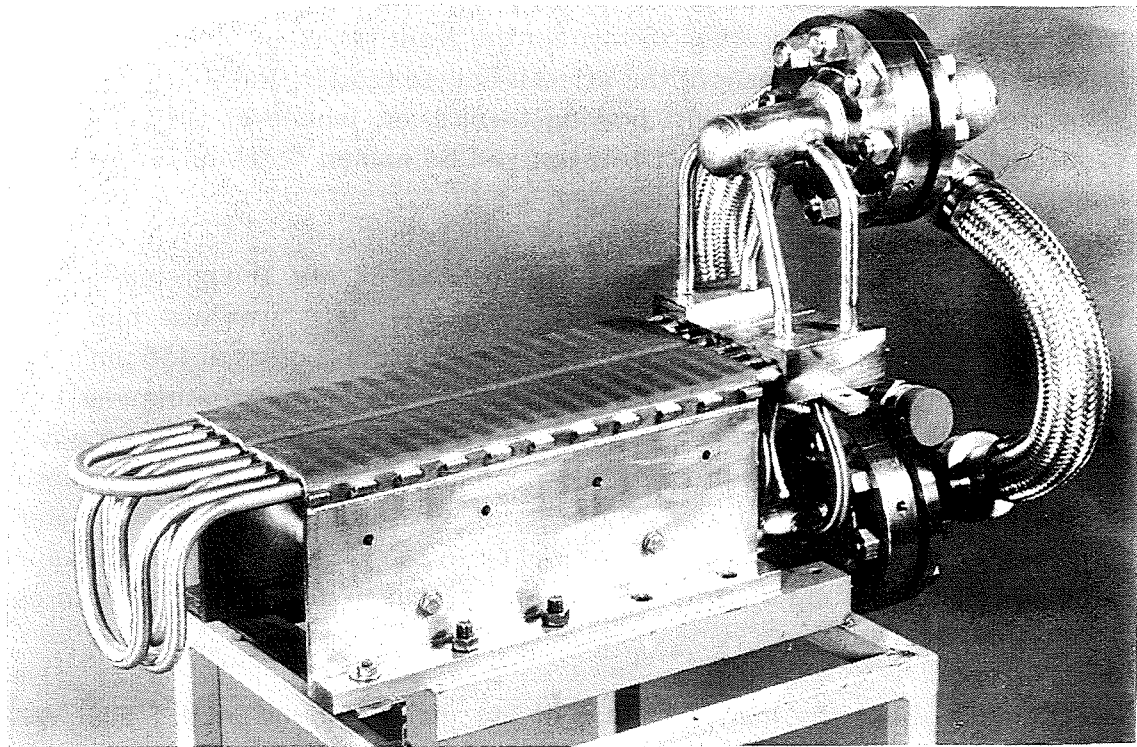


Fig. 2.2 First wall mock-up TS1, as originally manufactured with heavy headers and coolant supply flanges

Transient readings were taken from the installed thermocouples and strain gauges including strain gauges attached to the i.d. of the coolant channels. It was observed that some temperature readings were remarkably higher during the first power cycle than during any following cycles and that they did not well agree with calculated temperatures especially in areas where strain gauges had been attached inside the coolant channels; there were also inconsistencies observed with the strain gauges installed in the coolant channels. These test at JRC Ispra are reported in [2] and [4]; in this reference the specimen TS1 is called FRA-1.

2.3 Constructive Changes to TS1

The TS1 arrived at KfK from Ispra in July 1991. The specimen had to be changed constructively at the coolant headers in order to make it fit geometrically into the FIWATKA facility. The heater in the FIWATKA facility is, by intention, larger than the specimen to be heated; this is done to avoid edge effects. The heavy headers and flanges of the TS1 would have been in conflict with heater and they were no more needed any way. The coolant tubes leaving the front plate of TS1 on both sides were cut at 7 mm from the edge of TS1. As shown in Fig. 2.3 new header boxes were welded to the remainders of the tubes. Each box united the flows of only two channels in order to minimize any constraints from the headers to the specimen. On the diversion side the boxes were connected to the corresponding boxes of the other TS1 subunit. At the inlet/outlet side the two boxes of each subunit were connected to headers in the back which carry the flanges to the supply lines.

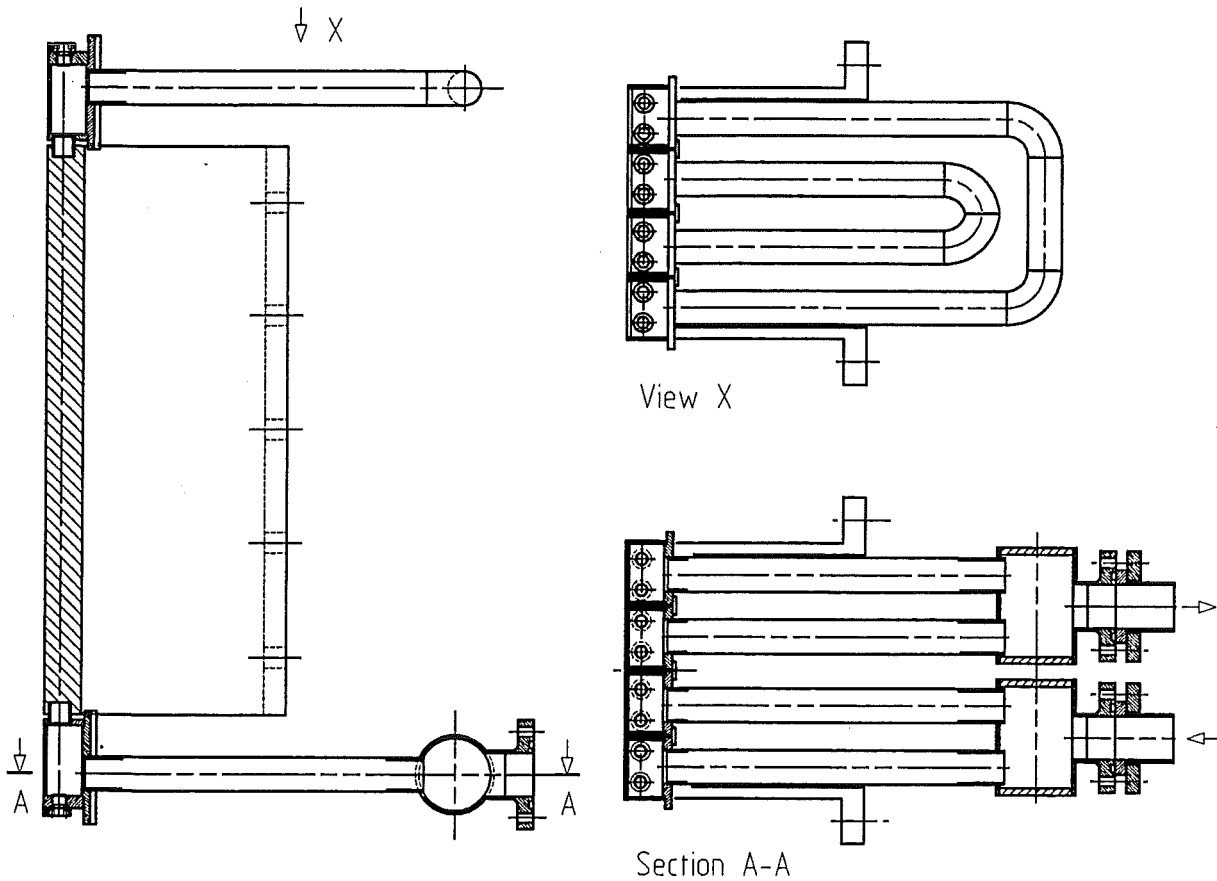


Fig. 2.3 First wall mock-up TS1 with modified coolant supply headers and connections

This reconstruction of TS1 resulted in a specimen which, including the headers, has a plane front side that may be confronted with the heater at a short distance; also the design is such that the radiation from the heater directed to the header area is caught there and does not penetrate it to the prejudice of the vacuum vessel. The header boxes include plugs for the visual inspection of the channels from both sides.

As another change to TS1 a 5 mm dia. hole and several smaller holes were drilled through the center of the front plate in the area of the weld between the two subunits indicated by "W" in Fig. 2.1; these holes were used for pyrometer measurements at the back side of the radiatively cooled tile and for TC measurements at the protection tiles reported in Chapters 5 and 6.

After the changes reported above had been applied to TS1 some coolant was observed leaking through a poor weld at the junction of the header connection tubes with the front plate (channel no. 1 of the Framatome numbering sequence); this weld obviously had been displaced when TS1 was manufactured. Since the leaking joint was not accessible to welding any more it was decided to close the leak with a sealing compound with capillary and high temperature properties (Loctite 290); this sealing survived all of the tests that followed.

2.4 Topography of the Heated Surface

Before tests with TS1 were started the flatness of its heated surface was determined; this seemed to be a valuable basic information for tests with protection tiles mounted to this surface.

The TS1 was mounted in a precision coordinate measuring device (Zeiss KMG M 550) and the topography of the surface was scanned by determining the z-coordinate in 40 points starting with $z=0$ at the coolant diversion side of TS1. The results are reported in Fig. 2.4; the dimension of the readings is 10^{-2} mm; negative readings indicate valleys.

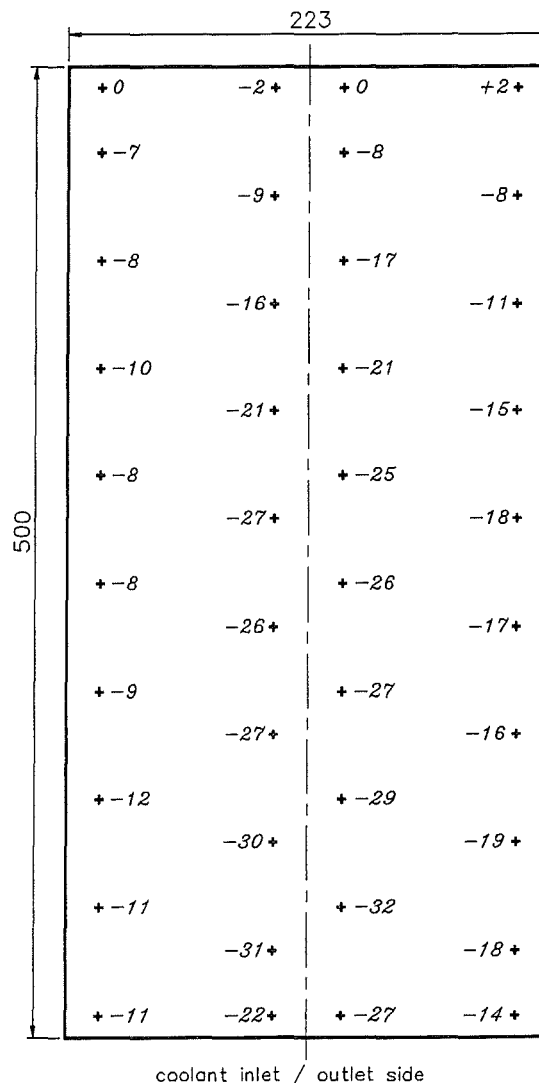


Fig. 2.4 Topography of the as received mockup TS1 (italic numbers indicate relative elevations in 10^{-2} mm)

Transversal to the coolant channels there is a flat valley covering the center part of the surface on both sides of the center groove; this valley is negligible in size on the coolant diversion side and increases to a depth on the order of 0,1 mm towards the inlet/outlet side.

Lines parallel to coolant channels and close to the TS1 edges appear rather straight (no "parallel" bowing) except for a short region close to the coolant diversion end which is bowed up somewhat.

In summary the surface seemed sufficiently flat to not cause initial problems when protection tiles were attached.

3. FIWATKA as a Test Environment for TS1

FIWATKA is a facility for thermo-mechanical tests; it was built and is operated at the Institut für Angewandte Thermo- und Fluidodynamik (IATF) of the Forschungszentrum Karlsruhe.

Its goal is to offer heat fluxes to the surface of the specimens to be tested and to also provide water flow for the specimen's cooling.

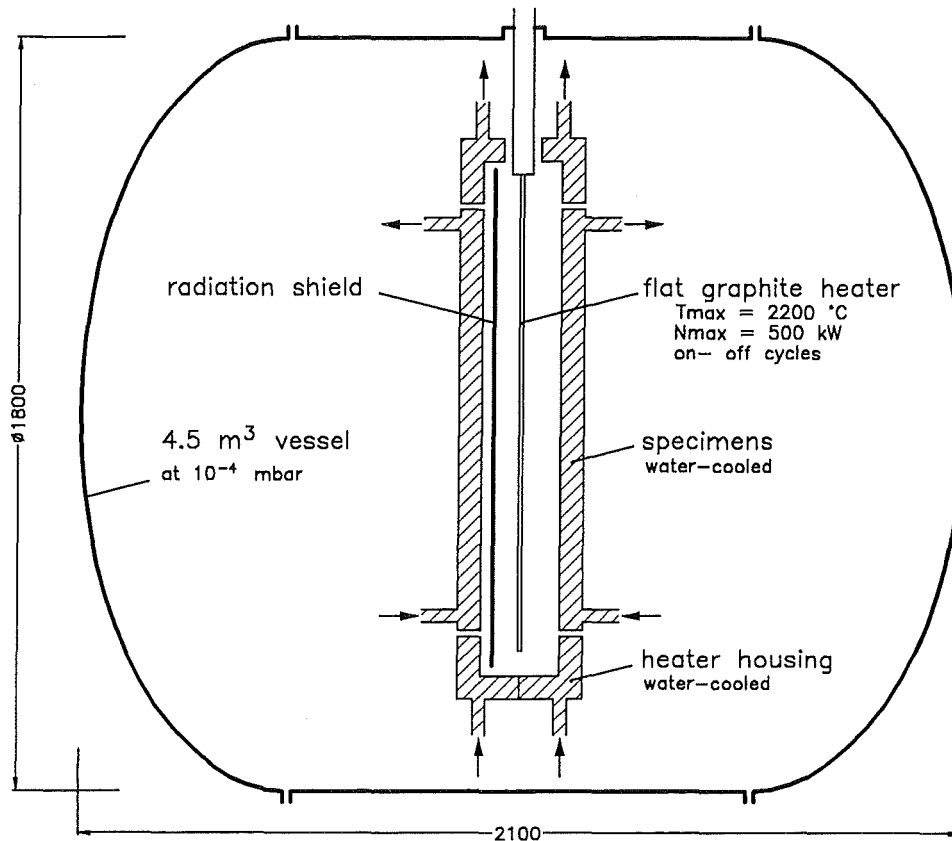


Fig. 3.1 Schematic of the FIWATKA vacuum vessel and specimen installation

3.1 Experimental Set-up

Fig. 3.1 shows schematically a vertical section through the general arrangement. The heater, shown as section and extending into the plane, hangs vertically in the center of a vacuum vessel. Specimens may face the heater on both sides or one specimen may be replaced by a dummy possibly being separated from the heater by a radiation shield; specimens may or may not be protected by tiles. Around the edges of the heater there is an additional water-cooled structure which together with the specimens forms a closed housing around the heater such that only a very small fraction of the heater power may reach the vacuum vessel through any gaps and instrumentation holes in the heater housing. The specimens and the remainder of the heater housing are water-cooled continuously while the power to the heater may be either "on" continuously (steady-state) or "on/off" periodically (cycles). The large vessel enclosing heater and housing (including specimens) is kept at a vacuum of 10^{-4} mbar in order to protect the heater from oxidation and to limit heat transfer mechanisms to radiation only.

More details on the FIWATKA facility including measurements on the uniformity of the heat flux received in the specimen plane are reported in Ref. [3].

For the investigations covered in the present report, TS1 was put in the position of the first wall specimen in Fig. 3.1; TS1 was placed there either as a bare specimen (see Chapter 4), as a specimen with a radiatively cooled protection tile (see Chapter 5), or as a specimen with two conductively cooled protection tiles (see Chapter 6).

Set-up features specific for the individual specimens are described within the respective Chapters on testing.

3.2 Experimental Procedure in General

Heating:

Heating of specimens is by thermal radiation originating from a plane high-temperature graphite heater (resistance heater). The heater may be run at temperatures of up to 2100°C and has an emissivity of about 0.7. Any specimen confronted to this heater at a distance of about 3 cm will receive a heat flux which depends on the specimens own surface temperature and on its emissivity and which may be on the order of 80 W/cm². The heat flux actually received is determined calorimetrically under steady-state conditions by measuring the heat-up and the flow rate of the cooling water passing the specimen.

Heating may be "steady-state" or "cyclic". For "cyclic" each cycle would consist of a heating phase (power-on) and a cooling phase (power-off) with cooling being continued. As the main test parameter, the electrical power to the three FIWATKA heaters is set, controlled, and cycled. Fig. 3.2 displays an example of a typical power cycle.

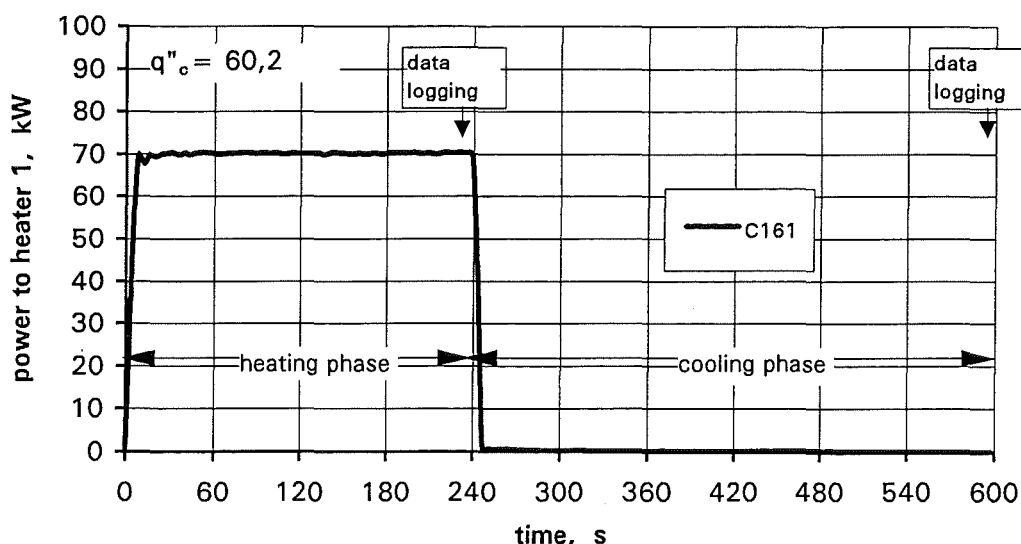


Fig. 3.2 Typical power cycle of one of three radiative heaters

The power is increased linearly to a pre-set value within 10 seconds; the power is kept constant until a total time of 4 minutes is reached. After this heating phase the power is decreased to zero and kept there until the end of the cycle at a total time of 10 minutes

when the next cycle starts. In the example the test cycle consisted of a 4 minutes heating phase and a 6 minutes cooling phase; in the tests to be reported the lengths of the phases were chosen at least such that at the end of a phase the temperatures and strains in the specimen had reached steady-state values. Transitions from heating to cooling phases and vice versa are fast since the heater consists of a thin and low density (low mass) graphite plate.

Cooling:

Water at about 0.8 MPa is circulated through the coolant channels of the specimen. The flow rate of 4 m³/h passes in parallel the four coolant channels of one subunit (the left subunit of the specimen as it is shown in Fig. 4.1 later in the report) and returns in parallel through the four channels of the second subunit. The water temperature at the specimen inlet is controlled by a mixing valve to be about 35 °C and even in the cyclic mode it oscillates only a few degrees. At the specimen outlet the water temperature is up to 50 °C depending on the heat flux applied. The coolant velocity of about 1 m/s results in a heat transfer coefficient at the channel walls of about 0.7 W/cm² K.

Data Acquisition:

Data acquisition included data from the FIWATKA operation (current, voltage, flow rates, temperatures, pressures and others) as well as data from the specimen sensors (temperatures, strains, and displacements).

The data were read and stored in one of three different fashions:

1. If the test was run in a steady-state mode, meaning that the boundary conditions were kept constant for at least 20 minutes, one data set was taken at the end of that period.
2. If the test was run in a cyclic mode, the data were recorded twice per cycle, one set each about 10 seconds before the ends of the heating and cooling phases, respectively; this in most cases could replace the reading from a steady-state test at sufficient accuracy.
3. If the test was run in a cyclic mode and the transient behavior was to be observed one data set was taken every two or three seconds over two or three consecutive cycles.

4. Thermo-mechanical Testing of the Bare TS1 without Protection Tiles

4.1 Goals of the Investigation

When the first wall mock-up TS1 was received it was instrumented with thermocouples and strain gauges at selected locations (see Chapter 4.2.2 for details). It was intended to prove with this instrumentation that FE codes are able to predict the measured temperatures and strains as part of the temperature and strain fields calculated for the geometry of the specimen and its thermal and mechanical boundary conditions. Therefore, the primary goal of the first test series was to measure with the existing sensors temperatures and strains for different heat fluxes to the heated surface under steady-state conditions; in addition the transient behavior during heating/cooling cycles was looked at, mainly for proving that steady-state conditions were reached at the end of a heating phase and at the end of a cooling phase.

Also these measurements were used to become familiar with the TS1 instrumentation and with the reliability of its readings as well as with the data acquisition system and the data handling.

It was not intended to perform thermal fatigue tests with TS1 by doing long-term thermal cycling until any cracks or failure in the steel of the specimen could be detected; the large number of instrumentation holes and the nonuniform testing history of the specimen would not allow a reasonable interpretation of such fatigue testing results.

4.2 Instrumentation of the Specimen TS1

When the specimen TS1 was manufactured by Framatome it was instrumented with a total of 40 thermocouples and 51 strain gauges. Details on the specification and installation of these sensors may be found in the TS1 Program Report no. 3 (MC/TS 89 2177) by Framatome (1989). The sensors were distributed over the specimen's front plate (installation from the back side) and its side walls.

Thermocouples (TC)

The TCs were of type J (iron/constantan), sheathed with a stainless steel tube of 1 mm o.d., and had an isolated junction.

The TCs were intended to measure local temperatures in the steel structure; the measuring points had been selected such that a comparison of the data with the results of FE calculations of the temperature field should indicate whether there is sufficient agreement and whether there is enough uniformity among the temperatures at equivalent points.

The TCs in the front plate were installed in holes drilled into the plate from the back side; the holes were 1.5 mm i.d. for most of their depths. To provide thermal contact between the front plate the tip of the TCs the holes were filled with a contact material (CERAMACAST 505) before the TCs were slipped-in and pushed in-place. The holes had been drilled such that 8 of the TCs were to measure 1 mm and another 18 TCs were to

measure 8 mm behind the heated surface of the specimen. The measuring positions may be read from Fig. 4.1; on the sketch the specimen is viewed from the back side and the numbers indicate the corresponding channel numbers of the data acquisition system. The TCs measuring close to the heated surface (1 mm) are given in the left part of the figure, the ones further off (8 mm) in right part.

The remainder of 14 TCs were to measure in different positions mainly at the side walls were they were attached by using spot-welded metal bands.

Also indicated on Fig. 4.1 are the channel numbers of the coolant inlet and outlet temperatures.

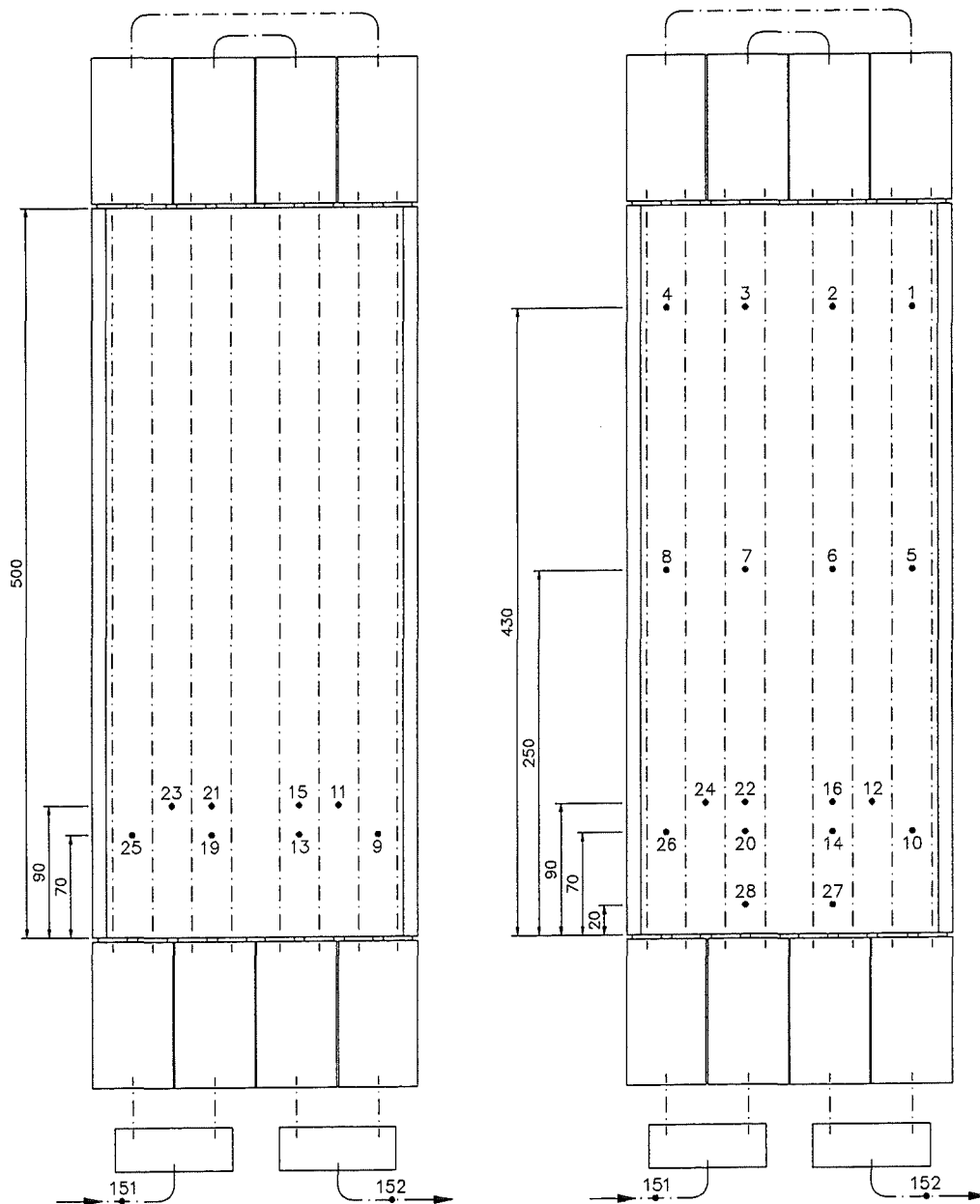


Fig. 4.1 Distribution of thermocouples on the TS1 front plate (view on backside)
left: 1 mm-positions;
right: 8 mm-positions
numbers indicate channels of the data acquisition system

Strain Gauges (SG)

The SGs were of type Vishay WK 076 062 AP 350 and were connected to the data acquisition system in a 3-wire mode with a dummy resistor of $350 \pm 1 \% \Omega$; the measuring current was set to 8 mA. This type of SGs provides some self-temperature-compensation if the SG is applied to a specimen having a coefficient of thermal elongation CTE of $\alpha = 12,1 \cdot 10^{-6} \text{ } 1/^{\circ}\text{C}$ meaning that under these conditions the temperature-dependent apparent strain due to thermal elongation is measured zero at room temperature and increases to a maximum of only 0,01 % at 100 °C, rather than to its full value of 1,2 % if the SG would be uncompensated.

In the present application the material of the specimen is AISI 316L with a CTE of $\alpha \approx 16,4 \cdot 10^{-6} \text{ } 1/^{\circ}\text{C}$ in the range between 0 and 100 °C. Therefore, the self-temperature-compensation is not as good as stated above; the SGs will indicate some additional apparent strain that is due to the higher CTE of the specimen material as compared to the SG reference material. The errors due to the apparent and additional apparent strains may be estimated as follows:

- for the two test series reported the temperature at the back side of the TS1 front plate (location of SGs) was on the order of 50 °C at the maximum heat flux of $q'' = 60 \text{ W/cm}^2$
- the apparent strain at 50 °C would be $\epsilon_a \approx 0,005 \%$.
- the additional apparent strain at 50 °C would be $\epsilon_{aa} \approx 0,013 \%$
- in summary the maximum total apparent strain is $\epsilon_a + \epsilon_{aa} \approx 0,018 \%$ or 180 microstrains of positive strain.

The strain gauge data reported below have not been corrected for this total apparent strain, which tends to make the data be a little higher than the strains really are, depending on the temperature level.

The SGs had been installed mainly on the back side of the front plate (numbers 61 through 87) and a few also on both sides of the side walls (numbers 89 through 111). It should be mentioned that originally some SGs had also been placed on the inside of the coolant channel walls; since these SGs during earlier tests had lost their contact to the walls and thus had become useless and since they had been covered with large amounts of coating material representing an undesired local thermal resistance to the heat flux, these SGs were taken off prior to the present tests. Also one SG originally placed in the center groove of the heated surface had failed earlier and was removed prior to the present tests.

Each measuring position indicated on Fig. 4.2 was instrumented with two SGs, one measuring parallel and one transverse relative to the coolant channel direction; on the sketch the specimen is viewed from the back side and the given numbers are the corresponding channels of the data acquisition system, on the left hand sketch for the parallel and on the right hand sketch for the transverse SGs.

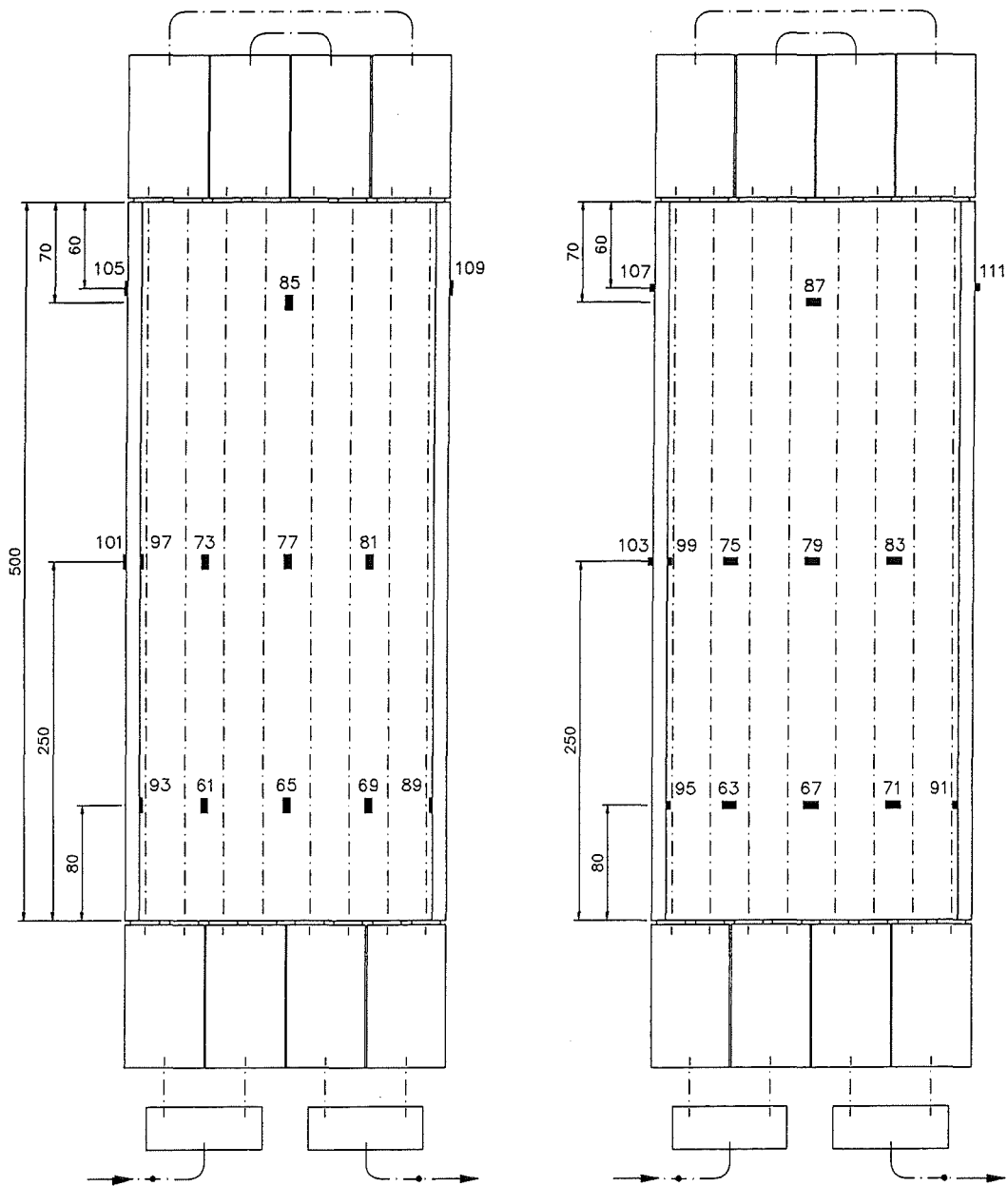


Fig. 4.2 Distribution of strain gauges on the TS1 front plate (view on backside)
 left: parallel to coolant channels; right: transverse to coolant channels
 numbers indicate channels of the data acquisition system

Table 4.1 Strain Gauge Numbering													
FIW = numbers used in FIWATKA tests and in the present report													
FRA-1 = numbers used by Framatome and at JRC Ispra tests													
FIW	61	63	65	67	69	71	73	75	77	79	81	83	85
FRA-1	25	26	27	28	29	30	31	32	33	34	35	36	37
FIW	87	89	91	93	95	97	99	101	103	105	107	109	111
FRA-1	37	39	40	41	42	43	44	45	46	47	48	49	50

The original SG numbering by Framatome which was also used by JRC Ispra in Ref. [2] was different from the present numbering in Fig. 4.2 and in this report; Tab. 4.1 relates the two numbering systems.

The readings of the SGs seemed reliable with the exception of channel 65 which seemed to have questionable readings when the sensor reaction was examined prior to testing.

In order to make the strain readings from different test series comparable, the following procedure was applied:

- the specimen was thermally cycled at a high heat flux level (60 W/cm²) to have all test series start with the same distribution of residual strains in the material
- the specimen was cooled uniformly to the coolant temperature (25-30°C)
- under these conditions the SG measuring channels in the data acquisition system were "initialized", which means that their readings were set to be new zero points.
- the following test series using this new zero point consisted of a couple of tests with increasing heat fluxes up to 60 W/cm² as discussed below.

4.3 Testing

4.3.1 Experimental Setup

As indicated in Chapter 3 the TS1 specimen was installed in a window of the FIWATKA heater housing and thus became part of this housing which surrounded the heater. Fig. 4.3 displays the geometrical situation.

The horizontal cross section at the bottom of the figure indicates:

- the specimen was installed at a distance of 26 mm from the heater
- the total width of the heater of 327 mm was greater than the width of the specimen (223 mm) in order to provide uniform heat flux also close to the edges of the specimen. Radiation shields made from 1 mm flexible graphite were installed at the back side (1 layer) and at the side faces (3 layers) of the heater to make the heater temperature uniform and to save energy.
(For details of the heat flux uniformity to be expected see Chapter 5.4 of [3].)
- the housing in the cross section consists of two halves, each with the shape of a 90° angle, which may be opened like doors by rotating them around the hinges which are shown in at the upper left and lower right corners; this makes the heater accessible after the specimen is removed.
- the specimen may be "constrained" by connecting the back ends of the TS1 side walls by five strong steel bars (40 by 40 mm in cross section) and bolts in order to limit thermal bowing of the front plate and to simulate the mechanical boundary conditions which are present in a Tokamak first wall. The "unconstrained" condition was realized by supporting the specimen at one side wall and by leaving the other one free with a gap of 3 mm between the flange and the connection bars; unfortunately this 3 mm gap turned out to be too small to allow unlimited bowing, as will be discussed later.

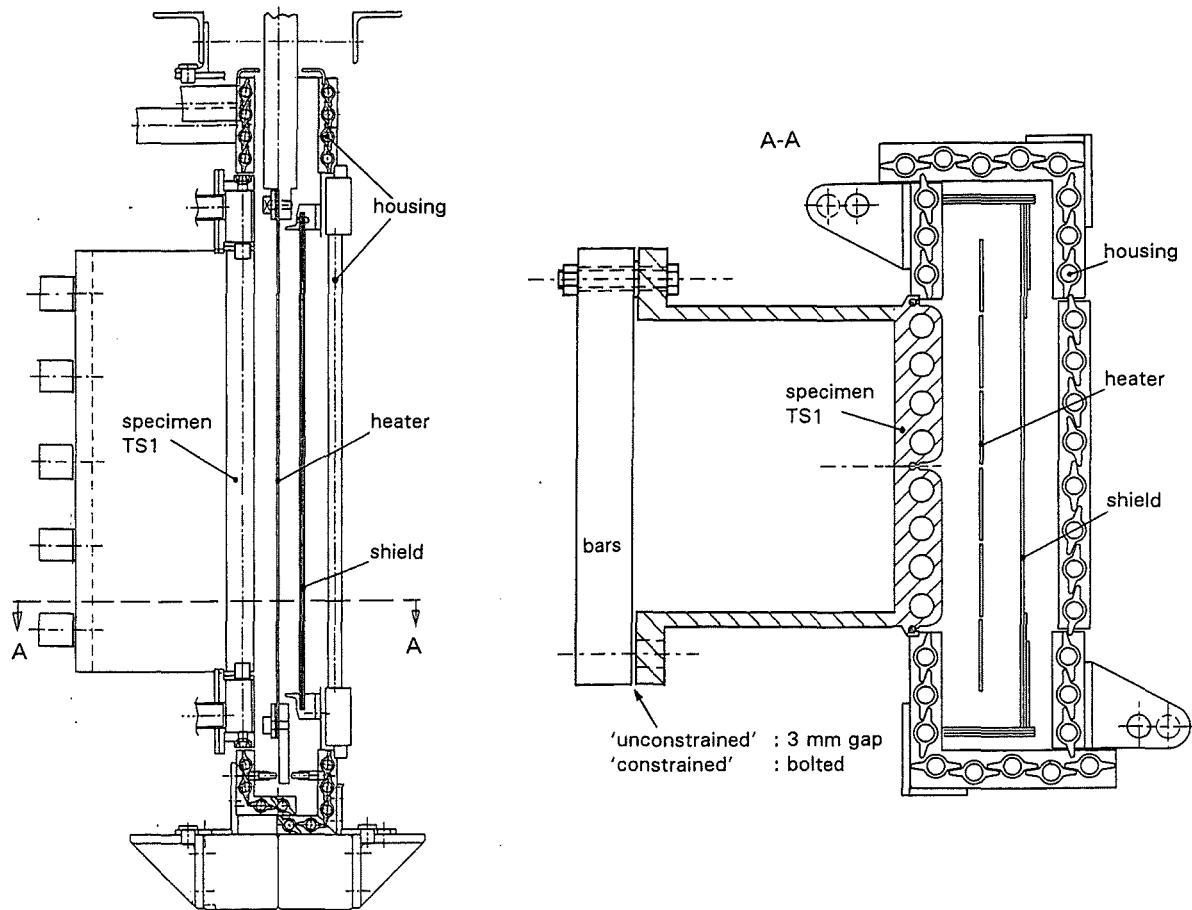


Fig. 4.3 Vertical and horizontal sections (different scales) through the experimental setup with the bare TS1 for tests TS1N

The vertical cross section in the figure indicates:

- the length of the heater (576 mm) was greater than that of the specimen (500 mm) again for heat flux uniformity reasons.
- the coolant headers at top and bottom of the specimen also received some power from the heater; since this power was included in the calorimetrically determined specimen's power it was subtracted before calculating the heat flux to the specimen (for details see Chapter 4.3.3).
- in the vertical direction the specimen was always constrained by the side walls welded to the front plate such that bowing in this direction was very limited especially close to the side walls.

The specimen was positioned in the window of the housing by attaching the steel bars to a support frame.

4.3.2 Experimental Procedure and Test Sequence

A large number of tests with the bare TS1 were run in both the steady-state and cyclic modes. Due to initial problems with a sufficiently precise measurement of the coolant inlet and outlet temperatures, which are important for the determination of the heat fluxes, it was decided that only the last two series of tests (TS1N-S6 and -S7) should be

evaluated further. For these two series the sequence of tests with their individual boundary conditions and measured test data is listed in Tab. 4.2. It happened that these tests were cyclic with 4 minutes heating phases and 6 minutes cooling phases. As indicated in Chapter 3.2 for the cyclic mode, data were recorded shortly before the ends of each of the heating and cooling phases.

1 Table 4.2 Selection of measured data from tests with the bare TS1																
2	Test	Mechanical	Data from	Power of	Heat Flux, W/cm ²	Temp., (C) at	Strain, %									
3	Boundary	Condition	the End of Phases	Heater 1	q"	q"c	(1 mm)	(8 mm)	p*	t*	p*	t*	p*	t*	p*	t*
4			H=Heating Phase	kW	at end	steady	TC 21	TC 16	C 061	C 063	C 065	C 067	C 069	C 071	C 073	C 075
5			C=Cooling Phase		of phase	state					?					
6																
7	TS1N-S6	unconstr.	steady state	0	-2.1	0.0	25	25	0.000	0.000	-0.001	0.000	0.000	0.000	0.000	0.000
8			H	20	14.4	17.9	112	66	0.010	-0.016	0.019	0.027	0.011	-0.018	0.039	-0.024
9			C	0	-2.8	0.0	36	36	0.005	0.006	0.011	0.008	0.005	0.005	0.005	0.007
10			H	40	32.7	36.1	199	109	0.017	-0.039	0.038	0.053	0.019	-0.043	0.078	-0.051
11			C	0	-3.1	0.0	37	37	0.006	0.006	0.011	0.008	0.006	0.004	0.006	0.007
12			H	50	40.9	44.6	226	110	0.015	-0.048	0.033	0.056	0.018	-0.054	0.080	-0.062
13			C	0	-2.1	0.0	37	36	0.006	0.007	0.012	0.008	0.006	0.004	0.006	0.007
14			H	60	47.8	53.1	254	120	0.016	-0.056	0.033	0.065	0.018	-0.064	0.088	-0.071
15			C	0	-2.1	0.0	36	37	0.006	0.007	0.012	0.008	0.006	0.005	0.006	0.007
16			H	70	56.8	60.2	283	135	0.016	-0.063	0.039	0.078	0.019	-0.070	0.098	-0.080
17			C	0	-3.8	0.0	36	36	0.006	0.007	0.011	0.007	0.007	0.006	0.007	0.007
18			steady state	0	0.0	0.0	23	23	-0.001	-0.001	-0.005	-0.001	-0.002	0.000	-0.002	-0.001
19																
20	TS1N-S7	constrained	steady state	0	-1.5	0.0	30	30	0.000	0.000	0.000	0.000	0.000	0.000	0.000	0.000
21			H	20	15.9	17.9	108	60	0.004	-0.017	0.006	0.054	0.005	-0.018	0.035	-0.026
22			C	0	1.0	0.0	31	31	0.001	0.000	0.000	0.001	0.001	0.000	0.001	0.000
23			H	40	33.0	36.1	185	90	0.008	-0.035	0.014	0.106	0.010	-0.037	0.065	-0.048
24			C	0	-1.1	0.0	31	31	0.001	0.000	-0.001	0.000	0.001	-0.002	0.002	0.000
25			H	50	41.3	44.6	221	104	0.009	-0.042	0.018	0.130	0.012	-0.045	0.078	-0.058
26			C	0	0.2	0.0	31	31	0.001	0.000	0.000	0.001	0.001	-0.002	0.002	0.000
27			H	60	50.7	53.1	247	120	0.010	-0.049	0.023	0.154	0.012	-0.053	0.089	-0.066
28			C	0	-1.2	0.0	31	31	0.001	0.000	-0.001	0.000	0.002	-0.002	0.003	0.000
29			H	70	58.0	60.2	284	132	0.010	-0.054	0.029	0.174	0.013	-0.058	0.099	-0.073
30			C	0	-1.6	0.0	30	30	0.001	-0.001	-0.002	-0.002	0.002	-0.001	0.003	0.000
31			steady state	0	0.7	0.0	30	31	0.001	0.000	-0.002	-0.002	0.001	0.000	0.001	0.000
32	* strain gauge orientation relative to coolant channel direction: p = parallel, t = transverse										? data questionable					

1 Tab. 4.2 (continued) Selection of measured data from tests with the bare TS1																	
		Strain, %															
3	p*	t*	p*	t*	p*	t*	p*	t*	p*	t*	p*	t*	p*	t*	p*	t*	
4	C 077	C 079	C 081	C 083	C 085	C 087	C 089	C 091	C 093	C 095	C 1097	C 099	C 101	C 103	C 105	C 107	C 109
5					?												
6																	
7	0.000	0.000	0.000	0.000	0.000	0.000	0.000	0.000	0.000	0.000	0.000	0.000	0.000	0.000	0.000	0.000	0.000
8	0.027	0.008	0.037	-0.026	-0.003	0.033	0.024	0.011	0.022	0.012	0.038	0.017	0.036	-0.013	0.018	0.015	0.017
9	0.005	0.007	0.005	0.007	0.006	0.007	0.005	0.006	0.005	0.005	0.005	0.006	0.005	0.005	0.006	0.005	0.006
10	0.051	0.016	0.073	-0.053	-0.013	0.067	0.048	0.024	0.040	0.024	0.073	0.031	0.071	-0.027	0.034	0.032	0.030
11	0.005	0.007	0.006	0.006	0.006	0.007	0.006	0.007	0.005	0.006	0.005	0.006	0.005	0.007	0.006	0.007	0.006
12	0.053	0.012	0.075	-0.065	-0.019	0.073	0.047	0.025	0.042	0.029	0.075	0.031	0.072	-0.034	0.032	0.028	0.029
13	0.005	0.007	0.006	0.006	0.006	0.007	0.006	0.007	0.006	0.006	0.006	0.006	0.005	0.007	0.006	0.007	0.006
14	0.058	0.015	0.083	-0.076	-0.024	0.084	0.050	0.030	0.046	0.039	0.081	0.038	0.078	-0.044	0.034	0.025	0.031
15	0.005	0.008	0.007	0.007	0.006	0.007	0.006	0.008	0.006	0.006	0.006	0.007	0.006	0.007	0.007	0.007	0.006
16	0.063	0.023	0.091	-0.085	-0.028	0.099	0.056	0.038	0.051	0.051	0.089	0.049	0.086	-0.054	0.037	0.024	0.035
17	0.006	0.007	0.008	0.006	0.007	0.006	0.007	0.008	0.006	0.006	0.006	0.007	0.006	0.008	0.007	0.007	0.006
18	-0.002	0.003	-0.002	-0.001	-0.001	0.000	-0.003	-0.002	-0.001	0.000	-0.001	0.000	-0.001	-0.004	-0.002	-0.002	-0.002
19																	
20	0.000	0.000	0.000	0.000	0.000	0.000	0.001	0.000	0.000	0.000	0.000	0.000	0.000	0.000	0.000	0.000	0.000
21	0.023	0.036	0.032	-0.028	-0.009	0.062	0.019	0.046	0.016	0.043	0.032	0.046	0.031	-0.051	0.013	-0.029	0.012
22	0.001	0.001	0.001	0.000	0.000	0.001	0.001	0.002	0.001	0.002	0.001	0.002	0.001	0.000	0.001	0.000	0.001
23	0.042	0.071	0.060	-0.051	-0.020	0.124	0.036	0.092	0.030	0.087	0.058	0.088	0.057	-0.098	0.023	-0.057	0.023
24	0.001	0.000	0.001	0.000	0.000	0.001	0.001	0.003	0.001	0.002	0.000	0.002	0.000	0.001	0.001	0.001	0.000
25	0.050	0.088	0.072	-0.060	-0.025	0.152	0.043	0.113	0.036	0.107	0.069	0.108	0.067	-0.118	0.028	-0.069	0.027
26	0.001	0.001	0.002	0.000	0.001	0.002	0.002	0.004	0.001	0.003	0.000	0.002	0.000	0.002	0.002	0.001	0.002
27	0.057	0.105	0.082	-0.069	-0.030	0.179	0.050	0.134	0.042	0.126	0.078	0.127	0.076	-0.137	0.032	-0.081	0.031
28	0.002	0.000	0.003	0.000	0.001	0.001	0.003	0.004	0.001	0.003	0.001	0.003	0.000	0.002	0.002	0.001	0.002
29	0.062	0.121	0.091	-0.076	-0.035	0.203	0.056	0.152	0.047	0.144	0.085	0.143	0.084	-0.153	0.035	-0.090	0.034
30	0.002	-0.002	0.003	-0.001	0.001	0.000	0.002	0.004	0.001	0.002	0.000	0.002	0.000	0.004	0.002	0.002	0.002
31	0.001	-0.001	0.002	0.000	0.001	0.001	0.001	0.001	0.001	0.000	0.001	0.000	0.001	0.002	0.001	0.001	0.001
32	* strain gauge orientation relative to coolant channel direction: p = parallel, t = transverse										? data questionable						

Mechanical Boundary Conditions and Pre-Conditioning:

Of the two valuable test series reported here one was run with the unconstrained specimen (TS1N-S6) and the other was run with the constrained specimen (TS1N-S7); constraint is described in Chapter 4.3.1.

Before the two test series were started, the specimen had experienced a large number of different tests at JRC Ispra and at KfK in the unconstrained as well as in the constrained condition.

In order to start a test series with defined distribution of residual strains the specimen, after applying the appropriate constraint, was preconditioned prior to the series by cycling it on a high heat flux level that was not exceeded during the following tests.

Pre-conditioning consisted of 10 cycles with each cycle consisting of a 4-minutes heating phase at a heat flux $q'' = 60\text{W/cm}^2$ and a 6-minutes cooling phase with $q'' = 0$; coolant flow was steady-state. For some of these cycles data were recorded transiently and are reported later in this report.

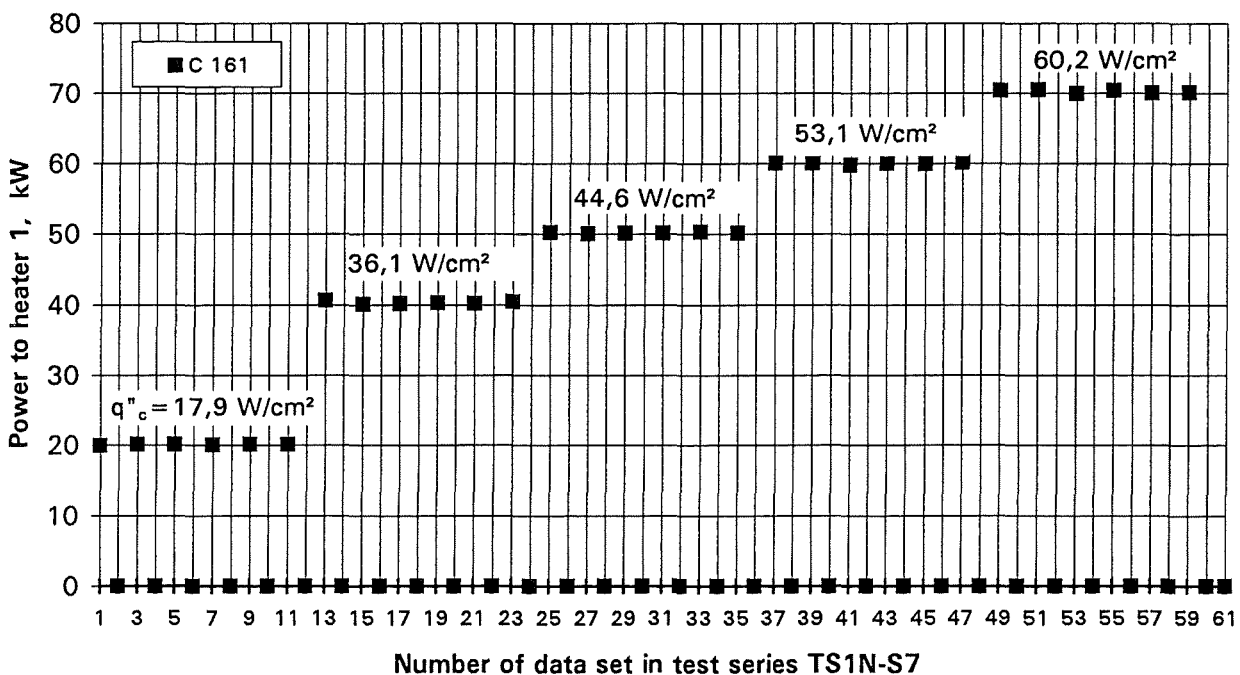


Fig. 4.4 Test sequence for a series of tests with data logging at the end of each phase

Test sequence:

After pre-conditioning a test series was started at zero heater power by initializing the strain gauge readings as described for the strain gauge instrumentation in Chapter 4.2.2 and by recording the first set of data reported in the first line of Tab. 4.2 for each series. Following this, a series consisted of 5 tests on different heat flux levels between 20 and 60 W/cm² as listed in Tab. 4.1 and shown in Fig. 4.4. Always six cycles were run on the

same heat flux level before the heat flux was increased to the next higher level. Temperature and strain data were recorded twice per cycle; at these points in time steady-state temperatures and strains in the specimen had been reached as will be shown when discussing the the transient data in Chapters 4.3.2 and 4.3.3. From the collected data only one set for each heat flux level (usually the one for the last cycle) was included in Tab. 4.2 together with the data set for the following cooling phase.

After having finished the series the specimen was continued to be cooled for several hours to make sure that also the side walls were cooled down to coolant temperature; then, the last reading of the series was taken to be compared with the first one taken after initializing.

4.3.3 Data Processing

The only processing necessary to the as-recorded data was the determination of the applied heat flux.

The heat flux received by the specimen's surface depends not only on the temperatures of the radiating partners but also on their emissivities, which are not well known. Therefore, the heat flux was determined calorimetrically from the heat-up and the mass flow rate of the coolant passing the specimen. Actually, the heat flux q'' to the specimen was calculated from the equation

$$q'' = \frac{N_{H_2O} - N_{headers}}{F_{TS1}}$$

N_{H_2O} is the power received by the cooling water as it passed the specimen (including headers); it is calculated from the flow rate \dot{V} [l/s], the heat-up rate ΔT [K], the density $\rho = 0.988$ [kg/l], and the specific heat $c_p = 4,183 \cdot 10^3$ [J/kgK]

$$N_{H_2O} = \dot{V} \cdot \rho \cdot c_p \cdot \Delta T \quad [W]$$

$N_{headers}$ is the power received by the coolant as it passes the specimen headers as estimated from a total heat balance in test TS1N-S10 with N_{el} [W] as the total electric power to the three heaters

$$N_{headers} = 0.0528 \cdot N_{el} \quad [W]$$

F_{TS1} is the heated surface of the specimen excluding the headers

$$F_{TS1} = 50 \cdot 22.3 = 1115 \text{ cm}^2$$

Since the calorimetrically determined power N_{H_2O} includes the power received by the headers, $N_{headers}$ was subtracted before dividing it by the TS1 area.

TCs measuring the water temperature were installed in some distance from the specimen. This is the reason why it took more time for the heat flux reading to become

steady-state than for any other reading and the heat flux readings q'' given in the Tab. 4.2 were not fully steady-state yet at the end of a 4-minute heating phase. Therefore the steady-state readings taken from test TS1N-S10 at corresponding heater power are also listed as q''_c and are used as a reference for the discussion of the results.

4.4 Experimental Results and Discussion

A selection of the data from the two test series is listed in Tab. 4.2. The table is subdivided in two blocks for the unconstrained and constrained boundary conditions, respectively.

Only data in the first and last lines of each block are taken under overall steady-state conditions; the remainder is taken during heating cycles a few seconds before the ends of the heating and cooling phases, respectively, as indicated in Chapter 4.3.2; at this time the front plate which is most important for the stress/strain distribution had reached a steady-state temperature distribution, but the side walls had not.

4.4.1 Temperatures in TS1

An example of the temperature distribution measured in the TS1 specimen is shown in Fig. 4.5 for a heat flux of $q''_c = 60,2 \text{ W/cm}^2$ in test TS1N-S7; the left hand and right hand sketches contain data for 1 mm and 8 mm positions (distances from the heated surface), respectively. In viewing the numbers it becomes evident that the scatter of the temperatures is much greater than would be expected from the measuring positions on the specimen. All measuring positions within one group (1 mm or 8 mm) are almost equivalent thermally since they all lie centrally between coolant channels; the only physically legitimated difference in temperature could originate from the coolant temperature which rises by 16 K between entering the lower end of the left four channels and leaving the lower end of the right four channels; another difference could be caused by the slightly wider heated area between the two central coolant channels which could have some distant effect on TC positions in the next row. But the differences between the readings are much greater than could be explained that way and the symmetry to be expected is missing.

A similar observation was made also during the earlier testing of the TS1 specimen at JRC Ispra (see Ref. [2]). The necessary conclusion from this observation is that the temperature readings are not reliable. It is believed that a nonuniform thermal contact in the measuring location between the steel of the specimen and the tip of the thermocouples is responsible for the differences. The TCs run along a steep temperature gradient which means that in the neighborhood of their tip the steel is on very different temperatures; it is assumed that the contact cement embedding the tip has developed cracks during drying or thermal cycling; depending on the extend and position of those cracks the temperature readings differ considerably. On this basis, the highest TC readings seem most reliable.

Considering this finding it was decided to not further evaluate, discuss, and report the temperature readings (though the data are available) except for the two channels TC 21 and TC 16 which produced the highest readings at 1-mm and 8-mm positions, respectively; they are used to demonstrate the transient thermal behavior of the specimen even if their absolute readings might be not correct.

Fig. 4.6 shows that these two temperatures increase linearly with increasing heat flux which should be expected since the thermal conductivity of the steel does not increase remarkably between 30 and 300°C.

The transient readings of these two TCs is plotted for one power cycle in Fig. 4.7 together with the electric power to heater 1 indicating the duration of the heating and cooling phases. Both temperatures exhibit a fast increase and level off to reach values that are very near steady-state before the heating phase comes to an end. The unmotivated changes in slope could be the result of developing contact problems (see above) and this behavior is being reproduced from cycle to cycle. During the cooling phase the temperatures decrease and reach steady-state conditions at a level from which the cycle started.

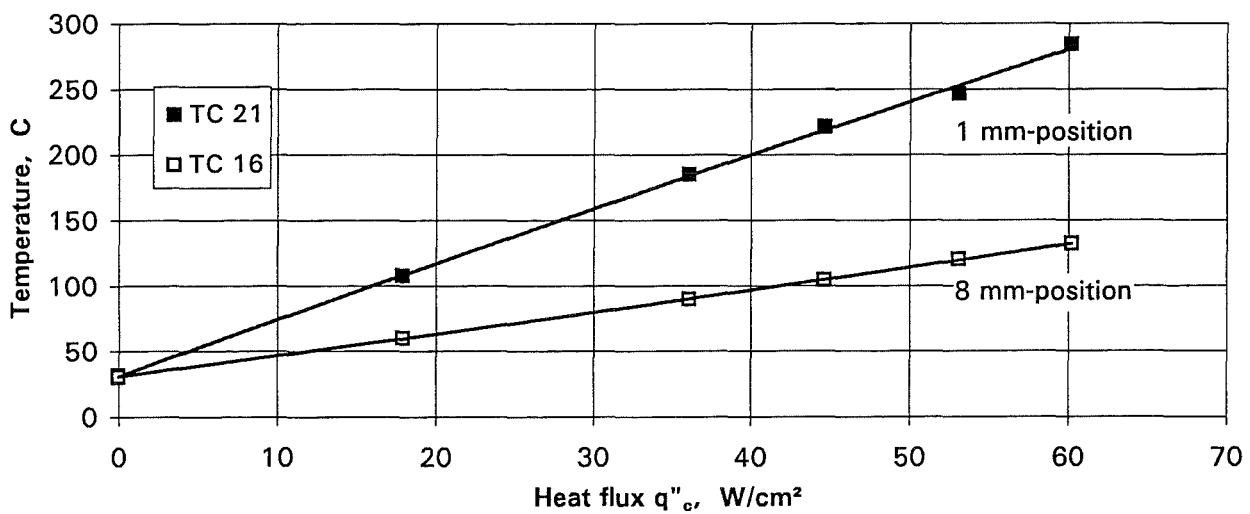


Fig. 4.6 Temperatures at selected positions increase linearly with heat flux (data from test series TS1N S7)

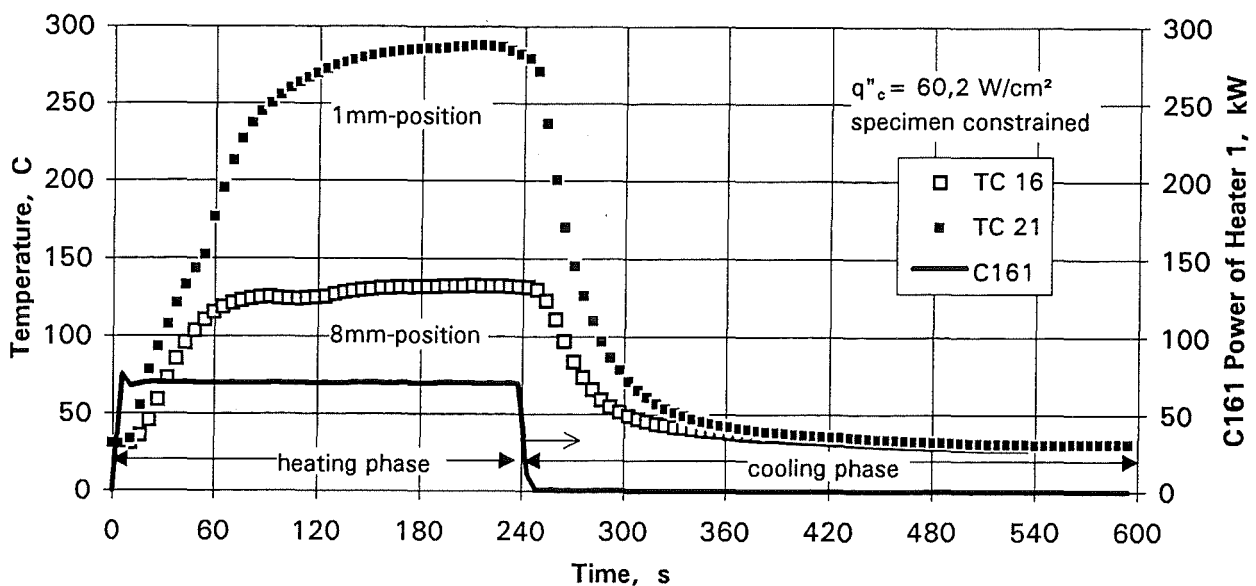


Fig. 4.7 Temperature transients at selected positions (from test TS1N-T3)

4.4.2 Strains on the Back Side of TS1

The readings for all strain gauges (SG), the channel numbers of which may be identified from Fig. 4.2 are listed in Tab. 4.2 for the five heat fluxes investigated and for the mechanical boundary conditions "unconstrained" and "constrained". Unfortunately only after the tests it turned out that in the "unconstrained" tests the 3 mm gap between one side wall and the constraint bars which was intended to allow free deflection of the specimen was too small; the gap was consumed at a certain heat flux and the resulting mechanical contact caused some undefined constraint in the so-called "unconstrained" tests; this should be kept in mind when looking to the results. Part of the following discussion is limited to the highest heat flux $q''_c = 60,2 \text{ W/cm}^2$ where the effects are most pronounced.

Strains parallel to the coolant channel direction

Fig. 4.8 offers an overview on the local distribution of parallel strains at $q''_c = 60,2 \text{ W/cm}^2$ for the unconstrained and constrained conditions. The readings are positive (elongation) since the thermal elongation of the front part of the plate is mostly transferred to its back side because the side walls do not allow considerable bowing of plate in the parallel direction. A comparison of the data in Fig. 4.8 shows that the parallel strains are very similar for the unconstrained and constrained conditions since any constraint in the transverse direction does not have a strong influence here.

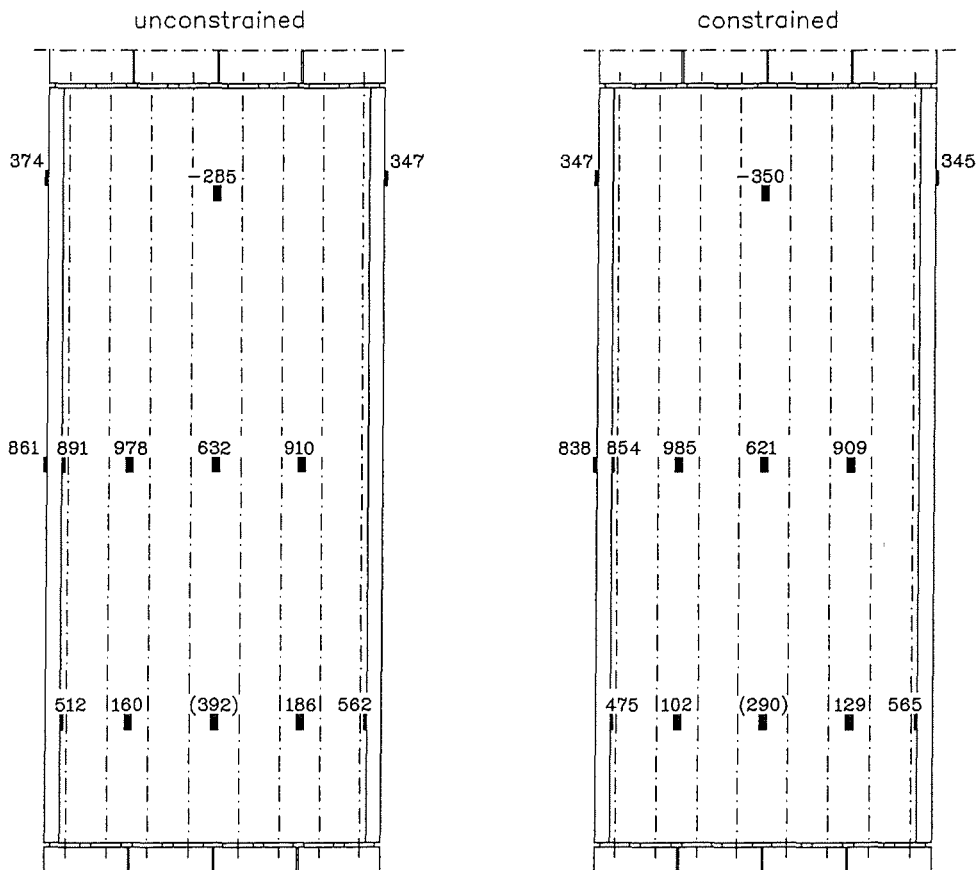


Fig. 4.8 Strains parallel to the coolant channels given in $10^{-4}\%$ (microstrains) at $q''_c = 60.2 \text{ W/cm}^2$ for the unconstrained (left) and constrained (right) conditions

This fact is again demonstrated in more detail in Fig. 4.9 where for the SGs 77 and 81 strain is plotted as a function of the heat flux and where the data stay essentially unchanged whether the specimen was unconstrained or constrained.

The only parallel strain gauge exhibiting a negative reading (compression) throughout the test is channel 85 at the center line close to the upper end. This reading is not understood; despite thorough reaction testing of each strain gauge prior to the test series it should not be excluded that this is a false reading; but it is also noted that with the test at JRC Ispra this strain gauge was also the only one reading negative in the parallel direction at the end of the heating phase.

Fig. 4.10 gives an impression on the reproducibility of the strain measurements. Plotted are all data taken for the SGs 77 and 81 during a test series, i.e. six data points for each power level of the constrained test series; each high reading at the end of a heating phase is followed by a close-to-zero data point at the end of a cooling phase. Fig. 4.10 also indicates that there is no considerable amount of thermal ratcheting even at the highest heat flux level.

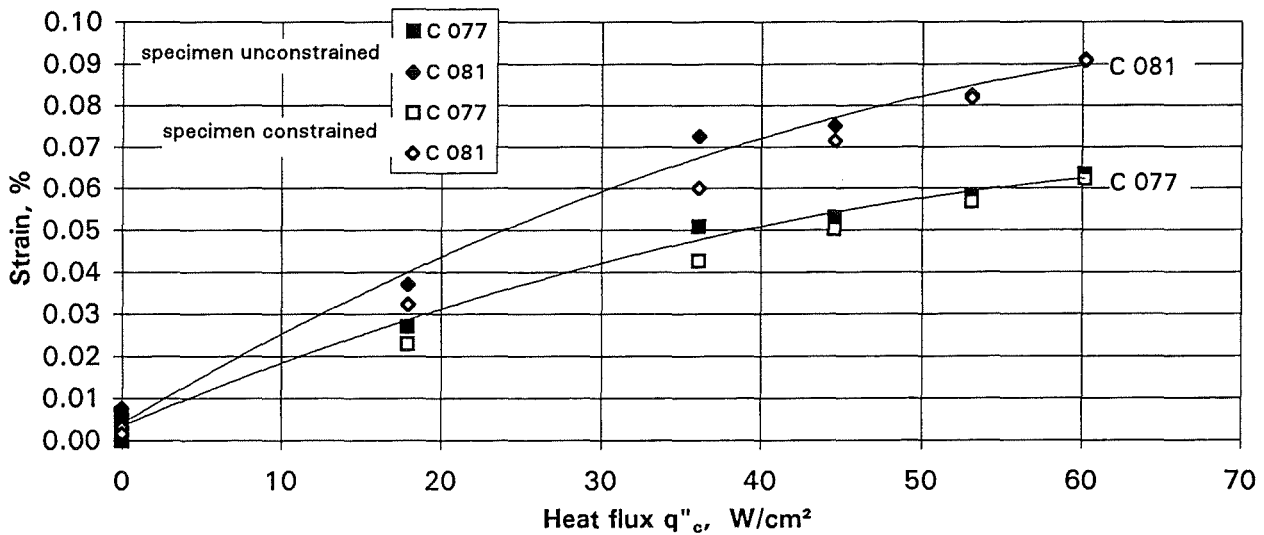


Fig. 4.9 Strain parallel to the coolant channels increases with heat flux and is very similar for the unconstrained and constrained conditions

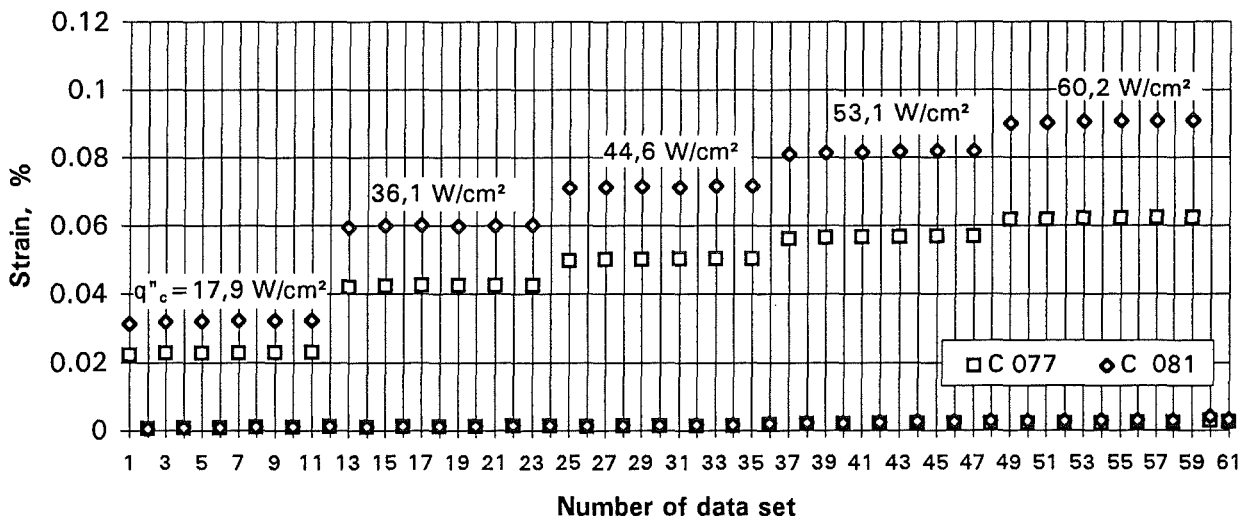


Fig. 4.10 Reproducibility of strains parallel to coolant channels at selected positions in test series TS1N-S7 (unconstrained)

As an example Fig. 4.11 illustrates the transient reading from two strain channels during one power cycle at $q''_c = 60,2 \text{ W/cm}^2$; the channels are the same as in Fig. 4.9. In the beginning of the heating phase the curves start with a small amount of residual strain generated in preceding cycles. The strain increases very fast and reaches a steady-state value within 30 to 40 seconds which is faster than the development of the temperature profile shown in Fig. 4.7; there is no question that the steady-state strain level is reached during the heating phase. During the cooling phase the strain decreases and reaches the starting value, again much faster than the temperature in Fig. 4.7. The maximum strain reached is on the order of 0,1 %; there is no difference between the traces for the unconstrained and constrained conditions.

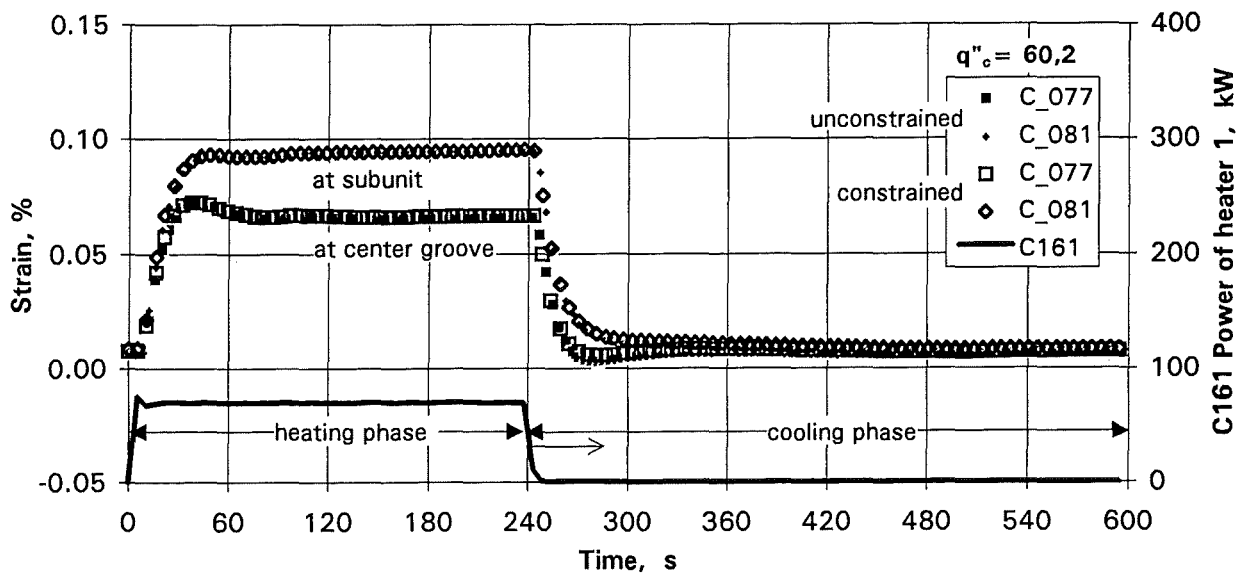


Fig. 4.11 Transients of strains parallel to coolant channels at two selected positions

Strains transverse to the coolant channel direction

For the transverse strains Fig. 4.12 again is an overview at $q''_c = 60,2 \text{ W/cm}^2$; the unconstrained and constrained conditions may be compared from this figure. Most of the readings from the back side of the plate are negative (compression) except for those from behind the central groove in the plate.

This may be explained by the geometry of the plate which consists of two subunits with four channels each and welded together in the groove area; at this groove the plate is much thinner (see Fig. 2.1). When applying a heat flux the front part of each subunit thermally elongates which in turn bows the subunit. If the temperature profile across the subunit was linear, there would be no elastic/plastic strain on its back side; but actually a nonlinear temperature profile with a steep gradient only in the front part and with most of the back part being close to coolant temperature causes a line of zero elongation somewhere in the subunit such that thermal elongation in the front part causes elastic/plastic compression in the back part.

If the specimen was constrained the above mentioned bowing of the subunit was impeded to some extent by a torque produced by the constraint and acting at the side

edges of the plate. This torque is limited in size because of the relatively weak side walls and weak groove area; but nevertheless this torque reduces to a small extent the strain on the back side of the subunits as may be seen from the data on left side of Fig. 4.12.

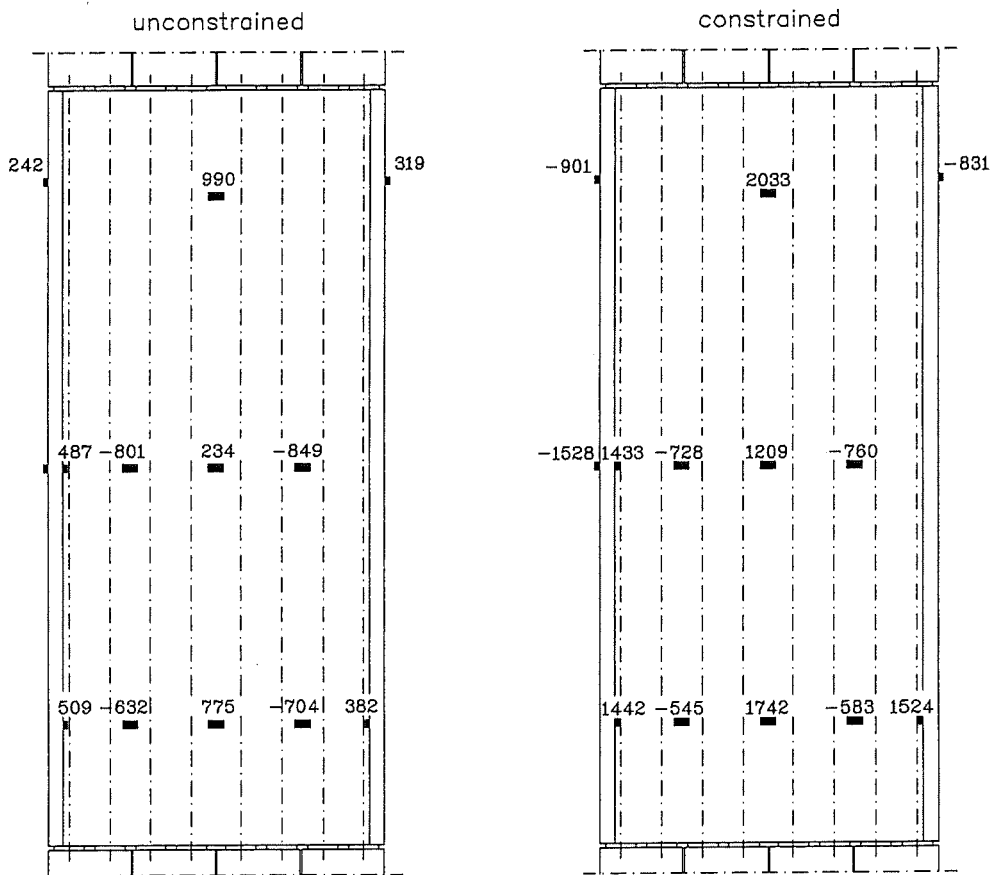


Fig. 4.12 Strains transverse to the coolant channels given in $10^{-4}\%$ (microstrains) at $q_c'' = 60.2 \text{ W/cm}^2$ for the unconstrained (left) and constrained (right) conditions

Much stronger is this influence on the back side of the central groove. In case of the unconstrained specimen the positive strain there could be understood probably only by a detailed consideration of the 3-d stress field but the strong increase in case of the constrained specimen may be easily explained by considering the torque mentioned above; it tries to bow the side edge to the front and has considerable success only at the relatively weak center groove (10,3 mm wall thickness) resulting in a large positive strain on the back side of the plate. For $q_c'' = 60 \text{ W/cm}^2$ the strain there reaches 2000 microstrains or 0,2 % which contains a plastic portion of deformation and would determine the fatigue life time of the specimen since it is reduced to almost zero strain during each cooling phase.

Fig. 4.13 demonstrates how in three selected locations the transverse strain varies with heat flux and constraint. All strains increase nearly linearly with the heat flux. The negative strain at SG 83 at the back of the subunit stays almost unchanged by the constraint. In contrast the positive strains at SGs 79 and 87 at the back of the center

groove are increased by about 0,8 % as a consequence of the constraint and for the $q''_c = 60 \text{ W/cm}^2$ case.

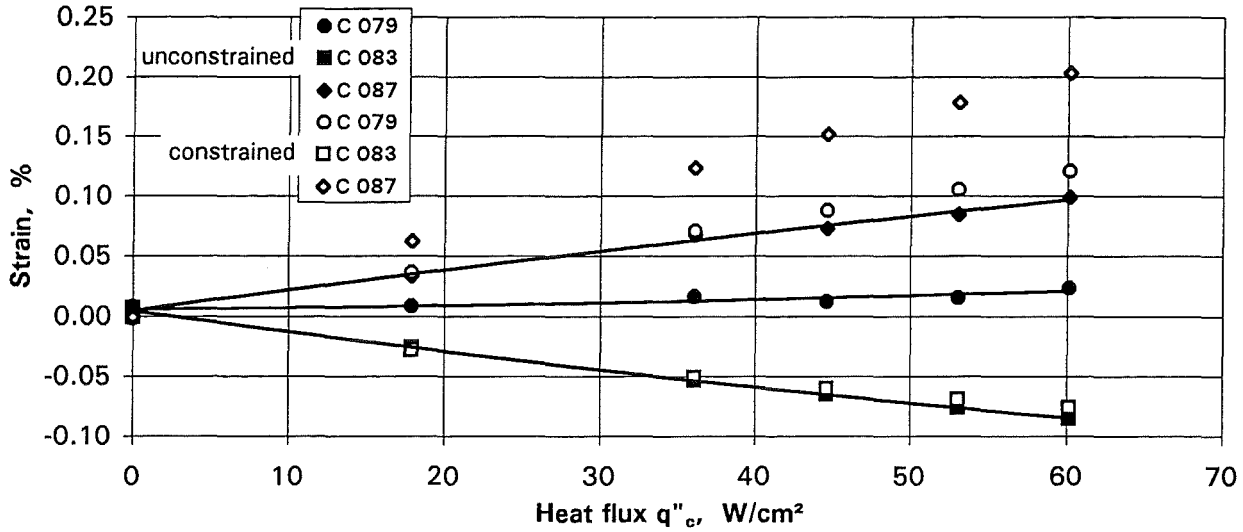


Fig. 4.13 Strain transverse to coolant channels changes with heat flux and in some positions strongly depends on constraint

Fig. 4.14 gives an impression on the reproducibility of the readings and at the same time shows that in the most strained locations at the back of the center groove readings fall back to almost zero which indicates the absence of ratcheting.

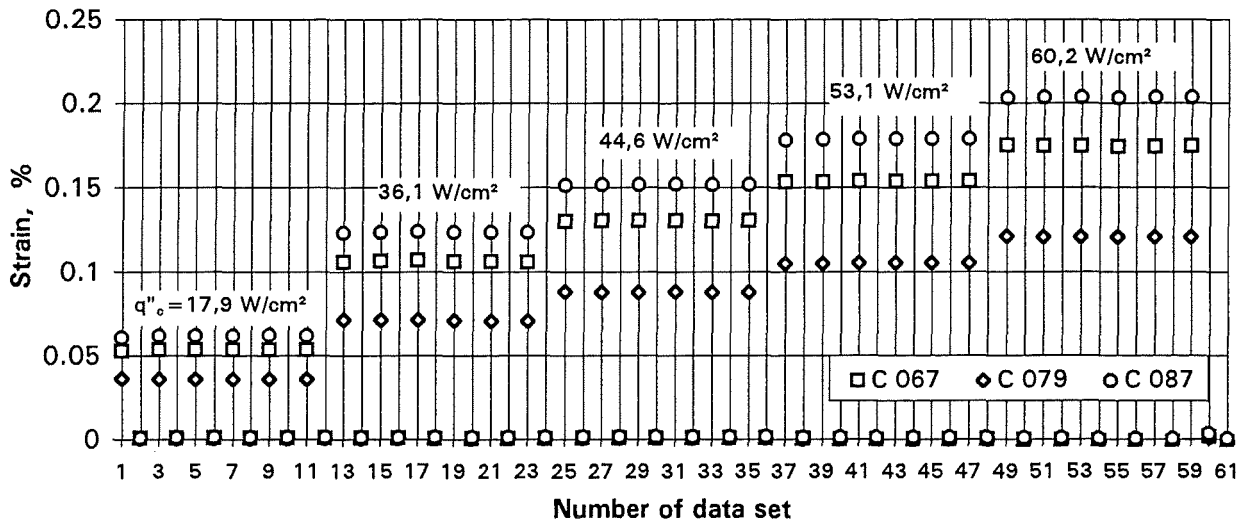


Fig. 4.14 Reproducibility of strains transverse to coolant channels at selected positions in test series TS1N-S7 (constrained)

In Fig. 4.15 the transient behavior at four locations is shown for both the unconstrained and constrained cases; the general behavior is like that discussed for the SGs parallel to the channels but two details are worth to be pointed out: (a) SG 79 of the unconstrained case passes a minimum early in the heating transient and then climbs to positive values; it is believed that the minimum indicates the point in time, where the 3 mm gap between the side-wall flange and the constraint bars was consumed by front plate bowing and that after this some constraint caused an elongation at this place. (b) SGs 87 and 67 do

not show a minimum though they are also positioned at the back of the center groove but near the edges of the front plate; this behavior will be discussed together with the modeling results.

The slight increase of the reading of SG 83 after having passed the minimum may be explained by the incomplete self-temperature-compensation of the SGs discussed in Chapter 4.2.2.

During the cooling phase the strains fall back quite fast to values close to zero.

In this Chapter only the obvious relations between the strain readings and the test conditions were discussed. A more detailed interpretation of the strain quantities and their local differences are possible only on the basis of a 3D analysis of the strain field.

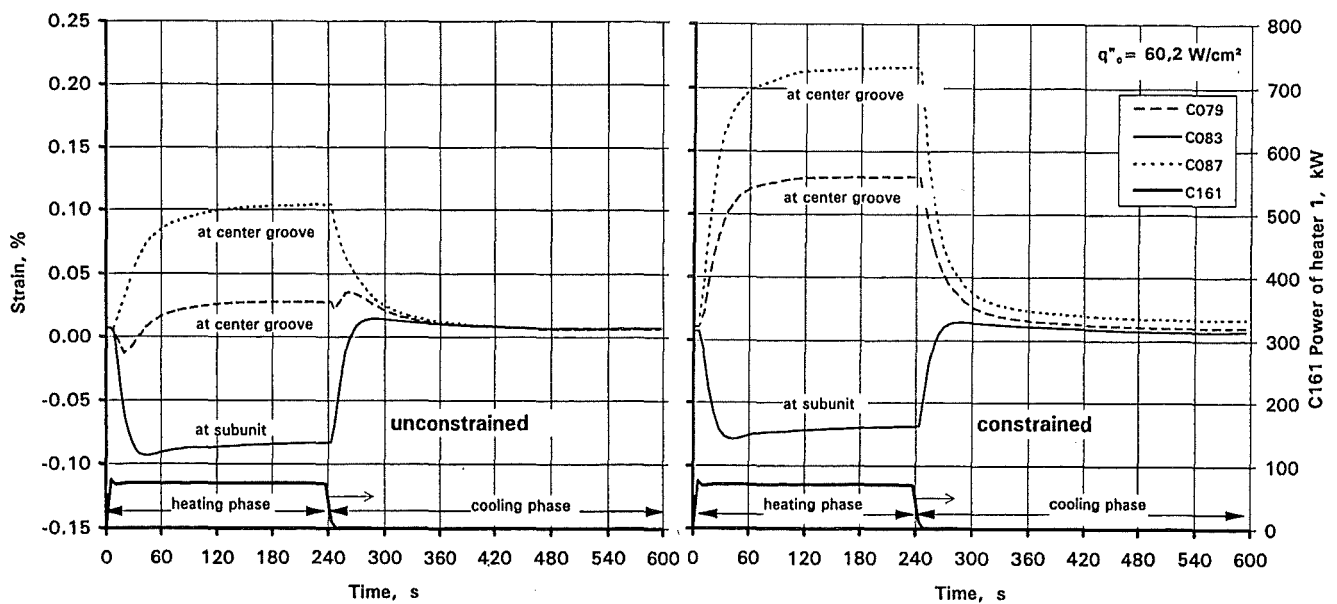


Fig. 4.15 Transients of strains transverse to coolant channels at three selected positions in the unconstrained (left) and constrained (right) conditions

4.5 FE Modelling Results and Comparison

4.5.1 General Remarks

Most of the accompanying thermomechanical FE-calculations with the FE-code ABAQUS [5] were based on the assumption of linear thermoelastic material behavior. The material parameters of SS AISI 316L were chosen according to [6] (see the table in Fig. 4.16).

Fig. 4.17 shows the meshes of the 2D- and 3D-models, which were used for the analysis and utilize obvious symmetry conditions and consist of quadratic elements with reduced integration. For economical reasons, the x-y-cross-section of the 3D-model could not be meshed as fine as the corresponding 2D-model. In the direction of the z-axis, the 3D-mesh is refined towards the free end.

The thermomechanical analysis was decoupled in the usual way: First the steady-state or transient temperature field was calculated by solving the thermal boundary value problem. In a second step, the thermal strain field related to this temperature field by the coefficient of thermal expansion was used as loading input in a mechanical analysis. Thus, the mechanical strain field (resulting in stresses) was calculated from the condition

of mechanical equilibrium under the given mechanical boundary conditions such that the total strains are compatible.

Temperature	Thermal Conductivity	Density	Specific Heat	Elasticity Modulus	Poisson's Ratio	Coeff. of Thermal Exp.
T	k	ρ	Cp	E	ν	α
(°C)	($10^{-3} W/mmK$)	(g/mm^3)	($J/g K$)	($10^3 MPa$)	(·)	($10^{-6} 1/K$)
20.	14.6	7.96 10^{-3}	0.476	192.	0.3	16.2
100.	15.7		0.491	186.		16.6
200.	17.1		0.508	178.		17.1
300.	18.6		0.526	170.		17.5
400.	20.0		0.544	161.		17.8
500.	21.4		0.561	153.		18.1
700.	24.2		0.597	137.		18.7
1000.	28.5		0.650			19.5

Fig. 4.16 Material parameters according to [6]

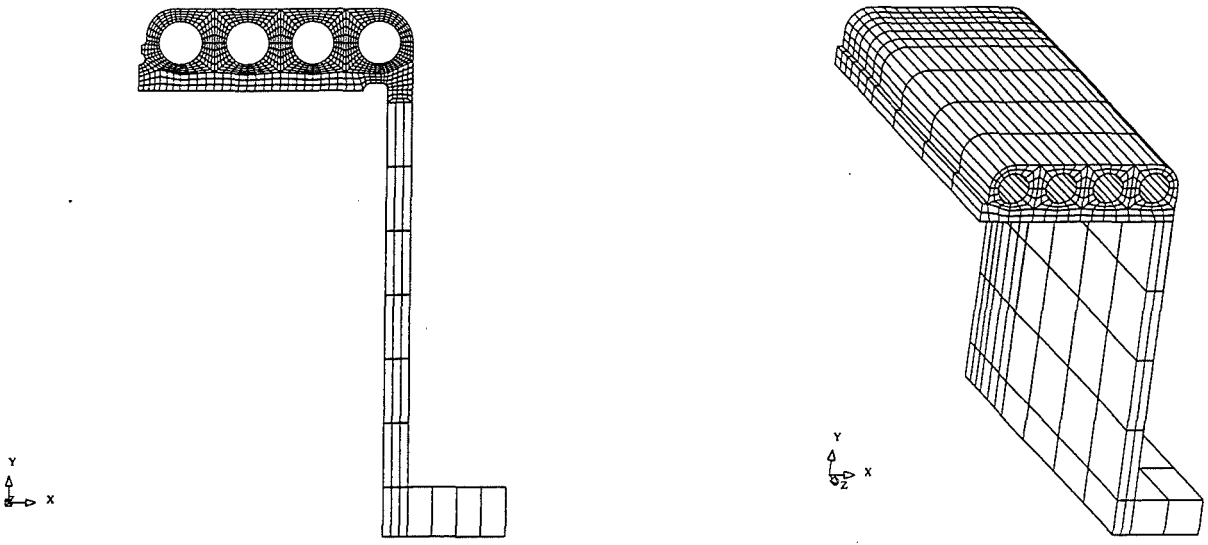


Fig. 4.17 2D- and 3D-mesh models of TS1

4.5.2 Thermal Analysis

The assumed spatial distribution of the heat flux from the heater to the mock-up may be seen from Fig. 4.18. Here, q'' means the nominal heat flux related to the area of the projection of the heated surface of the mock-up into the x-y-plane (see section 4.3.2). A similar assumption has been made in [2]. Fig. 4.19 shows the applied heating cycle.

The coolant temperature was chosen to be 41°C , while the heat transfer coefficient was estimated to have a value of $0.7\text{ W}/(\text{cm}^2\text{K})$. Fig.4.20 shows the resulting temporal evolution of the temperature at the nodes located most closely to the position of the thermocouples TC21 (+) and TC16 (*) for $q'' = 60.2\text{ W}/\text{cm}^2$.

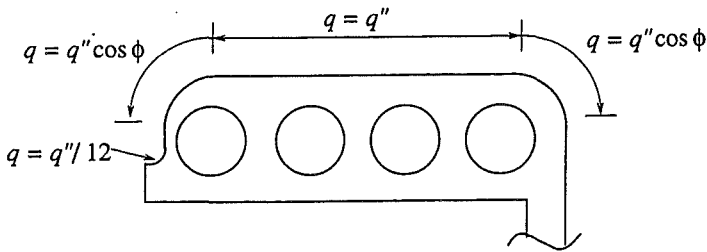


Fig. 4.18 Distribution of the heat flux received from the heater

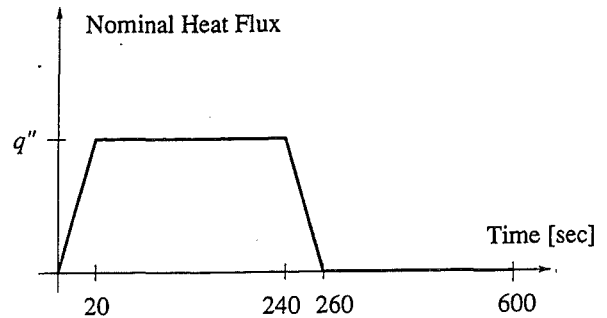


Fig. 4.19 Heating cycle

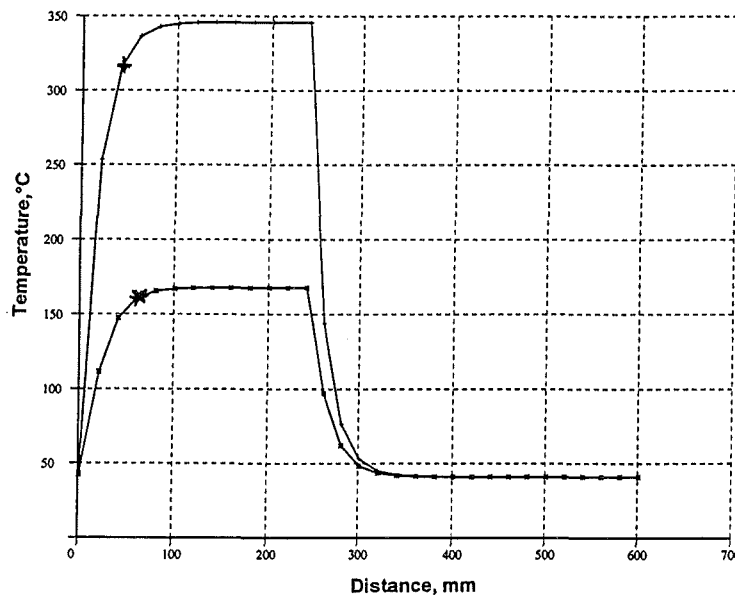


Fig 4.20 Time-dependence of the temperature at locations TC21 (+) and TC16 (*) at $q'' = 60,2\text{ W}/\text{cm}^2$

By comparing with the measured results in Fig. 4.7 indicating maximum temperatures of 290°C and 135°C , it may be seen immediately, that the calculated temperatures are much higher. The steady-state temperatures at the exact positions of TC21 and TC16 may be interpolated from Fig. 4.21. This figure shows the temperature plotted along the vertical line of symmetry between the two inner cooling channels. The line starts at the

heated surface (0 mm) and ends at the back side of the front plate (33 mm). Because of the temperature gradient, which is very steep, the interpolated value at the exact positions of TC21 and TC16 are even higher than the values in Fig.4.20, namely 370° C and 180° C, respectively.

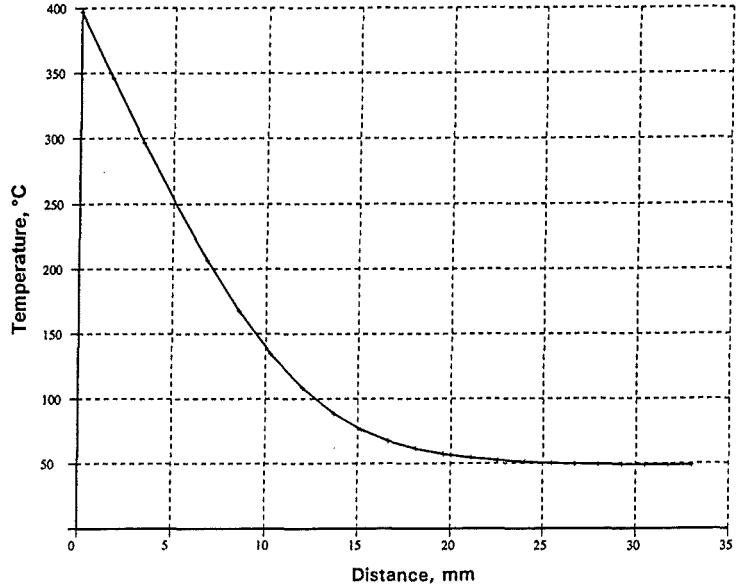


Fig. 4.21 Temperatures along a line of symmetry between the two inner cooling channels

A deviation of the same order of magnitude between measured and calculated results has also been reported by [2], where two reasons are discussed. The first one is subcooled boiling in the cooling channels: The stirring effect of steam bubbles originating from the channel surface, where temperatures up to 150° C are reached, increases the heat transfer coefficient. This effect has been taken into account by increasing the heat transfer coefficient from 0.6 W/(cm²K) to 0.7 W/(cm²K). However, in order to reduce the temperatures to the measured values, the heat transfer coefficient would have to be increased by a factor larger than 3. The more relevant explanation for the difference between calculated temperatures and thermocouple readings is the cracking of the conductive cement in the thermocouple boreholes. The transient thermocouple readings plotted in [2] clearly show a significant drop of the temperature amplitude after the first heating cycle, thus indicating immediate cracking of the brittle bonding cement and consequently a loss of thermal conductivity towards the thermocouples. Because of the steepness of the temperature gradient in the front region of the mock-up (see Fig. 4.21), a position change of the thermocouple contact by one tenth of a millimeter leads to a deviation of 2° C to 3° C.

While the highest thermocouple readings clearly are the most reliable ones, it is very unlikely, that they should not have been affected by cement cracking. Rather, the correct temperatures still have to be higher, but it is not clear by what amount. Finally, since on the other hand the material parameters and the boundary conditions are known with sufficient accuracy, we tend to accept the results of the thermal analysis as to be realistic.

As will be seen later on, the strains calculated on the basis of these temperatures confirm this conjecture.

4.5.3 Mechanical Analysis

As mentioned in section 4.3.1, the mock-up was subjected to two different types of mechanical boundary conditions, called "constrained" and "unconstrained" conditions. Fig. 4.22 is supposed to illustrate the corresponding remarks found in section 4.2.1.

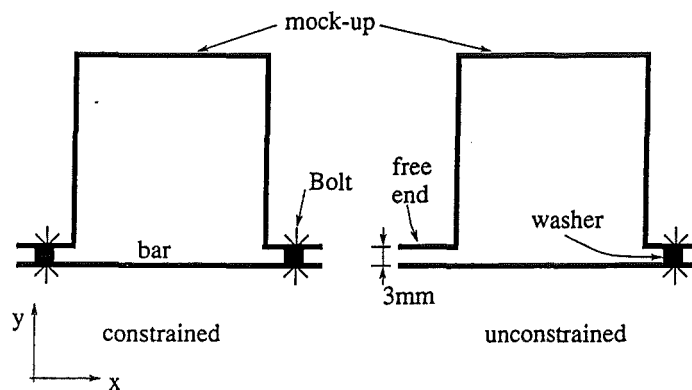


Fig. 4.22 Mock-up under constrained and unconstrained conditions

Under the given loading conditions, the x-y-cross-section of the boundary problem of the mock-up at $z=250$ mm is a plane of symmetry. The weak z-dependence of the coolant temperature does not disturb this symmetry significantly. Furthermore, the extension of the component in z-direction is large compared to its other dimensions. As a consequence, plane deformation conditions in the sense of the concept of generalized plane strain (GPE) prevail in this middle cross-section: A thin slice normal to the z-axis cut from the mock-up at $z=250$ mm deforms such that each of the free ends of the slice remains on a plane. These planes may translate in direction of the z-axis and rotate about the x-axis, such that no resulting force or moment acts in these directions. Thus, we may demand that a 2D-analysis based on the GPE-concept has to yield correct stress and strain results for the inner region of the mock-up. This is not only to hold for the xx-, yy- and xy-components of these tensors, but also for the zz-stresses and strains.

In order to verify the mechanical analysis in the above sense, the calculated mechanical strains may be compared with the strains measured at the back side of the middle cross section of the mock-up in directions parallel and transverse to the cooling channels.

In doing so, the following has to be kept in mind because of the incomplete temperature compensation between strain gauges and mock-up: According to the discussion given in section 4.2, the readings of the strain gauges during the heating phase have to be reduced by $1 \div 2 \cdot 10^{-4}$ to yield the correct measured mechanical strains. For the sake of brevity, we denote in the remainder of this section calculated "mechanical strains" simply as "strains".

After these preparing remarks, the strains parallel to the direction of the cooling channels are considered first (Figs. 4.23 and 4.24). It can clearly be seen, that the results calculated for the two different boundary conditions are the same. This is in complete accordance with the measured results in Fig. 4.11. Furthermore, the calculated and the

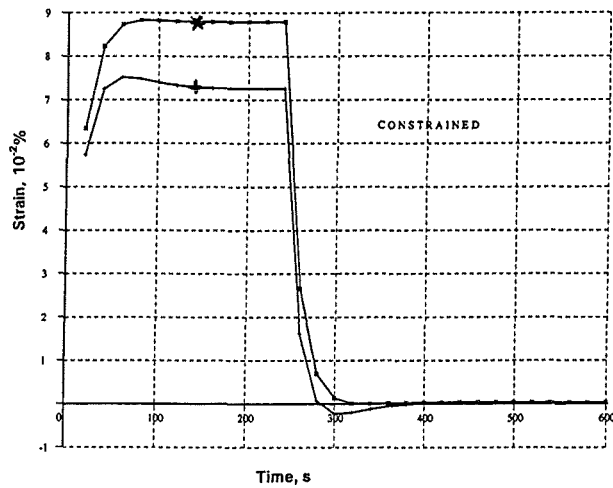


Fig. 4.23

Time-dependence of strains parallel to cooling channels at locations SG77 (+) and SG81 (*) for $q'' = 60,2 \text{ W/cm}^2$ under constrained (left) and unconstrained (right) conditions

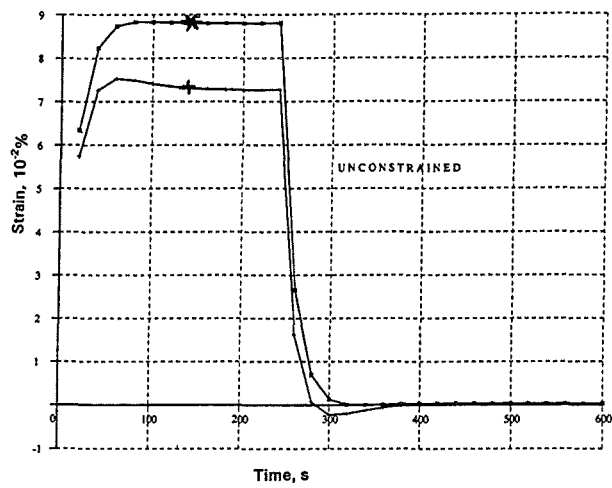


Fig. 4.24

measured values are the same, if the latter are reduced by $1 \cdot 10^{-4}$. Finally, the shapes of the calculated and measured strain-time-curves coincide for both strain gauge positions in detail. Thus, the discussion of the measured results given in section 4.4.2 is confirmed and does not have to be repeated here.

Next, consider the strains in direction transverse to the cooling channels:

- If for the constrained condition Fig.4.25 is compared with Fig. 4.15 (SG79 and SG83), the same degree of agreement is found as for the parallel strains before. Therefore we refer to section 4.4.2 without further discussion.
- Finally, for the unconstrained condition, the agreement for SG83 (* in Fig. 4.26) is still quite well. But for the reading of SG79, no coincidence at all may be found.

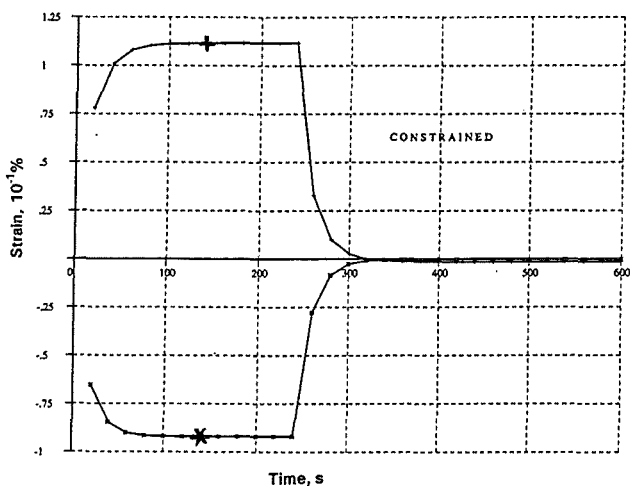


Fig. 4.25

Time-dependence of strains transverse to cooling channels at locations SG79 (+) and SG83 (*) for $q'' = 60,2 \text{ W/cm}^2$ under constrained (left) and unconstrained (right) conditions

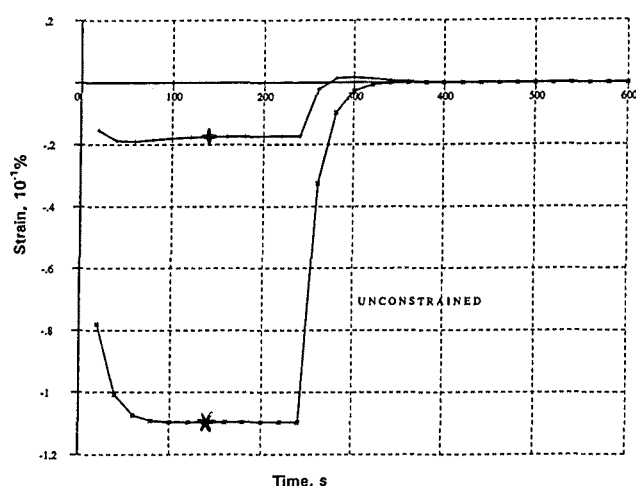


Fig. 4.26

As mentioned before (see section 4.4.2), the positive transverse strain measured right beneath the center groove cannot be understood in the case of unconstrained conditions. As calculations showed, positive transverse strain at this position are only possible, if the center groove would have been heated much more intensively than possible (at least by 100% of q''). By inducing large thermal strains in all directions, this would lead at the back side to the positive transverse strain read from SG79. But at the same time, because of the plane deformation conditions in the middle cross section, this would induce compressive parallel strains of about the same absolute value, which is in clear contradiction to the readings of SG77. It follows, that the discussed discrepancy cannot be explained by erroneous assumptions about the thermal boundary conditions.

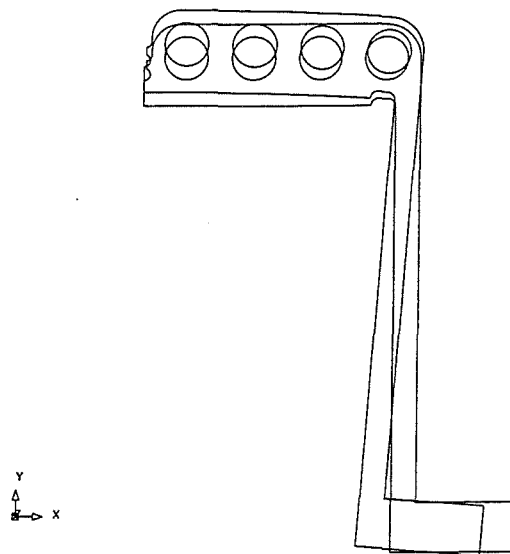


Fig. 4.27 Deformed and undeformed cross sections under constrained conditions at $q'' = 60,2 \text{ W/cm}^2$

Fig. 4.27 shows the deformed and the undeformed cross section of the heated mock-up (the deformation has been magnified by a factor of 4). In view of the deformation behavior, one might have the suspicion, that the unconstrained conditions did not hold during the heating phase. As can be seen from Fig. 4.22, the width of the gap beyond the free end of the side wall was 3 mm, as long as the mock-up was not heated. It is conjectured, that the gap was not wide enough, and that after a certain amount of heating the free end of the side wall touched the bar indicated in the figure. Suppose this to be the case, the mock-up would behave similar as under constrained conditions from then on, thus explaining the positive readings of SG79 observed in Fig. 4.15 for the test after a short time had elapsed.

A simple geometrical consideration, sketched in Fig. 4.28, confirms the above conjecture on the basis of the numerical values of the displacements calculated for the nodes indicated in Fig. 4.28. Under steady-state conditions, the required width δ of the gap would have been 1.7 mm, 3.4 mm, 4.2 mm, and 5.5 mm for $q'' = 17.9 \text{ W/cm}^2$, 36.1 W/cm^2 , 44.6 W/cm^2 , and 60.2 W/cm^2 , respectively. During a heating cycle with an amplitude of $q'' = 60.2 \text{ W/cm}^2$, the calculated results show, that the closing of the gap can be expected to happen not later than at $t=20 \text{ sec}$. This is in accordance with the appearance of a

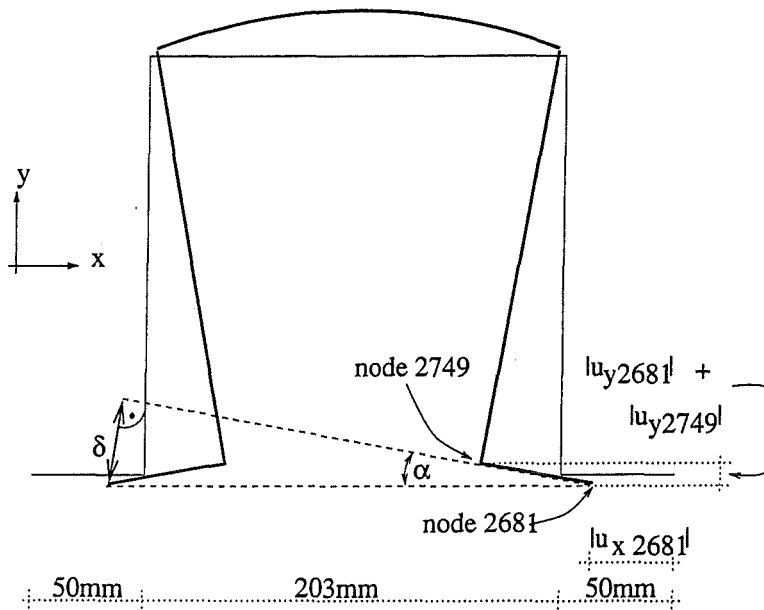


Fig. 4.28 Calculation of the gap width δ required beneath the free end of the TS1:
 $\delta = (303\text{mm} - 2 * |u_{x2681}|) * \sin\alpha$; with $\sin\alpha = (|u_{y2749}| + |u_{y2681}|) / 50\text{mm}$

minimum at that time in the reading of SG79 recorded in Fig. 4.15 for the unconstrained case.

As a result of the preceding discussion we may give the following judgement on the decoupled analysis based on thermoelasticity and the concept of generalized plane strain: By retaining the economical advantages of a 2D-modeling, this method yields reliable results for the 3D-stress and strain state, as long as the middle region of the mock-up is considered ($z \approx 250\text{mm}$).

Now, at other locations of SG85 and SG87 that are close to the free end of the mock-up, it cannot be expected, that a calculation based on a plane-strain-assumption is capable of reproducing these results. In the neighborhood of the stress free surfaces at $z=0\text{mm}$ or 500mm , only a small degree of constraint in direction parallel to the cooling channels can be opposed across the cross section of the mock-up. This missing constraint affects the parallel strains, as can be seen from looking at the readings of SG77 and SG85 in Fig. 4.8.

For comparison, mechanical strains were calculated from a 3D-model (constrained conditions). For economical reasons the 3D-mesh had to be rather coarse (see Fig. 4.17), and only steady-state conditions were considered. Although the mesh is refined towards the free end, it is not fine enough to catch the details of the stress-strain-state in this region.

In Fig. 4.29, the parallel strains are plotted over a line running on the back side right beneath the center groove from the free end ($z=0\text{mm}$) to the middle of the mock-up ($z=250\text{mm}$). For $z=250\text{mm}$, the value is quite close to steady-state value for the location of SG77 (+) in Fig. 4.23. Towards the free end ($z=0\text{mm}$), the parallel strains fall continuously, and even change sign. At the location of SG85 ($z=70\text{mm}$), the calculated

value is -300 microstrains, which compares quite well with the measured value of -350 microstrains in Fig. 4.8.

At first sight, this negative value (compressive mechanical strains) is surprising (see section 4.4.2), since one would expect, that the thermal expansion of the heated surface will cause mechanical tension in x- and y-direction at the "cold" back side. However, close to the stress free end ($z=0$ mm), the zz -stress component parallel to the cooling channels vanishes, and a nearly plane stress state results. At the back side, also the yy -stresses are zero, leaving an uniaxial stress state in x-direction. Thus, the only mechanism which is left to induce a mechanical strain in z-direction is the contraction strain, which is related to the uniaxial stress in x-direction by the Poisson-ratio. Since this uniaxial xx -stress is tensional (which is easily understood at least under constrained conditions, see the reading of SG87 in Fig. 4.12), the parallel component of the mechanical strain is negative. Furthermore, according to the Poisson-ratio of AISI 316L, the absolute value of the parallel strain is expected to be about one third of the absolute value of the transverse strain at the stress-free end.

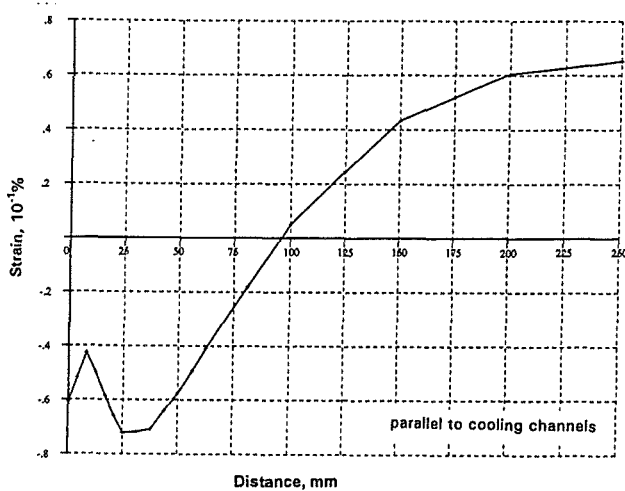


Fig. 4.29

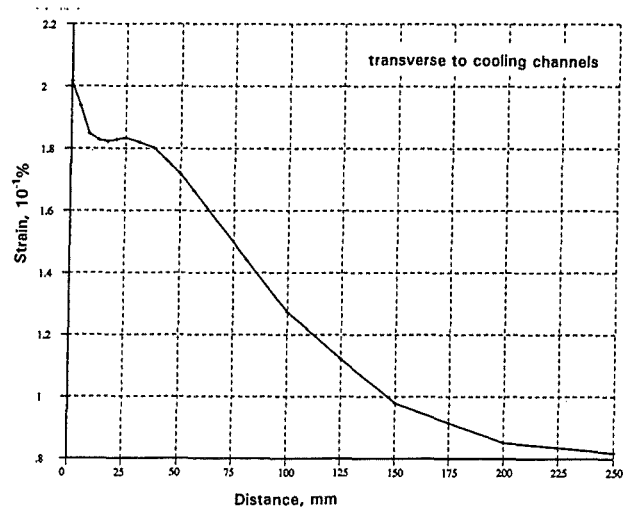


Fig. 4.30

Strains (parallel:left and transverse:right) from a 3D-model along a line running on the back side beneath the center groove from the free end ($z=0$) to the middle of the TS1 ($z=250$) calculated for $q'' = 60,2 \text{ W/cm}^2$ and constrained conditions

The transverse strains show a significant rise towards the free end of the mock-up (see Fig. 4.12). This dependence on the z -coordinate cannot be explained by the missing constraint in the surrounding of the free end in the first place. Rather, the overall deformation behavior of the mock-up, which is discussed in the next section, is responsible for this. Referring to this section, we postpone a closer discussion of this point, and restrict ourselves to comparing the reading of SG87 with the calculated results in Fig. 4.30. For $z=250$ mm, the value is almost the same as the steady-state value for the location of SG79 (+) in Fig. 4.25. Towards the free end, the transverse strains increase to a value of nearly 2000 microstrains, which is in accordance with the readings in Fig. 4.12. In closing this section, a short remark on ratchetting is made. As soon, as a process with cyclic plastic deformation is considered where a constant load is superposed, one may think of the possibility for ratchetting. But in the case of the experiments discussed in this

report, the coolant pressure was low enough, not to induce such a superposed constant load. Thus, ratchetting was not expected to occur.

Nevertheless, for the purpose of verification by an elastic-plastic FE-analysis the same bilinear ORNL plasticity law was used as in [2]. The shaded area in Fig. 4.31 indicates the region, where plastic deformation occurred after four heating cycles. Plastic deformation was said to have occurred at a location, if the accumulated plastic strain was larger than 10^{-4} at the time considered. It turns out that the region defined in such a manner does not change further significantly after the first heating cycle.

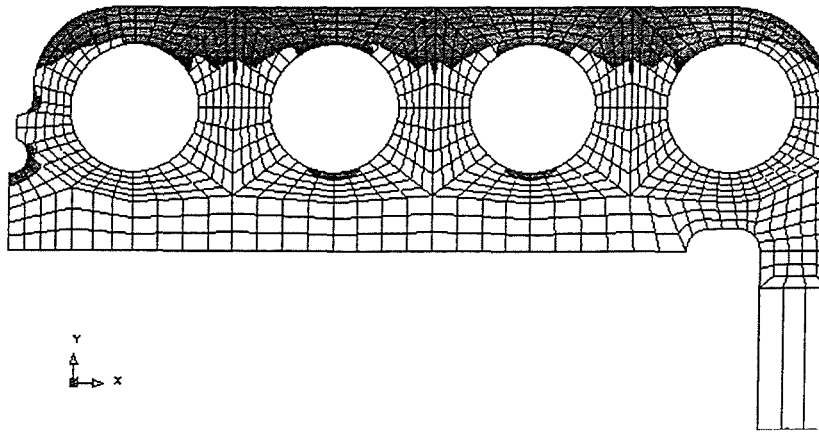


Fig. 4.31 Region of accumulated plastic strain greater than 0.01% for $q'' = 60,2 \text{ W/cm}^2$

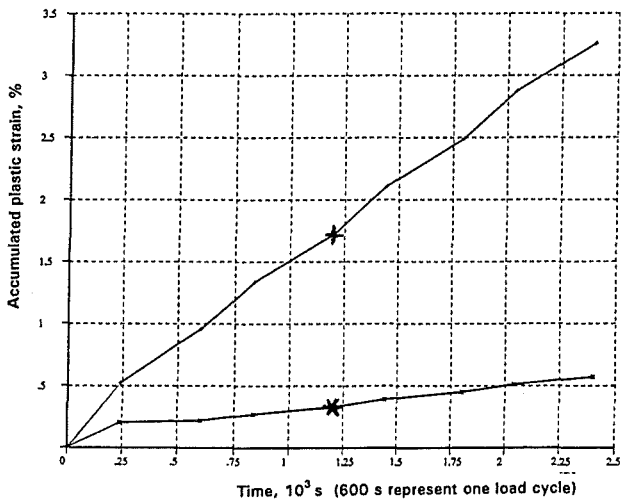


Fig. 4.32

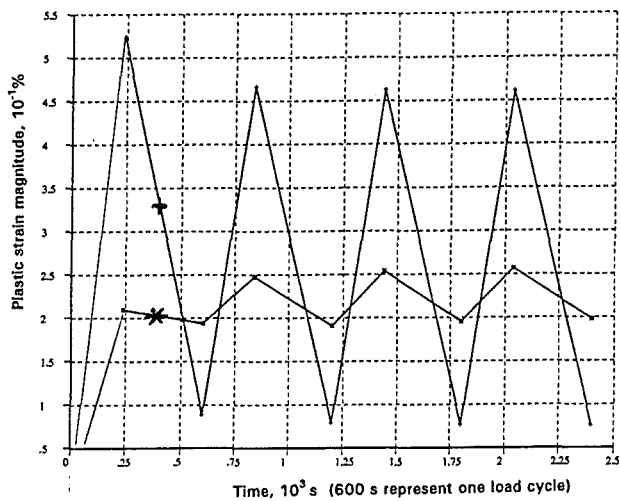


Fig. 4.33

Evolution of accumulated plastic strain (left) and plastic strain magnitude (right) for a point on the heated surface right above the second cooling channel (+) and for a point on top of the fourth cooling channel (*) at $q'' = 60,2 \text{ W/cm}^2$

The points of maximum accumulated plastic strain lie on the heated surface right above to the cooling channels. Furthermore, the top of the cooling channel walls experiences significant plastic deformation. Fig. 4.32 shows the evolution of accumulated plastic strain for a point on the heated surface right above the second cooling channel (+) and for a point on top of the fourth cooling channel (*) ($q'' = 60.2 \text{ W/cm}^2$). The absence of a ratchetting effect may be inferred from the (more or less) constant slop of these curves.

The latter conclusion can be drawn more firmly from Fig. 4.33, where the evolution of the plastic strain magnitude for the same points as in Fig.4.32 is shown. The plastic strain magnitude is a measure of the magnitude of the current plastic strain state at a point. After the second cycle, the plastic strain magnitude oscillates between fixed bounds and does not show an increasing mean value. Thus, no ratchetting takes place.

4.6 Conclusions

The temperature distribution in the TS1 was measured with the as-received TC instrumentation and calculated with a finite element code. Both the measurement itself and its comparison with the calculation showed that the TC readings were unreliable due to the reasons discussed above. Nevertheless, measurement and calculation proved that in cyclic tests burn and dwell phases of 4 and 6 minutes, respectively, are long enough to establish very near to steady-state conditions in the front plate of the TS1.

Local strains on the back side of the TS1 were measured with the as-received strain gage instrumentation and were calculated with a finite element code; the results of both agree reasonably well and help to better understand the deformation behavior of the TS1 under thermal load.

5. Thermo-mechanical Testing of TS1 with Radiatively Cooled Tiles

5.1 Design Concept and Specimens

The concept of a First Wall with radiatively cooled protection tiles was to place a 2 cm thick graphite tile in front of the stainless steel wall such that the tile could thermally deform independently from the wall. The heat would be transferred by radiation from the back side of the tile to the frontside of the wall; this heat transfer mechanism would be reliable in spite of thermal bowing of the partners. The maximum temperature of the tile would run well above 1500°C depending on its thermal conductivity and on the heat flux. The tile was to be held by two attachment studs as described below for the specimens.

The specimens to be tested consisted of the TS1 as a water-cooled SS wall (see Chapter 2.1 for details) and a 2 cm thick graphite tile sized 500x228 mm to cover the whole heated surface of the TS1. Fig. 5.1 shows an assembled specimen. The tile is mechanically held in position by the two attachment studs (AS) which are described below in some detail. The attachment is such that the tile to some extent is free to tilt over the attachment points mostly over the longitudinal center line. The amount of tilting is limited by eight spacer pads (SP) made of CFC which are attached to the back side of the tile; if at room temperature the tile is tilted to contact the SP with the TS1 surface on one side then the typical gap between the SP and the TS1 on the other side is on the order of 0.5 mm.

As shown in the schematic drawing of Fig. 5.2 the AS is essentially a flat and triangular piece machined from two-directional CFC with both fiber directions being parallel to the main plane of the stud; the minimum thickness of the AS is 2 mm. The AS is anchored on one side in the attachment groove of the TS1 which is formed in front of the weld joint between the two TS1 subunits; anchoring there is by the two cylindrical foot portions of the AS (5 mm dia.) with which the AS is slid into respective holes behind the shoulders (S) that form part of the machined TS1 attachment groove. The AS may tilt around its foot as far as the gaps between the AS and the S would allow it. Sliding of the AS longitudinally downward out of the anchoring position is blocked by a transverse pin (P) through the AS as the pin hits one of the shoulders (S). The small 2 mm dia. pin that originally was made of 2-d CFC was replaced for the tests by a stainless-steel pin since it seemed too fragile to survive the tile mounting and testing.

The AS is anchored on the other side in a reception hole of the tile. There were two different designs (A and B) for this side. Design B was used for the tests SZ1. When mounting design B the two halves of a collar (C) are slipped behind the T-shaped head end of the AS and a cap with a conically shaped bottom is to hold the collar in place. Design A was used for the tests SZ2 and SZ3; when mounting design A a conical nut is turned onto the threaded head end of the AS until it contacts the conical hole in the tile.

In the original design the protection tile was to consist of a three-directional CFC material. The company in charge of manufacturing the CFC material for the tests seemed to be not successful in delivering a material with the specified characteristics. Therefore, tests SZ1 and SZ2 were performed with tiles made of fine-grained graphite (Type FE 219

by Schunk und Ebe); only tests SZ3 were performed with a tile made of 3-d CFC (Type FU 2939 by Schunk und Ebe) with a rather low density of the graphite matrix. In SZ1 the TS1 was unconstrained, in SZ2 and SZ3 it was constrained (see Chapter 2.1 for details).

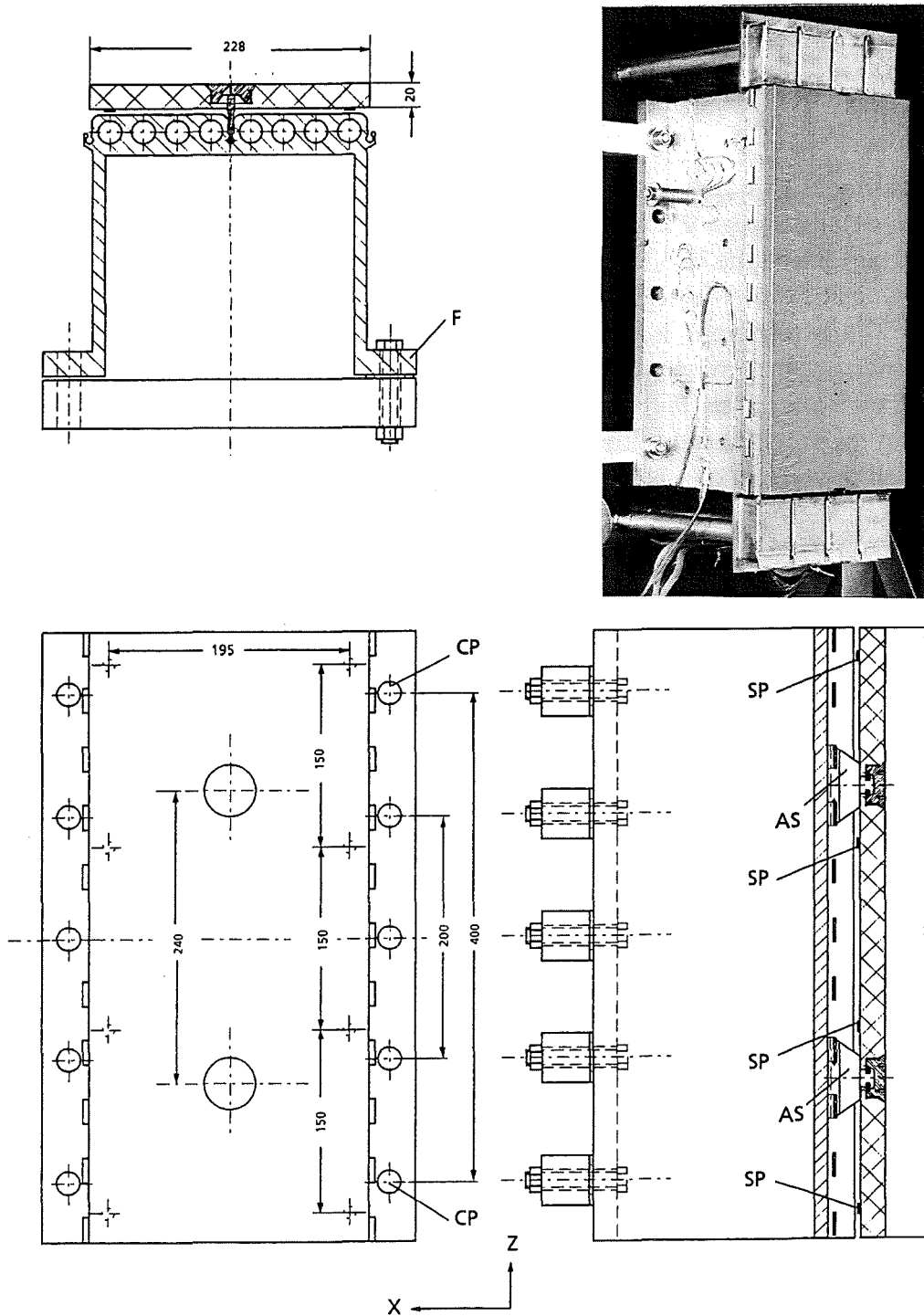


Fig. 5.1 Specimen TS1 with a radiatively cooled protection tile

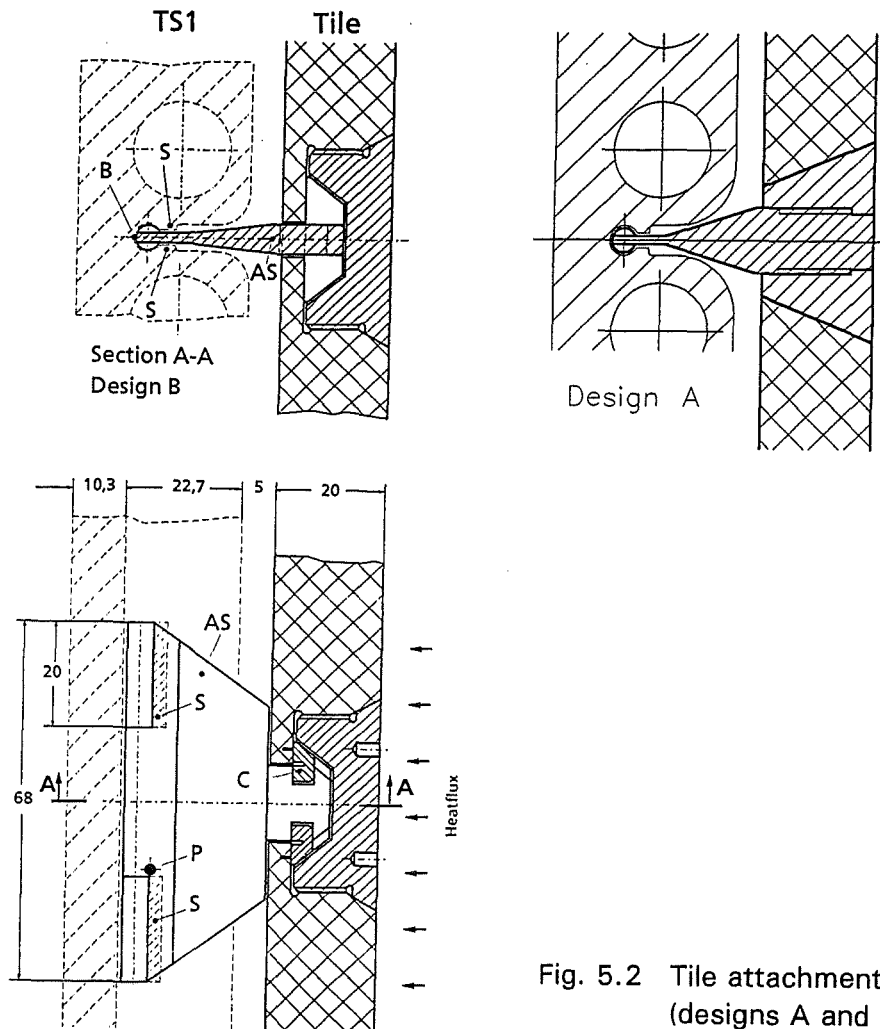


Fig. 5.2 Tile attachment area (designs A and B)

5.2 Goals of the Investigation

The investigation was performed in order to answer, to some extent, the question whether a first wall with a radiatively cooled protection tile of a certain design would stand the thermomechanical loads generated by a given heat flux applied to the plasma-facing surface of the design.

The attention was directed to three areas:

- (a) Tile attachment scheme:
Would the attachment scheme prove reliable under thermal loads? It was tried to identify and understand any unexpected behavior.
- (b) Thermal bowing of TS1 and tile:
How much clearance would be necessary between TS1 and tile to allow separate and different thermal bowing of both partners? On the back surface of the TS1 its global deformation was measured in some positions; on the back side of the tile the displacement relative to the TS1 was measured in one position. Both measurements were compared to model predictions.
- (c) Thermal conduction through the attachment stud:
Would the attachment stud as a thermal conduction path carry enough heat from the tile, which is at high temperature, into the attachment groove area of the TS1

to cause there harmful temperature and stress gradients? With a number of TCs temperatures were measured in the attachment studs and on the TS1 close to the anchoring points of the studs' feet.

Strain gauge readings from the back side of the TS1 were also acquired during this test series but no major attention was given to them since they have been evaluated for the test series with the bare TS1 and the presence of a tile should not change these results.

5.3 Instrumentation of Specimens

The TS1 was kept instrumented with thermocouples and strain gauges as reported in Chapter 4.2.

For the tests with the radiatively cooled tiles three types of instrumentation described in the next Chapters were added.

- a. a pyrometer to measure the temperature of the tile's back side
- b. thermocouples to measure temperatures in the attachment studs and close to their anchoring points in the TS1
- c. linear variable differential transformers (LVDTs) to measure the global deformation (bowing) on the back side of the TS1 and the relative displacement of the tile

5.3.1 Pyrometer Directed to the Tile Back Side

Through the bottom of the TS1 attachment groove a 5 mm dia. hole was drilled to allow spatial access to the back side of the tile close to its center; the position of the hole was 24 mm above the midplane (Fig. 5.3). The pyrometer used was a spectral pyrometer type Pb50 AF S17 made by Keller GmbH at Ibbenbüren-Laggenbeck measuring at a wave length of 0.85 μm from 800 to 2300°C. Since the measurement was performed through a view glass in the vacuum vessel onto the surface of the tile the pyrometer had to be calibrated to take care of the view glass transmissivity and the tile's emissivity both being smaller than 1. This was done by measuring the true tile temperatures in the same spot with a two-color pyrometer and by adjusting the emissivity-setting (ϵ) of the PB50 such that it displayed the same temperature; the calibration resulted in an ϵ setting of 0.54 for tile temperatures between 1340 and 1500°C. Temperatures below the lower end of the pyrometer's measuring range at 800°C were always displayed and recorded as "800°C".

5.3.2 Thermocouples in the Area of the Attachment Studs

TCs were placed in the area of the attachment studs with the goal of gathering some rough information on the heat flow through the studs and on the local temperature increases which are caused by this heat flow into the steel of the TS1 anchoring zone; both quantities were expected to be mainly determined by the thermal contact resistances at the anchoring points at the tile and the TS1, respectively.

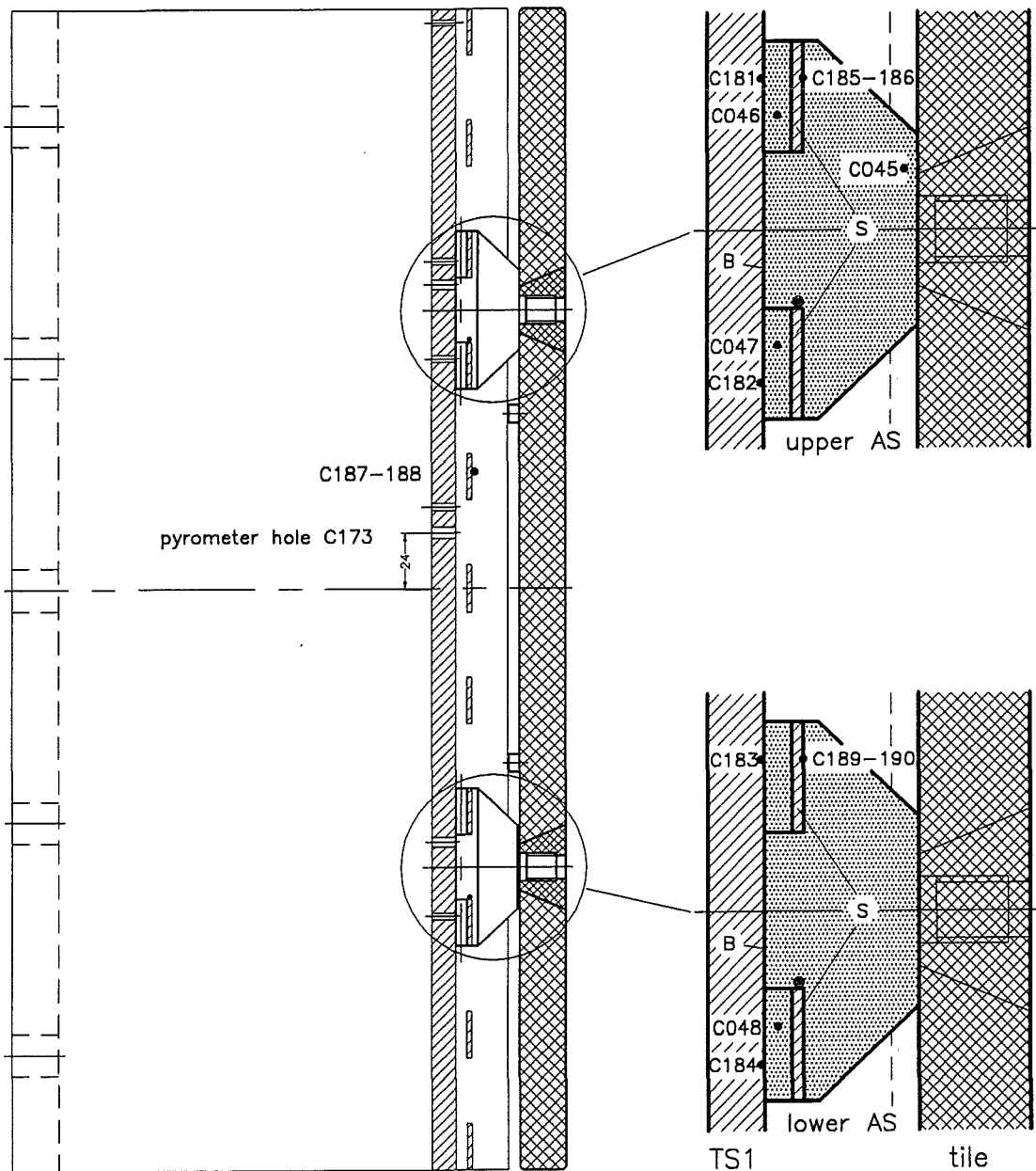


Fig. 5.3 Thermocouple positions in the vicinity of the tile attachment studs

TCs in the Studs

The upper stud was instrumented with three TCs, one (CO45) measuring close to the contact point with the tile and the other two (CO46 and CO47) in the center of the two cylindrical foot portions (Fig. 5.3). The lower stud received one TC (CO48) in the center of its lower foot. The TC numbers indicate the corresponding channels of the data acquisition. To install these TCs adequate holes had been drilled through the bottom of the TS1 attachment groove and these holes were extended into the CFC studs; for the last few millimeters these holes were 0.6 mm in diameter. After the tile was mounted 0.5 mm dia. sheathed and insulated type K TCs were slipped into the holes and held softly spring-loaded in position. Unfortunately, the TCs could only be run along a temperature gradient in the stud which may have reduced the precision of the readings; anyway the signal's fast response to power changes indicated that a reasonable thermal contact at

the TC junction had been reached. For the highest heat fluxes the TC nearest to the tile reached almost 1200°C and the TC sheath together with the carbon formed an eutectic which kind of brazed the TC into the stud without causing false readings.

TCs on the TS1

There was an interest to collect knowledge about the local temperature distributions in the steel in the vicinity of the contact points between the attachment studs and the TS1.

There was no chance to measure such distributions. There were several obstacles: (a) it could not be known in advance where the contact points would be located; even a moving of these points during each heat-up/cool-down cycle would be possible; (b) an instrumentation with a large number of TCs would have disturbed the conductivity and heat flux in the area to be investigated; (c) with the TS1 specimen, as it was, there was only a very limited possibility to bring additional instrumentation into the area to be investigated. Contact points were expected either on the back side of the shoulder (S) or on the bottom of the groove; therefore, some TCs were placed as close to these points as possible, i.e. on the frontside of the shoulders and in the bottom of the groove (Fig. 5.3).

Sheathed TCs type K of 1 mm dia. were used and their junctions were formed by unsheathing the tip and by welding the wires directly to the TS1 in the positions to be measured. On the shoulders the wires were spot-welded besides each other with a gap of some 0.2 mm in between; false junctions, if any, away from the measuring point could be detected by visual inspection or by observing the signal after contact-heating the measuring point. In the bottom of the groove the TC junctions were formed by bringing in the TCs through a hole from the back side and by laser-melting down the protruding TC wires together with the stainless steel at the bottom of the groove; the exact depth of junction below the surface is not known but the circumstances of installation indicate that it should be less than 2 mm.

The TCs in the TS1 groove area were located according to the expected contact points; the hanging tile tends to tilt the studs such that their upper foot is pressed against the back of the shoulder (S) and their lower foot is pressed against the bottom of the groove (B). Fig. 5.3 shows the measuring positions and the related channel numbers; in each of the shoulder positions two TCs were placed, one on each of the opposite shoulders (both sides of the stud). In addition to positions where the feet of the two studs are engaged an equivalent shoulder position without stud engagement (C187-188) was instrumented for comparison.

5.3.3 Displacement Sensors (LVDTs)

The spring-loaded LVDTs used were of type 108/4 made by TWK Electronic, Düsseldorf in a circuit of supply, calibration, and conversion units assembled by Lamberz, Euskirchen. The output transferred to the data acquisition system is in microns. The resolution is a few microns but because of time- and temperature-dependent instabilities of the system and because of thermal expansions of the structure between the reference plane and measuring spot the accuracy of the measurement is much poorer; the results should be regarded only as a rough approximation if the absolute values are taken; the accuracy is

much better though if results of several LVDTs mounted on the same structure are compared to each other.

A common reference plane for all LVDT sensors was created by fixing the LVDTs to a support structure of rods which as a whole was again mounted to the TS1 in only two points as explained below.

Figure 5.1 shows that five massive stainless steel bars were provided at the back end of the TS1 side walls; they were clamped with large-sized 3 mm thick washers to the flange (F) at one of the side walls (south). For the mechanical boundary condition of an "unconstrained" specimen the other side wall stayed unconnected to the bars and a 3 mm gap there was expected to allow free transverse bowing of the TS1 under thermal loads. For the condition "constrained" the other side was clamped also after filling the gaps with appropriate washers.

The outermost two of the five bars were used as a reference for the LVDTs by attaching their support structure to them in places close to the longitudinal center line of the TS1. So all sensors had a common reference plane that moved as a whole relative to the TS1 front plate as a consequence of thermal expansion of the side walls and of changes at the open 3 mm gap due to bowing of the unconstrained TS1. The reference plane may be assumed to in general have been parallel to the flange F with the reservation that the flange did not stay perfectly straight in the z-direction under thermal loads; more precisely, in the x-direction the reference plane was parallel to the flange (S) in the clamping points (CP) and in the z-direction it was parallel to a straight line through the two clamping points (CP).

LVDTs were positioned in 13 locations on the back side of the TS1 front plate and in addition 4 LVDTs measured in locations on one of the TS1 side walls (south) as indicated in Fig. 5.4. The figure views the TS1 from the back side; the numbers indicate the channels of the data acquisition. The LVDTs were distributed to cover the longitudinal center line of the specimen (z-direction) and a transverse line 10 mm above the center (x-direction). The dashed lines mark the coolant channels. There were also two positions close to corners (121 and 132).

For the test series SZ2 and SZ3 an additional LVDT 138 (Fig. 5.4) was installed and touched to the back side of the tile; it was expected together with LVDT 122 to provide a direct measurement of the gap between the TS1 and the tile as it changes by bowing of the components under thermal load. The sensor reached the tile through a 2.3 mm hole drilled through the bottom of the TS1 attachment groove close to the top end of the specimen. Since the sensor could not touch directly the tile's back side at up to 1600°C a 75 mm long piece of alumina tubing (2 mm OD by 0.5 mm wall) was placed between the tip of the sensor and the tile. Since this extension tube experienced a thermal expansion resulting from its elevated temperature the LVDT signal had to be corrected adequately. This correction is described in Chapter 5.4.3.

Zero adjustment of all the LVDTs was made at room temperature and prior to each series of tests.

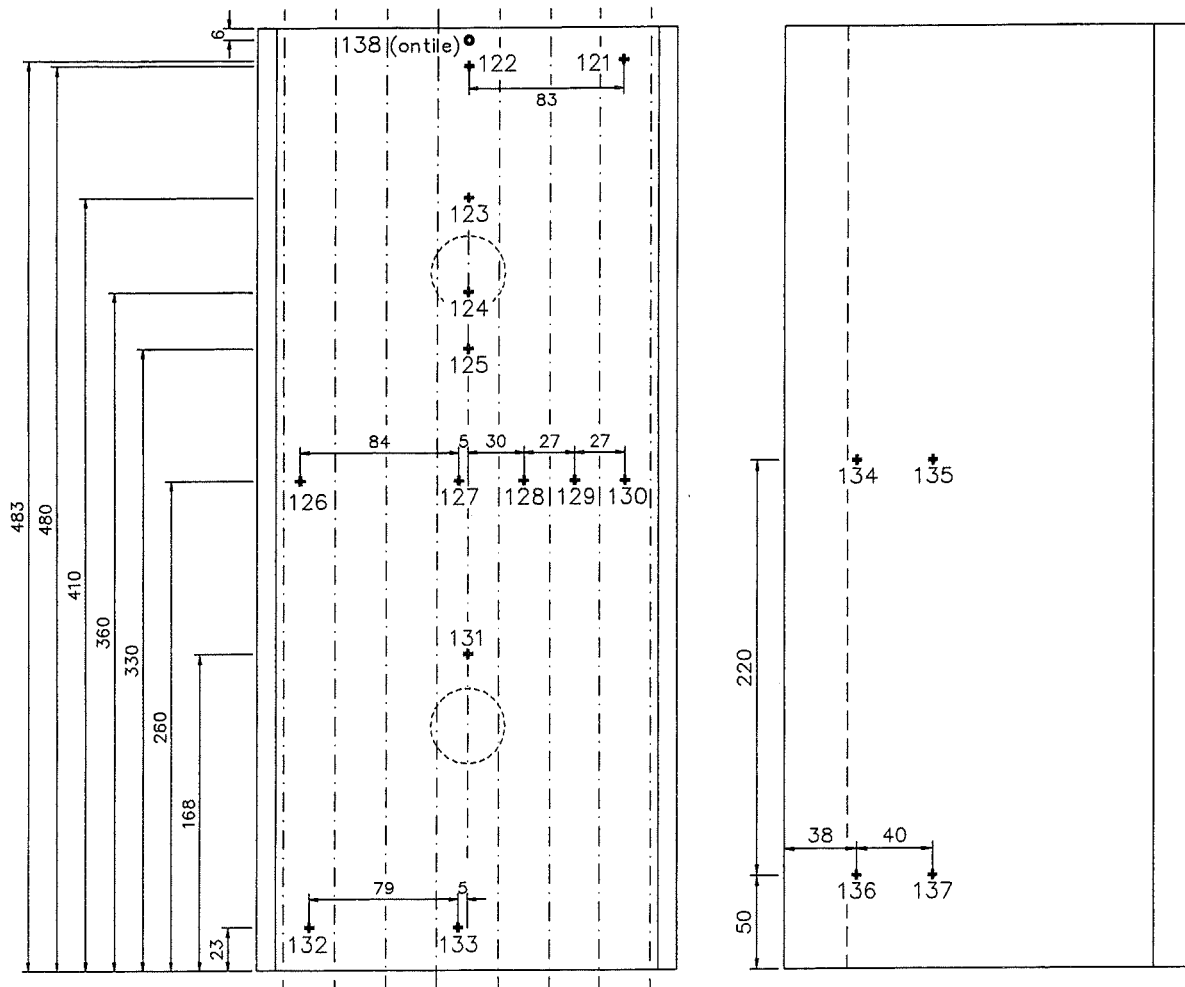


Fig. 5.4 Distribution of LVDT sensors on the back side of TS1 front plate (left) and on the outside of its side wall (right)

5.4 Testing

5.4.1 Experimental Set-up

Very similar to the experiments with the bare TS1, the specimen with the radiatively cooled tile was installed in a window of the FIWATKA heater housing and thus became part of this housing which surrounded the heater (compare Chapter 4.3.1). Fig. 5.5 shows vertical and horizontal sections through housing and specimen; there is a graphite tile in front of the TS1 and the only other differences of the setup as compared to Fig. 4.3 are:

- the left part of the housing was moved by about 20 mm to the left to make room for placing the tile between the heater and the TS1; the final distance between the heater and the surface of the tile was 25 mm.
- around the tile a collar of radiation shielding (3 layers of 1 mm flexible graphite) was mounted in order that in this area the high temperature heater does not face the cold TS1 coolant headers and housing structure directly; calculations had shown that this collar thermally behaved pretty much like the tile and that steep local temperature changes at the heater close to the edges of the tile were avoided.

All other characteristics of the set-up listed in Chapter 4.2.1 apply here as well.

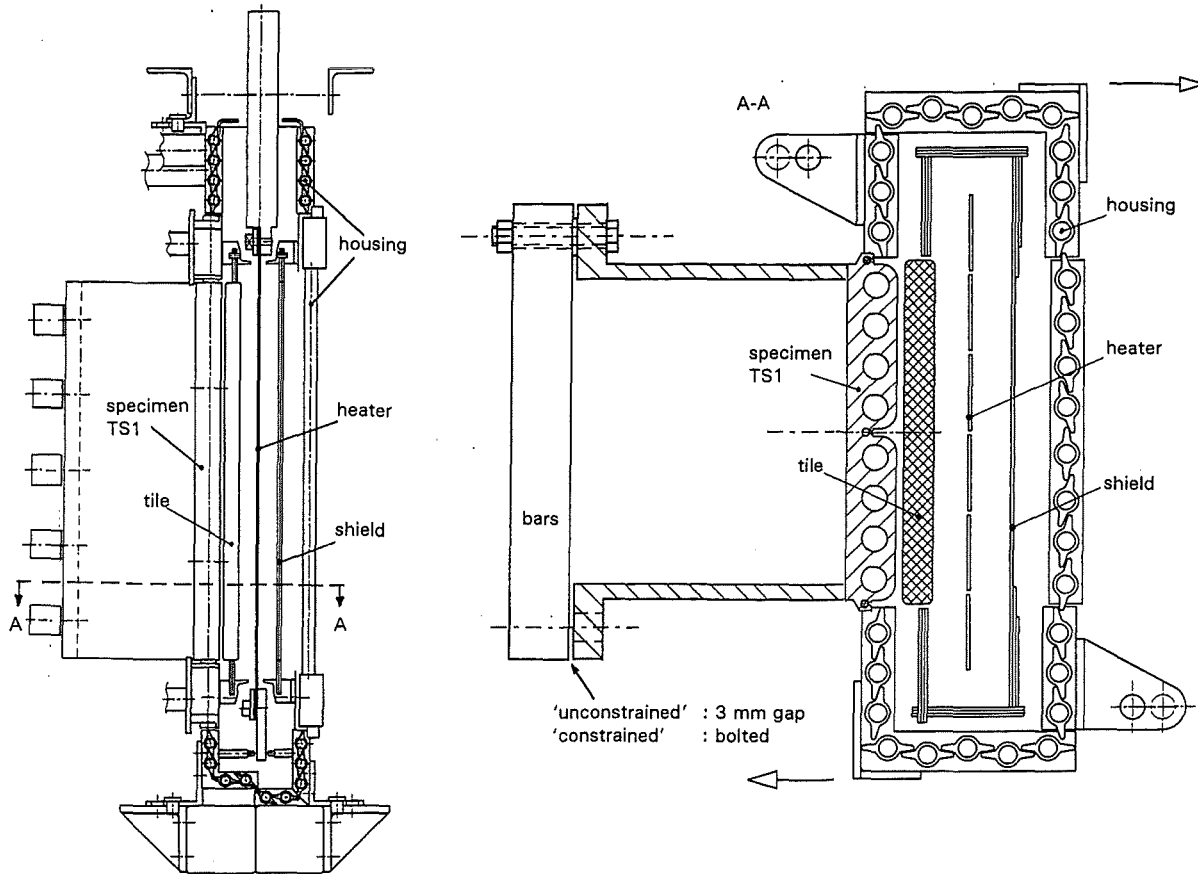


Fig. 5.5 Vertical and horizontal sections (different scales) through the experimental setup with the radiatively cooled tile for test groups SZ1 through SZ3

5.4.2 Experimental Procedure and Test Sequence

Tests with a radiatively cooled tile were performed in three groups:

group	tile no.	graphite of tile	attachment design	number of spacer pads	constraint of TS1
SZ1	1	fine-grained	B	8	unconstrained
SZ2	2	fine-grained	A	4	constrained
SZ3	3	CFC	A	4	constrained

The experimental procedure applied to each of the three groups was as follows:

- the tile was mounted on the TS1;
- the constraint of the TS1 was applied, if applicable;
- the gaps between each of the spacer pads (SP in Fig. 5.1) and the TS1 surface were measured after the tile had been tilted around its vertical axis to contact the spacers on the other side; note that in test groups SZ2 and SZ3 only the four central spacers were mounted to the tile;

- after mounting the specimen in the window of the FIWATKA heater housing the LVDTs were adjusted to read zero;
- after evacuating the vessel and circulating coolant through the specimen at room temperature for at least one hour the strain gauge measuring channels were adjusted to read zero (initializing);

Steady-State Tests

- a data set at zero power was recorded;
- the heat flux to the specimen was increased stepwise by increasing the heater power appropriately;
- at five selected power levels steady-state tests were performed, each by recording one data set after a waiting time for equilibrium of at least 20 minutes;
- another data set at zero power was recorded after several hours of cooling or the next morning;

Cyclic Tests

- for three power levels (out of the five above) cyclic tests were performed;
- for each power level the duration of the heating phase was varied; in some cases from 4 to 8 and to 12 minutes to investigate the approach to steady-state;
- these tests were done in sequences of usually 8 cycles that were run with the same power setting;
- in each sequence for the first 5 cycles data were recorded at the ends of the heating and cooling phases and for the last three cycles data were recorded transiently.

power per heater, kW		24			35	45			52			64		mech. bound. condition ¹⁾		
heat flux, W/cm ² (appr.)		16			24	30			35			43				
heating mode ²⁾		s/s	cycl			s/s	s/s	s/s	cycl			s/s	cycl			
			4/6	8/6	12/6				4/6	8/6	12/6		4/6	8/6		
test designation ³⁾	test group															
	SZ1-	S00				S00	S00	S00					S00			U
								S20								U
			S10	S11	S12				S21			S20		S30	S31 ⁴⁾	U
			T10	T11	T12				T21			T20		T30		U
	SZ2-	S00				S00	S00	S00					S00			C
			S10	S11					S20	S21				S30	S31	C
			T10	T11					T20	T21				T30	T31	C
																C
	SZ3-	S00					S00						S00			C
				S11					S20						S31	C
				T11					T20						T31	C
															C	

¹⁾ U = unconstrained; C = constrained
²⁾ s/s = steady state; cycl = cyclic (4/6, ... indicates duration (min) of power-on / power-off phases)
³⁾ e.g. SZ1-T10 means: transiently recorded data from 4 min. power-on / 6 min. power-off cycles at approx. 16 W/cm² on radiatively cooled tile no. 1
⁴⁾ tile no.1 failed during this test
 shaded fields indicate that results of these tests are included in table 5.2

Table 5.1 offers an overview on the tests performed within the three groups. Entries into the fields of the table indicate for which points in the test matrix a test was performed, whether the data were read as a single set (S) or as a transient reading (T), and what the designation of the respective data file was.

5.4.3 Data processing

Processing of the raw data was performed to determine the applied heat flux and to correct the LVDT signals for thermal elongations of the TS1 side walls.

Heat Flux:

Similar to the tests with the bare TS1, in the present tests with the radiatively cooled tile the calorimetrically determined power included some heat that was received not by the surface of the specimen itself but by the coolant headers welded to the specimen. For the present tests the headers were shielded with a three-fold radiation screen and received less heat than in tests with the bare TS1. Therefore, the correction procedure given in Chapter 4.3.3 was applied here after being modified by calculating the power to the headers slightly differently as

$$N_{headers} = 0.034 \cdot N_{el} [W] \quad \text{with } N_{el} [W] \text{ being the total power to the three heaters.}$$

LVDT signals:

The reference plane of the displacement sensors was attached to the flanges of the TS1 side walls as described in Chapter 5.3.3. As a result, the LVDT signals contained some thermal expansion of the side walls when the side walls heated up during the tests. The raw signals C_x (C121 through C138) were corrected for this side wall expansion by using the information on the side wall temperature measured in two positions 2 mm and 142 mm away from the back of the TS1 front plate and recorded on channels C29 and C31. The corrected values cx were calculated from

$$cx = Cx - \Delta l_F [\mu m]$$

Δl_F is the correction for the flange thermal expansion based on its original length of 180 mm at 25°C.

$$\Delta l_F = \alpha_{SS} \cdot l_F \cdot \Delta T_F \cdot 1000 [\mu m] \quad \text{with} \quad \alpha_{SS} = 16.5 \cdot 10^{-6} \frac{1}{K}$$

$$l_F = 180 \text{ mm}$$

$$\Delta T_F = \frac{C29 + C31}{2} - 25$$

The LVDT measuring on the back side of the tile (C138) needed an extra correction Δl_R for the thermal expansion of its alumina extension tube (compare Chapter 5.3.3). This correction was based on the three pieces of temperature information below and on the assumption of a linear temperature distribution between these support points:

- (a) the hot end was assumed to be at the temperature of the tile back side as measured with the pyrometer (C 173);
- (b) the temperature at the axial center of the 75 mm long tube was measured with a 0.5 mm dia. TC installed in the center hole of the tube (C 193);
- (c) the cold end in contact with the LVDT tip was assumed to be at room temperature (25°C).

The total thermal elongation of the tube Δl_R consisted of two parts, one for each half of the tube length with its averaged temperature

$$\Delta l_R = \alpha_{Al_2O_3} \left[l_1 \left(\frac{C_{173} + C_{193}}{2} - 25 \right) + l_2 \left(\frac{C_{193} + 25}{2} - 25 \right) \right] \cdot 1000 [\mu m]$$

with $\alpha_{Al_2O_3} = 8 \cdot 10^{-6} \frac{1}{K}$

$l_1 = 38 \text{ mm}$

$l_2 = 37 \text{ mm}$

This extra correction Δl_R was applied to c 138 to become the corrected displacement *b* 138:

$$b_{138} = c_{138} + \Delta l_R [\mu m]$$

The precision of the corrected displacement measured with LVDT 138 should not be overrated though, since the necessary correction based on a limited knowledge of the temperature distribution was on the order of 200 to 300 μm which is a considerable fraction of the measured signal.

5.5 Experimental Results

Though all the tests listed in Tab. 5.1 were performed and their data were recorded, in this paper only a selection of the tests and a selection of the data will be reported; the selection was done in view of the three goals given in Chapter 5.2, namely (a) survival of the tile attachment scheme, (b) thermal bowing of TS1 and tiles, and (c) thermal conduction through the attachment studs.

An overview on the selected data is presented in Tab. 5.2. The choice of the presented data was guided by the following criteria:

- Tests from all three test groups with different tiles (SZ1 through SZ3) are included.
- Most of the tests reported in each group were of the steady-state type since they seemed most useful to observe the thermal bowing of the TS1 and tile as one of the experimental goals; these steady-state tests were run in timely sequences with increasing heat fluxes; at the beginning and end of a sequence a reading at zero heat flux was taken for comparison.

- In each group some end-of-the-heating-phase readings out of cyclic tests are reported also to demonstrate how far a quantity has reached steady-state conditions after 8 or 12 minutes heating phases.
- All tests included in the table were run at one out of five defined power settings. This should result in comparable tests for each setting; small differences in heat fluxes are attributed mainly to the necessity of measuring heat-up rates of the cooling water very precisely to some tenth of a degree.
- Transient readings are not suitable for being listed; they will be reported when discussing the results on tile failure and on thermal conduction through the attachment studs.
- From the temperature readings of the original TS1 instrumentation only channels C16 and C21 as the highest values are included in the table because of the reasons discussed in Chapter 4.2; in addition, channels C 29 and C 31 are included as a basis for correction of the side wall thermal expansion.
- Temperature readings from additional instrumentation at and near attachment studs (C45 - C48 and C 181 - C 190) are reported for the evaluation of heat conduction into the attachment groove area.
- Strain gauge readings are reported for comparison but will not be further evaluated since strains were discussed already in Chapter 4.3.2 for comparable conditions.
- LVDT readings form the main block of data to be evaluated.
- Readings from the FIWATKA operating instrumentation are excluded from the table.

1 Table 5.2 Selection of measured data from tests with radiatively cooled tiles																												
2	Test	Date/Time	Type*	Heat Flux q", W/cm²	N _{heat} kW	Temp. at TS1 °C				Temperatures at attachm. studs, °C				Strain gauge readings, microstrains or 10 ⁻⁴ %														
3						C161	C016	C021	C029	C031	C045	C046	C047	C048	C061	C063	C065	C067	C069	C071	C073	C075	C077	C079	C081	C083	C085	C087
4	specimen unconstrained, tile from fine-grained graphite																											
5	SZ1-S00	20.01.93 09:32	s/s	0.0	0.0	23	22	23	23	23	23	23	23	23	4	5	-49	-22	3	-62	8	-1	5	-4	11	-4	4	-2
6	SZ1-S00	20.01.93 13:10	s/s	15.7	24.2	57	116	43	44	822	509	403	572	97	-167	111	166	109	-243	385	-255	267	41	376	-274	-36	255	
7	SZ1-S00	20.01.93 13:45	s/s	23.2	34.9	77	155	45	53	946	528	441	611	128	-230	190	272	150	-317	529	-345	368	96	513	-370	-58	426	
8	SZ1-S00	20.01.93 14:40	s/s	28.5	44.7	92	192	54	62	1030	552	463	613	163	-281	278	358	192	-388	658	-415	459	135	637	-444	-64	546	
9	SZ1-S00	20.01.93 15:26	s/s	34.1	52.2	103	218	61	69	1075	543	471	605	193	-325	335	403	218	-426	740	-465	523	149	718	-496	-69	605	
10	SZ1-S00	20.01.93 16:11	s/s	42.3	64.1	114	260	68	78	1143	509	463	625	216	-392	413	493	252	-486	862	-546	606	187	830	-581	-95	740	
11	SZ1-S00	21.01.93 09:02	s/s	0.0	0.0	22	22	22	22	22	22	22	22	4	4	-67	-36	3	-26	2	4	1	2	-1	6	5	-2	
13	SZ1-S12	22.01.93 17:07	cycl/12	16.0	24.2	54	114	31	37	838	512	445	570	64	-200	102	161	75	-201	360	-290	247	24	343	-308	-75	254	
14	SZ1-S20	01.02.93 16:55	cycl/12	35.2	52.1	95	217	41	57	1082	543	461	506	140	-448	199	435	163	-485	709	-526	500	58	673	-560	-136	608	
15	SZ1-S31	03.02.93 16:18	cycl/8	42.8	64.8	120	263	47	73	1060	600	754	729	204	-448	388	622	237	-503	864	-552	618	200	809	-578	-98	830	
16	specimen constrained, tile from fine-grained graphite																											
17	SZ2-S00	17.06.93 08:00	s/s	0.0	0.0	25	25	23	24	24	24	24	24	23	33	-24	0	23	27	24	25	22	27	30	23	26	24	
18	SZ2-S00	17.06.93 09:24	s/s	16.6	24.1	68	82	33	50	892	416	511	628	119	-61	176	560	142	-94	399	-145	277	415	403	-162	-25	654	
19	SZ2-S00	17.06.93 10:27	s/s	24.2	35.5	81	104	42	57	1002	427	505	613	140	-129	210	767	171	-181	539	-247	374	569	542	-269	-62	909	
20	SZ2-S00	17.06.93 11:31	s/s	31.6	45.2	92	124	50	64	1121	440	463	617	156	-193	234	934	196	-257	656	-337	460	711	659	-364	-99	1128	
21	SZ2-S00	17.06.93 12:32	s/s	36.8	52.1	102	141	58	69	1159	439	444	609	170	-244	249	1062	210	-308	740	-392	520	800	745	-424	-120	1282	
22	SZ2-S00	17.06.93 13:25	s/s	44.6	64.1	108	165	65	75	1197	439	425	617	172	-313	271	1246	225	-377	847	-482	594	944	852	-518	-163	1507	
23	SZ2-S00	17.06.93 16:47	s/s	0.0	0.0	26	26	41	28	55	49	51	58	39	40	-51	-60	40	7	46	36	47	30	55	34	48	18	
25	SZ2-S11	23.07.93 11:13	cycl/8	16.0	24.3	65	83	35	48	823	406	418	560	100	-97	186	579	118	-112	376	-178	270	404	374	-195	-42	630	
26	SZ2-S21	23.07.93 14:25	cycl/8	35.7	52.1	97	133	46	65	1104	428	399	585	132	-275	273	1108	165	-307	695	-422	482	777	693	-454	-159	1264	
27	SZ2-S31	26.07.93 11:18	cycl/8	44.5	63.7	110	150	46	71	1176	428	401	593	139	-343	296	1291	187	-386	797	-500	550	939	798	-541	-205	1492	
28	specimen constrained, tile from CFC																											
29	SZ3-S00	17.08.93 08:40	s/s	0.0	0.0	27	26	25	26	25	26	25	26	7	8	6	3	7	8	7	9	6	6	5	8	7	6	
30	SZ3-S00	17.08.93 10:57	s/s	17.0	24.0	65	82	36	48	899	400	571	653	111	-100	194	553	112	-104	397	-185	279	405	368	-184	-45	648	
31	SZ3-S00	17.08.93 11:54	s/s	30.8	45.4	88	115	44	57	1061	405	473	714	136	-234	252	915	139	-238	642	-372	439	674	590	-369	-127	1116	
32	SZ3-S00	17.08.93 13:47	s/s	43.2	64.1	104	145	55	66	1164	409	426	752	165	-347	306	1216	167	-345	837	-513	564	902	761	-502	-191	1507	
33	SZ3-S00	18.08.93 07:32	s/s	0.0	0.0	29	28	28	28	28	28	28	28	22	28	2	-8	21	19	21	29	22	22	26	25	28	17	
35	SZ3-S11	18.08.93 11:43	cycl/8	17.0	24.2	63	77	33	45	890	418	554	622	89	-120	152	523	90	-111	363	-201	250	379	327	-196	-64	610	
36	SZ3-S31	18.08.93 14:55	cycl/8	43.3	64.0	107	145	46	62	1160	411	424	757	129	-367	279	1205	132	-353	790	-532	522	878	712	-519	-223	1473	

* indicates whether the test was s/s = steady state or cycl/8 = cyclic/duration of heating phase in minutes

1 Table 5.2 (continued) Selection of measured data from tests with radiatively cooled tiles																																
2		Strain gauge readings, microstrains or 10 ⁻⁴ %											LVDT readings corrected for side wall and extension tube thermal expansions, μm																			
3		c089	c091	c093	c095	c097	c099	c101	c103	c105	c107	c109	c111	c121	c122	c123	c124	c125	c126	c127	c128	c129	c130	c131	c132	c133	c134	c135	c136	c137	c138	
4																																
5	8	3	4	-5	9	-1	7	10	5	-1	4	1	3	-15	-15	-13	-3	-20	-74	-79	-90	-94	-29	-19	-24	64	54	53	49			
6	226	137	197	89	356	154	337	-59	171	180	162	167	-990	-491	-299	-272	-234	-8	-242	-259	-612	-627	-307	-142	-434	-88	-52	-67	-93			
7	308	197	274	152	489	254	465	-134	229	175	217	162	-1121	-596	-328	-273	-225	7	-254	-271	-712	-727	-335	-166	-532	-148	-81	-101	-192			
8	385	264	346	211	599	325	572	-157	292	217	277	200	-1281	-725	-397	-320	-264	14	-303	-319	-862	-877	-409	-204	-649	-207	-124	-144	-267			
9	434	304	390	244	670	359	639	-163	329	261	314	240	-1427	-831	-466	-384	-320	6	-367	-383	-1015	-1030	-487	-237	-747	-241	-153	-174	-308			
10	500	368	456	298	773	430	738	-208	377	273	362	249	-1615	-986	-550	-448	-373	0	-443	-460	-1210	-1224	-576	-283	-883	-286	-182	-203	-391			
11	-1	5	3	1	-1	-9	-2	19	-1	1	3	3	111	93	-53	-47	-25	-41	-92	-103	-130	-134	-56	-26	-36	99	83	81	65			
13	200	96	174	75	337	133	320	-118	139	149	134	140	-942	-441	-268	-244	-217	10	-198	-215	-551	-566	-255	-106	-384	-126	-57	-75	-90			
14	456	248	359	191	631	299	626	-235	285	238	274	223	-1751	-830	-471	-387	-342	45	-360	-376	-1033	-1048	-448	-189	-740	-259	-144	-165	-269			
15	550	347	470	299	779	437	771	-263	379	265	356	232	-1840	-934	-503	-399	-346	54	-385	-402	-1133	-1147	-476	-229	-840	-328	-189	-209	-377			
16																																
17	29	21	25	15	32	25	28	19	26	14	24	14	3	3	0	-2	-1	5	11	9	10	11	-4	-2	1	1	2	1	3	2		
18	258	532	228	484	354	505	342	-357	193	-174	203	-129	14	34	166	201	211	93	245	251	236	184	195	-10	41	-120	-9	-146	-60	-391		
19	332	733	294	671	480	709	461	-563	244	-292	256	-228	13	40	233	284	299	131	346	355	332	265	270	-21	50	-166	-16	-193	-77	-673		
20	392	906	346	830	586	897	561	-756	284	-386	304	-315	4	42	290	355	373	152	431	444	415	316	334	-34	57	-194	-8	-227	-83	-941		
21	438	1042	385	961	657	1023	629	-883	314	-443	340	-369	-9	38	323	395	417	156	480	499	467	357	370	-48	60	-216	0	-253	-88	-1123		
22	499	1236	440	1143	748	1197	716	####	353	-530	378	-449	-16	43	383	467	493	172	567	593	555	427	436	-58	77	-217	34	-274	-77	-1417		
23	45	48	46	44	48	64	38	32	44	81	39	65	-47	-40	-63	-69	-72	-103	-63	-54	-40	-28	-84	-61	-30	131	114	157	137	-179		
25	236	504	212	463	351	496	341	-419	170	-205	187	-172	12	31	188	235	254	114	267	275	256	204	232	-11	38	-100	11	-135	-53	-347		
26	408	1002	357	924	633	964	609	-925	278	-503	299	-432	31	56	354	430	454	160	475	491	455	345	409	-26	73	-186	34	-244	-82	-958		
27	462	1177	407	1077	725	1124	698	####	314	-594	336	-593	106	88	451	541	568	200	572	588	547	413	518	-18	104	-193	67	-267	-67	-1239		
28																																
29	9	7	8	6	6	5	6	8	5	8	8	8	-4	-1	0	0	0	0	-1	-2	-4	-2	-1	0	0	-4	-3	-5	-1	1		
30	231	496	222	488	359	520	351	-401	181	-195	185	-166	-1	29	175	215	230	122	268	270	252	196	210	0	39	-174	-37	-198	-97	137		
31	351	842	336	840	566	875	552	-760	266	-411	265	-360	11	58	315	382	403	198	454	459	428	330	364	9	75	-263	-53	-305	-144	157		
32	444	1137	428	1149	726	1168	709	####	339	-572	322	-509	7	70	412	494	520	210	546	552	506	372	463	1	83	-344	-73	-424	-169	112		
33	25	15	25	18	26	22	19	33	23	33	25	30	-3	-7	-11	-12	-15	-25	-34	-39	-40	-44	-14	-13	-19	-40	-39	-25	-21	-27		
35	202	452	197	450	332	476	329	-424	157	-213	155	-182	9	31	180	224	244	134	277	282	263	210	220	5	46	-117	10	-144	-52	153		
36	410	1089	390	1098	695	1111	687	####	301	-604	283	-534	33	81	422	500	527	219	558	567	521	369	474	7	102	-289	-7	-338	-120	141		
37																																

1 Table 5.2 (continued) Selection of measured data from tests with radiatively cooled tiles																				
2		Water			Tile		Temperatures at TS1 near attachment studs, °C											Water		Temp. at ext. tube to c138, °C
3		in, °C	out, °C	l/h	back, °C		c181	c182	c183	c184	c185	c186	c187	c188	c189	c190	c191	c192	c193	
4																				
5	22.6	22.6	5008			22	23	22	23	22	23	22	23	22	23					
6	28.8	33.0	4172	1223		64	64	48	58	66	165	97	65	95	74					
7	32.8	38.9	4162	1352		90	70	59	54	85	211	110	84	120	102					
8	37.2	44.8	4157	1445		89	73	68	63	101	243	133	100	137	124					
9	40.0	49.0	4175	1490		73	76	74	69	137	249	143	111	147	135					
10	43.7	54.9	4174	1586		82	85	82	77	179	281	164	128	163	152					
11	22.5	22.4	4241			22	22	22	22	22	22	22	22	22	22					
13	24.4	28.7	4065	1206		79	51	45	41	64	165	110	63	96	74					
14	31.1	40.8	4018	1500		65	69	66	62	149	246	168	108	142	128					
15	44.3	56.0	4029	1594		80	112	78	83	126	267	185	134	120	112					
16																				
17	25.5	25.5	3961			25	25	25	25	24	25	25	25	25	25	25.8	25.8	24		
18	35.5	40.4	3973	1248		58	61	59	157	183	125	95	81	101	84	35.8	40.4	185		
19	35.6	42.5	3967	1374		65	68	68	184	209	157	121	100	197	184	35.8	42.5	180		
20	35.7	44.4	3987	1453		72	74	74	193	233	183	143	114	219	206	35.6	44.3	195		
21	35.8	46.2	3980	1506		75	78	78	200	242	196	165	124	230	218	35.7	45.9	201		
22	35.7	48.3	3985	1586		81	84	84	209	256	217	198	141	244	232	35.6	47.9	207		
23	25.6	25.9	3951			26	26	26	26	26	25	26	26	26	26	26.2	26.2	39		
25	35.4	39.9	3978	1197		56	59	57	164	172	111	116	80	95	79	35.8	40.2	165		
26	35.6	45.7	3956	1498		74	78	78	210	240	186	203	126	217	208	35.9	45.9	206		
27	35.5	48.0	3963	1581		80	84	84	221	255	207	234	143	233	228	35.5	47.9	211		
28																				
29	26.2	26.5	3952			26	26	26	26	26	26	26	26	26	26	26.7	26.7	26		
30	35.9	40.8	3952	1183		59	58	57	62	170	117	77	81	87	83	36.2	40.9	174		
31	35.6	44.4	3958	1412		70	72	72	76	220	158	108	114	201	206	35.8	44.4	191		
32	36.6	48.9	3949	1553		80	83	83	78	248	194	134	142	236	236	36.6	48.7	213		
33	23.9	23.2	0			28	28	28	28	28	28	28	28	28	28	26.6	25.9	28		
35	35.2	40.2	3943	1174		57	57	56	88	165	110	76	80	92	109	35.7	40.5	194		
36	35.9	48.1	3963	1551		79	83	83	76	248	193	133	141	236		36.1	48.1	240		
37																				

5.5.1 Tile Attachment Scheme

The tile was to be held vertically in place by two attachment studs as shown in Chapter 5.1. Essentially, the studs, made from 2-d CFC material, were to carry the weight of the tile. In addition, during Tokamak operation the tile would receive a thermal load and there could be a mechanical disruption load; the latter is not subject of this investigation.

The thermal load would cause a temperature increase and an elongation and buckling of the tile. The elongation would tend to increase the distance between the two attachment studs; this results in transferring the weight of the tile to the lower stud (if it has not been there before yet accidentally) and by sliding the upper stud somewhat upward in the TS1 attachment groove. The elongation and sliding is repeated back and forth with every heating cycle.

The thermal load would also develop a temperature profile in the tile and as a result bow the tile. The bowing would do two things:

- (1) It would tend to reduce the clearance between the spacer pads ("SP" in Fig. 5.1) and the TS1 surface; this clearance must not become $s \leq 0$.
- (2) It would tend to rotate the axis of the studs out of the direction normal to the TS1 surface, which could damage the foot portion of the stud or at least restrain it at sliding.

5.5.1.1 Clearance at the Spacer Pads

There was a clearance between the spacer pads (SP) of the tile and the surface of the TS1 front plate; this clearance is a result of the chosen design dimensions of the attachment stud and of the SP and it may be influenced by manufacturing inaccuracies and by any bowing of the tile and/or the TS1. Some clearance is needed there at any time to make sure that the tile can freely expand and bow.

As a result of this clearance the tile may be rotated somewhat around a vertical axis in the center of the attachment groove until the first SP on either side contacts the TS1. The clearance was measured at room temperature outside the test facility prior and after each group of tests in order to call attention to any large permanent changes caused by permanent deformations of the partners and also in order to know what clearance at most may be consumed by differential bowing of the partners under heat load. The measurement was performed by determining the clearance with a feeler gauge under the left SPs after having rotated the tile into contact at the right SPs and vice versa. The results for the three groups of tests are given in Fig. 5.6; the numbers in parentheses represent the clearances after the tests of the group and they are missing in SZ1 since that tile failed during the test. All clearances given must be approximately cut in half if the clearance should be distributed uniformly to both sides. When doing so, the clearance was on the order of only 100 to 300 μm for SZ1; for SZ2 and SZ3 which included the attachment scheme A the clearance was greater and on the order of 500 to 700 μm . During the tests the clearance was decreased in SZ2 and somewhat increased in SZ3; it is not known whether this is due to permanent deformations of the tile or of the TS1.

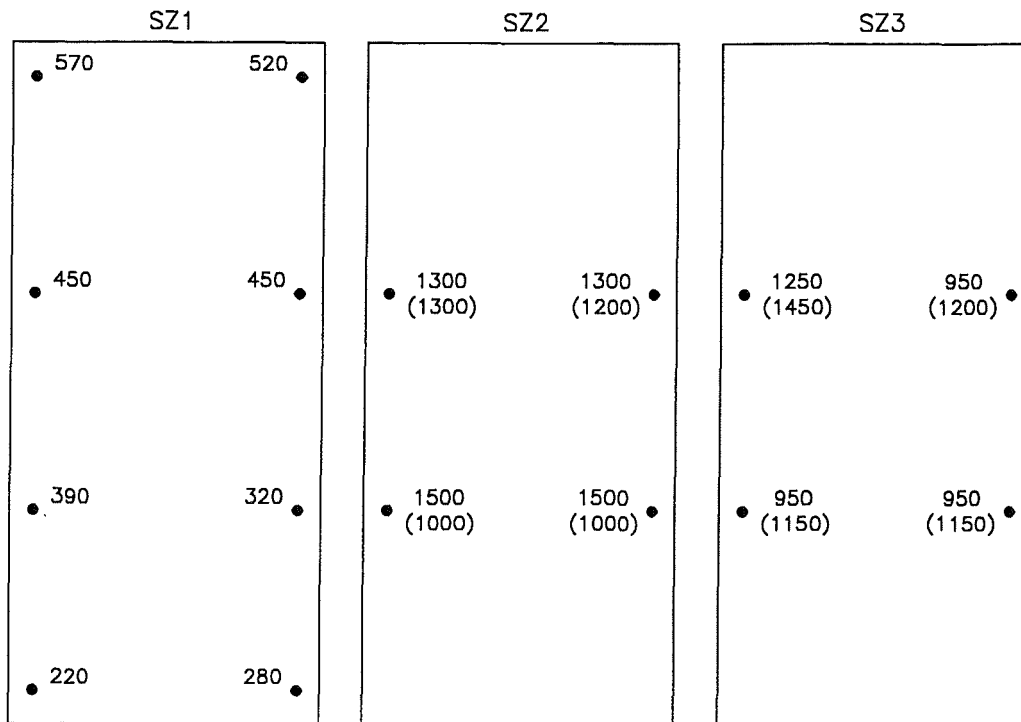


Fig 5.6 Clearances between spacer pads and TS1 in μm at RT before the tests and after the tests (in parentheses); the tile is viewed from the back side and was tilted around the vertical axis to contact SPs on the opposite side

5.5.1.2 Survival of the Attachment Scheme

Testing the three different tiles with their attachment schemes under thermal loads of up to $q'' = 44 \text{ W/cm}^2$ revealed the following results:

- Under "reasonable" test conditions the attachment scheme survived steady-state tests plus about 50 thermal cycles in tests SZ2 and SZ3. From the above considerations on mechanical consequences of thermal loads it seems clear that steady-state tests are sufficient to prove the survival of the attachment scheme except perhaps for testing an abrasive attack on the foot portion of the studs when they slide in the attachment groove at each cycle. The latter would need a much larger number of cycles and should be done only with the very grade of CFC material finally selected for a design and with a well specified roughness at the steel surface of the attachment groove.
- In test SZ1 the tile no. 1 failed; but in this test the test conditions were not "reasonable" since it could have been foreseen that due to thermal bowing of the tile the clearance between the outermost spacer pads and the TS1 surface became $s < 0$. This was a result of using in SZ1 a tile made of fine-grained graphite rather than of CFC as expected for the design. Since the coefficient of thermal elongation is much larger for fine-grained graphite than for CFC the tile no. 1 bowed much more than the designer had anticipated for CFC when he made the clearances under the spacer pads to be roughly 0.25 mm each (see Fig. 5.6 for clearances measured at RT with tile no. 1 in test group SZ1). As a consequence the tile was not free to bow but first contacted the TS1 with its four outermost spacer pads and then developed a growing tensile force in its two attachment studs until the tile failed, the attachment stud came free, and the tile fell off. It is pointed out that the tile and not the attachment

studs failed. The actual amount of the tile bowing and the corresponding consumption of the gap between the tile and the TS1 as it was measured and model-calculated may be found in Chapters 5.5.2.2 and 5.6, respectively. Though this failure must be called a "planning error" it nevertheless demonstrated the sturdiness of the attachment stud which was not designed for such high forces normal to the specimen surface; especially the strength of the foot portion was questionable since in the 2-d CFC material no carbon fibers run in the direction of the short dimension of the stud such that the foot portion should be susceptible to being sheared off.

A detail of the broken tile is shown in Fig. 5.7; the upper attachment stud is shown as it is still engaged with the round piece broken off from the back side of the tile. The right picture is taken from the back side of the tile in a corresponding position; it shows the broken zone and looks onto the back of the attachment cap.

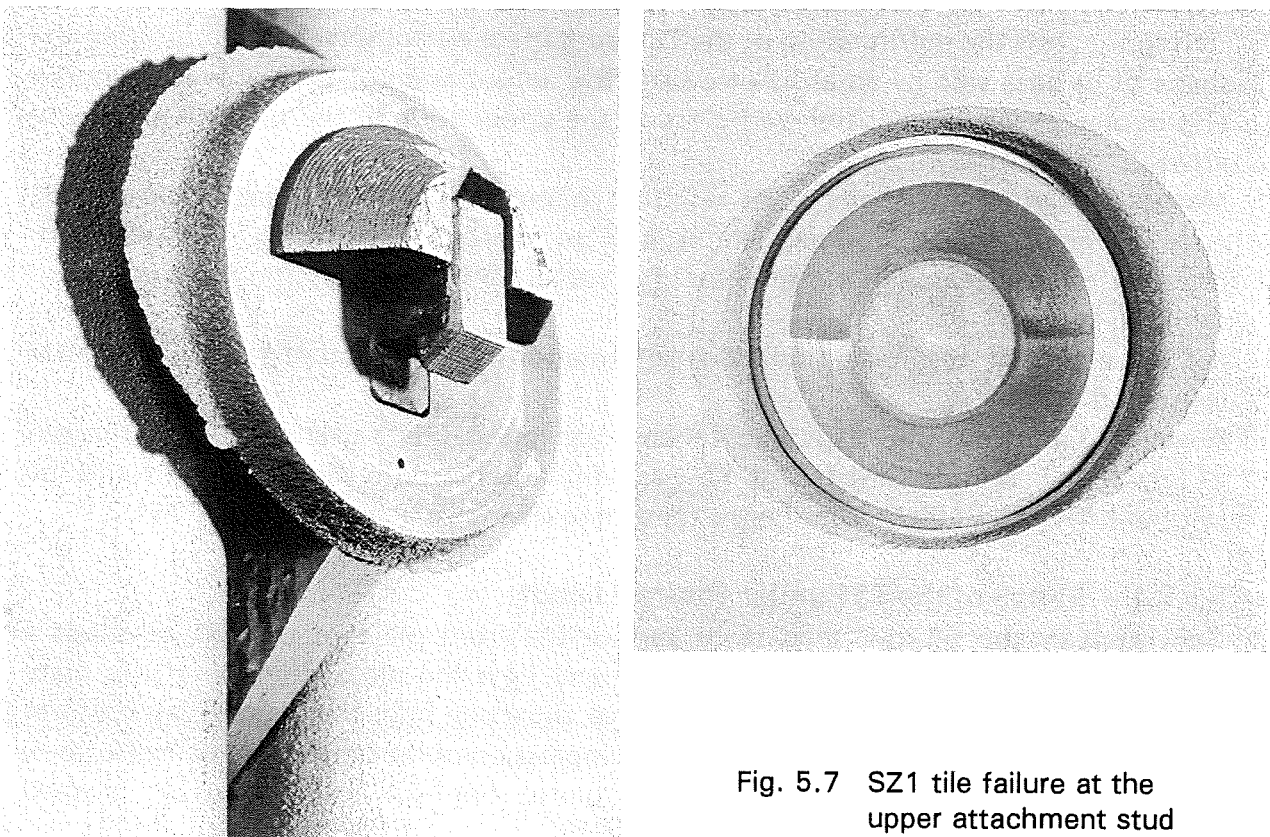


Fig. 5.7 SZ1 tile failure at the upper attachment stud

- Of the two different attachment designs A and B the design A was used in tests SZ2 and SZ3 since the tile had been machined correspondingly. When assembling design A it became evident that here the stud is fixed to the tile much more rigidly (form-locked) than with design B.

This could be a disadvantage since under these conditions the foot portion of the attachment stud is not free to individually adjust to the axis of the attachment groove by somewhat swivelling around its attachment point in the tile. The result could be a tilting and clamping of the attachment stud in the attachment groove when it is expected to slide there as the tile elongates and bows under thermal load. From this point of view a stiff design should be avoided though during the limited present testing no such problems became evident.

5.5.2 Thermal Bowing of TS1 and Tiles

Thermal loads on the surface of the tile together with the water-cooling in the channels of the first wall generate temperature distributions in both the CFC of the tile (linear profile normal to the heated surface) and the steel of the first wall (complex distribution due to the discontinuity of the heat sink). These temperature fields result in thermal bowing of the tile and of the TS1 front plate, both with the tendency to bow the edges away from the heat source and both at a different rate due to different temperature gradients and different coefficients of thermal elongation (CTE). The resulting shape of the TS1 front plate will be influenced by any mechanical constraint that is applied to the specimen. The tile must be free to bow without any constraint; otherwise tile failure, as in test SZ1, will result. The tile stays free to bow only if the clearance between the tile (spacer pods) and the TS1 either opens up or is at least not completely consumed by differential bowing of the two partners.

During the tests the deformation of the TS1 front plate was observed by monitoring the shape of its back side by an array of LVDTs; the deformation of the tile was measured also in one center line position very close to the upper edge of the tile, the only place accessible to instrumentation.

Most of the deformations and of the resulting changes in clearance between tile and TS1 were expected to be non-permanent and to disappear with the thermal load; nevertheless the clearance was monitored at room temperature to find any permanent changes.

For some sets of test conditions the deformations of TS1 and tile were also FEM calculated.

A comparison of both the experimental and calculational data will result in conclusions of (a) whether the tile stays free to bow and (b) whether both the experiment and the calculation reveal similar results on the remaining clearance between tile and TS1.

5.5.2.1 Shape of the TS1 under Thermal Load

Generated by the thermal load to its surface the front plate of the TS1 develops a temperature distribution which in turn tends to bow the plate; in general the plate becomes convex on the side of the heat source, since one finds the higher temperatures and elongations on this side. Fig. 5.8 gives an impression of the general shape (solid lines) into which the front plate would deform from an originally plane structure (dashed lines). In the test this deformation was fully elastic.

For lines in the z-direction bowing is strongly impeded since the front plate is inherently constrained by the presence of the side walls; this is true especially for the lines along the edges at the long sides and only to a smaller extent for the center line. As a general rule the presence of the side walls to some extent impede the four corners of the front plate as they try to bow away from the heat source. The above inherent side wall constraint is common to all tests covered in this report and is not called a "constraint" in the following.

Another type of constraint originates from connecting the flanges at the bottom of the side walls by transverse bars as shown in Fig. 5.1; this type of constraint was varied as a test parameter. If the transverse bars were not connected on one side (3 mm gap) the tests were called "unconstrained" and the front plate behaves like it is sketched in Fig. 5.8 and discussed above. Unfortunately only after the tests it turned out that the 3 mm

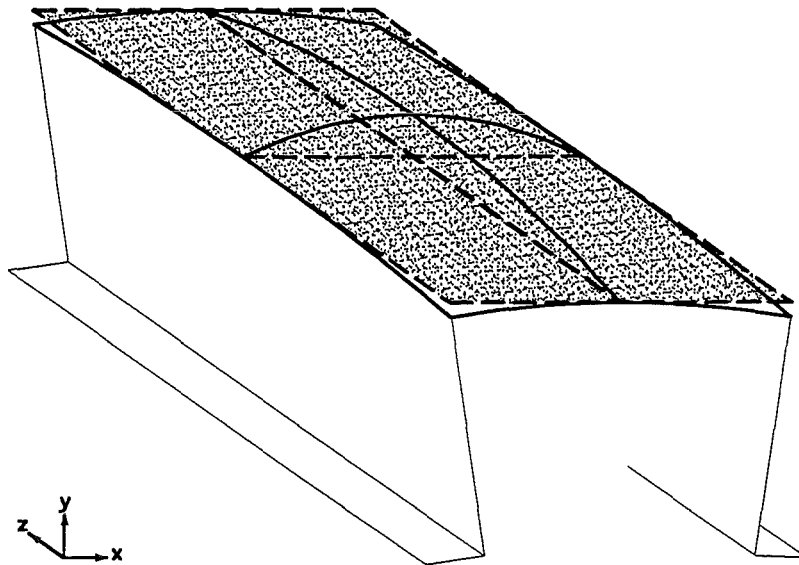


Fig. 5.8 Deformed Shape (exaggerated) of Unconstrained TS1 Structure under Thermal Load.

gap was chosen too small to allow for the full deflection of the specimen. The gap was consumed at a certain heat flux and the resulting mechanical contact caused some undefined constraint in the so-called "unconstrained" tests; this should be kept in mind when looking at the results.

When the transverse bars were clamped to the side wall flanges on both sides the tests were called "constrained". The resulting general shape of the front plate looks a little different. Fig. 5.9 shows that there is an almost unchanged bowing of the two subunits of the frontplate themselves; but since the lower ends of the side walls cannot approach each other the structure is bowed in its weakest zones; these zones are the side walls themselves and in addition the front plate at its center line where its thickness is reduced because of the tile attachment groove. As a result the front plate is somewhat folded along this groove and in Fig. 5.9 the bowed center line in z-direction as a whole runs lower than in Fig. 5.8 whereas the maximum deflection within that line stays about the same.

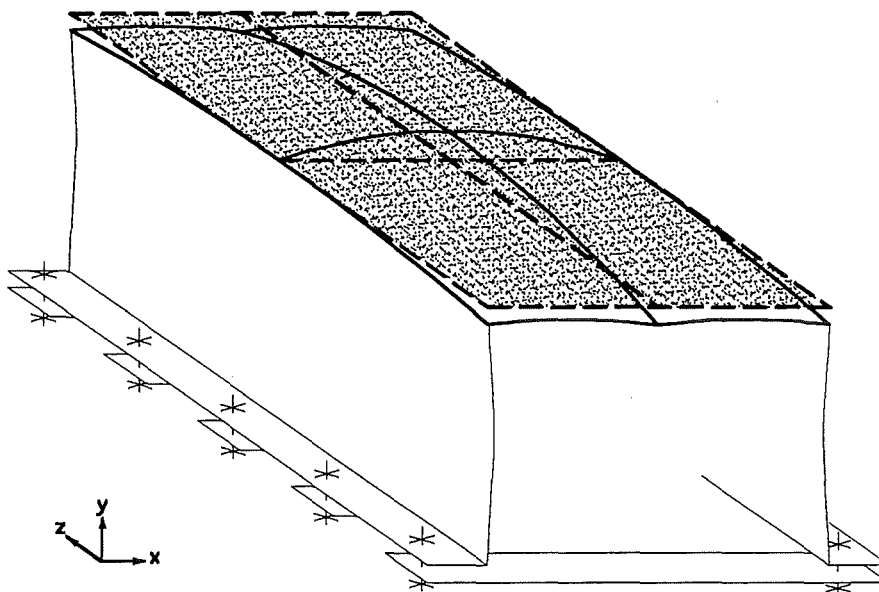


Fig. 5.9 Deformed Shape (exaggerated) of Constrained TS1 Structure under Thermal Load.

Experimentally the bowing of the front plate was observed by an array of LVDTs positioned on the back side of the plate (see Fig. 5.4). The measured data listed in Tab. 5.2 are related to a reference plane which during tests moved reproducibly as a whole relative to the front plate; for the "unconstrained" test condition where the reference plane was clamped to the flange of one side wall only the reference plane also tilted relative to the front plate at bowing (Fig. 5.10). To nevertheless get a direct measure for the bowing of the plate the data were transformed geometrically such that the deflections at positions C126 and C130 (the outermost near the center line in x-direction) became zero and that the deflections at positions C122 and C133 (the outermost at the center line in z-direction) became about equal; with this transformation and with the assumption that the front plate has experienced symmetrical bowing the reference plane was artificially tilted back into a position parallel to the undeformed front plate.

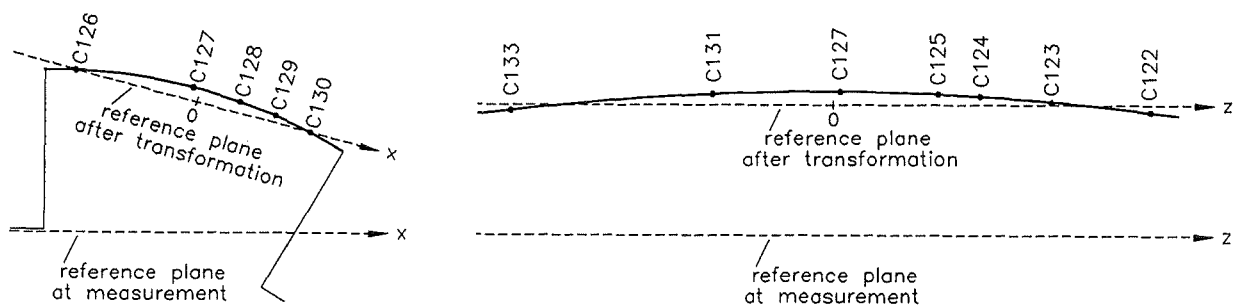


Fig. 5.10 Transformation of the LVDT data to a new reference plane

Tab. 5.3 Relative displacements at the back side of the TS1 front plate and of the tile

Test	Date/Time	Heat Flux q", W/cm²	relative displacements in μm from LVDT sensors															ΔA, μm change of gap width	
			at center line parallel to coolant channels (z-direction)							at center line transverse to coolant channels (x-direction)					in other positions		at the tile		
			sensor	b122	b123	b124	b125	b127	b131	b133	b126	b127	b128	b129	b130	b121	b132		b138
			x-coord.,mm	0	0	0	0	-5	0	-5	-89	-5	30	57	84	83	-84	0	0
			z-coord.,mm	230	160	110	80	10	-82	-227	10	10	10	10	10	233	-227	244	244
specimen unconstrained																			
SZ1-SO	20.01.93 16:11	42.3		-55	367	459	528	394	293	-43	0	394		245	0	-398	-248		
specimen constrained																			
SZ2-SO	17.06.93 08:08	0.0		-5	-8	-10	-9	3	-12	-7	0	3	0	0	0	-9	-7	-6	-2
SZ2-SO	17.06.93 09:24	16.6		-105	27	61	71	106	55	-99	0	109	96	66	0	-169	-106	-530	-398
SZ2-SO	17.06.93 10:27	24.2		-154	38	89	104	151	76	-144	0	155	139	97	0	-241	-155	-868	-675
SZ2-SO	17.06.93 11:31	31.6		-195	53	119	137	194	97	-180	0	199	179	124	0	-311	-191	-1177	-933
SZ2-SO	17.06.93 12:32	36.8		-222	63	136	157	221	110	-200	0	226	205	141	0	-365	-210	-1382	-1104
SZ2-SO	17.06.93 13:25	44.6		-260	79	163	189	264	132	-226	0	271	246	168	0	-442	-237	-1720	-1392
SZ2-SO	17.06.93 16:47	0.0	not completely cooled down	24	1	-4	-8	1	-20	34	0	3	-3	-1	0	-19	40	-114	-143
SZ3-SO	17.08.93 08:40	0.0		0	1	1	1	0	0	1	0	0	-1	-2	0	-2	-1	2	1
SZ3-SO	17.08.93 10:57	17.0		-131	15	55	70	107	50	-122	0	109	97	67	0	-197	-124	-23	137
SZ3-SO	17.08.93 11:54	30.8		-208	49	116	137	188	98	-191	0	192	171	119	0	-318	-193	-109	150
SZ3-SO	17.08.93 13:47	43.2		-223	119	201	227	253	170	-210	0	258	231	160	0	-364	-214	-181	110
SZ3-SO	18.08.93 07:32	0.0		27	24	23	20	1	21	16	0	1	-1	1	0	41	13	7	-21

The resulting transformed deflections are called "relative displacements"; they are listed in Tab. 5.3 and plotted in Fig. 5.11 for tests from groups SZ1, SZ2 and SZ3. It should be pointed out that with the small number of displacement sensors no high local resolution of the gained information on the deformation can be expected. Also the value of the curve for the x-direction of test group SZ1 (unconstrained) should not be overrated since

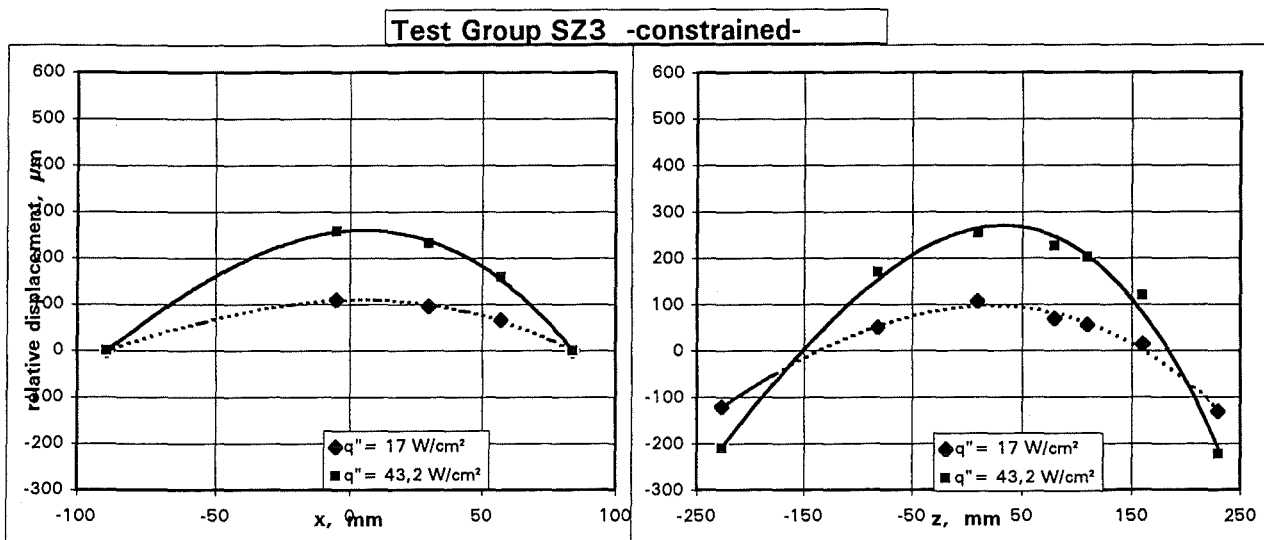
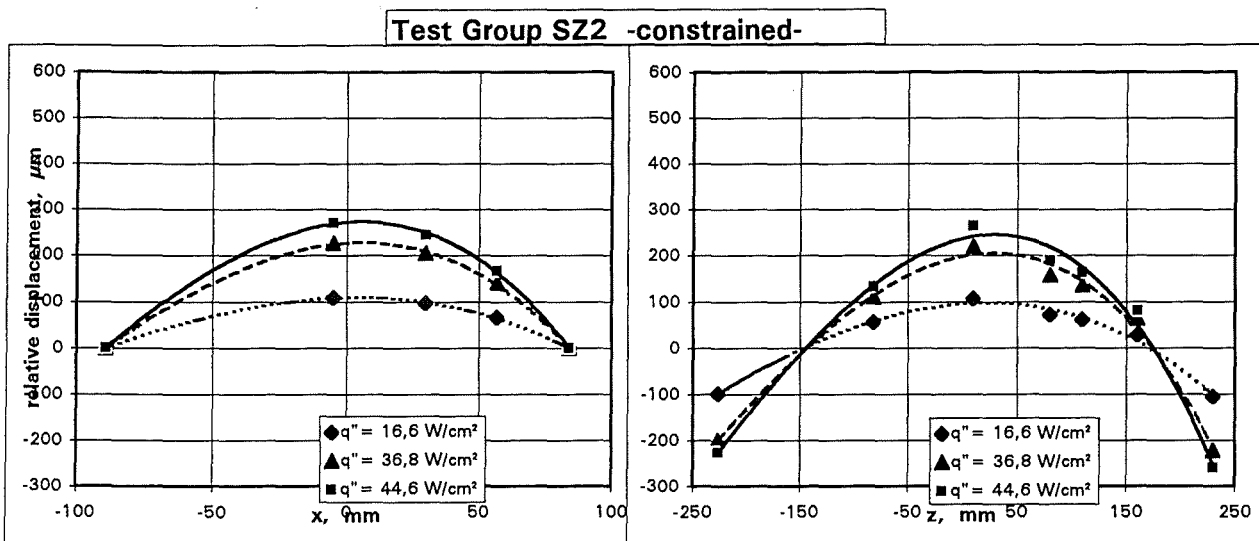
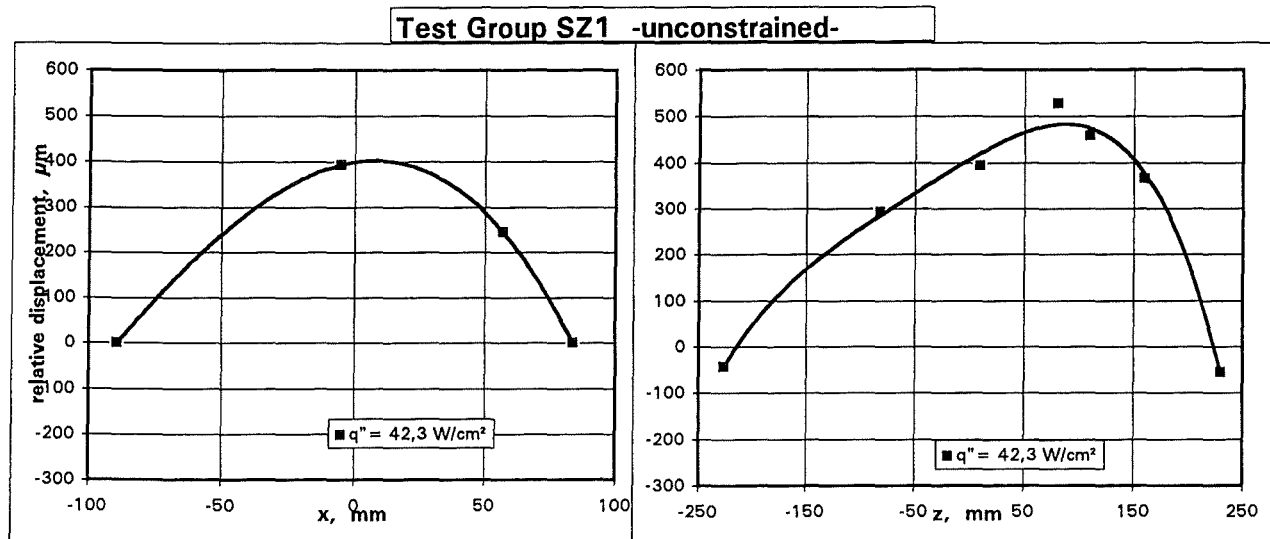


Fig. 5.11 Buckling of the TS1 front plate at center lines in x- and z-directions from test groups and for heat fluxes q'' as indicated

there are indications that the 3 mm gap at the constraint bars was consumed before the maximum bowing was completed; this should work out like a kind of undefined constraint and should make the data unreliable for high heat fluxes.

The figures indicate:

- The shapes of the bows in the x- and z-directions seem reasonable in general but the unsymmetry of the z-curves surprises; the most probable explanation seems to be that by some reason sensor C122 reads lower than sensor C133 and due to the above transformation this appears as an unsymmetry.
- The quantities of the displacements for groups SZ2 and SZ3 should be the same, since the tests were run under equivalent boundary conditions for the TS1; the figure shows that they are similar.
- Comparing the $q'' \approx 44 \text{ W/cm}^2$ lines for SZ1 (unconstrained) and SZ2 (constrained) for the z-direction shows that the height of the buckle at the center line is on the order of $500 \mu\text{m}$ and almost independent of the constraint. However for the x-direction the buckle is much higher for the unconstrained specimen, which may be understood from viewing the above figures 5.8 and 5.9: The constraint causes a folding of the front plate along the attachment groove.

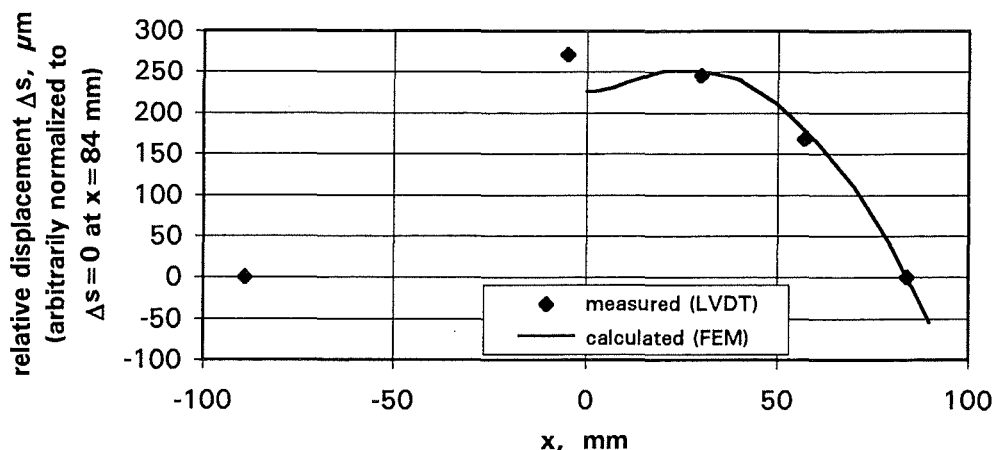


Fig. 5.12 Relative displacements along the center line in x-direction; comparison of measured (group SZ2) and calculated (2d model) data for the constrained specimen at $q'' = 44.6 \text{ W/cm}^2$

The measured shape of a buckle in x-direction may be compared with the calculated shape in Fig. 5.12. This comparison was done for the constrained specimen (group SZ2) at a heat flux of $q'' = 44.6 \text{ W/cm}^2$. The calculation was performed with the 2D FE model of a symmetric half of the cross section (see Chapter 4.5 for details). The agreement is astonishingly good except for the center where the calculated shape shows a folding of the constrained front plate along the attachment groove whereas the measured shape does not contain this. An explanation would be that a 2D model cannot reflect buckling in the third direction, which tends to reduce the folding in the relatively weak center whereas the buckling of the thicker plate areas stays almost unchanged; also the measurement at only a few points cannot reflect the details at the groove area.

The relative displacement of course increases with increasing heat flux. this dependence is demonstrated in Fig. 5.13 for the center of the constrained specimen with the measured data from sensor C127 of test group SZ2 for $q'' = 44.6 \text{ W/cm}^2$. Also plotted

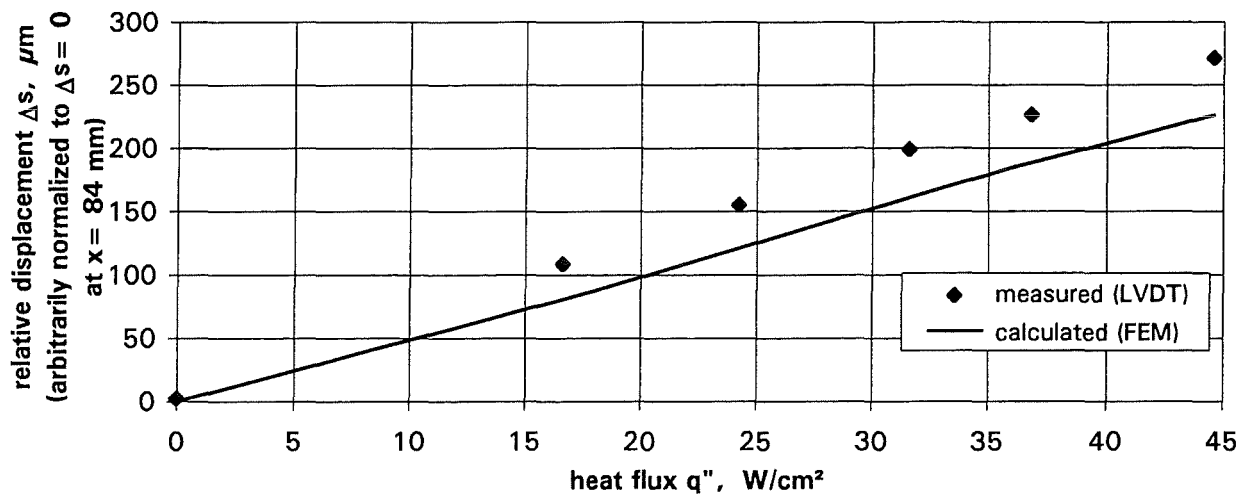


Fig. 5.13 Relative displacement at center of specimen; comparison of measured (group SZ2) and calculated (2d model) data for the constrained specimen at $q'' = 44,6 \text{ W/cm}^2$

are the data from the 2D FEM calculation which again are lower because of the reason mentioned above.

Fig. 5.14 illustrates the relative displacements and bowing of the constrained specimen along its center line in z-direction as a function of time during a heating cycle. The transients at the individual LVDT-positions are shown left; they indicate that steady-state with maximum displacements was reached at the end of the heating phase and that the cooling phase ended before the displacements had come back to zero completely. The right part of the figures shows again how the plate bows during the cycle; plotted are the extreme shapes at the ends of the heating and cooling phases between which the plate changed during each cycle.

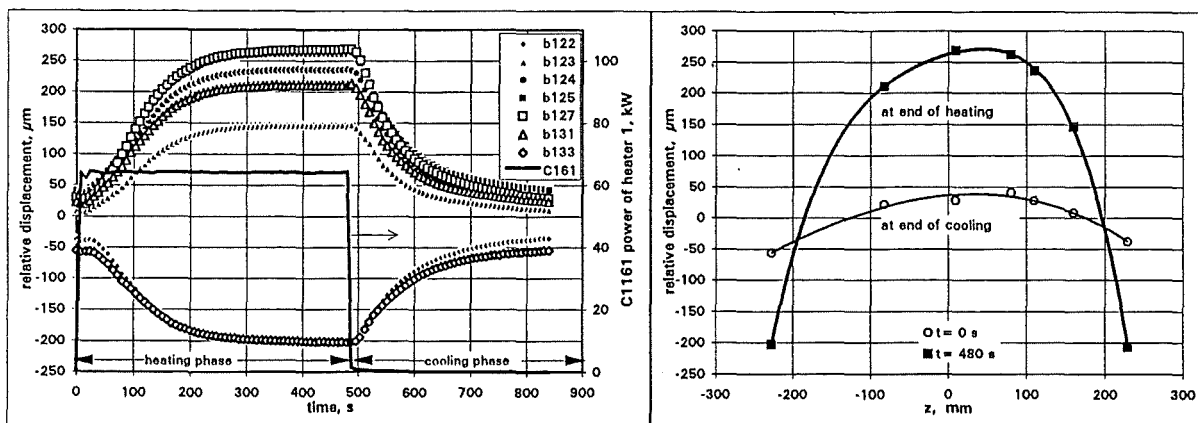


Fig. 5.14 Relative displacements along the center line in z-direction as they change during a heating cycle at $q'' = 44,6 \text{ W/cm}^2$ in test SZ2-T31 (constrained)

5.5.2.2 Change of the Gap between TS1 and Tile under Thermal Load

A thermal load causes the tile to bow its edges away from the heat source.

The displacement measurements performed do not allow to report on the shape of the tile under thermal load since there was only one LVDT (138) that monitored the back side of the tile close to its upper edge and the position at the attachments studs is not known

very precisely due to the thermal expansion of the studs and their attachment areas in the TS1 and the tile.

Nevertheless LVDT 138 contains interesting information if it is compared with LVDT 122 which very close to LVDT 138 monitored the back side of the TS 1 front plate. They together indicate how the gap between the tile and the front plate of nominally 5 mm changes under thermal load in a position close to the upper edge of the specimen. This change is a result of the tile and the front plate both bowing at a different rates under thermal load and it also includes all dimensional effects which were active in the stud area. It is of interest for the design. With the present design, a bowing must not strongly decrease the gap width since the 5 mm gap is filled to a larger extend with the spacer pads (SP in Fig. 5.1); a negative gap change would result in first consuming the remaining little open gap under the pads and in then causing tensile forces in the attachment studs that finally break the stud or tile, which happened in test SZ1.

After the experience with the SZ1 failure the LVDT 138 was installed and used in test series SZ2 and SZ3. Both SZ2 and SZ3 were run without the two pairs of outermost spacer pads (see Fig. 5.6) in order to allow unconstrained gap changes close to the upper lower edges where the changes are greatest.

From steady-state tests the measured LVDT data for the gap change are included in Table 5.3 as b132 (for the back side of the front plate) and as b138 (for the back side of the tile). Both were listed after corrections had been applied that take care of thermal expansions (see Chapter 5.4.3) and that relate the signals to a common reference plane (as described in Chapter 5.5.2.1.).

Both b 122 and b 138 had been adjusted close to zero at zero heat load and at a nominal gap of 5 mm. Compression of the LVDT (i.e. movement away from the heat source) is indicated as a negative signal. Thus the change of the gap $\Delta A'$ at any level of the heat load would roughly be

$$\Delta A' = b 138 - b 122$$

Since sensors 138 and 122 are 14 mm apart from each other the signal of LVDT 122 was extrapolated linearly with the help of LVDT 123 to the location of sensor 138 which resulted in

$$\Delta A = b138 - (b122 + (b122 - b123) \cdot 14/70)$$

The change ΔA of the gap under thermal load is listed in the last column of Table 5.3. The size of the change in gap is plotted in Fig. 5.15 as a function of the heat flux for steady-state conditions.

The solid line represents the data for the SZ2 tile made from fine-grained graphite which has a rather high coefficient of thermal expansion. It therefore bows stronger than the underlying TS1 front plate does and the gap between the two decreases rather heavily. In fact for $q'' = 45 \text{ W/cm}^2$ the nominal gap of 5 mm decreases by 1,4 mm which is much more than was allowed for in test SZ1 where the nominal gap was almost filled with the spacer pads and only on the order of 150 to 250 μm was left at room temperature; under these circumstances the failure in SZ1 is not surprising.

The broken line represents the data for the SZ3 tile made from CFC which has a much lower coefficient of thermal expansion. It happens that the gap does not change with the heat flux meaning that tile and front plate bow to the same extend. The small and constant increase in gap width of about 100 μm could be a result of a false correction for the thermal elongations of the LVDT extension tube or the attachment studs.

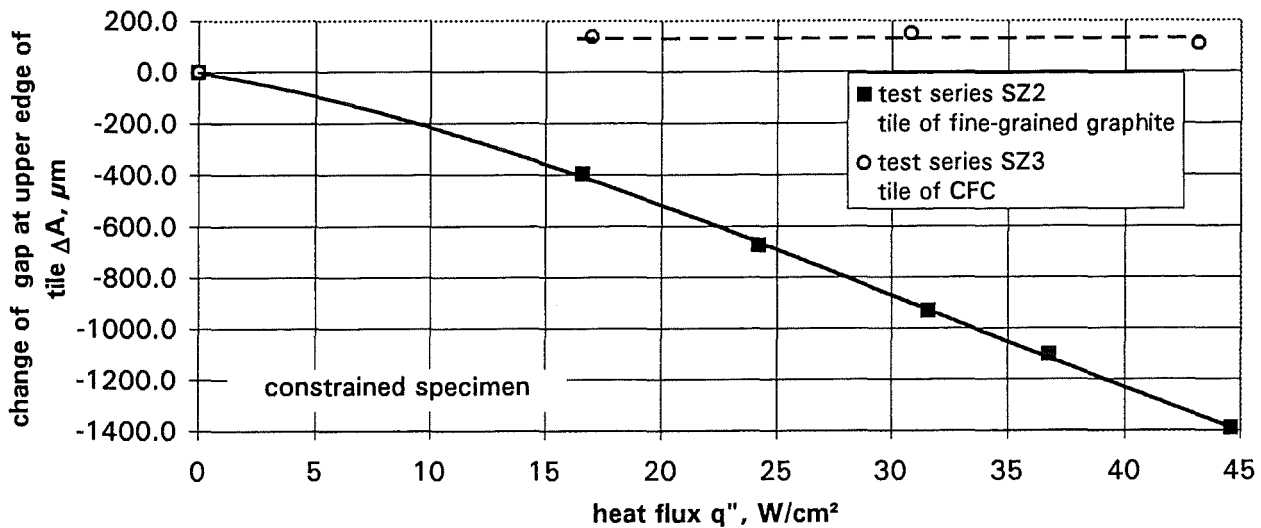


Fig. 5.15 Change of the gap size between the back of the tile and the front of the TS1

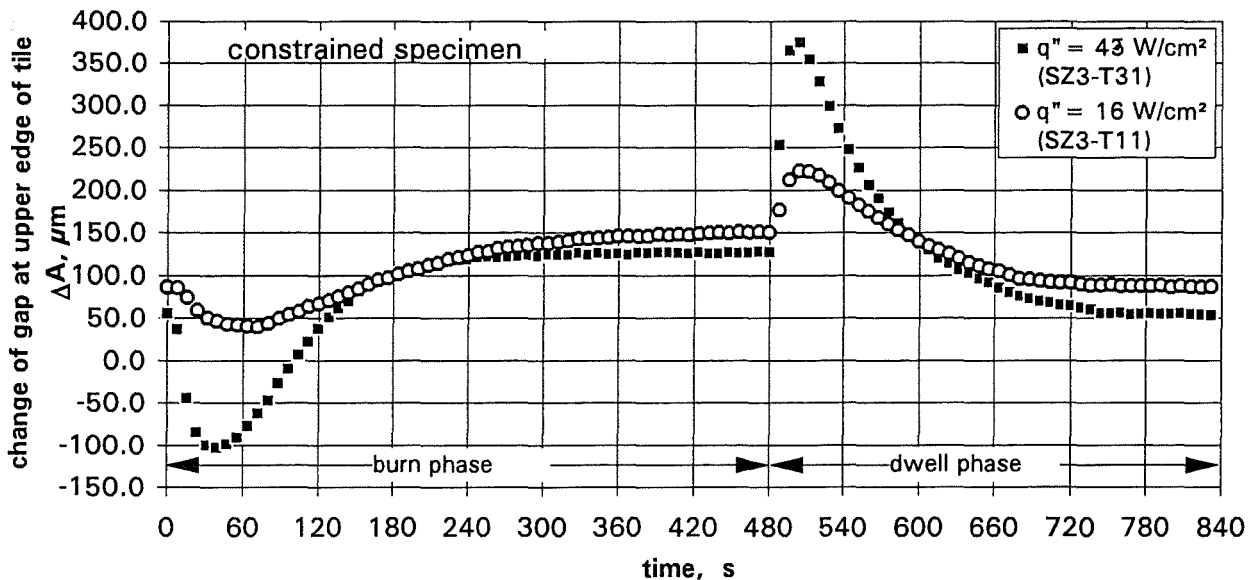


Fig. 5.16 Change of the gap size between the back of the tile and the front of the TS1 during one power cycle

At a first glance this result for the CFC tile would confirm the design to be reasonable from a differential bowing point of view. The result is less comfortable if one looks at the transient behaviour. Fig. 5.16 shows the transient changes of the gap width for one test cycle and for two different heat fluxes from tests SZ3-T11 and -T31, respectively. The gap width decreases rather quickly early in the burn phase, when only the tile and not yet the TS1 is reached by the heat flux; the generated temperature profile first bows only the tile. About half a minute later when the heat flux has reached the TS1 front plate and starts bowing it also the gap change turns around and the gap increases to roughly its initial size where it stays for the rest of the burn phase. The size of the initial gap change of course depends on the heat flux which determines the temperature gradient and the amount of bowing in the tile. For a heat flux of $q'' = 43$ W/cm² an initial gap

decrease of about 150 μ was measured which must be accounted for when the design clearance under the spacer pads (SP) is determined. As the power of the heat source is cut at the end of the burn phase the temperature gradient in the tile disappears rather quickly and the tile bows back to become plane on a still high temperature level. This increases the gap considerably before the TS1 also reacts to the power-off situation and the gap decreases back to its starting value.

The results reported in this Chapter should draw the attention on the importance of the relative movement between the tile and the steel structure of the FW during the thermal transients. The early heat-up of the tile (prior to the steel structure) does not only cause initially isolated tile bowing and corresponding gap changes; it also causes initially isolated tile elongations which makes the tile attachment studs slide back and forth in the attachment grooves of the steel structure and could generate an abrasive problem to the CFC attachment studs during the life time of many thousand cycles.

5.5.3 Thermal Conduction through the Attachment Studs

With the design concept of a radiatively cooled protection tile the main heat transfer mechanism between tile and steel structure is radiation.

As a result the tile is on a high temperature level. Only at the two tile attachment points there is a thermally conductive bridge between the hot tile and the cold steel structure. This bridge cannot be very effective thermally since the attachment stud is rather small in cross section and it has only point contacts with both the tile and the steel structure. Nevertheless there was some concern whether the heat flux that enters the steel structure at the contact points cyclically could cause local damage by thermal fatigue. Because of the unknown quality of the conduction path it seemed of interest to try experimentally to shed some light at least on the resulting local temperatures. Therefore the attachment area was instrumented to the extend reasonably possible as described in Chapter 5.3.2 and some measured temperatures are reported below. The most valid information may be drawn from transient temperature traces taken for typical test cycles; it was confirmed that these temperature transients were perfectly reproduced from cycle to cycle, such that a sometimes surprising curve should be expected to have a physically reasonable background as discussed below.

First an overview on the rather complicated mechanical behaviour at the attachment studs will be given. Then the resulting temperatures measured in the attachment area will be discussed for a cycle of each the test series SZ2 and SZ3. Finally temperature traces for SZ1 will be shown in which the mechanism of tile failure may be recognized.

5.5.3.1 Mechanical Behaviour at the Tile Attachment

As may be seen from Figs. 5.1 and 5.2 the tile is held in front of the TS1 by two attachment studs. The studs transfer the forces (originating mainly from the weight of the tile and from balancing it against tilting) to the attachment grooves in the TS1. The stud is like a triangle with its top corner embedded in the tile and the two corners at its base fitted into the attachment groove. The stud may rotate somewhat around its anchor point in the tile, which was more pronounced with design B in test series SZ1. The stud may slide with its two cylindrical feet in the attachment groove, a feature which is provided for mounting and for thermal expansion of the tile.

Pins (P in Fig. 5.2) in each of the two studs limit the freedom of the studs to slide downward when the first of them contacts the upper end of the shoulder S of the attachment groove. This pin will carry the weight of the tile; for the following it is assumed, as an example, that the pin in the upper stud first carries the weight at room temperature. Fig. 5.17 should help to illustrate the resulting contact points of the upper foot (UF) and lower foot (LF) of the CFC stud with the shoulders (US) or (LS), respectively, or with the bottom of the groove (B) for both the upper and the lower stud. Contact points are marked in the figure with arrows.

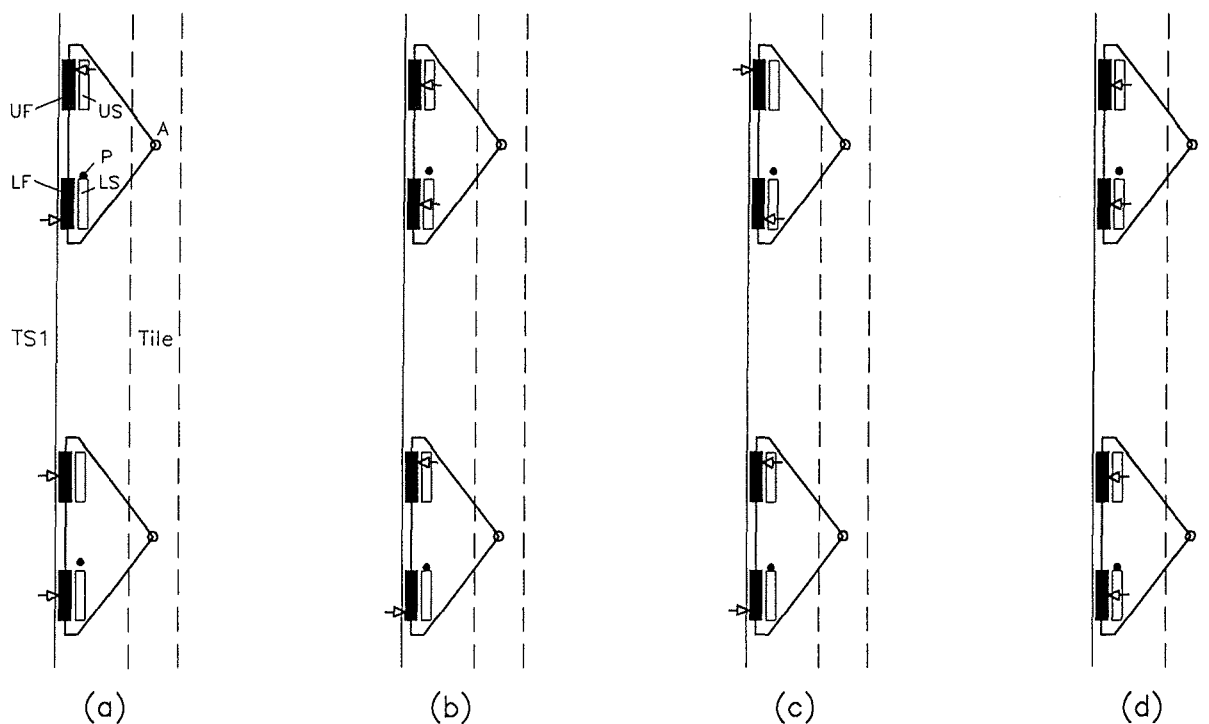


Fig. 5.17 Attachment stud contact points at different stages of thermal expansion and bowing of the tile

- a) At room temperature the weight of the tile which is supported at the pin causes the upper stud to rotate a little clockwise and with its UF contact the US and with its LF contact B. At the same time the tile rotates somewhat around its anchor point (A) at the upper stud and leans with both the UF and the LF of the lower stud uniformly against B.
- b) As the tile expands with increasing temperature the lower stud slides downward until its pin hits LS and takes over the weight of the tile; this rotates the lower stud a little clockwise until its UF contacts the US and its LF is pressed more strongly against B. At the same time the weight of the tile is taken off the upper pin and the upper stud is slightly pulled away from B and its UF and LF lean against US and LS, respectively.
- c) As the temperature of the tile further increases the upper stud slides upwards in the attachment groove. As it does, it may tend to tilt counter-clockwise due to some friction between its feet and the attachment groove which may result in contact points at UF/B and LF/LS (this tilting would be the other way around when the tile cools down during the dwell phase).

The same distribution of contact points would result from a strong concave bowing of the tile towards the heat source after some rotational allowance at the tile anchor points (A) has been consumed.

- d) If, like in test SZ1, the tile bows more than the clearance under the outermost spacer pads would allow both the upper and lower studs are strongly pulled away from B and all four feet are pressed against their corresponding shoulders (also this extremely good contact is released when the tile forms back in the dwell phase).

The above consideration demonstrates the rather complex mechanical interaction between the attachment studs and the steel structure resulting in moving contact points during each thermal cycle; correspondingly heat is transferred from the stud to the attachment groove area in changing locations and partly only for a short period during each cycle. Closing and opening of those contacts may be recognized by inspecting the temperature transients of the partners concerned for unexpected slopes. Because of its small heat capacity the temperature of the attachment stud reacts rather strongly and very fast to any changes in the contacts with the steel structure; closing of a contact results in a sudden decrease of the temperature in the stud even if this happens during a burn phase and opening of a contact is accompanied by an increase of the stud temperature even if it happens during a dwell phase. The corresponding temperature changes in the massive steel structure are less pronounced because of its great heat capacity; also it is only by chance that a thermocouple tip was located close to a contact point. In the two following Chapters such temperature transients measured in the attachment area are reported.

5.5.3.2 Temperature Transients at the Attachment Areas of SZ2 and SZ3

In order to demonstrate the typical mechanical interactions the temperature transients measured in the attachment area are plotted as small graphs located close to their measurement points in enlarged sketches of the attachment area in Figs. 5.18 and 5.19. Shown are the areas of the upper stud (left) and the lower stud (right) both including a pair of shoulders (at TC 188) without stud interaction. Each of the graphs in a figure covers the same power cycle of 14 minutes consisting of 8 minutes burn and 6 minutes dwell as indicated by the broken line for the heater power. For both figures the heat flux has been about $q'' \approx 43 \text{ W/cm}^2$ during the burn phase. The numbers in the upper right corners indicate the numbers of the plotted temperature channels with the tile temperature (173), the stud temperatures (45-48), and the steel temperatures (181 - 189).

Figure 5.18 covers a cycle from test SZ2-T31 featuring a tile of fine-grained graphite with the outermost spacer pads removed. At its back side (173) the tile gets up to 1600 °C at end of burn. This is reflected by 1200 °C in the head of the stud (45) and by a maximum of about 670 °C in feet of the studs (46-48). It is interesting to note that all three of the measured foot temperatures show their maxima not at the end of burn but early in the dwell phase indicating that their contact to the steel structure had been better during burn and got lost, at least to some extent, at end of burn (see Chapter 5.5.3.1 for mechanisms). It is also visible that the lost contact to the heat sink is regained early in the burn phase when the temperatures decrease where an increase would be expected from the heat load. A mirror image of the above should be expected from the transients

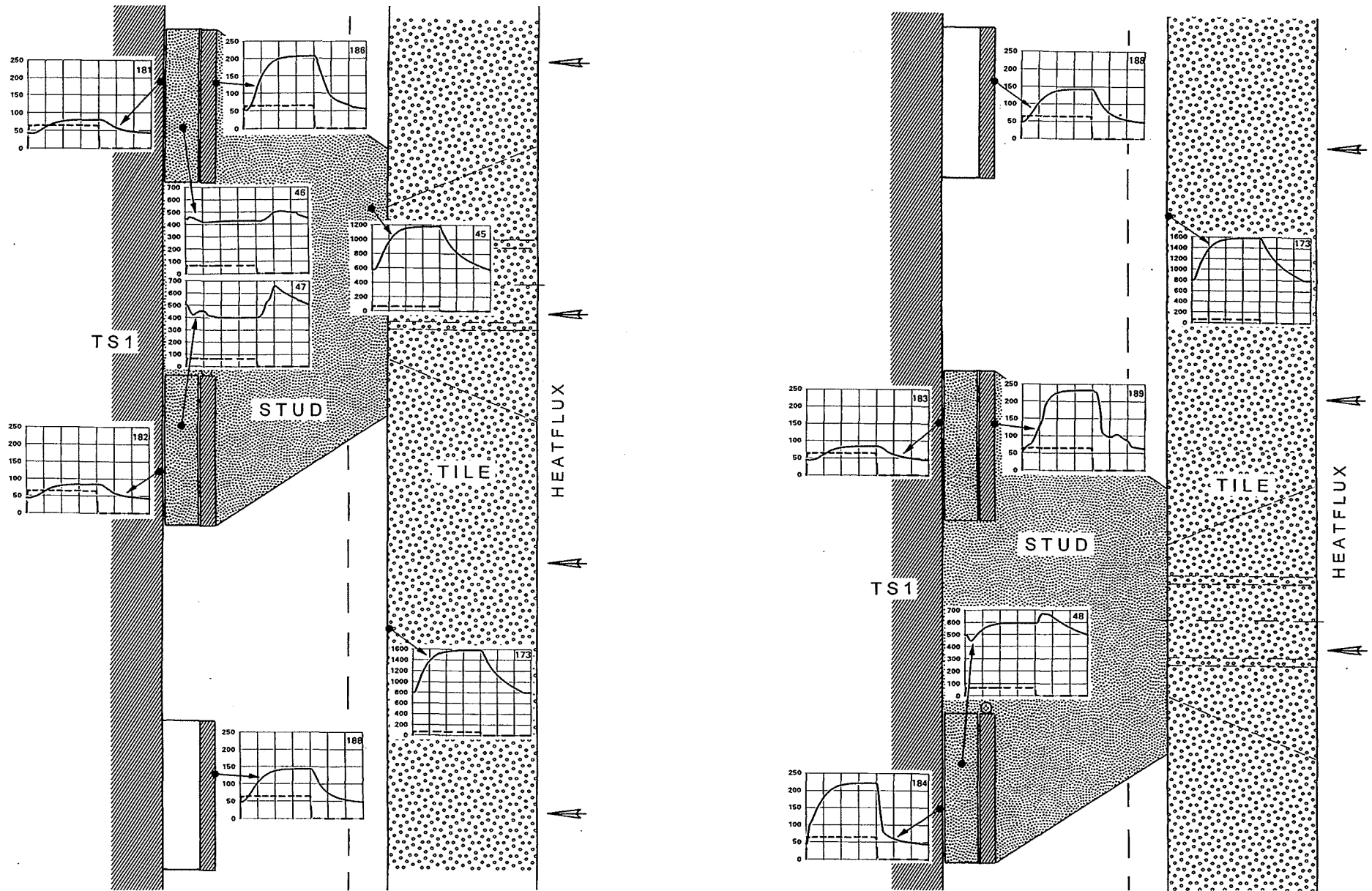


Fig. 5.18 Temperature transients at points in the attachment areas from test SZ2-T31 at $q'' \approx 43 \text{ W/cm}^2$

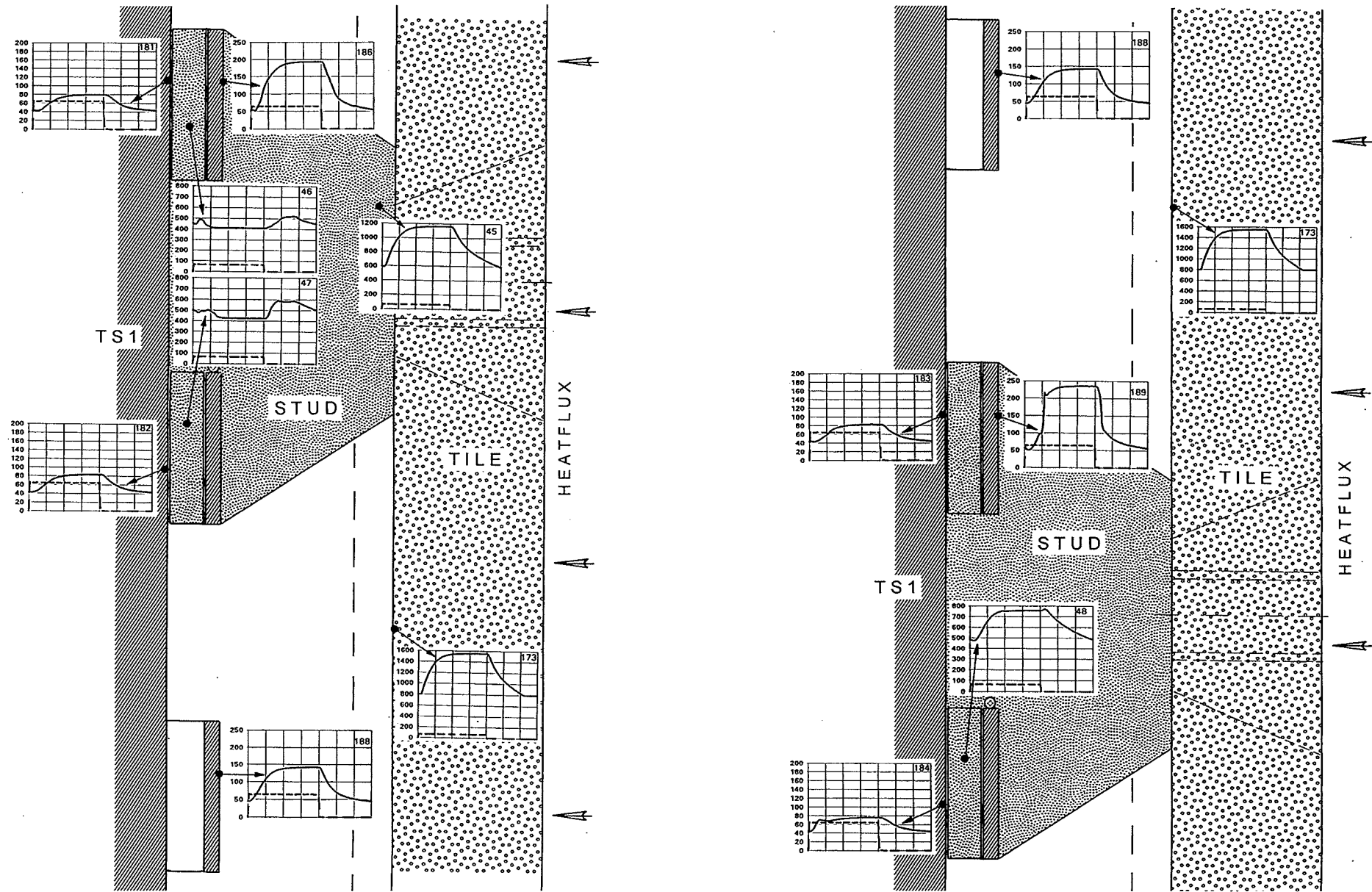


Fig. 5.19 Temperature transients at points in the attachment areas from test SZ3-T31 at $q'' \approx 43 \text{ W/cm}^2$

measured in the steel structure close to the studs' feet. And indeed some of it is found, small effects though because of the differences in heat capacity and the possible distance of the related TC locations: the change in slope of (184) at the bottom of the groove early in the dwell phase indicates that a good contact with the stud's foot during burn (high steel temperature) got lost at end of burn such that (184) fell back with a steep slope to a temperature level which it would have without contact and it continues from there to decrease its 'normal' way. Similar changes in slope are found in (186) and (189) from TCs at shoulders. The 'normal' shape of the curve, influenced by radiation from the tile only, may be taken from the position (188) without attachment stud. The transient at (189) with its initially steep increase in the burn phase is a good example to prove that the hot foot of the stud got in contact with the shoulder early in the burn phase. The maximum steel temperatures measured are 230 °C at a shoulder (189) and 220 °C at the bottom of the groove (184); the latter is assumed to lie rather close to a contact point. The maximum temperature ranges measured in the steel during a cycle are on the order of 180 K. Due to the measurement technique applied it should be expected that maximum temperatures and temperature ranges in the steel are higher at the contact points themselves.

Similarly, Fig. 5.19 covers a cycle from test SZ3-T31 in which a tile of CFC was mounted, again with the outermost spacer pads removed. In fact after the end of the SZ2 series the attachment studs were left in the grooves and only the tile was replaced to become test SZ3. Comparing the corresponding temperature transients from Figs. 5.18 and 5.19 in detail, one will find an extremely great similarity except for location (184) where obviously very little contact existed in test SZ3 which is confirmed by higher temperatures in (48) of the corresponding stud foot. The overall similarity is interesting since the CFC tile with its very small coefficient of thermal expansion could be expected to feature only little of the expansion-controlled effects listed in Chapter 5.3.3.1. On the other hand both the SZ2 and SZ3 tiles were mounted on the attachment design A with almost no rotational clearance at the anchor point in the tile which limited the freedom for stud tilting and thereby the number of mechanisms involved.

In summary test SZ3 shows that a small amount of differential thermal elongation and differential thermal bowing between the tile and the steel structure is sufficient to cause unexpected movements of the contact points. The maximum temperatures of 230 °C and the maximum temperature range of 180 K measured in the steel structure in the neighborhood of contact points do not seem to be a basis for major concern about the fatigue life of the structure. Nevertheless it seems advisable to perform well instrumented small scale tests covering the stud heat transfer and add a thermo-mechanical model calculation for the contact area of a final stud design before it will be applied.

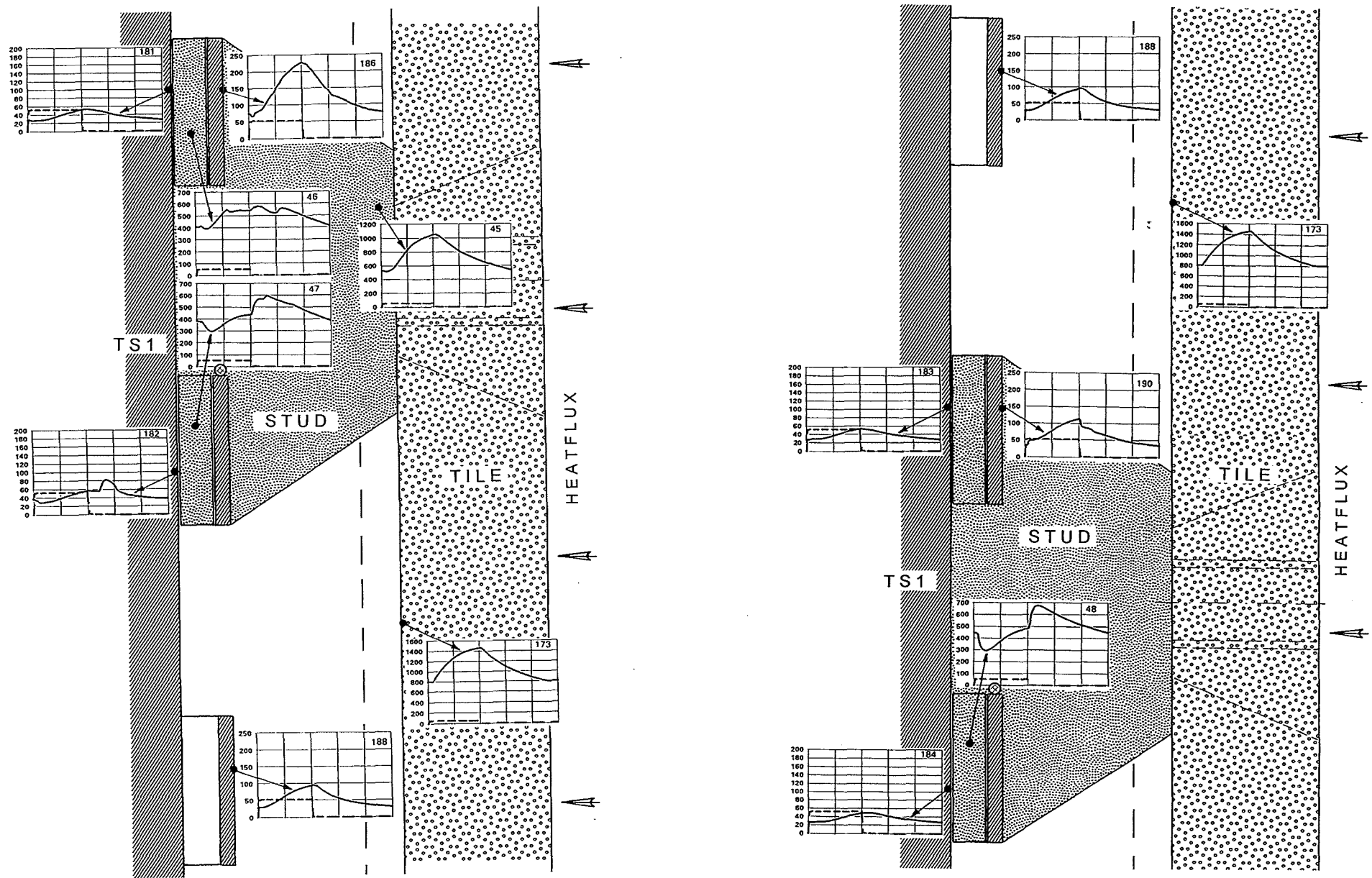


Fig. 5.20 Temperature transients at points in the attachment areas from test SZ1-T21 at $q'' \approx 35 \text{ W/cm}^2$

5.5.3.3 Temperature Transients at the Attachment Areas of SZ1

There was an unforeseen and strong mechanical interaction between the tile and the TS1 in test SZ1. Under heat load the fine-grained graphite tile bowed more than it was allowed for with the outermost spacer pads in place. The tile finally broke in the studs anchor areas since it did not stand the tension forces that developed in the studs; this was an extreme example of case (d) described in Chapter 5.5.3.1. Under heat load the studs' feet must have been pressed against the steel shoulders and the resulting good thermal contact should be discernible in the temperature transients. Certainly the contact pressure was strongest in test SZ1-T31 with $q'' \approx 43 \text{ W/cm}^2$ but its temperature transients cannot reasonably be used because of the failure; therefore test SZ1-T21 with $q'' \approx 35 \text{ W/cm}^2$ will be discussed and its temperature transients are plotted in Fig. 5.20. In difference to the two figures above the power cycle of only 10 minutes consisted of 4 minutes burn and 6 minutes dwell resulting in temperatures that did not become fully steady-state.

The temperatures measured in three of the studs' feet do not increase as they should during the burn phase; in fact two of them first strongly decrease indicating an improved thermal contact to the steel structure as a heat sink.

None of the bottom TCs (181) through (184) shows contact to a stud's foot during the burn phase but a shoulder TC (186) does with a strong temperature increase (it is not clear, why (190) does not show a strong heat-up, but the small sudden drop at the beginning of dwell confirms that there had been a contact before). Another proof for a good contact during burn is a temperature increase in the feet early in the dwell phase since it must be the result of losing a contact that had existed before; this clearly happens in (47) and (48) and to some extent in (46). TC (182) indicates that the corresponding foot suddenly touches the bottom of the groove early in the dwell phase which is reasonable when the tile straightens back and with its weight tilts the stud clockwise.

As a result, the temperature readings seem to prove the presence of tension in the attachment studs during burn and support the assumption of the SZ1 failure mechanism given in Chapter 5.5.1.2.

5.6 FE Modelling Results and Comparison

5.6.1 General Remarks

The FE modelling described below refers to the change of the gap between the TS1 and the tile made of fine-grained graphite. The material parameters for the fine-grained graphite FE 219 were chosen according to data provided by the manufacturer (Schunk und Ebe). Missing data was completed by data taken from [6] for H451 graphite. See the table in Fig. 5.21 for the numbers.

Temperature	Thermal Conductivity	Density	Specific Heat	Elasticity Modulus	Poisson's Ratio	Coeff. of Thermal Exp.
(°C)	(1) $(10^{-2} \frac{W}{mmK})$	(2) $(10^{-3} \frac{g}{mm^3})$	(2) $(\frac{J}{g K})$	(2) $(10^3 MPa)$	(2) (-)	(1) $(10^{-6} \frac{1}{K})$
20.		1.80	0.71	7.5	0.11	1.9
100.	7.7					
500.	5.2		1.62	8.0		3.3
1000.	4.0		1.89	8.5		3.6
1500.	3.1		1.99	9.0		3.7
2000.	2.6		2.05	9.6		3.9

Fig. 5.21 Material parameters for the fine-grained graphite FE219 according to the manufacturer Schunk und Ebe: (1) and to [6]: (2)

The 2D model shown in Fig. 5.22 allowed the simulation of the radiation between the graphite tile and the TS1 with the ABAQUS [5] option *GAP RADIATION using DINTER3 interface elements. The emissivities of graphite and the coated steel were assumed to be 0.8. In particular this model yields surface temperatures of both sides of the tile and of the heated surface of the TS1.

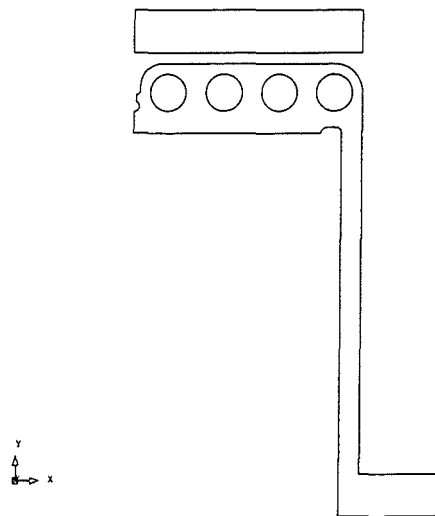


Fig. 5.22 Two-dimensional model for the simulation of the radiation conditions between the graphite tile and the TS1

The 3D model described in Chapter 4.5 allows the calculation of displacements at the TS1.

The deformation of the tile was simulated by a plate model. The plate was subjected to a surface heat flux on one side and it radiated into a heat sink on the other (ABAQUS option *RADIATE). The temperature of the heat sink was chosen according to the temperature results for the surface of the TS1 obtained by the 2D radiation model above. In this way, we obtained in the plate model the same linear temperature distribution, that we observed in the tile of the 2D radiation model.

5.6.2 Clearance at the Spacer Pads

We checked the clearance at the spacer pads for a surface heat flux of 44.6 W/cm². The attachment studs of the tile are fixed at the TS1 in the central groove at a distance of 120 mm away from the free end. This location at the TS1 is called LMS. The point on the surface of the TS1, which is situated opposite to the spacer pad in the corner region of the tile is called LMP. From the calculations for Chapter 4.5 we obtain for the differential displacement in the vertical (y-) direction of the locations LMS and LMP to be $\Delta u_{Y_{SM}} = 0.68$ mm. In particular, LMS suffers more vertical displacement than LMP. (For a detailed discussion of the deformation of the mock-up see Chapter 5.5.2.1).

The locations of the attachment stud and the spacer pad at the graphite tile are denoted by LTS and LTP, respectively. The graphite tile plate assumes the shape of a part of a sphere because of its nearly linear temperature gradient. We obtain for the differential displacement in the vertical (y-) direction of the locations LTS and LTP: $\Delta u_{Y_{ST}} = 1.5$ mm. (For simplicity, LTS was fixed in vertical direction and thus $\Delta u_{Y_{ST}} = u_{Y_{LTP}}$.)

For the following discussion, we neglect the thermal expansion in the attachment area itself. The spacer pad is shifted 1.5 mm towards the TS1 because of the deflection of the tile. Point LMP of the TS1 moves in the same direction relative to the attachment stud. However, since the differential displacement of LMP and LMS is only 0.68 mm, a gap of at least 0.8 mm would have been needed, if contacting between spacer pad and TS1 was to be avoided at a surface heat flux of 44.6 W/cm².

5.6.3 Differential Displacement of TS1 and Tile

Measured and calculated data for the differential displacement of TS1 and tile will be compared. As described in Section 5.5.2.2 the displacements of the constrained TS1 and the tile were measured at a position, which is located 6 mm from the free end of the central groove (cf. Table 5.3). The corresponding locations on the TS1 and tile are called LMD and LTD, respectively. The computed differential displacement of LMD and LTD was obtained in the same manner as in the previous section for the spacer pads, see the table in Fig. 5.23.

q'' [$\frac{W}{cm^2}$]	u_y [mm]				Δu_y [mm]
	tile		mock-up		
	LTS	LTD	LMS	LMD	LMD-LTD
5.0	0.0	-0.116			
17.9	0.0	-0.445	0.235	-0.00316	-0.210
36.1	0.0	-1.16	0.455	-0.0426	-0.692
44.6	0.0	-1.53	0.545	-0.0602	-0.955

Fig. 5.23 Vertical displacements at locations LTS, LTD, LMS, and LMD and resulting differential displacements LMD-LTD for various surface heat fluxes q'' ; negative values indicate that the gap between TS1 and tile becomes smaller

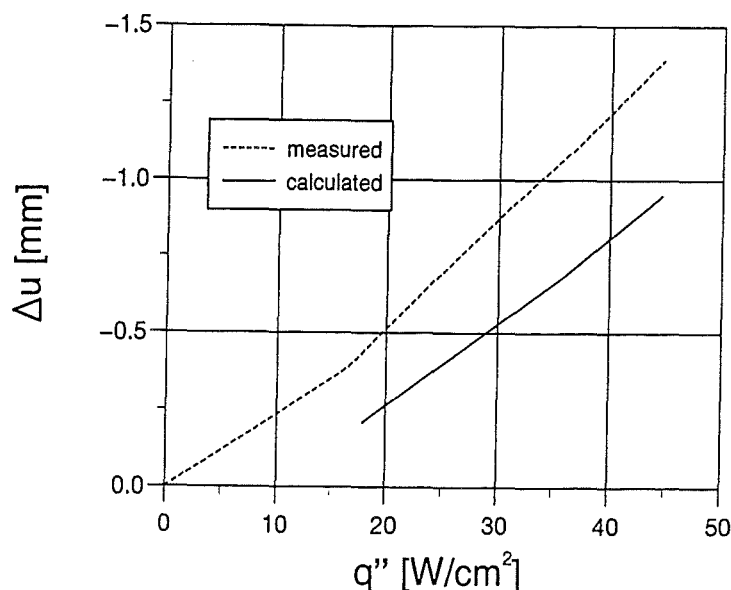


Fig. 5.24 Differential displacement of TS1 and tile at the free end of the central groove

If measured and calculated results are plotted in a single plot, we observe a significant deviation (see Fig. 5.24). One reason for this may be the uncertainty about the coefficient of thermal expansion of the tile material. Furthermore, the thermal expansion in the attachment area was neglected in the calculations. Finally, the correction that was applied to the measured LVDT signals may have been incorrect.

The nonlinear behaviour of the differential displacement as a function of the applied heat flux q'' is caused by the corresponding nonlinearity of the vertical displacement of LTD. This displacement is proportional to $\alpha/\lambda q''$, where α is the coefficient of thermal expansion and λ is the thermal conductivity. The significant increase of α/λ as a function of the temperature (cf. the table in Fig. 5.21) causes the mentioned nonlinearity.

As a conclusion of the above discussion, we hesitate to compare measured and calculated results for the differential displacement of TS1 and tile quantitatively. However, qualitative statements such as the one of the previous section concerning the possibility of contact between spacer pads and TS1 are still justified.

5.7 Conclusions

The present design of a radiatively cooled protection tile in principle proved to be feasible with the restriction that no tile of high quality CFC and no attachment studs made of 3D CFC were available for the test, yet better materials are expected to even improve the performance since they would have lower coefficients of thermal expansion, higher strength and better abrasive qualities.

The unexpected failure of the tile in test SZ1 is clearly due to the small open gap between tile and steel structure not being adjusted to the strong bowing of a tile made of fine-grained graphite that was used.

From the observation of the transient changes of the gap size it became evident that the minimum gap between tile and steel structure does not appear under steady-state conditions but very early in the burn phase when the tile has bowed already before the steel structure has received enough heat to bow also.

From this point of view the clearance under the outermost spacer pads of the tile should be increased in the present design and future designs should take care of transient deformation behaviour which may be calculated appropriately.

Thermal conduction through the attachment studs does not seem to transport enough heat via the contact points into the steel structure to establish a threat for the fatigue life of the steel. Nevertheless well instrumented small scale tests of the final stud design accompanied by FEM calculations for the contact area in the steel would be recommended.

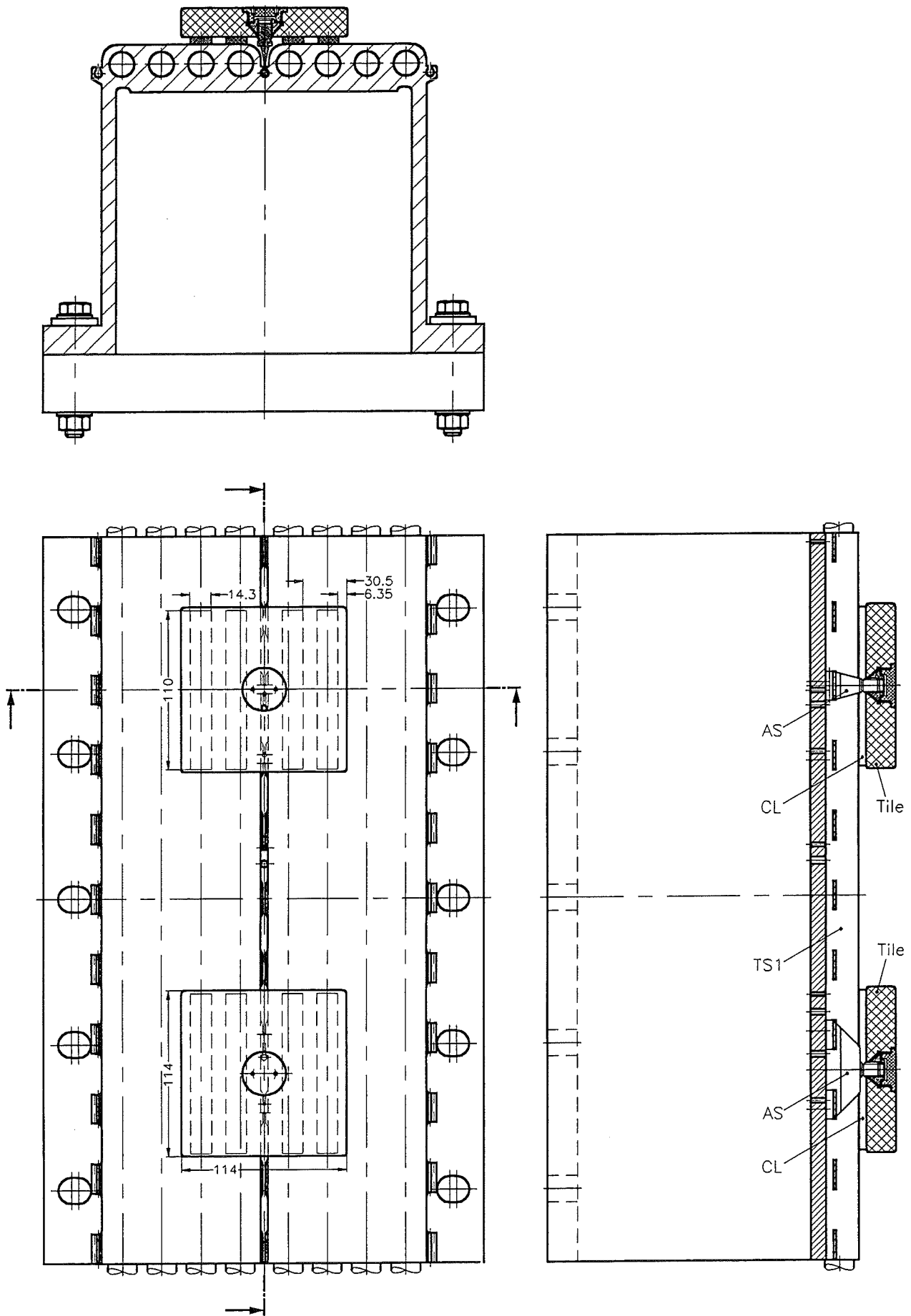


Fig. 6.1 Specimen TS1 with two conductively cooled tiles

6. Thermo-mechanical Testing of TS1 with Conductively Cooled Tiles

6.1 Design Concept and Goals of the Investigation

The design concept of 'conductively cooled tiles' utilizes a compliant layer to thermally couple the protection tile to the structural material which contains the heat sink. The compliant layer is to improve the thermal contact between the components where the bare rigid partners would be in point contact with very poor average heat transfer only. The tile is pressed to the first wall structure by a single bolt with a force that is limited by the strength of tile material and the size of the tile is limited such that the force causes sufficient pressure to adequately deform the compliant layer. The compliant layer needs to be flexible in order to provide thermal contact even if the components deform differently under heat load. In order to be flexible the compliant layer needs to be thick enough but at the same time it needs to be thin enough to not cause a high thermal resistance and consequently too high temperatures at the tile. The design concept investigated experimentally is the NET/ITER-Integrated First Wall Tile Attachment - Type 5 as of November 1992 featuring a compliant layer of a flexible graphite (special order Papyex) up to 5 mm thick.

It is the goal of the investigation to determine the mechanical and thermal properties of the compliant material and the resulting heat transmittance between the rear side of the tile and front side of the steel structure. Of special interest is the question whether the heat transmittance is uniform over the contact area and whether it changes in size when cyclic heat loads are applied. In addition, it was to be checked if the cap screwed into the tile to cover the attachment stud would develop high over-temperatures due to poor thermal contact.

6.2 Test Specimens

The specimens tested consisted of the TS1 as a water-cooled first wall structure (see Chapter 2.1 for details) and two conductively cooled CFC tiles mounted on the surface of the TS1 (Fig. 6.1); in most of the test series the TS1 was used in the so-called 'constrained' condition indicated by a 'V' as the third digit of the test designation (see Chapters 2.1 and 4.3.1 for details). Compliant layers (CL) of different sizes and materials improved the thermal contact when the tile was pressed to the TS1 by its central attachment stud (AS). The different specimens for the test program were assembled from the same two tiles in the same places on the TS1; only the compliant layers and the applied contact pressures were different.

The tiles were 20 mm thick plates 114 mm by 114 mm in size made from carbon fibre reinforced carbon (CFC Aerolor 05) by Le Carbone Lorraine. A central hole in the tile (Fig. 6.2) was shaped to receive the attachment stud and above the stud's nut the remainder of the hole was filled with a CFC cap to make a smooth carbon surface of the tile.

Both the attachment stud and its conical nut (Fig. 6.3) were made of Molybdenum (TZM). There were two different stud designs: Stud A, the larger one, was engaged with two feet in the attachment groove; this stud was used to mount the lower tile. Stud B, the smaller one, was engaged with only one foot in the attachment groove; it was used to mount the upper tile. They will not be distinguished for the remainder of the

report since they showed no difference in the behavior of the tile attachment. The threads of the attachment studs were CVD-coated with a 5 μm thick layer of Titaniumcarbonitride in order to avoid fretting between the stud and the nut and to make friction reproducible when the torque to the nut was calibrated to be representative for the contact pressure at the compliant layer. In addition a mixture of graphite powder and alcohol was used as a lubricant.

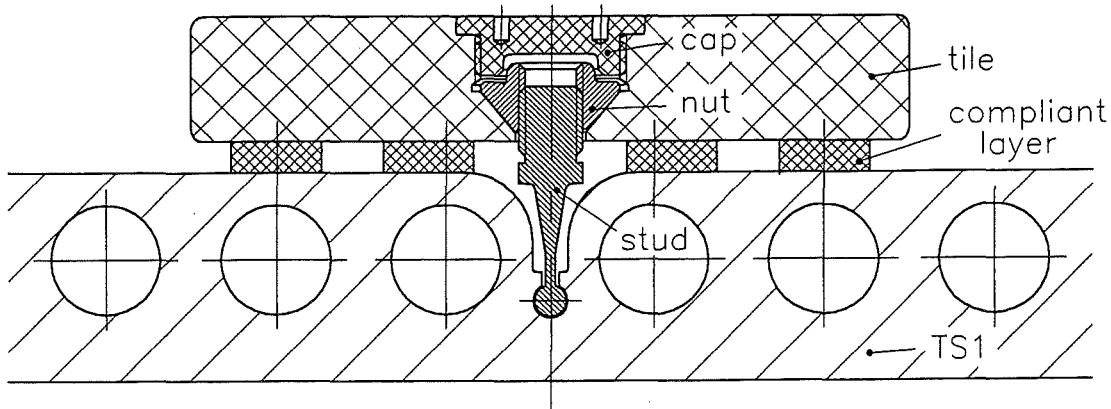


Fig. 6.2 Conductively cooled tile

6.2.1 Compliant Layer

The compliant layers (CL) consisted of laminated flexible graphite, known as trademarks Papyex (Carbone Lorraine, France) or Sigraflex (Sigri, Germany). The material is pressed from pure graphite flakes. The regular trade qualities are foils or plates up to 2 mm thick at a density of up to 1 g/cm³. The materials used in the test were:

- special order Papyex, with a density of 0.4 g/cm³ and 5 mm thick; for one test group it was machined to become 2.5 mm thick
- regular order Sigraflex TH, with a nominal density of 1 g/cm³ (the density measured in the laboratory was 0.85 g/cm³) and actually 2.4 mm thick.

The CL material was cut into 14.3 mm wide stripes such that four stripes distributed over the width of the tile would cover 50 % of the tile's surface. The stripes were mounted centered above the coolant channels of the TS1 (as far as the rounded edges at the attachment groove would allow this) in order to direct the heat flux to the heat sink via the shortest way through the steel structure. The force that could be transferred from the AS to the tile was limited to 3150 N; to nevertheless reach a contact pressure at the CL of 5 bar the contact area was limited to 50 % of the tile area; as a parameter, in one of the tests the contact area was increased to cover the maximum possible of 72.5 % of the tile area which resulted in a contact pressure of 3.35 bar.

6.2.2 Mounting of the Tiles

The contact pressure was considered an important parameter for the heat transfer at the compliant layer. Therefore it had to be adjusted to a given value at mounting of the tiles even if it should change during the tests due to thermal expansions and CL deformation. The only means of setting a given contact pressure was using the applied torque to the nut of the attachment stud as a measure. As a prerequisite the torque had to be related

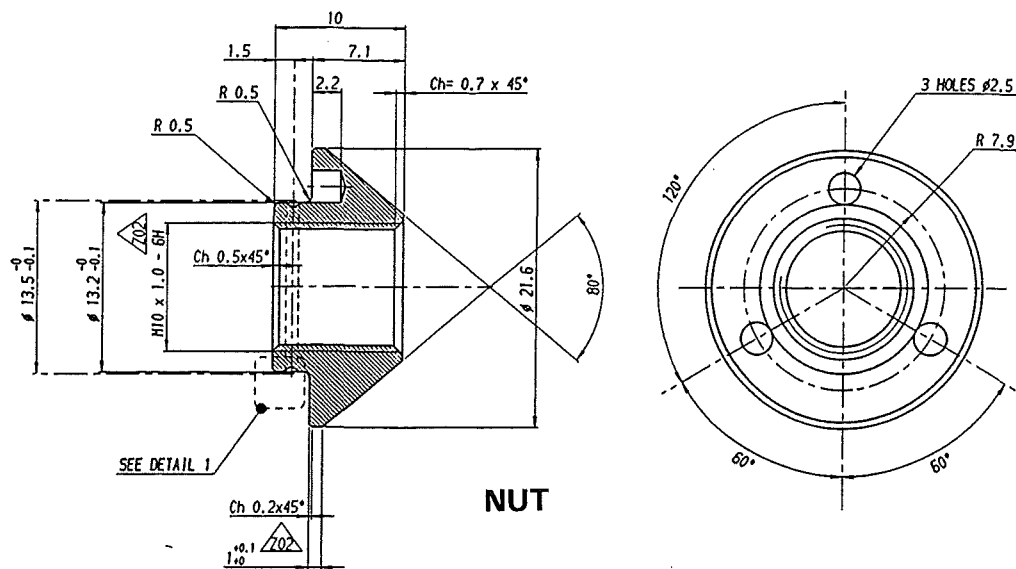
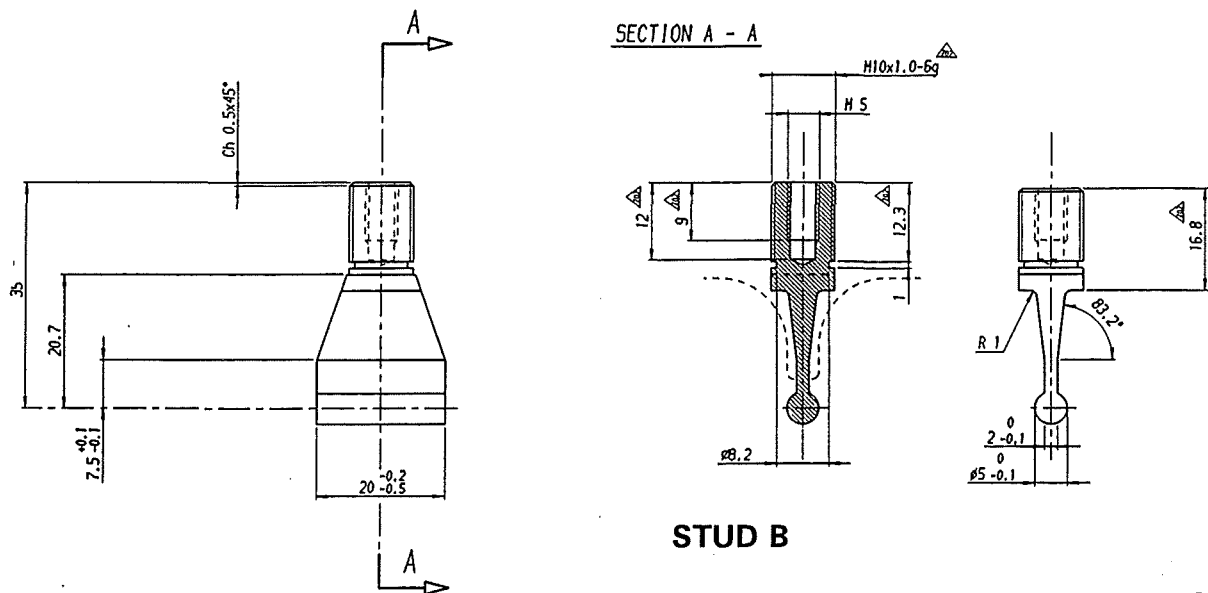
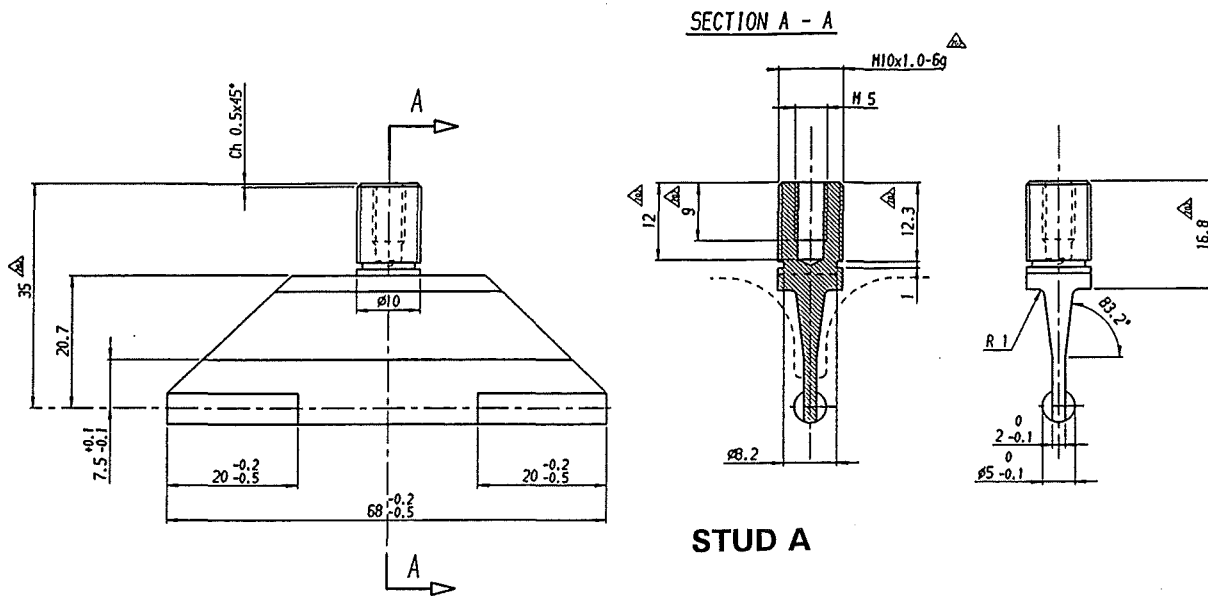


Fig. 6.3 Tile attachment studs A and B

experimentally to the resulting force in the attachment stud and thereby to the contact pressure. This calibration was done by replacing the CL by an electric load cell (Burster type 8524, 0-2 kN) and by using a torque indicator wrench (0-10 Nm) to tighten the nut. It revealed an almost linear dependence between torque and force up to a torque of $M=9$ Nm. It was verified that the measured data were well reproducible provided that the thread was lubricated at mounting with a mixture of graphite powder and alcohol. On this basis $M=8$ Nm results in a force of 3150 N and corresponds to a contact pressure of 5 bar at 50 % CL coverage.

The tiles were mounted on the TS1 after the CL was put precisely in place; the contact pressure was adjusted at room temperature by applying a given torque with a torque indicator wrench. The torque was checked and corrected, if necessary, after a few hours before the specimen was installed in the test device.

Finally the four 2 cm wide side faces of the tiles were covered with a radiation shield made of a stripe of 1 mm thick flexible graphite. This seemed necessary since these surfaces would have been exposed to the radiative heat source with the consequence that the heat flux entering there would have confused the one-dimensional heat flux pattern entering the main face. The shield also protected the TCs that entered the tile at one of its side faces.

At the end of a test series the torque was again determined at room temperature in order to find out how much of the initial contact pressure had got lost by CL densification during the test.

When the CL had to be replaced for the next test series, the nut was removed and the fully instrumented tile was lifted just enough to change the CL stripes.

6.2.3 Instrumentation of Specimens

With the regular instrumentation of the facility the flow rate and the heat-up rate of the coolant were measured in order to determine the power received by the specimen as a whole.

Pyrometers were directed to the back side of the heater in order to measure its temperatures in places where its front side faced one of the tiles or the 'naked' steel wall of the TS1.

Most of the instrumentation for this test consisted of TCs inserted in the tiles; they are described below. The goals were to determine temperatures in the tile close to the CL contact area and their uniformity over the tile area, temperature gradients parallel to the heat flux, and the maximum temperature expected in the cap because of its relatively poor thermal contact to the tile.

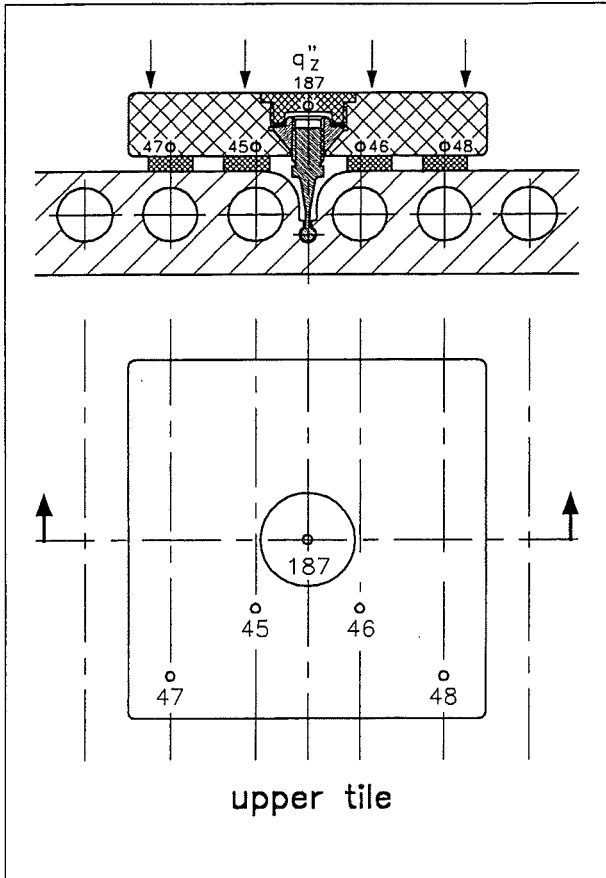
Sheathed and insulated type K TCs of 0.5 mm outer diameter were used. In order to avoid measurement errors due to temperature gradients the TCs were inserted along isotherms in the tiles, i. e. holes were drilled into the side face and parallel to the heated surface of the tile. The holes of 1.0 or 1.5 mm in diameter were reduced to 0.6 mm for the last 7 mm of their lengths to receive the 0.5 mm TCs. The TCs were slipped into the holes without any contact medium, which was not needed because the TC leads ran along isotherms and for the measurements the test conditions were steady-state. After leaving the tile behind a side face radiation shield the leads as a bundle passed through a hole in the bottom of the attachment groove of the TS1.

The spatial distribution of the TCs is shown in Fig. 6.4 (the numbers indicate the channels in the data acquisition system); it was slightly different for two groups of test series as marked. As a general rule the TCs in the tiles were placed above the center of a cooling channel in the TS1, except for (187), (197) and (198). The distances from the tiles' side faces (depth of the TC holes) were either 13.5 or 35 mm. Over the thickness of the tile two planes were instrumented: for all tests one such plane was 3 mm away from the rear face of the tile; for test groups L1-L2 the second plane was 3 mm away from the front face of the tile and for test groups L3-L6 the second plane was 13 mm away from the front face of the tile (i. e. 4 mm distant from the first plane). The TC187 in the cap was placed in its center and 4 mm below its heated surface after the cap had been screwed in place.

During test series L2 temperatures of 1200 °C were reached at TCs 195, 197, 199 and 187 being closest to the heated surface; at the radiation shield, covering and touching the TC leads, the temperature will have been even higher. This caused failure of several TCs since just below 1200 °C their stainless steel sheath forms an eutectic with carbon. To avoid such failure in the following test series several measures were taken for L3-L6:

- TC 187 in the cap was not replaced since the information collected from it in group L2 seemed sufficient.
- Radiation shielding of the TC leads was improved by completing a second shield layer.
- The second TC plane was moved from 3 mm below the heated surface to 13 mm below the heated surface for both tiles and at the same time more TCs with a different numbering were installed to better cover the temperature distribution across the tile. As a rule pairs of equally spaced (4 mm) TCs were placed close to the different CL stripes hoping that the temperature differences they would show would be an indicator for the uniformity of the heat flux through the individual CL stripes (the uniformity could be disturbed by the wider spacing of the stripes in the center area, by differences in heat transmittance through the individual stripes, and by the presence of the attachment stud). To install the new distribution of TCs shown in Fig. 6.4 (right) both tiles were rotated around the attachment stud by 180° and new TC holes were drilled.

test groups L1 - L2



test groups L3 - L6

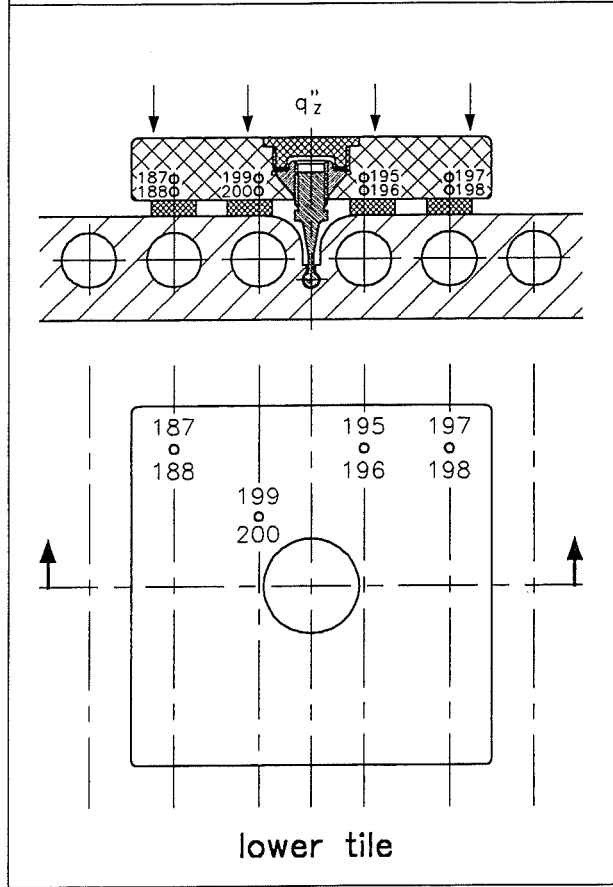
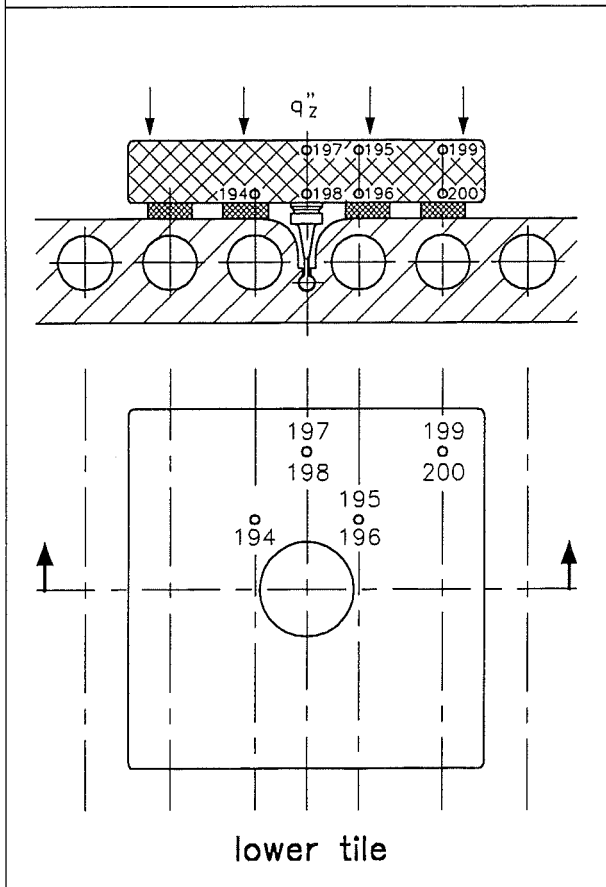
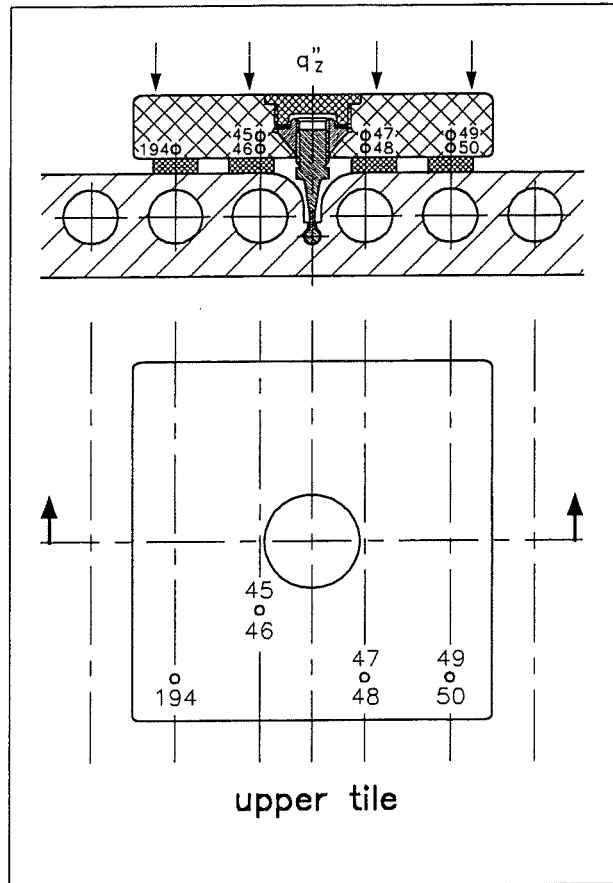


Fig. 6.4 Thermocouple instrumentation in conductively cooled tiles

6.3 Testing

6.3.1 Experimental Set-up

Very similar to the experiments with the bare TS1 (see Chapter 4.3.1) the specimen with the two conductively cooled tiles was installed in a window of the FIWATKA heater housing which surrounded the radiative heater. Figure 6.5 shows vertical and horizontal sections through housing and specimen. As compared to Fig. 4.3 the only difference is that the left part of the housing was moved by about 20 mm to the left to make room for the tiles between the heater and the TS1; this resulted in a distance of about 25 mm between the heater and the surface of the tiles. All other characteristics of the setup listed in Chapter 4.2.1 apply here as well. The TS1 was used in the so-called 'constrained' condition.

To the left the heater would see a partner surface which is on a low temperature level except for the surfaces of the two tiles that are on intermediate temperatures and cover only part of the TS1. It will be discussed in Chapter 6.3.3. how this situation is handled when the heat flux into the tiles is to be determined.

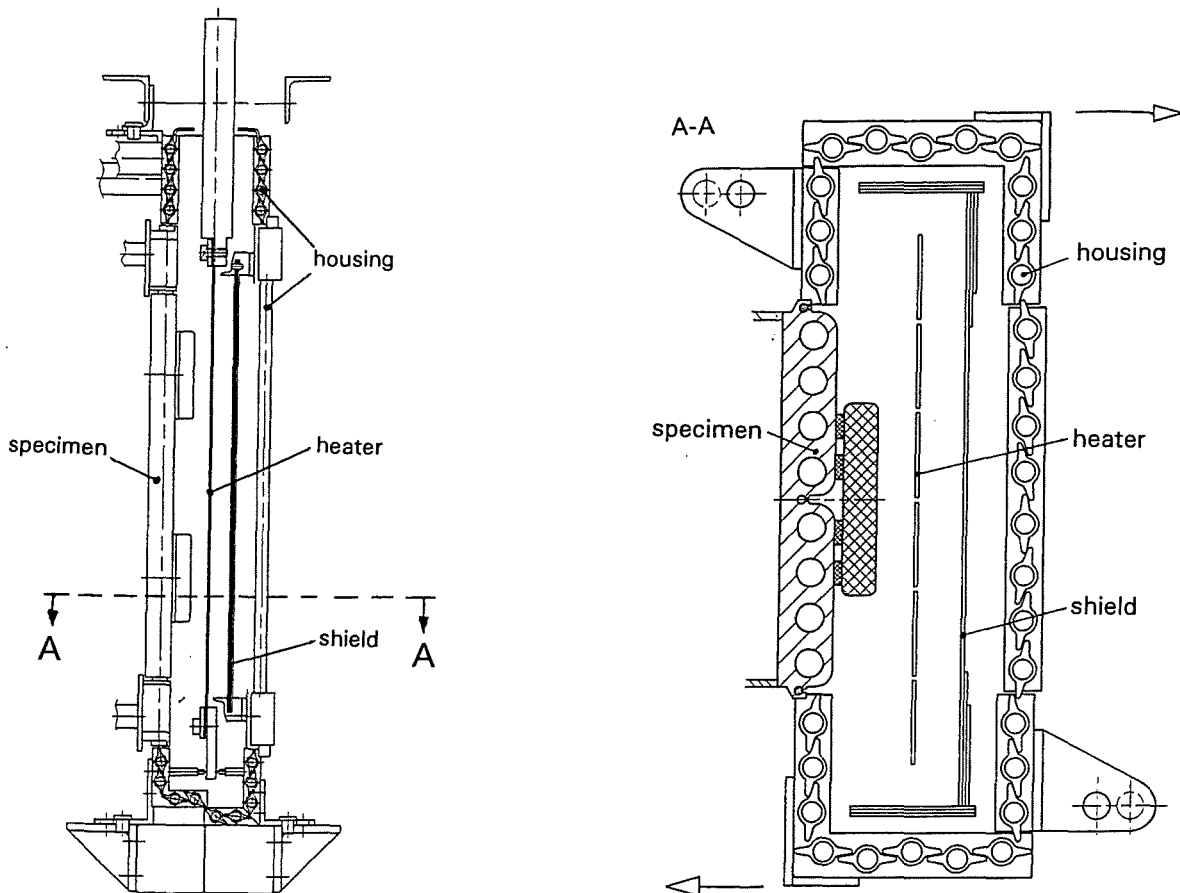


Fig. 6.5 Vertical and horizontal sections (different scales) through the experimental setup with the TS1 and two conductively cooled tiles for test groups L1 through L6

6.3.2 Experimental Procedure and Test Sequence

The parameters to be investigated were

- type, thickness and covered area of the compliant layer (CL) material
- contact pressure at the CL before applying the heat load
- size of the applied heat flux
- application of load cycles

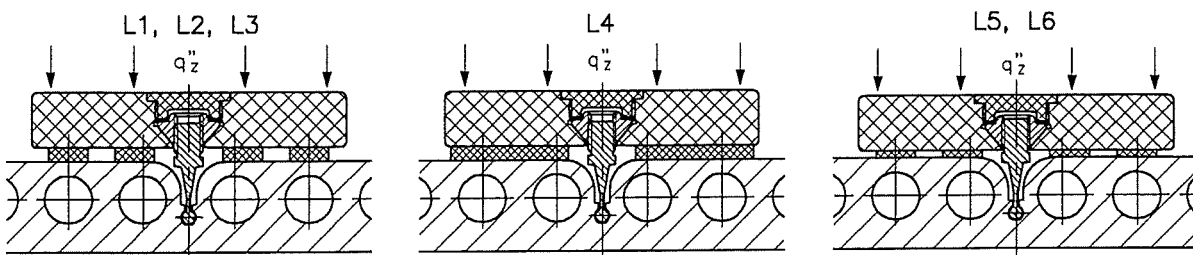
The regular experimental procedure consisted of the following steps:

- The CL stripes were cut from a plate of CL material by using a thin blade rolling knife in order to minimize undesired deformation at the edges.
- The alignment, which the stripes had in the plate, was kept when they were placed under the tiles; this was done to make the CL contact faces as a whole as plane as possible for each tile.
- The contact pressure was applied by adequately fastening the nut of the attachment stud (see 6.2.2 for details).
- The CL thickness was determined by measuring the CL thickness together with the known tile thickness.
- The specimen was mounted in the window of the heater housing and the test vessel was evacuated.
- The power to the heater, and thereby the heatflux to the specimen, was increased in steps. The power increase to the maximum heat flux applied was subdivided into four to seven steps.
- After the maximum heat flux had been reached the power was usually reduced in the same steps in order to be able to identify any changes in the heat transfer performance of the CL, which could be attributed to the earlier exposure to higher heat loads.
- After each power step and a waiting time of at least 20 minutes (to guarantee steady-state conditions) a data set was measured and stored in a file designated '-S'.
- At some of the power steps a small number (4 or 10) of cycles were run each consisting of 4 minutes burn and 4 minutes dwell phases; the purpose was not to fatigue the heat transfer quality of the CL but to log transient data for the last two of these cycles. These transient data were stored in files designated '-T'.
- In two of the test groups (L2 and L6) a larger number (several hundred) of cycles were included in order to check whether thermal cycling changes the heat transfer behavior of the CL. These cycles were not recorded transiently but only one data set was logged shortly before the ends of each the burn and dwell phases of each cycle; these data for near-steady-state conditions are stored in files designated '-Z'.
- Within each test group only one set of CL stripes was used. Whenever the contact pressure was adjusted or increased within a test group the CL that had been used before in the same test group was kept.
- When the specimen was removed from the test facility in order to adjust the contact pressure or to finish the test group any changes at the CL were observed with two measures: (a) the thickness of the CL was again determined and (b) the actual contact pressure that was left at the end of the preceding test series was measured by applying an increasing torque to the nut and by observing when the nut started to move.

- For each test group a new set of CL stripes was used. The CL stripes were different concerning their thickness and their density (compliance), their manufacturer, and the size of the covered area of the tile (coverage).

Table 6.1 Test groups and compliant layers mounted

test group	compliant layer			contact pressure bar	max. heat flux, q''_z W/cm ²	remarks	
	type	thickness mm	density g/cm ³				coverage %
L1 (V2)	Papyex	5	0.4	50	2	30	screening tests; results are not reported
(V4)					4		
(V5)					5		
L2 (V5)	Papyex	5	0.4	50	5	44	valid tests; several TCs overheated at the highest heat flux
L3 (V5)	Papyex	5	0.4	50	5	38	repetition of L2 with rearranged TC pattern
L4 (V3)	Papyex	5	0.4	72	3.35	44	increased contact area with decreased contact pressure
L5 (V2)	Sigraflex	2.4	1	50	2	44	different CL material and CL thickness
(V5)					5	44	
L6 (V2)	Papyex	2.5	0.4	50	2	38	CL thickness similar to L5 but Papyex
(V5)					5	38	



Tests with the conductively cooled tiles were performed in six groups with different compliant layers as shown in Table 6.1.

- Group L1 contains screening tests for various test conditions; since the behavior of the CL cannot be related to a clear test history the results are excluded from further evaluation.
- Group L2 covers 5 mm thick CL stripes of 50 % coverage at 5 bar and delivered the basic stock of data but at the highest power level several TCs failed due to overheating in positions close to the heated surface.
- Group L3 repeated group L2 but was limited to lower heat fluxes and the tiles contained rearranged TCs in order to avoid overheating and to be of better use for the determination of local heat fluxes in the close vicinity of the CL contact areas.
- Group L4 was to check whether the same limited stud force distributed over a larger contact area (smaller compliance) would result in different heat transmittance through the CL.
- Group L5 investigated a different CL material (Sigraflex) of smaller thickness and higher density (smaller compliance).
- Group L6 covered the reference CL material (Papyex) also with smaller thickness.

Table 6.2 Sequence and designation of tests (entries indicate that the condition was covered and where the data are filed; test sequence was top to bottom with one set of CL within each group)

heat flux into the tile $q''_z, \text{W/cm}^2$ ¹⁾	test group	L2-			L3-			L4-			L5-			L6-		
	p, bar ²⁾	5			5			3.35			2			2		
	heating mode ³⁾	s/s	cycl		s/s	cycl		s/s	cycl		s/s	cycl		s/s	cycl	
	logging mode ⁴⁾	S	T	Z	S	T	Z	S	T	Z	S	T	Z	S	T	Z
5		S			S			S			S			S		
10		S	T10		S			S			S			S		
15		S			S			S			S			S		
20		S	T20		S			S			S			S		
25		S														
30		S	T30		S			S			S			S		
				Z30 (125)												
		S	T30													
20		S														
10		S														
5		S														
38		S	T38		S	T38		S			S			S	T38	
				Z38 (125)												
		S	T38													
44								S	T45		S	T45				
38								S			S					
30		S			S			S			S			S		
20		S			S			S			S			S		
10		S			S			S			S			S		
5		S														
	p increased to p', bar	5									5			5		
5											S			S		
10		SZ									S			S		
20											S			S		
30											S			S		
38		SZ									S			S	T38	
														S	T38	ZA (153)
44		SZ									S	T45				
38											S					
30											S			S		
20											S			S		
10		SZ									S			S		
38														S		ZB (156)
														S		ZC (169)
														S		

¹⁾ approximate values (see results for precise values)
²⁾ initial contact pressure at mounting of tile
³⁾ s/s= steady-state; cycl= cycles consisting of 4 min. burn and 4 min. dwell
⁴⁾ S= one data set after at least 20 of heating; T= transient logging
Z= one data set at end of each load phase (numbers in parentheses indicate number of cycles performed)

For each group the sequence of tests and the designation of the respective data files may be taken from Table 6.2. From top to bottom is listed how the heat flux was changed in steps; the entries indicate which of the power steps were applied in the different test groups. After steady-state conditions were reached for a step a data set was logged in the S-file. At some power levels a transient reading was logged as a T-file. In some cases (shaded areas) a larger number of cycles (number given in parentheses) were run and logged as Z-files; cycles were run in order to learn whether any changes of the heat transfer through the compliant layer occur during cycling (some kind of CL fatigue) or if changes become obvious when steady-state results from before and after cycling are compared.

6.3.3 Test Evaluation and Data Processing

The quantity of interest to be evaluated is the heat transmittance h' through the CL. It describes the heat transfer at the CL and includes the effects of both the heat conduction through CL and the two thermal contact resistances between the CL and the tile on one side and the TS1 on the other side. h' has the dimensions of a heat transfer coefficient and is defined by

$$h' = \frac{q_p}{\Delta T_{CL}} \left[\frac{W}{cm^2 K} \right]$$

with q_p being the local heat flux through the CL and ΔT_{CL} being the temperature difference between the rear surface of the tile and the front surface of the TS1, both in positions of the CL contact. q_p and ΔT_{CL} could not be measured directly and are somewhat hard to determine. Figure 6.6 shows why: Open circles mark the quantities q_p (q_3 or q_4) and ΔT_{CL} needed and crosses mark the quantities that are known from measurements.

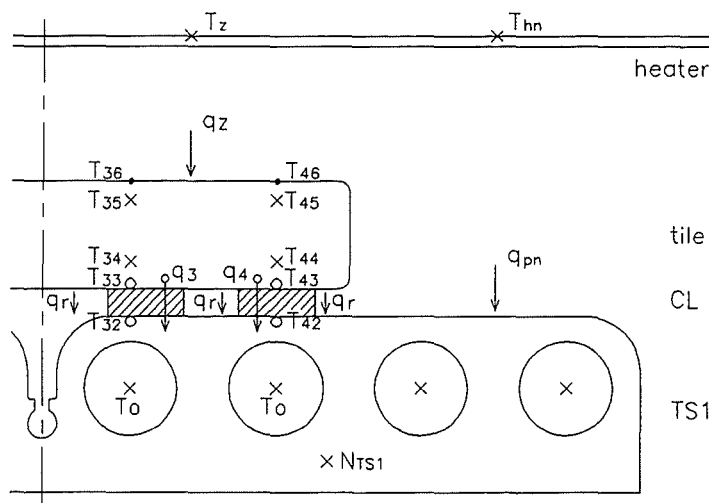


Fig. 6.6 Test evaluation: measured (x), needed (o) and interesting (•) quantities

The earlier method of determining the heat flux into the specimen (see Chapters 4 and 5) by dividing the calorimetrically determined power to the specimen N_{TS1} by the specimen's surface area would not be correct here since the tile-covered and naked areas of the TS1 absorb radiation power differently due to their different surface temperatures. In addition the heat flux finally absorbed by the tile cannot be related directly to q_3 and q_4 at the CL by only considering the reduction in area since some of the heat bypasses the CL by radiation q_r from the rear side of the tile to the surface of the TS1 and also the power may be distributed nonuniformly to q_3 and q_4 ; on one hand due to a displacement of the central CL stripe q_3 could drain a larger portion of the tile than q_4 does, on the other hand the attachment stud could transfer heat that would be lost for q_3 . How q_3 and q_4 were determined, is summarized below and reported in more detail in Appendix A. When the local heat fluxes q_3 and q_4 are known, surface temperatures like T_{42} and T_{43} may be calculated from T_0 and T_{44} , respectively. Because of the obstacles mentioned above the test evaluation contains some uncertainties; they were partly reduced by iterative procedures; nevertheless the precision of the absolute values of the reported heat conductances h' should not be overrated. But since similar evaluation procedures were applied to all tests and all heat transfer paths any differences or time-dependent changes found should be reliable as relative results.

Heat flux q_z :

The power N_{H_2O} received by the total specimen including the coolant headers was determined calorimetrically and the power to the headers was subtracted (see Chapter 4.3.3) to get the power N_{TS1} to the surface of the TS1 including tiles

$$N_{TS1} = N_{H_2O} - N_{headers} = N_{H_2O} - 0.0528 \cdot N_{el}$$

The radiation power N_{TS1} would not enter the surface of the specimen uniformly since the surface of tiles is much hotter than the surrounding steel surface of the TS1. In fact their temperatures depend on the power level and in addition the tile's surface temperature depends on its further heat transmission qualities including thermal conductance in the tile and transmittance at the CL stripes. Therefore N_{TS1} is subdivided into a fraction N_z to the two tiles and a fraction N_N to the surrounding naked steel surface. This subdivision is performed with a special BASIC code (QF-LT-ZI) which models the different parallel heat transfer paths (two through the tile and one outside) and determines N_z iteratively for an assumed CL transmittance h' (see Appendix A for details). With the area of the two tiles $F_z = 260 \text{ cm}^2$ the heat flux to the tiles becomes

$$q_z = N_z / F_z$$

As a result q_z is a function of N_{TS1} for an assumed h' and for the CL coverage f of the actual test group; h' could be approximated iteratively and its influence on q_z is relatively small as may be seen from Fig. A3 in Appendix A.

The following functions were applied for evaluating the different test groups with N_{TS1} in kW and q_z in W/cm²:

test groups	h'	f	$q_z = f(N_{TS1})$
L1, L2, L3, L6 (V2)	0.1	0.5	$q_z = (-0.00346 + 0.248 \cdot N_{TS1} - 7.44 \cdot 10^{-4} \cdot N_{TS1}^2 + 8.26 \cdot 10^{-7} \cdot N_{TS1}^3) \cdot 3.846$
L5, L6 (V5)	0.13	0.5	$q_z = (-0.00591 + 0.246 \cdot N_{TS1} - 4.61 \cdot 10^{-4} \cdot N_{TS1}^2 + 1.61 \cdot 10^{-6} \cdot N_{TS1}^3) \cdot 3.846$
L4	0.1	0.72	$q_z = (-0.08358 + 0.253 \cdot N_{TS1} - 5.26 \cdot 10^{-4} \cdot N_{TS1}^2) \cdot 3.846$

Heat flux q_p :

The power entering the tile as heat flux q_z will leave the tile to a larger extent as heat flux q_p through the CL stripes and to a smaller extent as radiative heat flux q_r through the gap areas between the stripes.

q_r depends on the temperatures of the radiating partner surfaces of the tile and the TS1 and is taken from the results of the above mentioned model calculation with the BASIC code (QF-LT-ZI) as a function of q_z (see Appendix A) as:

test groups	$q_r = f(q_z)$
L1, L2, L3, L6 (V2)	$q_r = (0.025 - 0.021q_z + 0.0045q_z^2 + 5.46 \cdot 10^{-5}q_z^3)$
L5, L6 (V5)	$q_r = (0.0127 - 0.0011q_z + 0.002q_z^2 + 5.65 \cdot 10^{-5}q_z^3)$
L4	$q_r = (0.00476 + 0.00897q_z + 4.047 \cdot 10^{-4}q_z^2 + 5.555 \cdot 10^{-5}q_z^3)$

q_p may be calculated from q_z by considering q_r as an additional heat sink and by concentrating the remaining power to the reduced area of the stripes at the coverage rate f as:

$$q_p = \frac{q_z - q_r (1-f)}{f}$$

The equation above is based on the assumption that q_p is uniform at all CL stripes of a tile but there are several reasons why q_p could be nonuniform: Firstly, the geometry is nonuniform such that the inner two stripes could drain the heat from a larger area of the tile than the outer ones and at the same time they could be thermally unburdened by heat conducted through the attachment stud. But an FE model calculation has shown that from this point of view the uniformity of q_p can be expected better than 3 %; the reason should be the very high thermal conductivity of the CFC tile parallel to its main surface.

Secondly, a nonuniform transmittance at the different stripes would make the respective values of q_p nonuniform also, such that a higher transmittance at a stripe would increase the local heat flux q_p . It was tried to determine the actual local heat flux q_p in the tests by making use of temperature gradients in the tile measured over a 4 mm distance close to most of the stripes. This resulted in relatively large differences between the stripes of a tile ranging up to 15 % of the mean value. However, these differences are attributed mainly to an inexact positioning of the individual TCs (0.5 mm out of 4 mm distance causes an error of 12 %); this explanation is supported by the fact that throughout the

test groups the steepest temperature gradients were always measured in the same positions. For path u4 at the lower tile, the results for which are reported in Chapter 6.4, the local heat flux q_p calculated from the measured temperature gradients was only up to 5 % different from the mean value for the tile. Also this second reason for q_p nonuniformities is believed to be of minor importance since after the evaluation the transmittances turned out to be rather similar for the different stripes.

As a result the above assumption of a uniform q_p seems acceptable but it might introduce an error into the absolute values of calculated transmittances.

Surface temperature T_{x2} and T_{x3} (ΔT_{CL}):

The temperatures at the surfaces facing the CL were determined by starting from measured temperatures available next to them and assuming the heat flux to be q_p over this distance.

For T_{x2} at the TS1 surface, unfortunately there was no measurement point next to it in the steel wall of the TS1; therefore the calculation was started from the known bulk temperature of the coolant T_0 which is slightly different for the positions in the different channels and was calculated by assuming a linear heat-up of the water on its way through the TS1. The first temperature step to the surface of the coolant channel wall T_{x1} is governed by the convective heat transfer coefficient α

$$T_{x1} - T_0 = q_p / \alpha$$

with $\alpha = 0.75 \text{ W}/(\text{cm}^2 \cdot \text{K})$ for the actual coolant velocity of 1.17 m/s. The second temperature step to the TS1 surface above the coolant channel is governed by heat conduction through the steel wall

$$T_{x2} - T_{x1} = q_p \cdot s / \lambda_{ss}$$

with $\lambda_{ss} = 0.17 \text{ W}/(\text{cm}^2 \cdot \text{K})$ and $s = 0.5 \text{ cm}$, assumed as thickness of the wall between the coolant channel and the surface (though parts of the wall are thicker, FE modelling confirmed this to be a reasonable 1-dimensional approach since in reality the heat flux is locally reduced by parts that are deviated to the sides and back of the coolant channel surface). Any temperature drop across the plasma-sprayed layer of $\text{Al}_2\text{O}_3 + \text{TiO}_2$ on the surface of the TS1 was not taken into consideration and thus would be included in the temperature drop at the CL.

As a result T_{x2} may be calculated from

$$T_{x2} = T_0 + q_p (1/\alpha + s/\lambda_{ss}) = T_0 + 4.27 q_p$$

For T_{x3} the local temperature measurement T_{x4} in the tile, only $s = 3 \text{ mm}$ away from the surface, could be used as a reference point. The temperature step to the rear surface of the tile is governed by heat conduction in the tile

$$T_{x4} - T_{x3} = q_p \cdot s / \lambda_t$$

with the heat conductivity of the CFC assumed to be $\lambda_t = 0.35 \text{ W}/(\text{cm} \cdot \text{K})$ and $s = 0.3 \text{ cm}$ (it was found later that λ_t could be as high as $0.5 \text{ W}/(\text{cm} \cdot \text{K})$ depending on temperature but the initial assumption was kept for simplicity since its influence on the evaluated temperatures is very small). From this T_{x3} may be calculated as

$$T_{x3} = T_{x4} - q_p \cdot s / \lambda_{ts} = T_{x4} - 0.857 \cdot q_p$$

In summary the temperature difference ΔT_{CL} across the compliant layer (including the two contacts) is calculated for the stripe from

$$\Delta T_{CL} = T_{x3} - T_{x2} = T_{x4} - T_0 - 5.13 q_p$$

in which T_{x4} , T_0 and q_p are quantities that were measured or determined before.

Heat transmittance h' :

With the local heat flux q_p through the CL and the individual temperature differences ΔT_{CL} across the CL, both as evaluated above, the heat transmittance h' may be calculated for each CL stripe, close to which a temperature of type T_{x4} was measured, as

$$h' = \frac{q_p}{\Delta T_{CL}}$$

Temperature profile across the specimen:

With the measured data and some evaluation a temperature profile across the specimen parallel to the heat flux could be constructed. It gives an impression where the major thermal resistances are located.

T_0 , T_{x4} and T_{x5} are measured quantities. A few more temperatures may be calculated on the basis of the local heat fluxes attributed to the areas:

- the temperature T_{x1} at the coolant channel wall and the temperature T_{x2} at the surface of the TS1

$$T_{x1} = T_0 + q_p / \alpha$$

$$T_{x2} = T_0 + q_p \cdot (1/\alpha + s/\lambda_{ss})$$

with the heat transfer coefficient $\alpha = 0.75 \text{ W}/(\text{cm}^2 \cdot \text{K})$, the TS1 wall thickness beneath the CL $s = 0.5 \text{ cm}$, and the thermal conductivity of stainless steel $\lambda_{ss} = 0.17 \text{ W}/(\text{cm} \cdot \text{K})$

- the temperatures T_{x3} at the rear and T_{x6} at the front surfaces of the tile

$$T_{x3} = T_{x4} - q_p \cdot s / \lambda_t$$

$$T_{x6} = T_{x5} + q_p \cdot s / \lambda_t$$

with the distances in the tile $s = 0.3 \text{ cm}$ and the thermal conductivity of the tile $\lambda_t = 0.35 \text{ W}/(\text{cm} \cdot \text{K})$.

Thermal Conductivity of the Tile λ_t :

With the limited possibilities of this test it was tried to evaluate the thermal conductivity of the CFC material of the tile.

There is a number of TC pairs in the tiles each with a distance $a_1 = 14 \text{ mm}$ between its TCs in test L2. The evaluation would be straight forward if the local heat flux would be constant between the two TC positions. This is not the case: the heat flux may be assumed uniform when it enters the surface of the tile but it is funnelled towards the contact areas of the CL stripes as it proceeds through the tile. Therefore the average heat

flux effective between the TC positions is not known. Instead the average driving temperature difference between the measurement planes was determined for a symmetry half of the tile from the limited temperature information available and was related to the average heat flux entering the tile. From test L2 three pairs of temperature readings are known: ΔT from (197)/(198) at the center line of the tile and rather far away from a CL stripe and ΔT s from (195)/(196) and (199)/(200) both above one of the CL stripes. These three ΔT s were used as benchmarks to construct a reasonable ΔT -distribution over the width of half a tile. This ΔT -distribution was integrated graphically which resulted in an average ΔT_{av} between the two measuring planes for the whole tile. From this a heat conductivity λ_{t1} was determined as

$$\lambda_{t1} = q_z \cdot a_1 / \Delta T_{av}$$

with $a_1 = 14$ mm. For different power (i. e. temperature) levels the evaluation resulted in λ_{t1} between 0.34 and 0.40 W/(cm·K).

In a second approach the large number of TC pairs in tests L3 through L6 in a distance $a_2 = 4$ mm were used. Here it was assumed that the heat flux q_p through the CL could be applied to the tile area between the TCs; the temperature difference ΔT between the TCs was used directly to determine

$$\lambda_{t2} = q_p \cdot a_2 / \Delta T$$

This procedure resulted in values for λ_{t2} between 0.35 and 0.55 at tile temperatures of roughly 900 °C. The results from some of the TC pairs were systematically higher than for others which points at differences in the relative narrow spacings of the TCs. The actual heat flux between the TCs is probably smaller than q_p since between the TCs an area in the tile that is wider than the CL stripe would participate in the heat conduction; therefore the λ_{t2} -values are probably too high.

In summary the thermal conductivity of $\lambda_t = 0.35$ W/(cm·K) assumed for the test evaluation might be a little low but seems acceptable.

6.4 Experimental Results

For the compliant layer (CL) between the tiles and the TS1 the heat transmittances h' will be reported as they were evaluated from the measured data. In addition an attempt will be made to distinguish within the transmittance between contributions from the thermal conductivity of the CL itself and from the two contact heat transfers; also an overview on the temperatures across the whole structure will be given.

6.4.1 Heat Transmittance

It is distinguished between different transmittance paths, each of them through one of the CL stripes; their designation is given in Fig. 6.7 for the upper and lower tile. With the exception of u1 in the test group L2 the transmittance h' was determined for each of the paths.

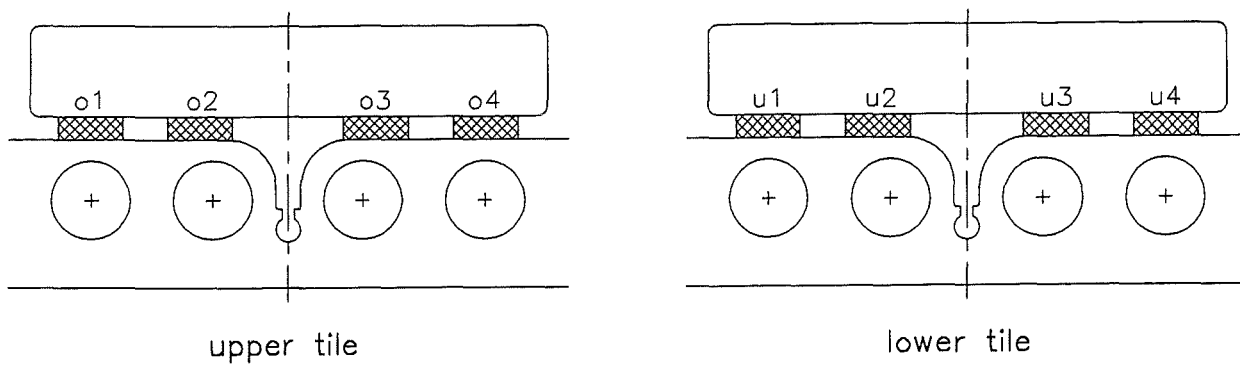


Fig. 6.7 Designation of indices to CL transmittances h' on the different paths

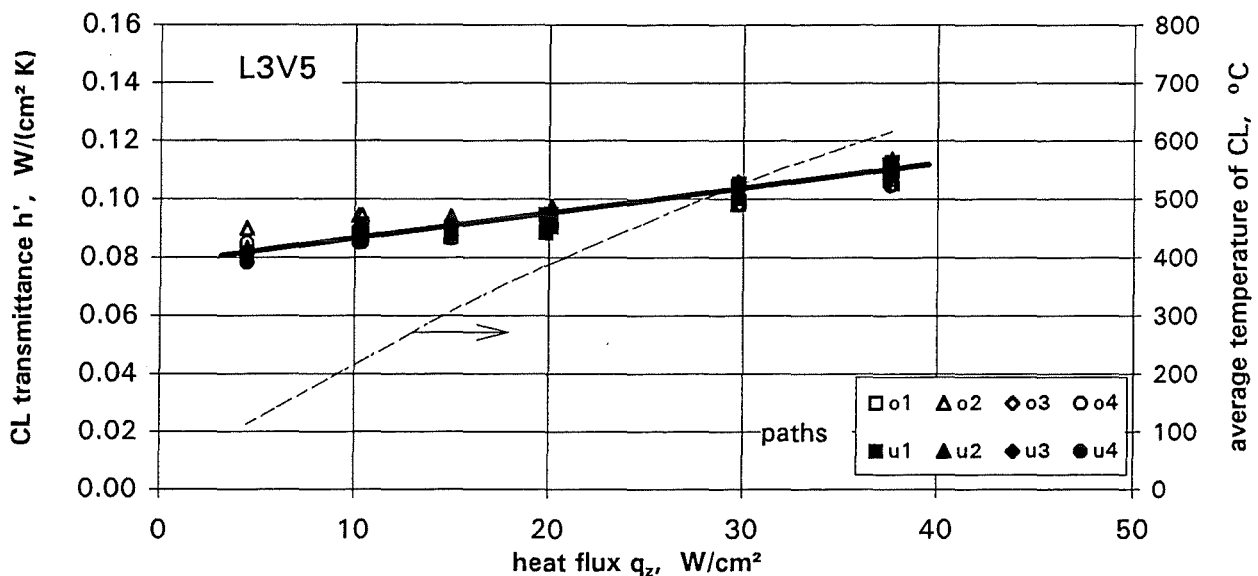


Fig. 6.8 Heat transmittance and average temperature at the CL; data for all eight paths and for all test situations (increasing and decreasing heat flux) of test group L3V5 are included

Figure 6.8 shows the results from test group L3. For steady-state conditions h' is plotted as a function of the heat flux q_z into the tile. All points measured in this group are included in the graph, i. e. the whole test sequence including stepwise increasing and decreasing heat fluxes (see Table 6.2) is covered. As general results, valid also for all other test groups, the figure reveals:

- h' increases with increasing q_z ; this is attributed to the temperature level at the CL (radiative heat transfer either in the CL or at the contacts). The average temperature of the CL is plotted as a dashed line for comparison. The change in h' is not attributed to any changes of the CL contact pressure, as will be discussed later.
- All points are grouped together in a relatively narrow band though they cover eight different paths through a CL, two different tiles, and the whole history of the test group starting with freshly mounted CL stripes at low q_z and ending again with low q_z after the test was run up to high q_z and back down.
- It appears that the differences in transmittance between the different paths are very small which is taken as an important result of the investigation. A closer look on a magnified plot (not shown here) reveals that for some paths h' tends to run high

within the band and for some paths it tends to run low; since this is true for the same paths also in the other test groups this trend is attributed to an inaccurate positioning of the TCs rather than to real differences in the heat transfer characteristics.

- There was obviously no or only very little change in h' after the CL was exposed to its heat flux history throughout the test group, as will be discussed later in more detail. At a first glance this seems surprising since one could expect h' to be smaller after a period of service at high CL temperature which due to CL creep should have relaxed the contact pressure.

In order to give the full information without overloading the body of the report the complete set of plots with $h' = f(q_z)$ for all test groups is shown in Appendix B. There, the data of each group are fitted by a line, which will be used for further discussion.

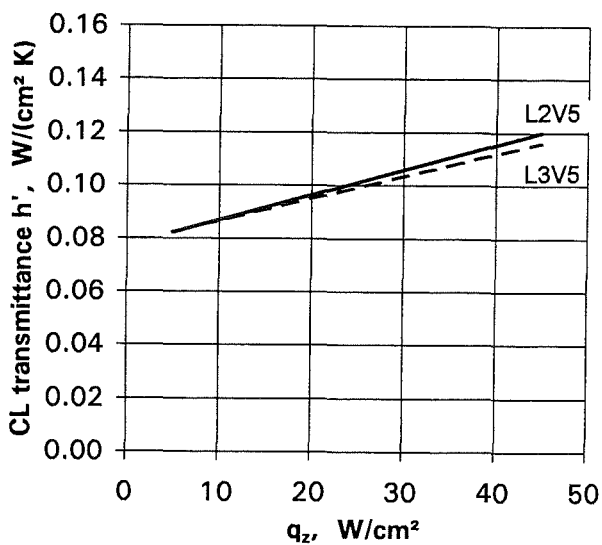


Fig. 6.9 Reproducibility of results in test setups with two different TC instrumentations

Fig. 6.9 compares the results of two test groups which were run with the same test parameters but with different TC instrumentation and each one with freshly mounted CL stripes. The figure shows a very good reproducibility. Since the figure represents the results for the NET design of the CL for a conductively cooled tile it should be noted that the heat transmittance at the CL would be on the order of $h' = 0.1 \text{ W}/(\text{cm}^2 \cdot \text{K})$ for a heat flux into the surface of the tile of $q_z = 30 \text{ W}/\text{cm}^2$ (or through the CL stripe of $q_p = 55 \text{ W}/\text{cm}^2$).

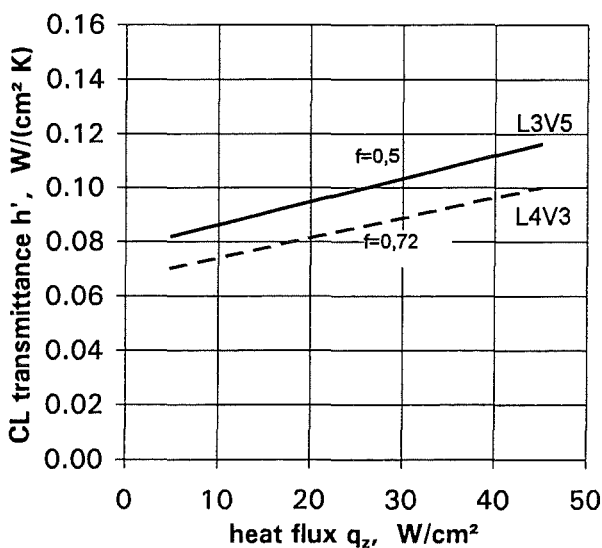


Fig. 6.10 Lower transmittance h' for a coverage of $f=0,72$ at constant tile mounting force (reduced initial contact pressure)

Fig. 6.10 shows that h' would be about 15 % lower if the CL coverage would be increased from $f=0,5$ to $f=0,72$ at keeping the tile attachment force the same and thus reducing the CL contact pressure at mounting from $p=5$ to $p=3,35$ bar. It should be noted that under these circumstances the tile temperatures would be lower, as will be shown in Fig. 6.21; the larger contact area overcompensates the loss in h' .

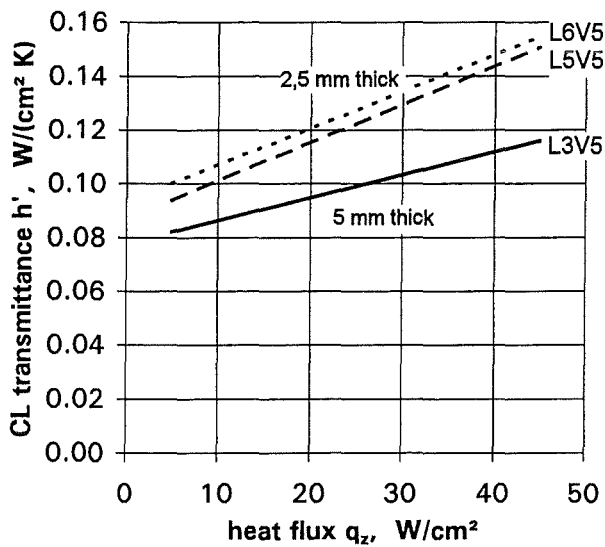


Fig. 6.11 Influence of CL material thickness and grade on transmittance h' (coverage $f=0,5$ and contact pressure $p=5$ bar)

Fig. 6.11 reveals that it would increase h' by 25 to 30 % if one would make the CL only 2.5 mm rather than 5 mm thick in test groups L5 and L6. The reason should be that the thermal resistance in the conducting CL would be reduced; it is interesting to note that the thinner CL with its lower deformability did not cause any contact problems even after some service time at elevated temperatures (compare Fig. C1 parts L5V5 and L6V5 which shows an even improved h' after service at elevated temperatures). The above statements are true for papyex (L6V5) as well as Sigraflex (L5V5) as compliant layer. Since Sigraflex had a much higher density this again points out that the flexibility of the CL was not the limiting parameter for h' , provided that the contact pressure at mounting is sufficiently high and the contact surfaces are smooth and plane enough to cause initial nestling with the CL.

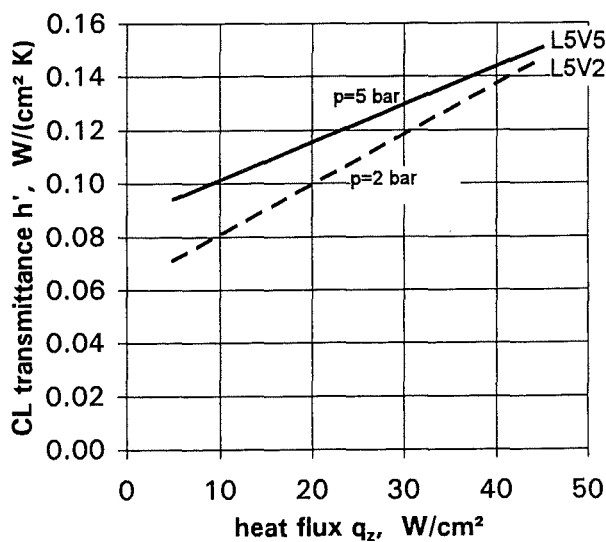


Fig. 6.12 Influence of initial contact pressure p on transmittance h' for $p=2$ and $p=5$ bar on 2,4 mm thick Sigraflex as CL

The influence of the initial contact pressure on h' is demonstrated in Figs. 6.12 and 6.13 for 2.4 mm thick Sigraflex and 2.5 mm thick Papyex, respectively. For both materials h' was increased when, after a first test series with a contact pressure of $p=2$ bar, p was increased to 5 bar. No influence of a heat load history was found. Trying to explain the differences between Sigraflex and Papyex curves is a little speculative: the little higher h' for Sigraflex at 2 bar could be due to the higher density and thermal conductivity of the material; the little higher h' for the Papyex at 5 bar could be due to a better nestling of the softer material which overcompensated its poorer conductivity.

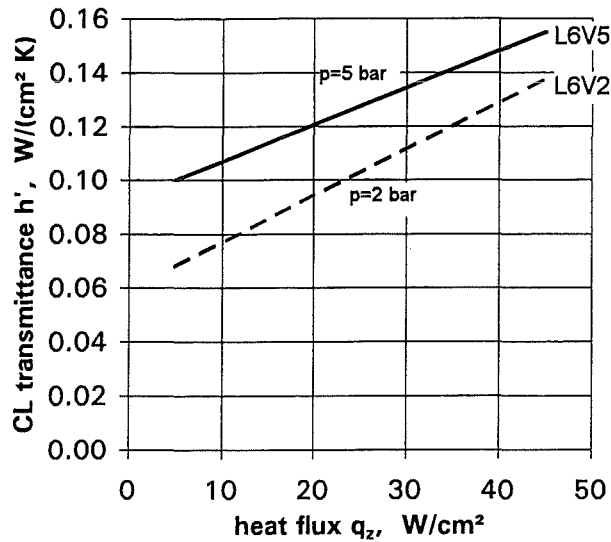


Fig. 6.13 Influence of initial contact pressure p on transmittance h' for $p=2$ and $p=5$ bar on 2,5 mm thick Papyex as CL

Figure 6.14 offers an answer to the question whether the CL transmittance h' deteriorates as a result of thermal load cycles. In test group L2V5 the thermal load was increased to $q_z=30$ W/cm². After 125 load cycles were run on this level the load was stepwise decreased to zero and again increased to a higher value of 38 W/cm². After another 125 load cycles the load was finally decreased to zero. At the hold points during the increasing and decreasing procedure and also before and after the cycling periods data were logged under steady-state conditions; the evaluated transmittances h' are plotted in Fig. 6.14 for path u4. No influence of the cycling on h' can be found. It seems that neither the cyclic load with its related geometric changes nor the elevated temperature with its potential to change the CL material characteristics did change the h' which was measured the same at the beginning and the end of the test group. It is important to note that h' stayed unaffected even though the contact pressure was found to be strongly reduced at the end of a test as will be reported in Chapter 6.4.4.

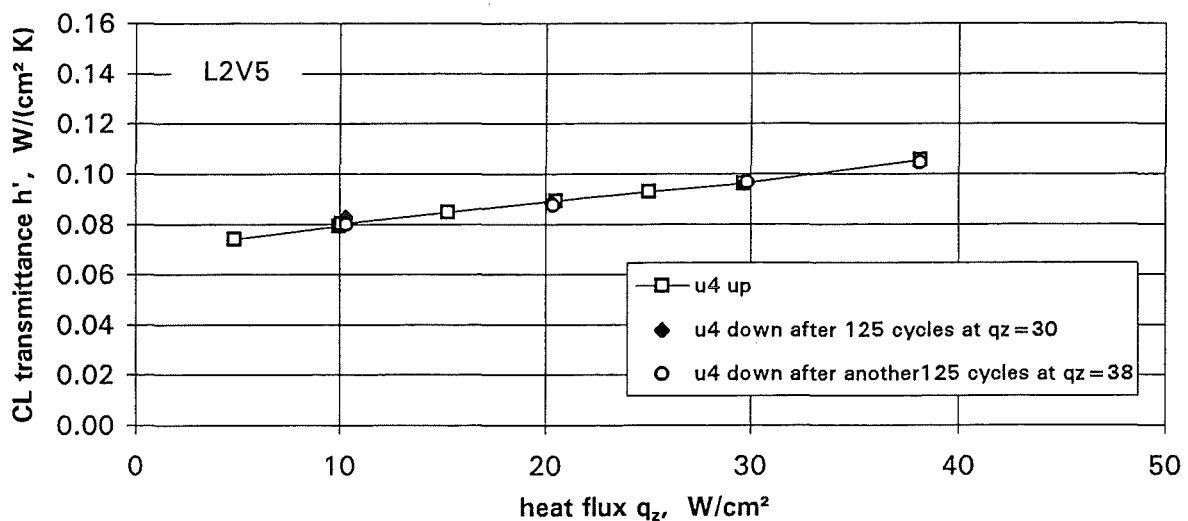


Fig. 6.14 No influence of 250 load cycles on the transmittance h'

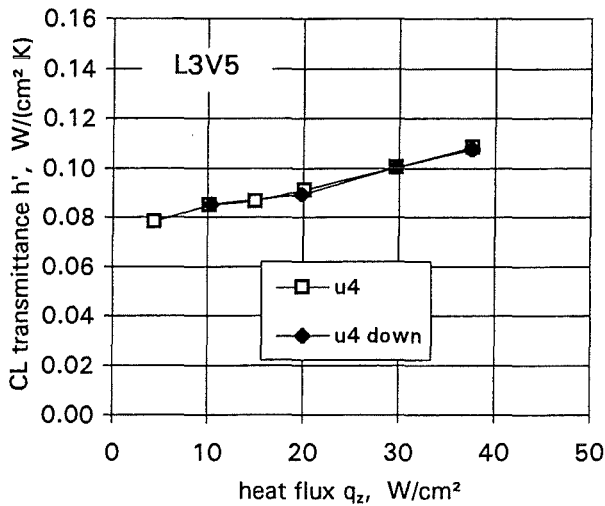


Fig. 6.15 No influence of test history on h'

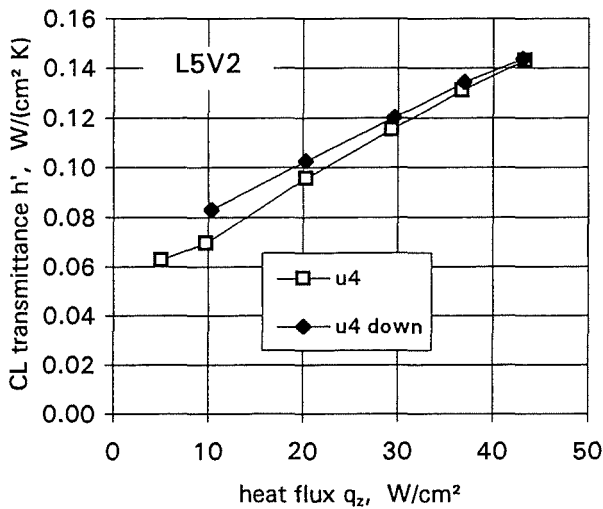


Fig. 6.16 Improved nestling during the test

Test L3V5, a repetition of L2V5 but without load cycles, nevertheless shows the same behavior as may be seen from Fig. 6.15. Both tests were performed with 5 mm thick CL stripes and started with 5 bar initial contact pressure. Obviously there was sufficient initial nestling that has not been improved during the test phase at elevated temperatures.

A slightly different behavior was found in the remainder of the tests with thinner CL and/or lower initial contact pressure. An example is test L5V2 which was performed with 2.4 mm thick stripes of the stiffer Sigraflex material and with an initial contact pressure of 2 bar. It seems from Fig. 6.16 that the contact resistances were reduced during the test such that h' was found slightly higher at the end of the test. A set of figures covering this behavior for all test groups is presented in Appendix C, Fig. C1. It is interesting to note that in test group L6V5 which included 153 load cycles at the highest heat flux a little improvement of h' was found after the cycles. It seems that for a thin CL layer cycling on a high temperature level could help to improve the contact but there is no indication that cycling could deteriorate h' .

6.4.2 Break-up of Transmittance into Conduction and Contact Heat Transfer

In test group L3 and L6 the CL thicknesses were 5 mm and 2.5 mm, respectively, with all other test parameters kept constant. This offers a chance to distinguish within the measured heat transmittances between the conductances λ/s in the CL itself and the heat transfer coefficients α' at each of the contacts on the faces of the CL.

Necessary assumptions would be that α' was the same on both faces of the CL and that α' and λ are the same in tests L3 and L6. These assumptions may be somewhat questionable since the partner surfaces to the CL were on one side a smooth tile and on the other side

a much rougher plasma-sprayed TS1; it is not known whether nestling at 5 bar could cause the same contacts on both sides; also the machined surface of the 2.5 mm thick CL may have behaved different than the surface of the original Papyex. Therefore and because of the uncertainties mentioned in Chapter 6.2 the quantities reported below should be taken as a rough estimate. Nevertheless they give an idea how the total thermal resistance at the CL may approximately be broken up into the resistances in the CL and at the contacts.

The thermal resistances sum up as

$$R = R_{CL} + 2R_C$$

where the indices CL and C stand for compliant layer and contact, respectively. With the corresponding conductances one may write

$$\frac{1}{h'_1} = \frac{s_1}{\lambda} + 2\alpha' \quad (1) \quad \text{and} \quad \frac{1}{h'_2} = \frac{s_2}{\lambda} + 2\alpha' \quad (2)$$

in which the indices 1 and 2 stand for the tests L3 and L6 with $s_1 = 5 \text{ mm}$ and $s_2 = 2.5 \text{ mm}$, respectively. From eqs. (1) and (2) the two unknowns λ and α' may be found as

$$\lambda = \frac{h'_1}{4(1 - h'_1/h'_2)} \quad (3) \quad \text{and} \quad \alpha' = \frac{h'_1}{h'_1/h'_2 - 0.5} \quad (4)$$

The above equations were applied to the results h' of tests from groups L3 and L6. Figure 6.17 shows the resulting thermal conductivity λ of the CL (special order Papyex); for clearness' sake it is again plotted as a function of the heat flux q_z to the tile and the corresponding average CL temperature is also included as a curve. If one discards the low heat flux data because the evaluation method causes large data scatter for h'_1/h'_2 close to 1, the figure reveals λ to be on the order of $0.12 \text{ W}/(\text{cm}\cdot\text{K})$ which is close to (a little higher than) the values reported elsewhere for exfoliated graphite in the direction normal to its main dimensions; a temperature dependence cannot be recognized.

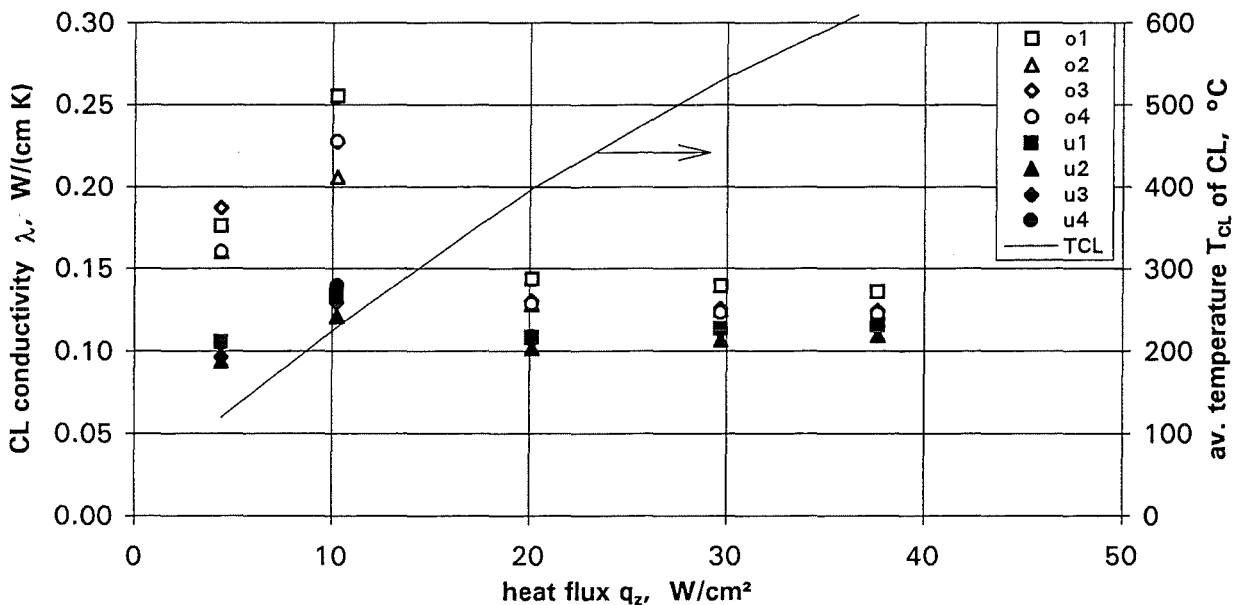


Fig. 6.17 Thermal conductivity for special order Papyex as determined from the transmittances for two different CL thicknesses

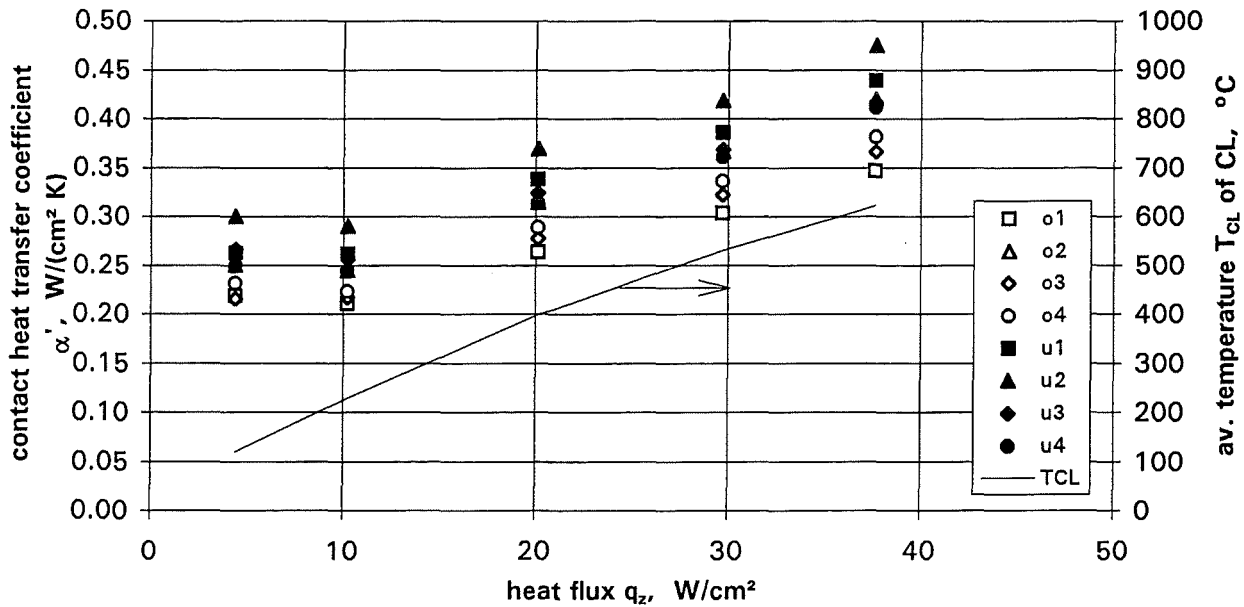


Fig. 6.18 Contact heat transfer coefficient at the CL as determined from the transmittances for two different CL thicknesses

Figure 6.18 shows the heat transfer coefficient α' at the contact as it results from eq. (4); it is again plotted versus q_z and the CL temperature is added as a curve. α' is on the order of 0.35 W/(cm²·K) and it seems to increase with the temperature level which could be attributed to some radiation which might be involved in the heat transfer.

Without overrating the precision of the results one may roughly distinguish between the three thermal resistances involved in the heat transfer at the CL as

$$R_{C_1} = 1/\alpha' \approx 2.9 \text{ K/(W/cm}^2\text{)} \quad \text{at contact 1}$$

$$R_{CL} = s/\lambda \approx 4.2 \text{ K/(W/cm}^2\text{)} \quad \text{through 5 mm thick CL}$$

$$R_{C_2} = 1/\alpha' \approx 2.9 \text{ K/(W/cm}^2\text{)} \quad \text{at contact 2}$$

The above numbers indicate that for the 5 mm thick CL about 58 % of the total temperature drop should be expected to happen at the two contacts; for the 2.5 mm thick CL this fraction would be 73 % and for smaller thicknesses it should become absolutely dominating since not only R_{CL} decreases but also R_C should increase due to poorer CL deformability and nestling. It should be repeated that the above numbers were gained as a rough estimate and from tests with a contact pressure of 5 bar and with the roughness present at the surface of the TS1. In order to avoid a misunderstanding it should be pointed out that the reported heat flux q_z represents the heat flux to the surface of the tile and that the local heat flux q_p effective at the heat transfer of the CL stripes covering only one half of the surface is almost twice as high (see Chapter 6.3.3).

6.4.3 Temperatures in the Structure

The temperatures are a good vehicle to get a clear overview on the behavior of the structure and on the transient performance of the test.

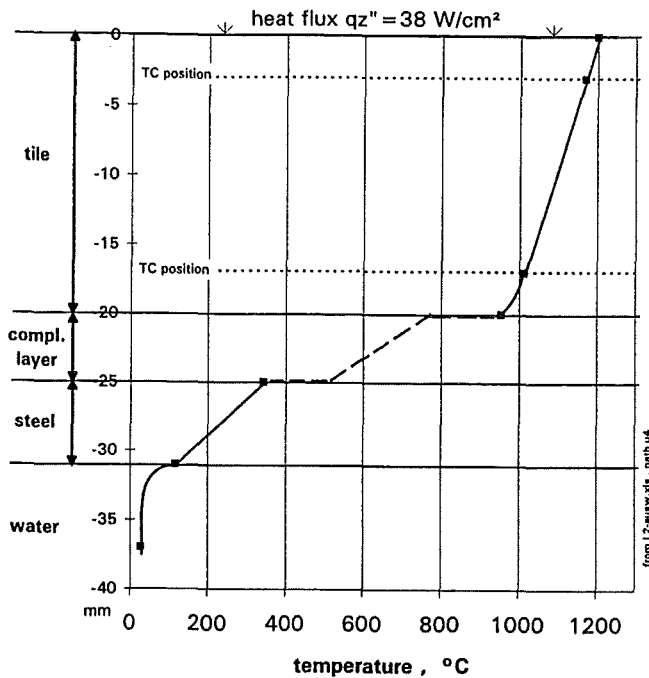


Fig. 6.19 Temperature profile across the first wall on path u4 of test L2V5 at $q_z = 38 \text{ W/cm}^2$

The radial temperature profile through the first wall starts with the highest temperature at the surface of the tile, crosses the tile, the CL, and the steel wall, and leads into the coolant channel. Figure 6.19 presents an example of such a profile as it was determined from test L2V5 at a heat flux $q_z = 38 \text{ W/cm}^2$ to the surface of the tile. The determination of the profile is based on two temperatures measured in the tile with TC199 and TC200 and on the bulk water temperature in the coolant channel; for details see Chapter 6.3.3. The figure shows that the tile surface temperature is at $1200 \text{ }^\circ\text{C}$. The temperature drop across the tile is 250 K . The temperature drop across the CL is 640 K in total and was subdivided following the somewhat speculative consideration in the preceding chapter into 178 K at each of the contacts and 193 K in the bulk of the CL material; the average temperature in the CL is $635 \text{ }^\circ\text{C}$. The remaining temperature drops in the steel wall (depending on the local wall thickness) and at the coolant heat transfer are 200 K and 90 K , respectively. In this example the temperature drop at the CL amounts to almost 60% of the total across the first wall but the CL certainly decreases the tile temperature from where it would be at a radiatively cooled tile without the CL.

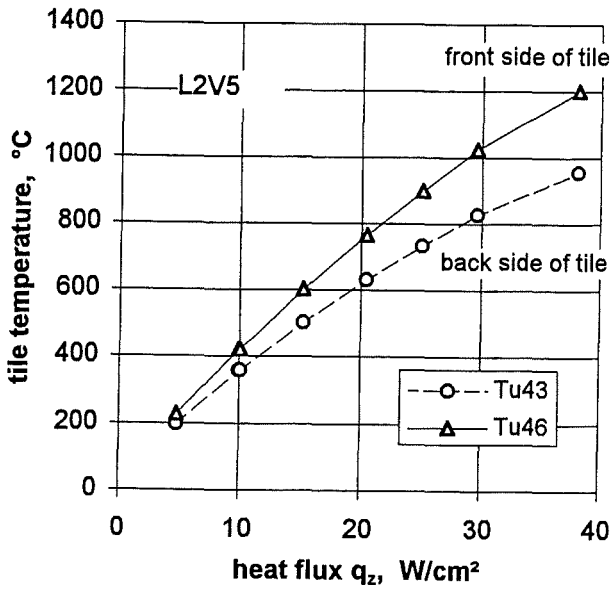


Fig. 6.20 Temperatures at the front and back side surfaces of the tile as calculated from the TC locations

Figure 6.20 shows how the temperature at the front and back sides of the tile and their difference change with the heat flux q_z to the surface of the tile in test group L2V5. For temperature-independent heat transport mechanisms one would expect a linear curve but in the case of CL stripes the fraction of the power that is transferred radiatively through the gaps between the stripes increases with the temperature at the back side of the tile.

When a larger fraction ($f=0.72$) of the tile's surface was covered with the CL in test group L4V3 the tile temperatures were lower than for stripes with $f=0.5$; this is shown in Fig. 6.21 by comparing the temperatures at the tile's back side from tests of the groups L4 and L3. The curves do not seem too surprising since one should expect lower tile temperatures as a result of the larger contact area. But considering the reduced heat transmittance h' shown in Fig. 6.10 for $f=0.72$ the present figure reveals that there are two counter-current effects of increased CL coverage: a lower h' and a larger effective area, of which the latter has a stronger effect on the temperature of the tile. One should remember that a smaller contact pressure went along with the larger coverage (same attachment force) in test group L4; if there was a possibility to increase the contact pressure for $f=0.72$ to 5 bar the solid curve in Fig. 6.21 would probably be shifted further down, even if this increased pressure would be applied only during the mounting (nestling) process.

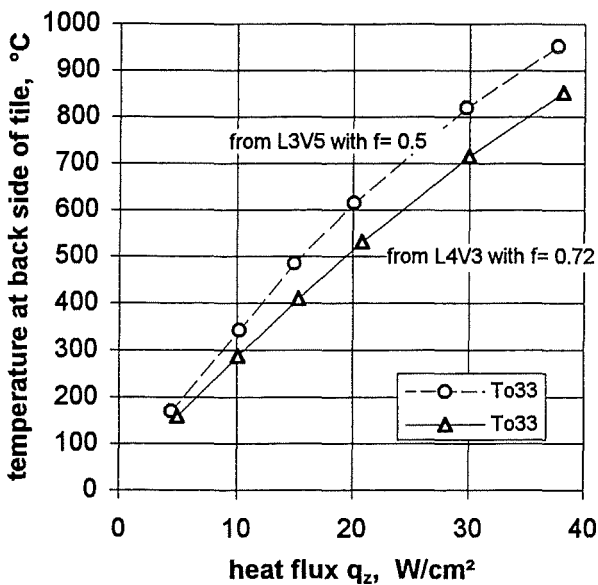


Fig. 6.21 Temperature at the back side of the tile for two different CL coverages f

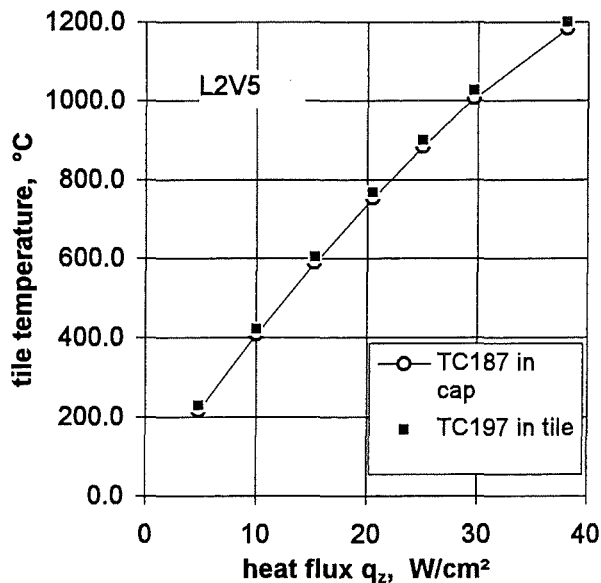


Fig. 6.22 Temperatures in the tile's cap and in the tile itself

There was a question whether the CFC cap in the center of the tile, which covers the nut of the attachment stud, would overheat because of an insufficient thermal contact at the thread between the cap and the tile. Therefore the temperature in the center of the cap was measured 4 mm below the heated surface. This temperature from TC187 is compared to a temperature (TC197) that was measured 3 mm below the heated surface of the tile itself in test group L2. Figure 6.22 shows that there is almost no difference in temperature. This result still holds if one considers that the 1 mm difference in TC depth would shift the curve for the cap by 12 K upwards.

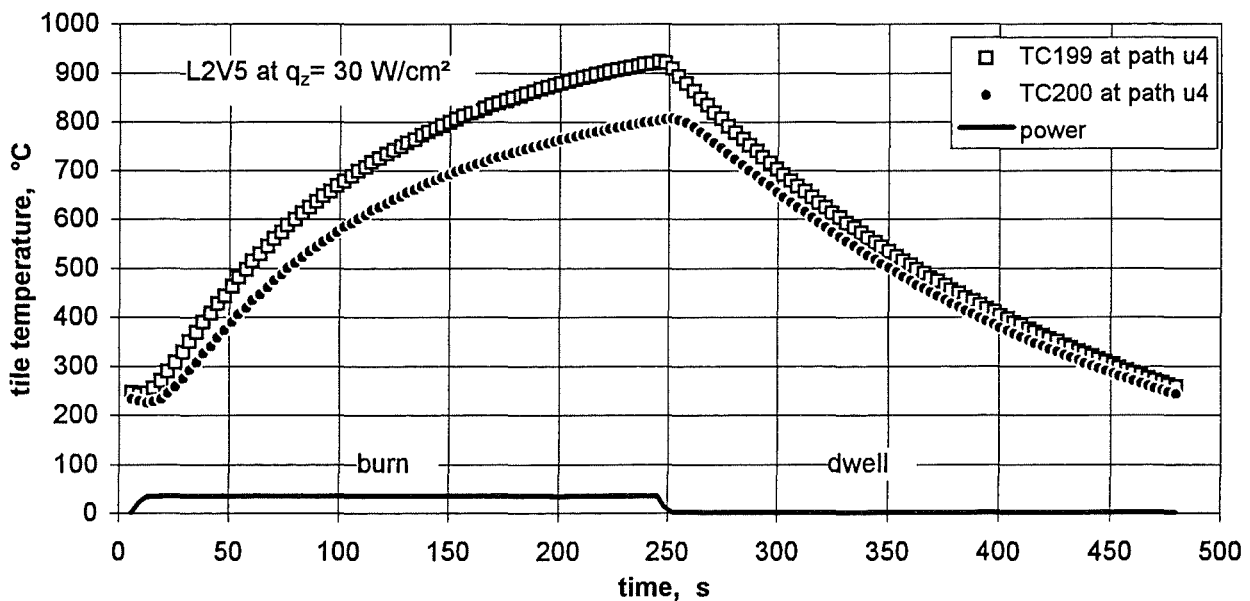


Fig. 6.23 Transient behavior of the measured tile temperatures during one power cycle

Finally some transient temperature information logged during load cycles in test group L2 at a heat flux to the tile of $q_z=30 \text{ W/cm}^2$ will be given. Figure 6.23 shows two temperatures that were measured in the tile 3 mm away from the front and back surfaces, respectively, as they changed during one full load cycle. During the power-on phase (burn) of 4 minutes the front surface of the tile heated up on the order of 700 K and ended not far away from a steady-state condition. The power-off phase (dwell) of another 4 minutes was just long enough to cool the tile down to about 250 °C. The automatic repetition of the load cycles with the related temperatures was very reliable as

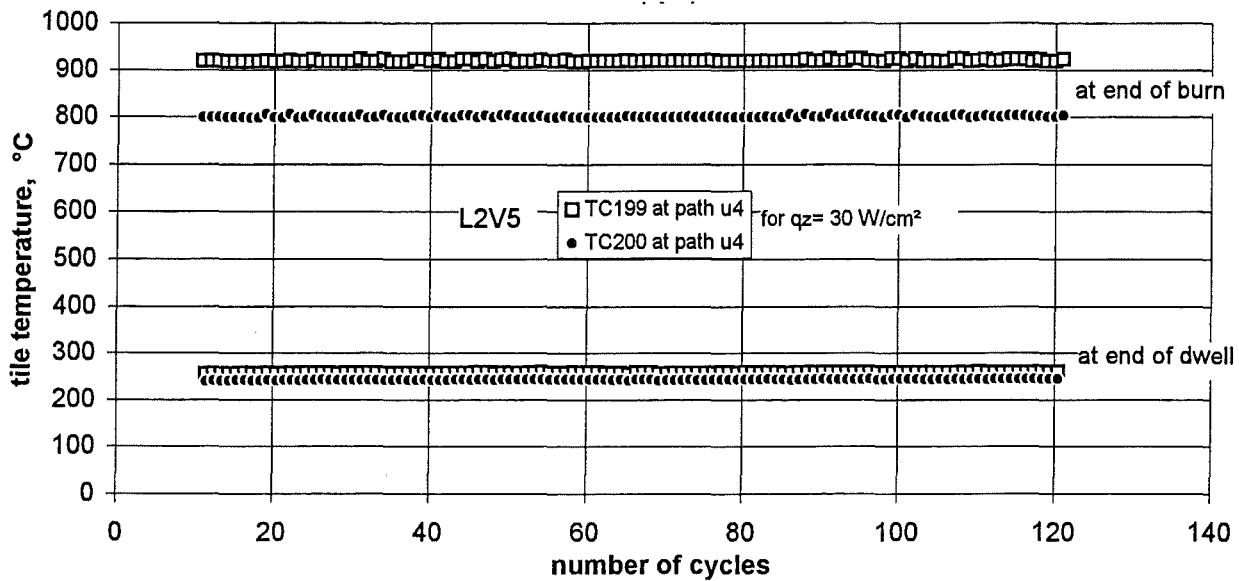


Fig. 6.24 Tile temperatures are correctly reproduced during 125 load cycles (17 hours)

shown in Fig. 6.24 where the two temperatures from Fig. 6.23 are plotted again, but with only two data points each per load cycle. One data point was logged shortly before the end of the burn phase (the two upper strings) and one data point was logged shortly before the end of the dwell phase of each cycle. It took about 17 hours to run the 125 load cycles, the majority of which is shown in the figure; there was obviously no change in test conditions and there was also no change in CL heat transmittance during that time as discussed in Fig. 6.14.

6.4.4 Behavior of the Compliant Layer

Before the test it was expected that the CL would be deformed permanently (become densified) under the influence of pressure and temperature during the test; as a consequence the contact pressure at the CL should become reduced. It was also expected that a reduced contact pressure could cause a reduced heat transmittance. In order to be prepared for such a test result two measures were taken: (1) the elastic and plastic deformation under mechanical load and at elevated temperatures were determined in separate CL characterization tests, the main results of which are reported in Appendix D, and (2) after the end of each group of heat transmittance tests the remaining contact pressure was measured at room temperature before demounting the tile.

The latter was done by looking with a torque wrench for the minimum torque necessary to move the nut of the attachment stud. It was found from test groups L3V5 and L6V5 that an initial contact pressure of 5 bar was reduced to roughly 1.5 bar after the CL had experienced a maximum temperature of about 750 °C and an average temperature of 650 °C during the tests at $q_z = 38 \text{ W/cm}^2$.

It is known from Chapter 6.4.1 that this reduction in contact pressure in fact did not influence the heat transmittance h' . Nevertheless it seemed interesting to try whether the reduction in contact pressure could be understood from a deformation of the CL point of view. This attempt will be performed for the test group L3V5 with 5 mm thick Papyex as CL since this material had been used for the separate CL characterization tests.

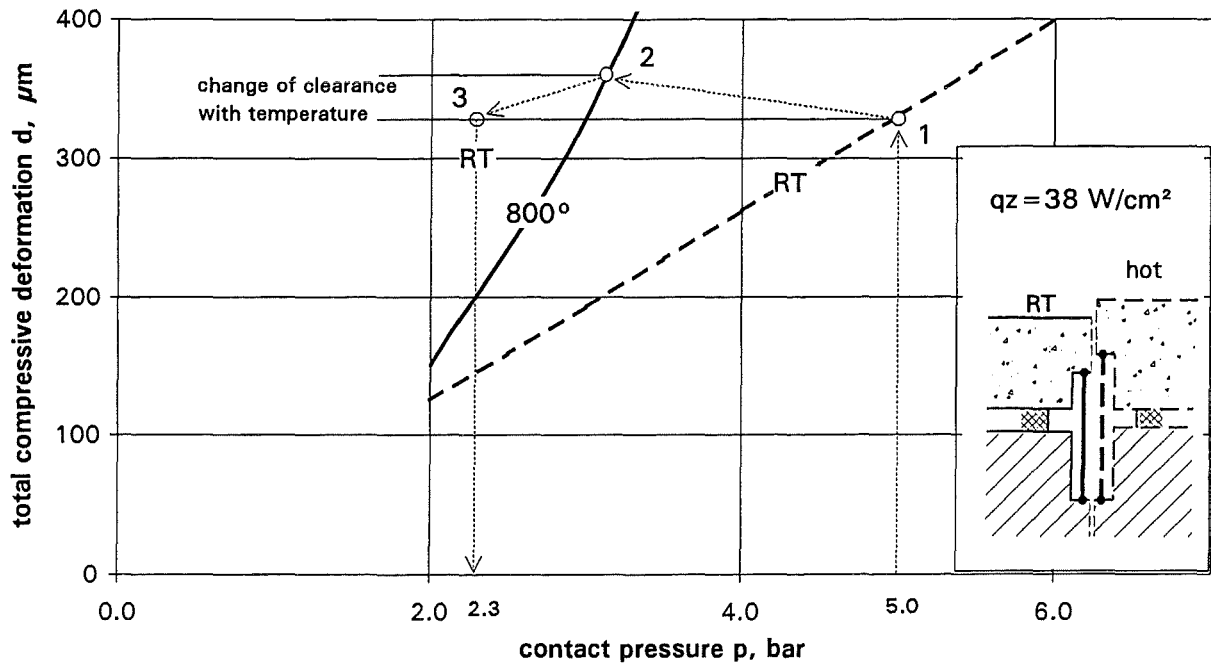


Fig. 6.25 Change of contact pressure under thermal load

The total compressive deformation d as a function of the contact pressure p from Fig. D.2 is replotted in Fig. 6.25 for room temperature and 800°C as dashed and solid curves, respectively. The tile mounted at room temperature applies a contact pressure of 5 bar to the CL and according to the RT curve in Fig. 6.25 it compresses the CL by $330 \mu\text{m}$. Heating up the specimen to temperatures corresponding to $q_z = 38 \text{ W/cm}^2$ will have two consequences:

- (a) The heat-up will narrow the clearance between the tile and the TS1 from the initial 5 mm by about $30 \mu\text{m}$; this is the result of the thermal expansions of the three partners involved. The TZM attachment stud expands but the CFC tile and the SS of the TS1 do also and to larger extent. Since the stud is fixed not at the surfaces but in the depth of its partners they are able to overcompensate the growth of the stud; the sketch inserted in the figure is to illustrate this situation. Narrowing the clearance between tile and TS1 means compressing the CL by another $30 \mu\text{m}$ to a total of $360 \mu\text{m}$.
- (b) At the same time the heat-up of the CL material will change its characteristics from the RT curve to one for elevated temperature; for a maximum CL temperature of 750°C the 800°C curve is used in Fig. 6.25 since it was available. Physically this means that at elevated temperature the permanent deformation of the CL takes over a larger fraction of the total deformation within the given clearance, which results in a reduction of the contact pressure.

As a result of consequences (a) and (b) one proceeds from point 1 to point 2 in the figures; accordingly the contact pressure for the situation at elevated temperature was about 3.1 bar as compared to the original 5 bar. Cooling the structure back to room temperature will inverse the change in clearance from (a) such that the CL can expand elastically into the additional $30 \mu\text{m}$ of gap offered to it. In Fig. 6.25 it would do so with a slope according to a Young's modulus for the CL of about 14 MPa (see Fig. D.3) which in Fig. 6.25 takes one from point 2 to point 3 and reduces the contact pressure by another

0.5 bar. The remaining contact pressure at RT that would be expected at demounting of the tile should be on the order of 2.3 bar.

In fact the measured contact pressure remaining after test group L3V5 was 1.5 bar. The agreement is not perfect but seems reasonable under the given conditions; it confirms the order of magnitude of the measured reduction in contact pressure.

Yet the most important result of this consideration is that an implication between the reduced contact pressure and the heat transmittance at the CL does not exist, as reported in Chapter 6.4.1. In order to underline this the data of Fig. 6.15 are repeated in Fig. 6.26.

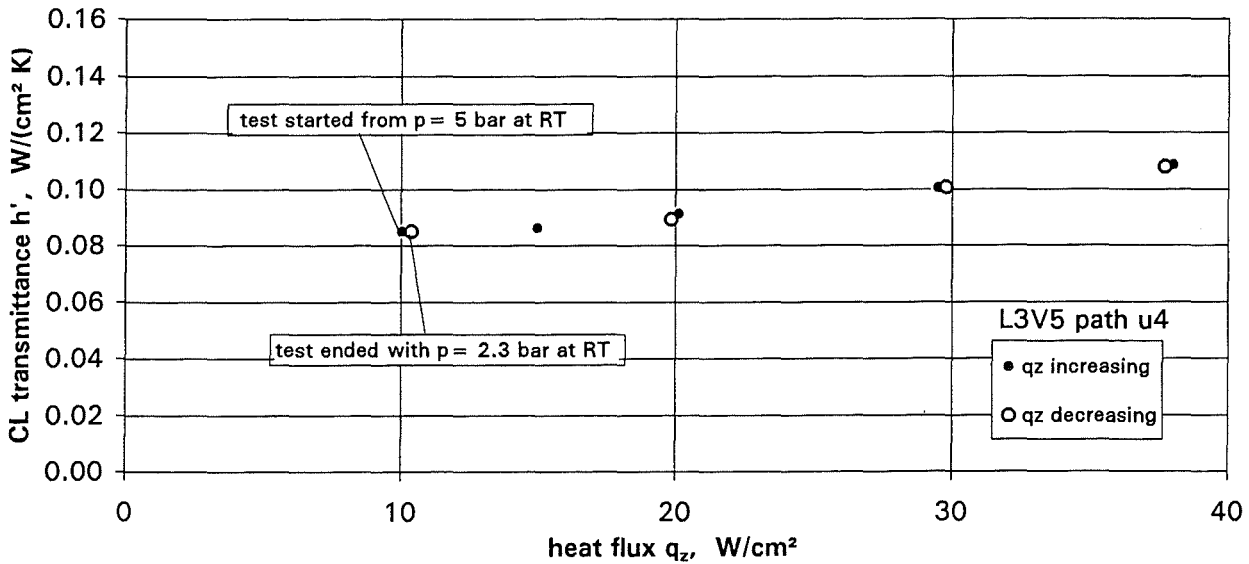


Fig. 6.26 No influence of change in contact pressure p on h'

It shows the thermal transmittance h' at path u4 of test group L3V5 as it changes with increasing and decreasing heat flux q_z and with the temperatures corresponding to q_z . The test was started from an initial contact pressure $p=5$ bar at RT. From the above discussion it should be expected that p decreased when q_z (and the temperature with it) was increased; solid symbols mark the data points gained during increasing q_z . The test does not allow to state whether h' would be the same if the contact pressure could have been kept constant at increasing q_z . But as q_z decreases one can be sure that the contact pressure was lower than on the increasing q_z route and nevertheless the h' data points (open symbols) are almost exactly the same as before indicating that in this range h' does not depend on p . This is true down to $q_z=10$ W/cm^2 corresponding to an average CL temperature of about 230 °C after which the contact pressure turned out to be reduced to 1.5 bar at RT. It seems that an initial contact pressure is important to cause a sufficiently close contact between the partner surfaces by locally deforming the CL made of flexible graphite (nestling). Once this nestling has been reached it is obviously sufficient to keep the surfaces in contact with a much lower pressure in order to maintain the same contact heat transfer.

6.5 Conclusions

A flexible compliant layer (CL) between the protection tile and the first wall was used in order to reduce the temperature of a conductively cooled tile as compared to that of a radiatively cooled tile. The CL consisted of 5 mm thick special order Papyex; 2.5 mm thickness was also tested. The heat transmittance through the CL including the two contacts was measured to be on the order of $h' = 0.1 \text{ W}/(\text{cm}^2\text{K})$. More than half of the thermal resistance through the CL was located at the two contacts together, which explains why a reduction of the CL thickness had only a limited effect on the heat transmittance. The heat transmittance was observed to be very uniform for each of eight paths located on two different tiles. No reduction in heat transmittance was found under thermal load, neither under steady-state nor under cyclic conditions; the heat transfer did not change during up to 250 thermal cycles. In contrary, a small improvement was found. In summary, the contact behavior appeared entirely unproblematic and no concerns about the thermal performance of the CL under load cycles seem necessary. The contact pressure at the CL was understood as an important parameter for the heat transmittance only in a sense that it is responsible for an initial close engagement (nestling) of the materials at the contact surfaces. Nestling can be reached at room temperature with a sufficiently high contact pressure during mounting of the tile. After initial nestling the thermal contact is kept even if the contact pressure is reduced. For practical applications the CL thickness and the contact pressure after mounting may be reduced such that they provide just enough elastic deformation of the CL for the geometrical and heat load conditions of a specific design.

A summary of Chapter 6 was published as a conference paper [7].

Acknowledgement

The work reported was performed and financially supported as NET-related task T9.2 within the European Fusion Technology Programme.

The authors want to thank E. Diegele, B. Schinke and C. Petersen of Institut für Materialforschung II for their valuable contributions during the course of the investigation. We appreciate the programme management and the helpful suggestions of G. Vieider and R. L. Shaw of the NET Team. We also thank F. Karge and I. Rössler for carefully typing this report.

References

- [1] A. Skokan and A. Salito; Heat Absorbing $\text{Al}_2\text{O}_3\text{-TiO}_2$ Coatings for a Tile-Protected First Wall; Proc. of the 17. Symp. on Fusion Techn., Rome, September 14-18, 1992, Vol. 1, p. 386-90
- [2] M. Merola; Evaluation of First Wall Thermal Fatigue Testing; Intermediate Report (Part 1) on contract ERB 5000 CT9400.46 NET, (NET 94-354)
- [3] G. Hofmann and E. Eggert; The First Wall Test Facility FIWATKA; KfK 5381 (Sept. 1994)
- [4] M. Merola, R. Matera, G. Vieider; Study on Thermal Fatigue Testing of a Prototypical First Wall Component; Fusion Engineering and Design 31 (1996), p. 245
- [5] Hibbit, Karlsson and Sorenson Inc.; ABAQUS User's Manual; Version 5.4 (1994)
- [6] E. Zolti; Material Data for Predesign Analysis of In-Vessel Components; NET Internal Note N/I/3300/5/A (Sept. 1990)
- [7] G. Hofmann et al.; Heat Flux Testing of Protection Tiles in front of a First Wall Mockup; Proc. of the 18. Symp. on Fusion Techn., Karlsruhe, August 22-26, 1994, Vol. 1, p. 379-82

Appendix A

Determination of the Heat Flux into the Conductively Cooled Tiles

Known is the power N_{TS1} transferred to the specimen TS1 as a whole. The conductively cooled tiles cover only part of the TS1 surface. The temperature and the emissivity of the tile's surface are different from those of the TS1 surface. Therefore the fractions of the total radiative power N_{TS1} that are absorbed by the surfaces of the tiles and the surface of the surrounding naked TS1 are governed not only by their relation of exposed areas.

To nevertheless be able to assign a fraction of N_{TS1} to the tiles and thereby determine the heat flux q_z into the tiles at least with a reasonable approximation the computer code QF-LT-ZI was written and applied. In order to qualify the procedure used in QF-LT-ZI and described below, the results for one example set of input data were compared to the results of a 2d FE model calculation and they were found reasonably accurate.

QF-LT-ZI is an essentially one-dimensional BASIC code that models, partly in parallel, four thermal paths that are present in the test setup and start from the heater. As shown in Fig. A1 path 1 enters the tile and is subdivided in two parallel branches, branch 1a that crosses the CL and runs into the heat sink TS1 and branch 1b which covers the radiation across the gaps between the CL stripes and also runs into the TS1. Path 3 covers the radiation from the heater to the naked portion of the TS1. To the right paths 2 and 4 cover the radiation to the radiation shield and further to the dummy heat sink behind it for both the areas which are tile-covered and naked on the left; paths 2 and 4 are modelled separately because of slightly different heater temperatures.

Input data are the layer thicknesses, the coolant temperature T_0 and the heat transfer properties needed (like the heat transfer coefficient to the coolant, the thermal conductivities of the TS1 and the tile, several emissivities, and also an assumed CL transmittance h'). The needed emissivities were assumed (or determined from some of the tests) as follows:

- the emissivity ε_z of the CFC tile is rather well known from the literature to be $\varepsilon_z \approx 0.8$.
- the emissivity ε_h of the heater facing the tile was calculated for several tests from the measured heater temperature T_h , the extrapolated surface temperature of tile T_v , and assuming as a first approximation that the heat fluxes q_z to the tile and q_{pn} to the naked area of the TS1 are equal (which was shown later to be not too far from being true); this calculation resulted in $\varepsilon_h \approx 0.65$, a value that may be found also in the literature for Papyex and Sigraflex.
- the emissivity ε_p of the naked TS1 surface facing the heater (and also parts of the back side of the tile) was calculated for several tests from the measured heater temperature T_{hn} for a position outside the tile areas and assuming again $q_{pn} = q_z$ and $\varepsilon_h = 0.65$ like above; this calculation resulted in $\varepsilon_p \approx 0.65$ which seems a little low for the plasma-sprayed surface but was nevertheless kept.

The thermal conductivity of the tile was assumed to be $\lambda_z = 0.35 \text{ W}/(\text{cm K})$.

Each run of the code is performed for a given heat flux q_z into the surface of the tile. It is first assumed that the total heat input to path 1 passes as q_p only at CL into the coolant. Starting from T_0 as an input quantity a temperature profile back to T_r is computed. With T_r at the tile's back side (T_r is assumed constant along the tile because of its very high

conductivity) q_r may be calculated. Now q_p may be reduced appropriately and the above process is repeated in a loop until the sum of the power that leaves the tile at q_p and q_r is close enough to the power that enters the tile at q_z . The temperature difference across the tile is then calculated from

$$T_v - T_r = \frac{q_z + 0.75 q_p}{2} \cdot \frac{s_t}{\lambda_t}$$

in which the first quotient takes care of the fact that the heat flux through the tile is not uniform but on the average somewhere between q_z and q_p (the quotient was taken from a comparison with the results of a 2d FE calculation); s_t and λ_t are the thickness and the conductivity of the tile, respectively. On the basis of T_v the heater temperature T_h is calculated from the radiation between parallel walls by applying q_z as heat flux.

For path 2 an assumed heat flux $q_d = q_z$ (as on path 1) allows to calculate a first approximation of T_d by starting from the coolant temperature T_0 . With the radiation law including the shield a better approximation to q_d between the surface temperature T_h and T_d is calculated. The above process is repeated a second time which results in a reasonable approximation to q_d .

For path 3 again $q_{pn} = q_z$ is used as a first approximation to determine a first T_{pn} from the coolant side with which the heater temperature T_{hn} may be calculated from the radiation law; q_{pn} will be improved later.

The procedure for path 4 corresponds to that of path 2; it results in a preliminary value for q_{dn} , which will be improved.

For an initially given value of q_p the specific power q generated by the heater in the tile-covered area (paths 1 and 2) is

$$q = q_p + q_d$$

The heater physically cannot but generating the same specific power q in the surrounding 'naked' area and accordingly q_{pn} is increased in the model until $q_{pn} + q_{dn}$ (for paths 3 and 4) reaches q ; usually only one additional calculation loop is necessary.

As a result, for a given heat flux q_z to the tile the corresponding heat flux q_{pn} to the surrounding area of the naked TS1 is determined.

The code is written to plot a sketch and fill in the input data and the calculated results (temperatures T and heat fluxes q) in the appropriate places. An example for an input heat flux $q_z = 40 \text{ W/cm}^2$ which gives an impression of the resulting temperature and heat flux distributions is shown in Fig. A2. The numbers indicate that the difference between the heat fluxes q_z into the tile and q_{pn} into the naked TS1 is not very big such that false modelling assumptions should not influence the result of the procedure heavily.

The input data that may be read from Fig. A2 are believed to be adequate for the present test; only h' , the thickness s , and the coverage f of the CL were changed according to the individual CL geometries. The code was run with a couple of different heat fluxes q_z for each CL geometry and delivered the corresponding values of q_{pn} and q_r .

The total power absorbed by the specimen is

$$N_{TS1} = q_z \cdot F_z + q_{pn} \cdot (F_{TS1} - F_z)$$

with F_z the area of the two tiles and F_{TS1} the area of the TS1 including tiles. For each input heat flux to the tile q_z the related values of N_{TS1} (power to the TS1) and q_r (radiative heat flux in gaps between the CL stripes) were tabulated. q_z and q_r were plotted as functions of N_{TS1} as shown in Fig. A3. Polynomial fits resulted in the functions $q_z = f(N_{TS1})$ and $q_r = f(N_{TS1})$ given in the respective subsection of Chapter 6.3.3.

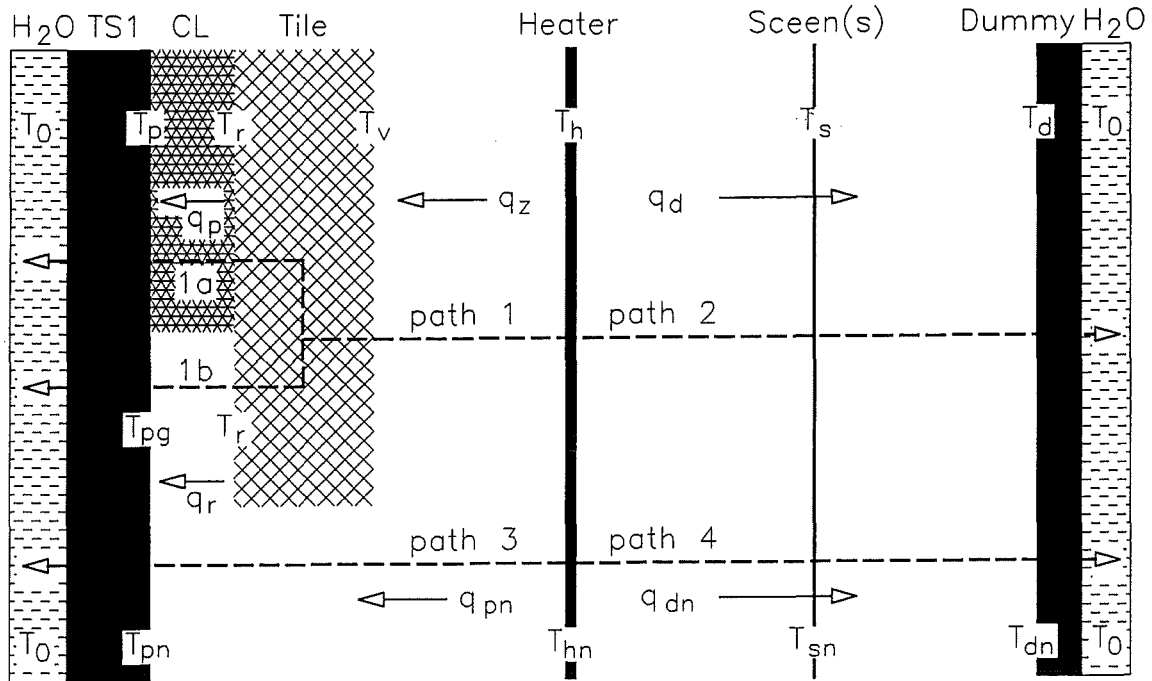


Fig. A.1 Model for BASIC code QF-LT-ZI

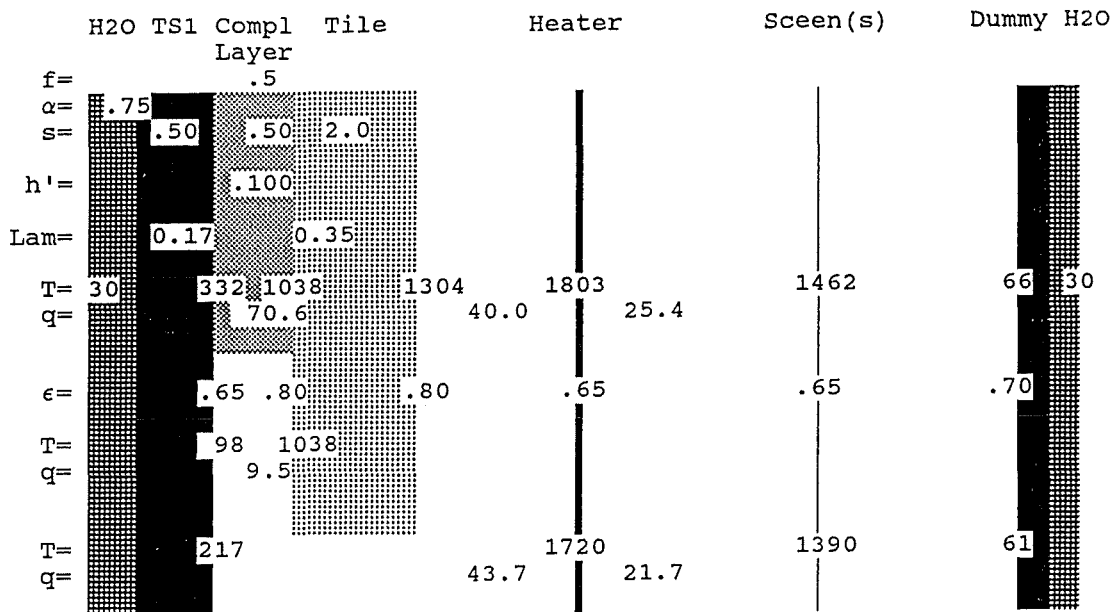


Fig. A.2 Temperatures (T) and heat fluxes (q) resulting from code QF-LT-ZI for the input data as shown

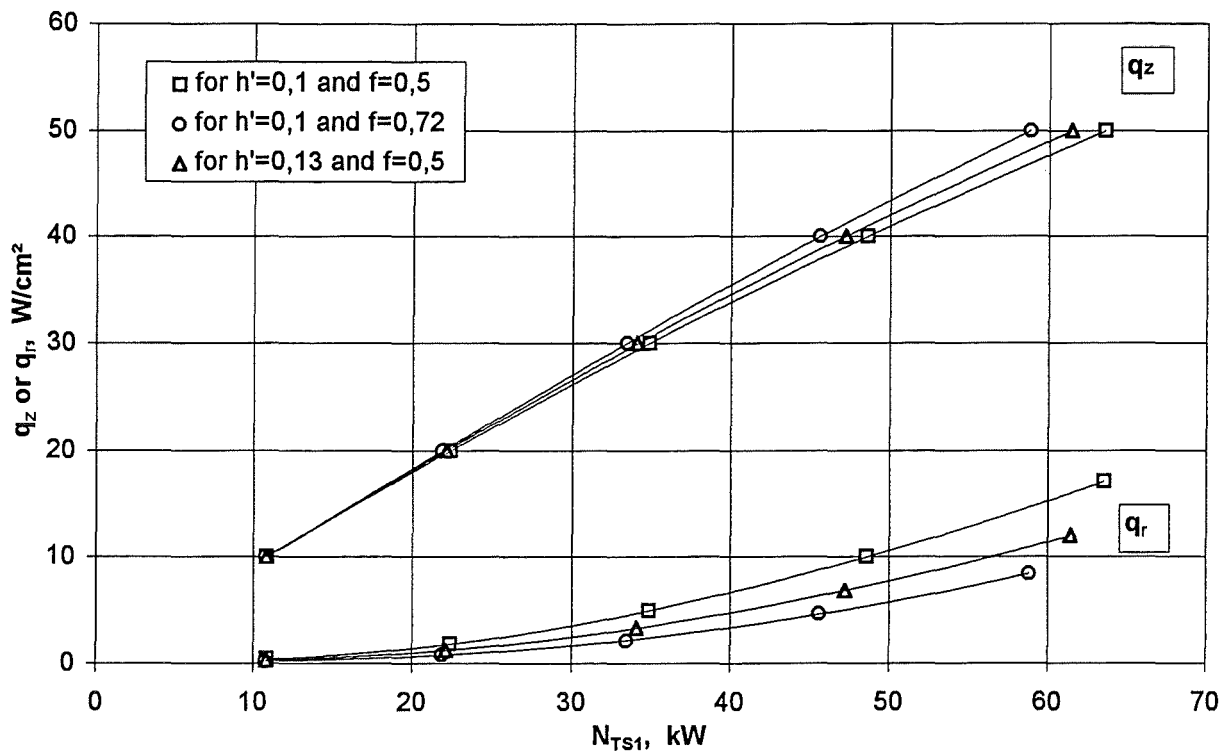


Fig. A3 Local heat fluxes q_z and q_r calculated as functions of the power to the specimen N_{TS1}

Appendix B

Data on CL Heat Transmittance

Figures B1 through B7 are an appendix to Chapter 6.4.1 of the report. They contain all data points on the CL heat transmittance gained. Each of the figures contains data points for one of the test groups. The groups according to Table 6.1 are characterized by the thickness s of the CL, by coverage rate f of the CL, and by the initial contact pressure p . A linear fit through the points is added as a heavy line in each figure; this fit line is used for further discussions in the body of the report. Also added to the figures is a dashed line which indicates the average CL temperature that corresponds to the actual heat flux.

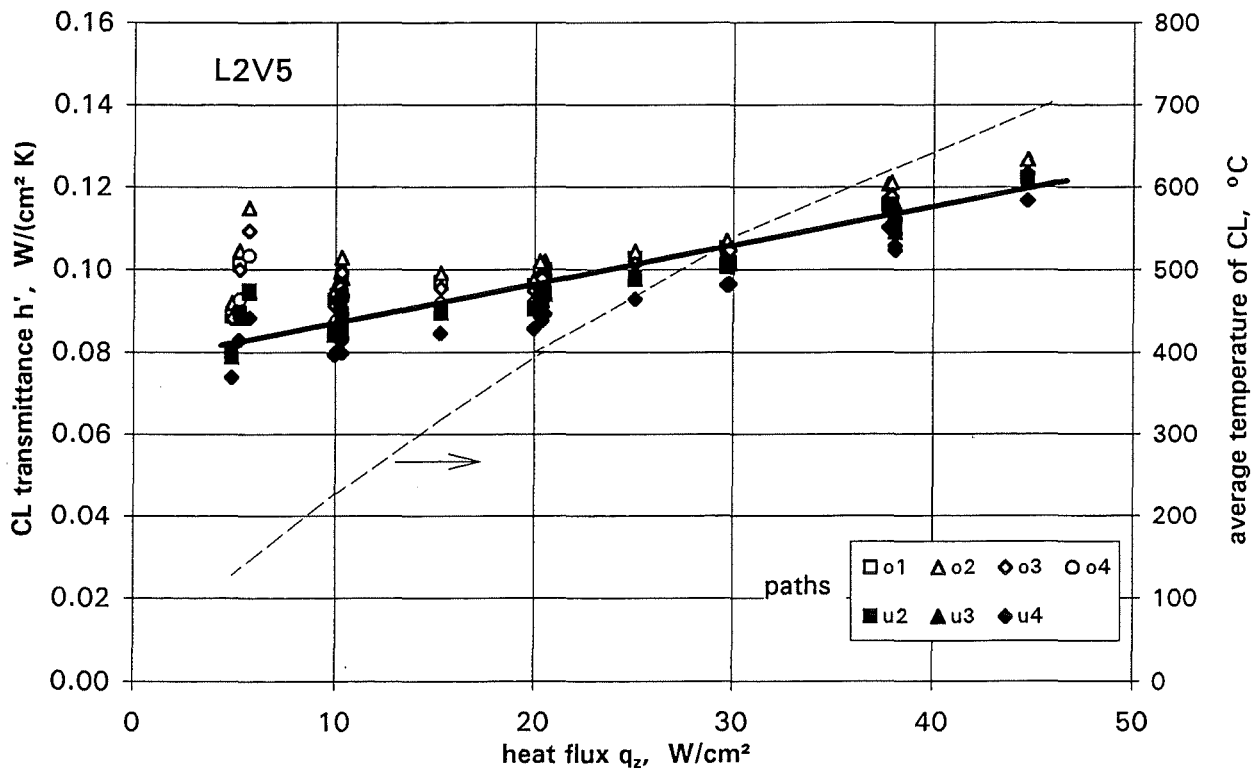


Fig. B.1 Data from test group L2V5 ($s=5$ mm; $f=0.5$; $p=5$ bar)

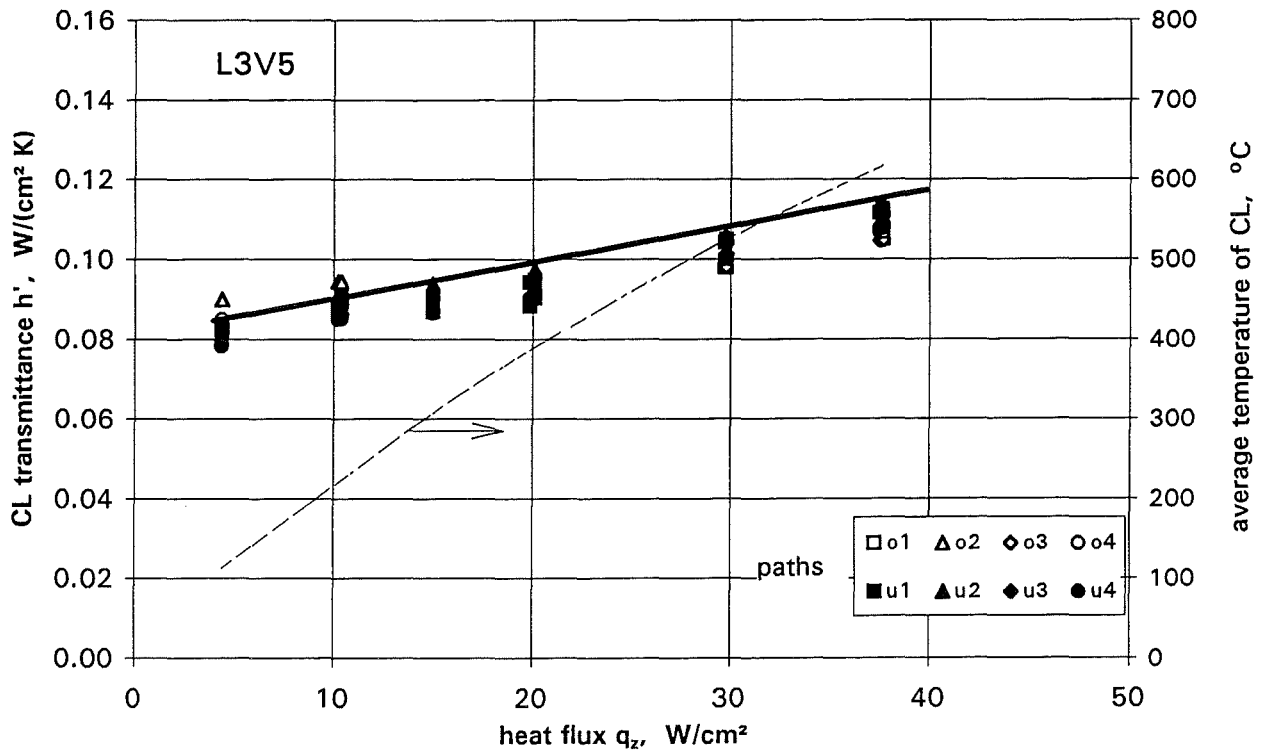


Fig. B.2 Data from test group L3V5 ($s=5$ mm; $f=0.5$; $p=5$ bar)

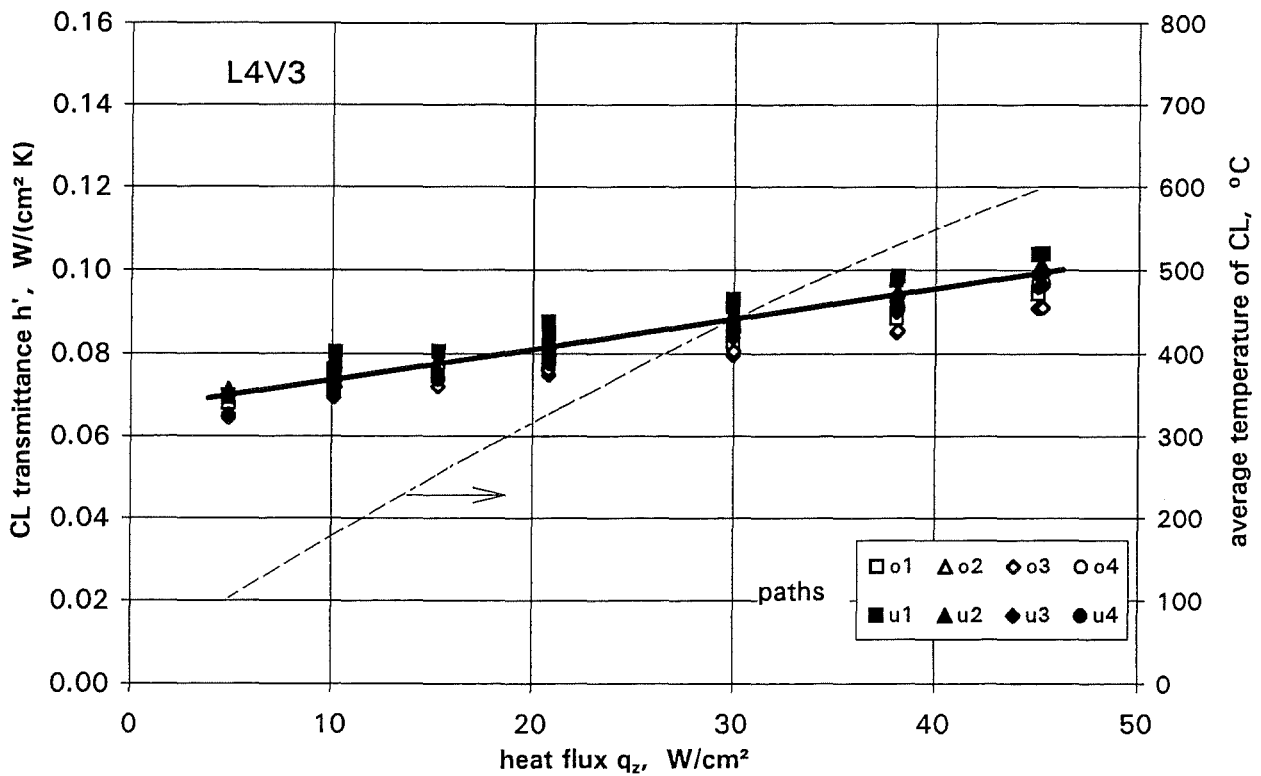


Fig. B.3 Data from test group L4V3 ($s=5$ mm; $f=0.72$; $p=3.35$ bar)

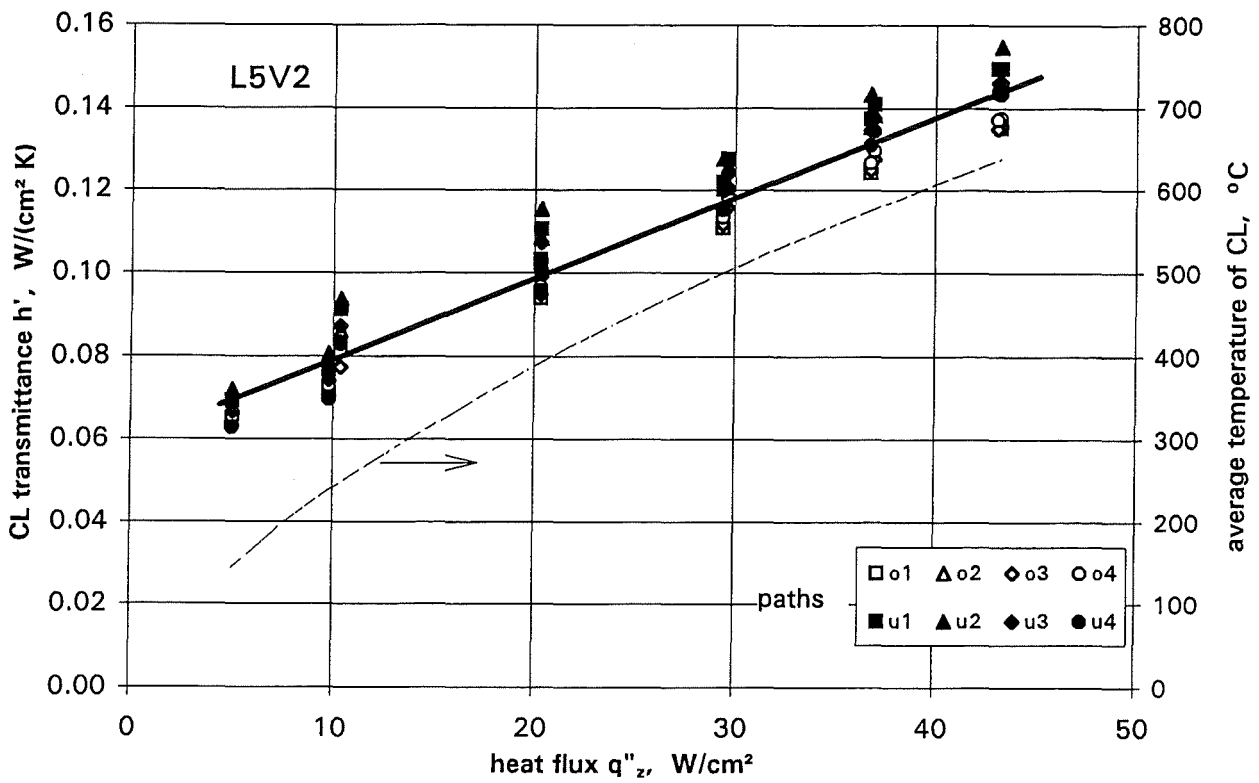


Fig. B.4 Data from test group L5V2, Sigraflex ($s=2.4$ mm; $f=0.5$; $p=2$ bar)

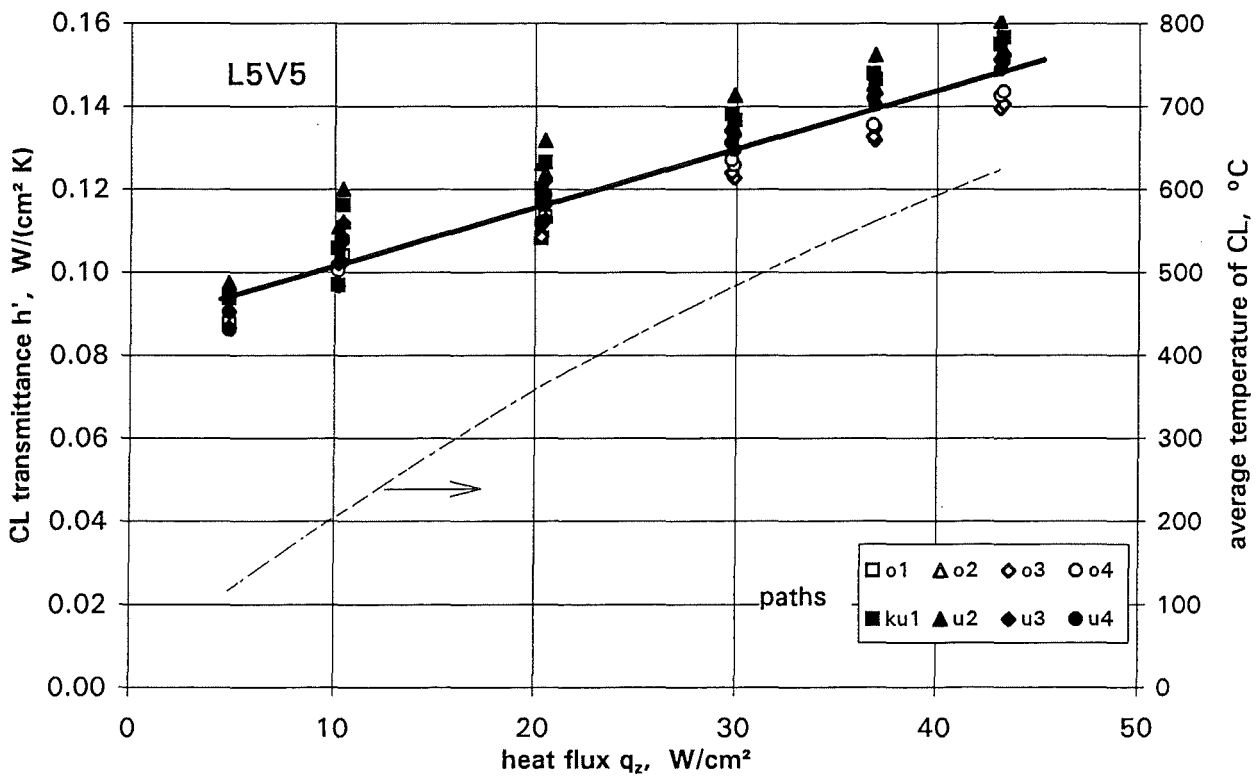


Fig. B.5 Data from test group L5V5, Sigraflex ($s=2.4$ mm; $f=0.5$; $p=5$ bar)

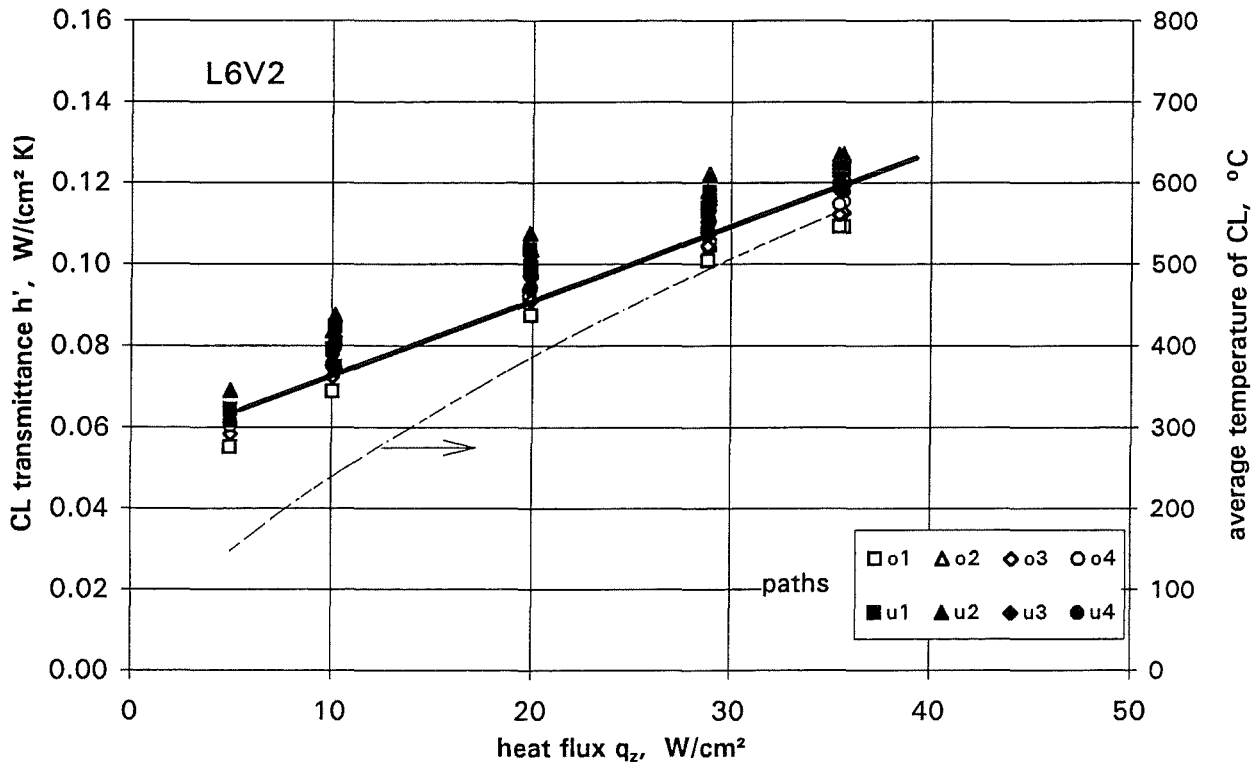


Fig. B.6 Data from test group L6V2, Papyex ($s=2.5$ mm; $f=0.5$; $p=2$ bar)

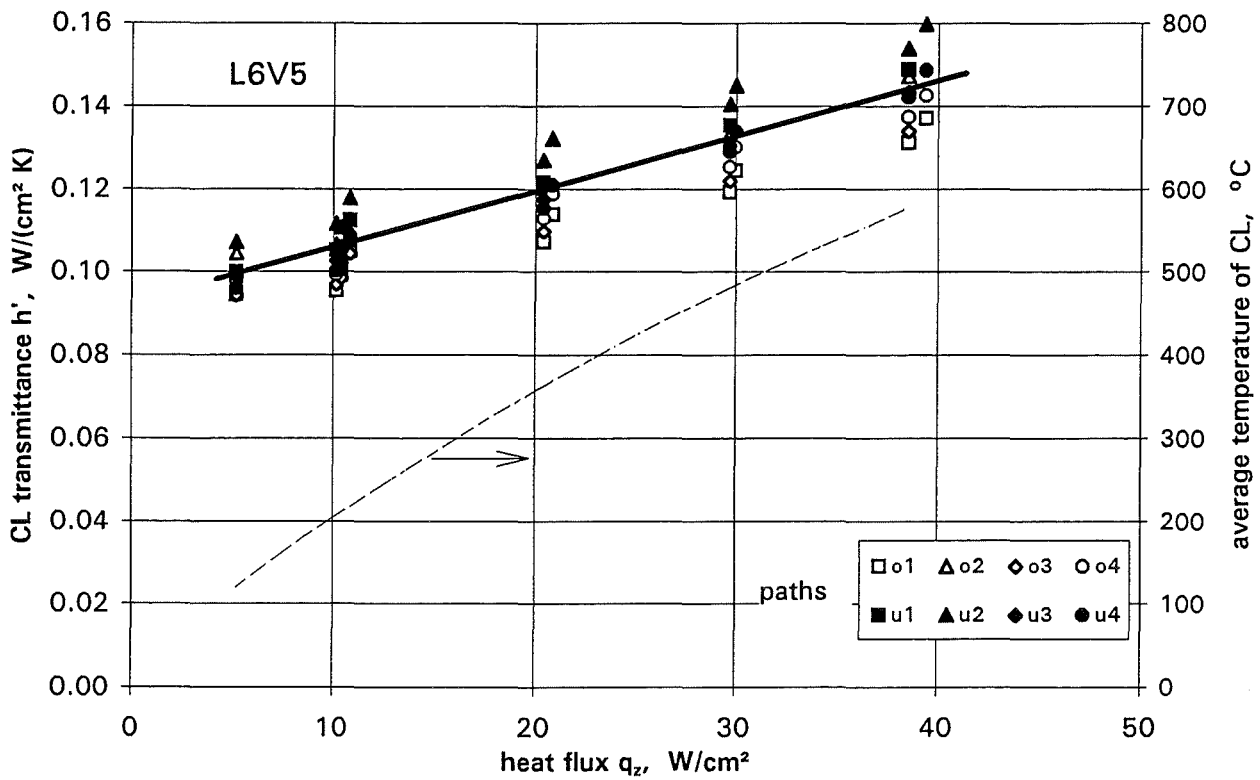


Fig. B.7 Data from test group L6V5, Papyex ($s=2.5$ mm; $f=0.5$; $p=5$ bar)

Appendix C

Influence of the Test History on Heat Transmittance

Figure C1 is an appendix to the end of Chapter 6.4.1 of the report. It shows for the different test groups (see Table 6.1) how the CL heat transmittance has changed as a result of the thermal load applied to the specimen. Open symbols mark the data points gained when, starting with a fresh CL, the thermal load was increased; solid symbols mark the points gained at decreasing thermal load after the CL had experienced the maximum load. There is actually almost no change.

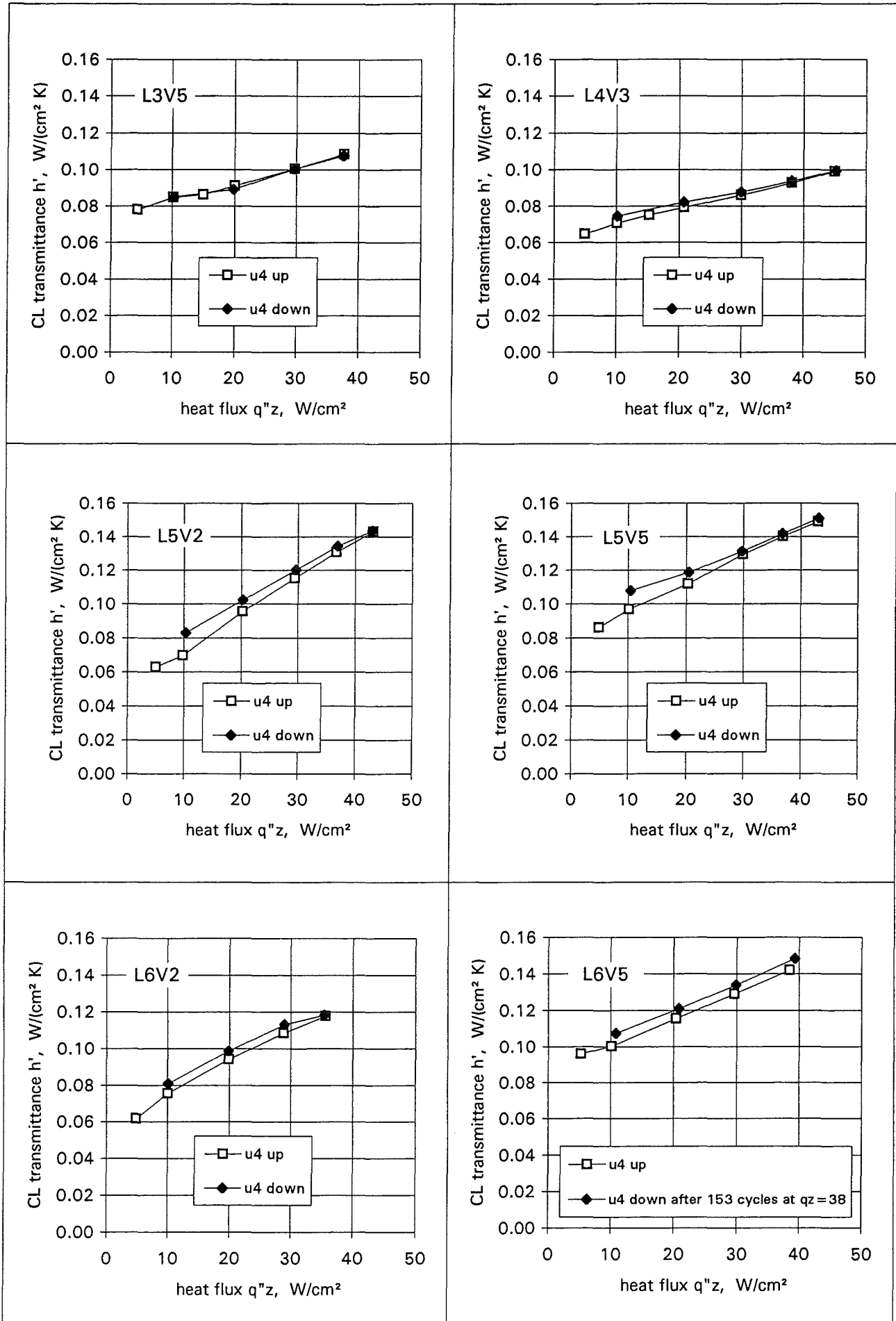


Fig. C1 Influence of the test history on the CL transmittance h' at path u4

Appendix D

Characterization of the Deformation Behavior of Papyex

The deformation behavior of the special order Papyex used as compliant layer with the conductively cooled tile (Chapter 6) was characterized in separate tests by C. Petersen of IMF II. The goal was to determine the compressive stress/strain curves for cyclically applied load at different temperatures.

The specimens used were 14.3 mm wide and 60 mm long stripes of the 5 mm special order Papyex with a density $\rho=0.4 \text{ g/cm}^3$. The testing device consisted of a universal material testing machine Instron 4505 with high-temperature elongation bars surrounded by a tube furnace. The furnace was scavenged with helium when tests at 800 °C were performed but nevertheless some oxidation at the edges of the Papyex specimens occurred.

Tests were performed at three different temperatures: room temperature (RT), 400 °C, and 800 °C. For a selected temperature level the device was heated up until the parts between the cross heads (including specimen, pressure plates and extension bars) had reached steady-state temperatures. Then the tests were run load-controlled and the accompanying deformation (strain) of the specimen was measured between the cross heads; an additional strain measurement between the pressure plates was possible. Load cycles were run on top of a base load of 0.005 MPa. During the cycles the load was increased and decreased at a rate of 0.078 MPa/s resulting in cycle times of between 5 and 15 seconds.

Testing of a specimen was started with 10 load cycles of $\Delta\sigma=0.2 \text{ MPa}$; subsequently the load was increased in steps of 0.1 MPa with 10 cycles at each step; the maximum load was $\Delta\sigma=0.6 \text{ MPa}$. According to this sequence three specimens at each of the three temperature levels were tested.

As an example Fig. D.1 shows some of the stress/strain data gathered. The upper part of the figure represents a test at RT. The small insert on the left shows the behavior during the ten 0.2 MPa cycles: a mixture of elastic and permanent compression is followed by almost purely elastic cycles with a small hysteresis. The elastic portion of the deformation d_e (80 μm) is read from the maximum and minimum values of the last cycle and forms the base for the calculation of the Young's Modulus. The permanent portion of the deformation d_p (45 μm) for this load is read from the decompressed end of the last cycle. The total deformation of the CL under this load would be $d_t=125 \mu\text{m}$ and saturation apparently is reached since d_t would not change any more for further cycles.

The test was continued with the same specimen by increasing the stress from 0.2 to 0.3 MPa and so on and the above evaluation was repeated for each step; for the last step at $\Delta\sigma=0.6 \text{ MPa}$ the results are shown in the large insert on the right: The deformation starts with the permanent deformation left over from the preceding 0.5 MPa step; it was confirmed in separate tests that the deformation at saturation will be the same independent from the preceding test history at lower stress levels. On the $\Delta\sigma=0.6 \text{ MPa}$ level the cycles show more hysteresis and not only the first but also some of the following cycles produce a mixture of elastic of a decreasing amount of permanent deformation; again saturation is almost reached at the tenth cycle and d_e , d_p and d_t may be read.

The lower part of the figure contains two corresponding inserts from a test at 800 °C resulting in a higher deformation which therefore is plotted on a different scale. It is obvious at the first glance and not unexpected that the total deformation is composed of a larger fraction of d_p than in the RT test. Most of this permanent deformation is generated during the first load cycle and only a little is added during the following cycles; therefore saturation may be estimated easily. There is almost no hysteresis left at this temperature level.

For each of the temperature and stress levels tested data from the last cycle (saturation) are plotted in Fig. D.2 as elastic deformation d_e and as total deformation $d_t = d_p + d_e$. Though d_e decreases with increasing temperature d_t strongly increases since the permanent contribution d_p becomes high at elevated temperatures which is important to consider for the evaluation of the tests with conductively cooled tiles.

For each temperature and stress level tested the data from the last cycle were also used to determine the Young's Modulus E as

$$E = \Delta\sigma \cdot s / d_e$$

with $s = 5000 \mu\text{m}$ being the thickness of the specimen and d_e being the elastic deformation at saturation. The results are plotted in Fig. D.3 which shows that E is almost constant with increasing stress amplitude; E does increase with increasing temperature which is understood as a result of the densification that goes along with the higher permanent deformation at elevated temperature.

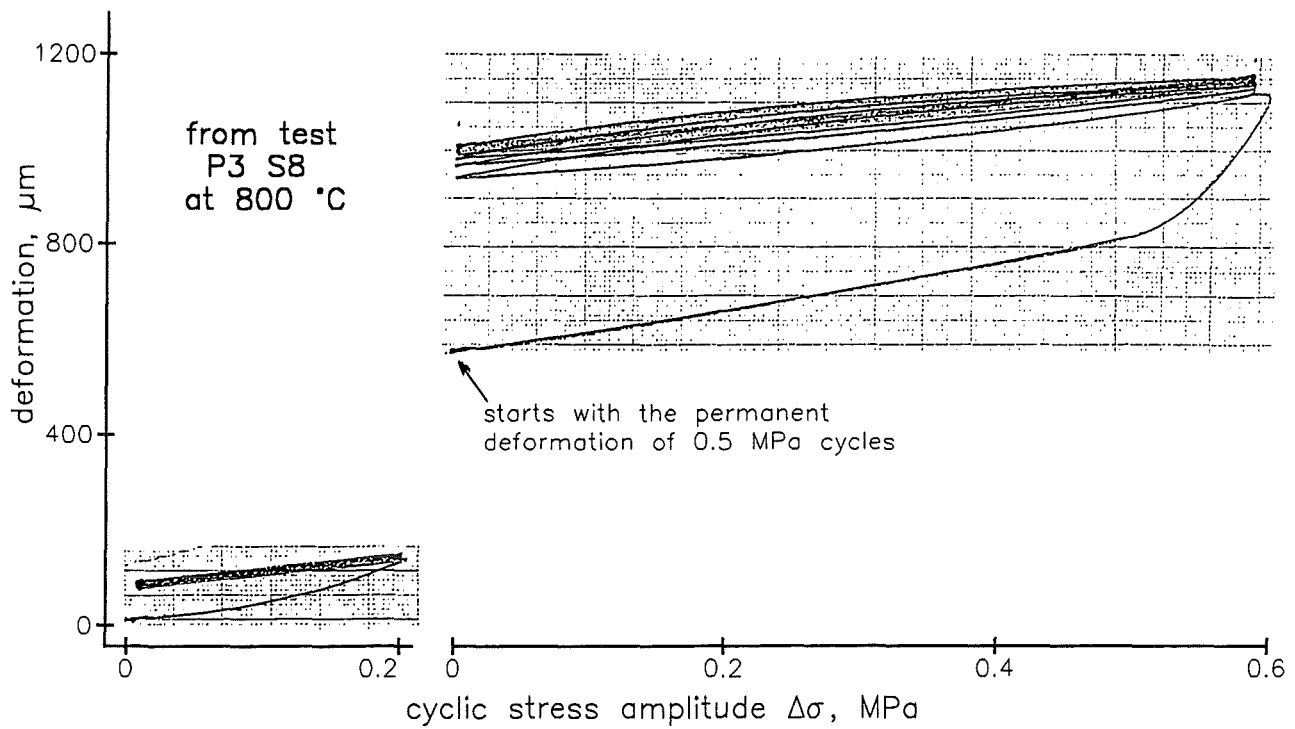
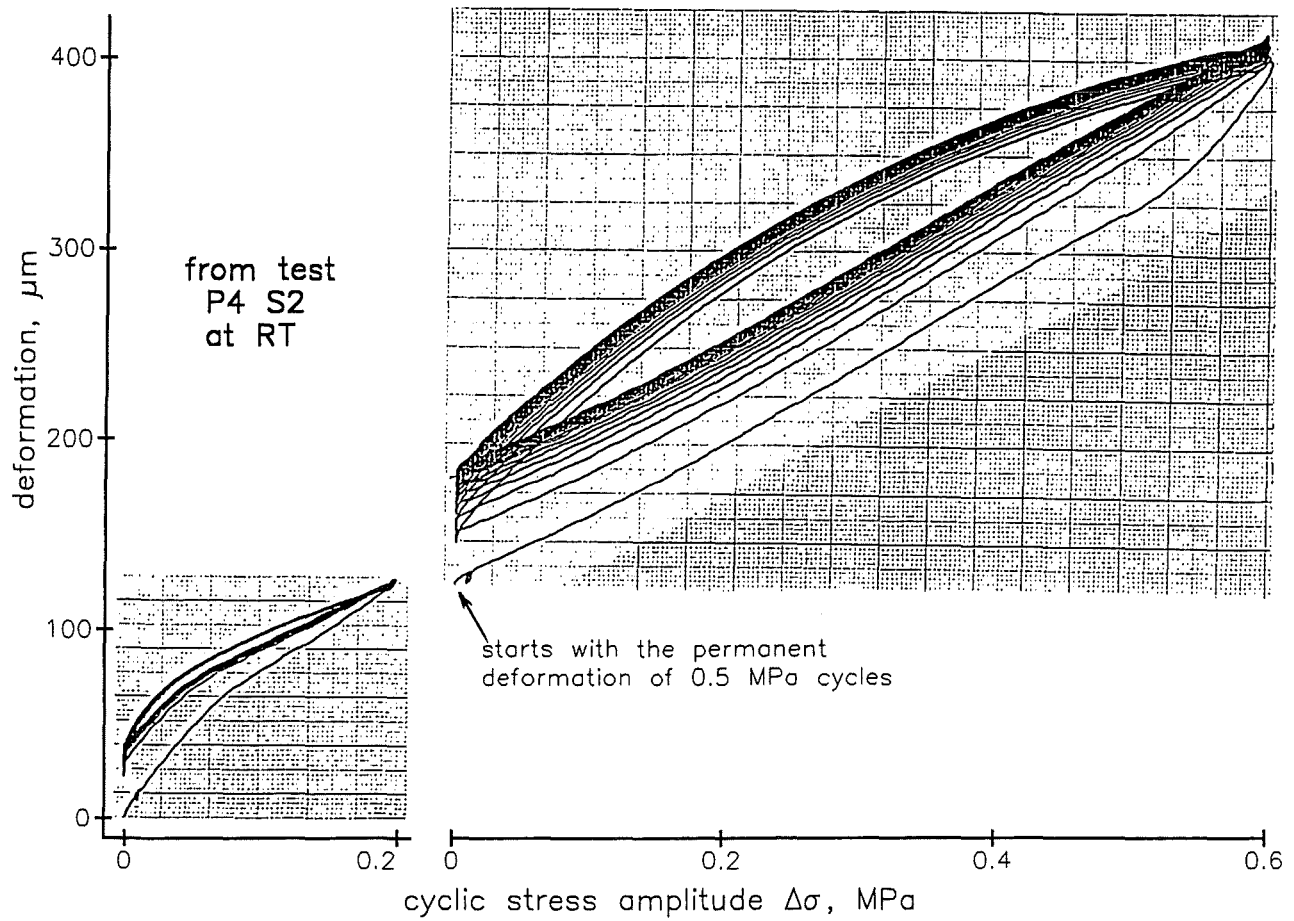


Fig. D.1 Cyclic stress/strain curves for 5mm Papyex at RT(top) and at 800°C (bottom)

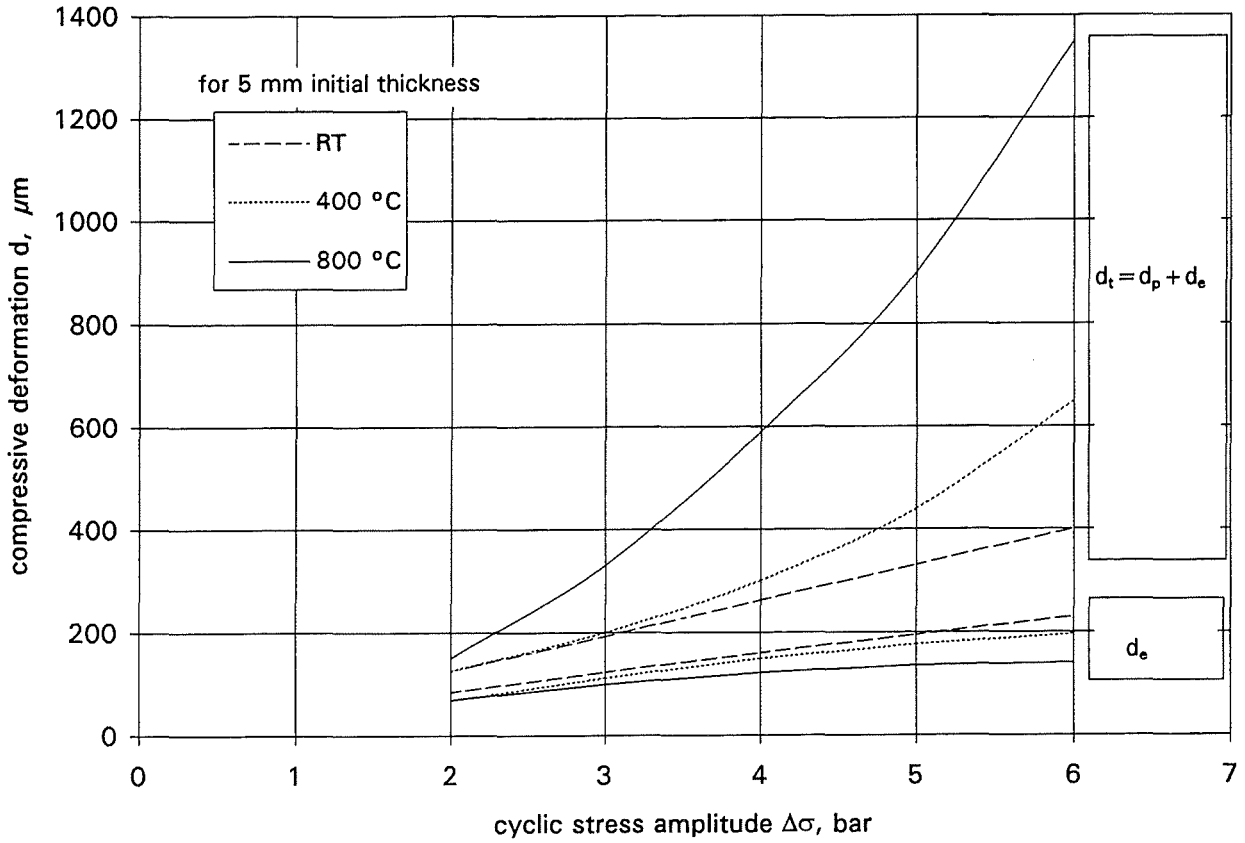


Fig. D.2 Elastic deformation d_e and total deformation d_t of 5 mm Papyex under cyclic load

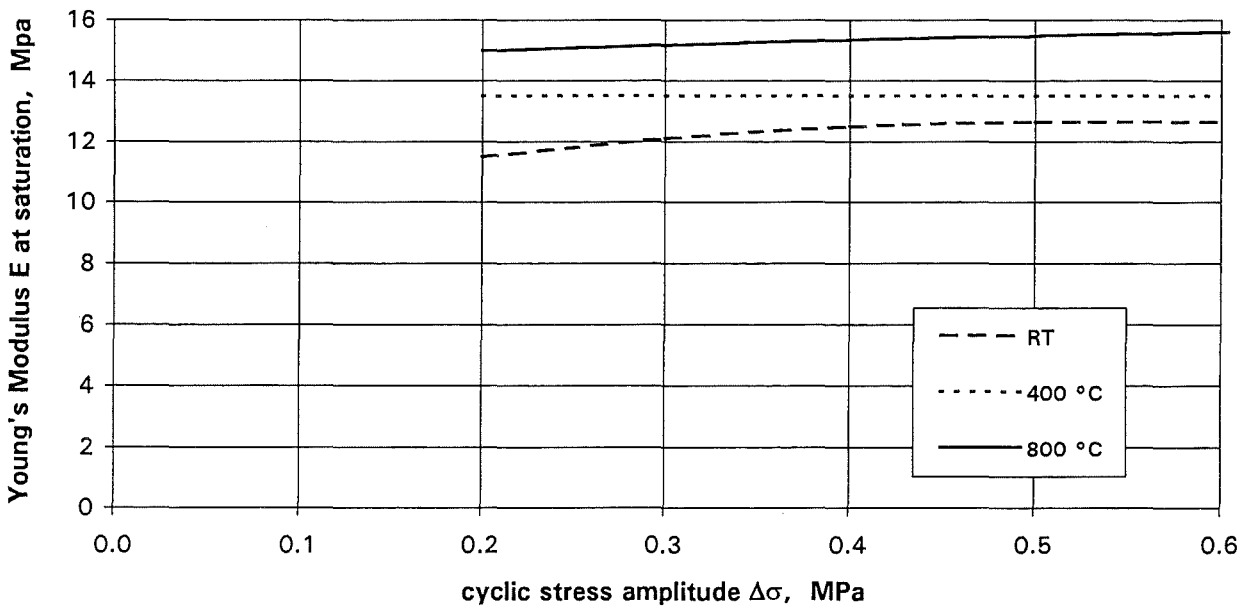


Fig. D.3 Young's Modulus E of 5 mm Papyex at different temperatures